UNIVERSITY OF SOUTHAMPTON

FACULTY OF ENGINEERING AND THE ENVIRONMENT

Fluid structures interactions research group

Development of optical techniques for the experimental analysis of local stress and strain distributions in adhesively bonded composite joints

by

George Crammond

Thesis for the degree of Doctor of Philosophy

April 2013

UNIVERSITY OF SOUTHAMPTON

ABSTRACT

FACULTY OF ENGINEERING AND THE ENVIRONMENT

Doctor of Philosophy

DEVELOPMENT OF OPTICAL TECHNIQUES FOR THE EXPERIMENTAL ANALYSIS OF LOCAL STRESS AND STRAIN DISTRIBUTIONS IN ADHESIVELY BONDED COMPOSITE JOINTS

By George Crammond

This research seeks to evaluate the local stress and strain distributions formed in adhesively bonded composite joints under quasi static and high strain rate loading. A literature review of current analytical, numerical and experimental studies of adhesively bonded joints is presented and identifies the lack of knowledge in the behaviour of composite bonded joints in the through-thickness direction. Detailed analysis of the stress and strain in the joint, and their impact on the development of damage prior to and during failure have been obtained using Digital Image Correlation (DIC).

An experimental methodology is established to perform DIC at the mesoscopic scale using high magnification optics, enabling accurate, high spatial resolution analysis of the strains around the geometric discontinuity between adherends. It is demonstrated that the small through-thickness strains are critical in the development of damage in the joint around the discontinuity between adherends. Errors in the DIC technique are assessed using a robust morphological methodology to evaluate the quality of different speckle patterns based upon the properties of the speckles in the pattern. The strain data is manipulated to evaluate the principal stresses in the joint, which govern failure in the brittle epoxy matrix of the composite, providing a concise evaluation of the transfer of load between the adherends and damage initiation within the joint.

The DIC results and methodology are validated against independent infra-red measurements using Thermoelastic Stress Analysis (TSA). Limitations in the TSA analysis approach are identified around joint discontinuity due to the varying principal stress direction. A new TSA analysis methodology is presented to overcome this. The results of the experimental analysis are used to validate a representative 2D finite element model modelling approach for adhesively bonded joints, showing good agreement to the experimental data.

Finally the full-field DIC methodology is applied to analyse the response of a single lap joint during high strain rate loading, providing unprecedented full-field measurement of the strain fields up to failure.

Contents

List of tables

List of figures

DECLARATION OF AUTHORSHIP

I, George Crammond

declare that the thesis entitled

Development of optical techniques for the experimental analysis of local stress and strain distributions in adhesively bonded composite joints

and the work presented in the thesis are both my own, and have been generated by me as the result of my own original research. I confirm that:

- this work was done wholly or mainly while in candidature for a research degree at this University;
- where any part of this thesis has previously been submitted for a degree or any other qualification at this University or any other institution, this has been clearly stated;
- where I have consulted the published work of others, this is always clearly attributed;
- where I have quoted from the work of others, the source is always given. With the exception of such quotations, this thesis is entirely my own work;
- I have acknowledged all main sources of help;
- where the thesis is based on work done by myself jointly with others, I have made clear exactly what was done by others and what I have contributed myself;
- parts of this work have been published as:

Conferences

1. Crammond, G., Boyd, S.W., and Dulieu-Barton, J.M. Analysis of adhesively-bonded composite joints. 1st UK Marine Technology Postgraduate Conference, 2010, Newcastle University, UK.

2. Crammond, G., Boyd, S., and Dulieu-Barton, J.M. Through-thickness analysis of adhesively bonded composite joints. International conference on full-field measurement techniques and their applications in experimental solid mechanics (Photomechanics), 2011, Brussels, Belgium.
3. Crammond, G., Boyd, S., and Dulieu-Barton, J.M. Full-field analysis of the through-thickness load transfer in composite double butt strap joints. International Conference on Adhesive Bonding, 2011, Porto, Portugal.
4. Crammond, G., and Boyd, S., and Dulieu-Barton, J.M. Speckle Pattern Characterisation for High Resolution Digital Image Correlation. International Conference on Advances in Experimental Mechanics: Integrating Simulation and Experimentation for Validation (ISEV), 2011, Edinburgh, UK.
5. Crammond, G., Boyd, S., and Dulieu-Barton, J.M. Through-thickness load transfer in adhesively bonded composite joints. SEM XII International Congress & Exposition on Experimental & Applied Mechanics, 2012, Costa Mesa, USA.
6. Crammond, G., Boyd, S., and Dulieu-Barton, J.M. A methodology for evaluating localised strains using high magnification DIC. SEM XII International Congress & Exposition on Experimental & Applied Mechanics, 2012, Costa Mesa, USA.
7. Crammond, G., Boyd, S., and Dulieu-Barton, J.M. A validated point-wise approach to the analysis of stresses and strains around complex composite geometries using Digital Image Correlation and Thermoelastic Stress Analysis. Modern Practice in Stress and Vibration Analysis (MPSVA) 2012 Glasgow UK

Publications

1. 'Speckle pattern quality assessment for digital image correlation' – Accepted Optics and Lasers in Engineering 2013
2. 'Dynamic analysis of composite marine structures using full-field measurement' Submitted - Journal of Marine Engineering and Technology 2013
3. 'Evaluating the localised through-thickness load transfer and damage initiation in a composite joint using digital image correlation' Submitted – Composites Part A 2013

Signed: ……..

Date:…….

Acknowledgements

I would like to express my thanks and appreciation to all those that have supported and entertained me during my PhD studies. Particular thanks go to Andy Robinson, Duncan Crump, Gary Battams, Marco Longana, Rachael Waugh, Richard Fruehmann, Richard Hebb and Shufeng Zhang for sharing their knowledge and advice in experimental mechanics. Thanks are also due to Angus Webb, Caleb Sawade, Chris Phillips, Ewan Tarrant, Mari Malmstein and Joe Banks for sharing in my journey, helping me through the good and bad times with laughter, fun and coffee. I'd also like to extend my gratitude to the support of The Institute of Marine Engineering, Science & Technology, and to my supervisors Prof Janice Barton and Dr Steve Boyd.

Nomenclature

1,2,3	Principal composite material direction
1^{p},2^{p}	Principal stress direction
$\alpha^{p}_{1,2}$	Coefficients of thermal expansion in principal stress direction
γ_{12}	Principal material shear strain
$\varepsilon_{1,2}$	Principal material strains
Θ	Principal stress angle
ν	Poisson's ration
$\nu_{12,\,21}$	Poisson's ratio in principal material directions
ρ	Material density
$\sigma_{1,2}$	Principal material stress
$\sigma^{p}_{1,2}$	Principal stress
σ_{peel}	Peel stress
τ_{12}	Principal material shear stress
τ_{a}	Average shear stress across joint
τ_{max}	Maximum shear stress
τ_{x}	Shear stress at distance x from centre of joint
$\bar{\tau}$	Distributed shear stress
Φ	Camera angle from perpendicular to specimen
a_{ij}	Pixel grey level value at location ij
$\bar{a}$	Mean subset grey level
c	Half overlap length
C_{p}	Specific heat capacity at constant pressure
$E_{1,2}$	Young's modulus in principal material directions
G_{12}	Shear modulus in principal material directions
H	Pixels across height of image
$I_{P,i}$	Pixel grey level value at location p, i
k	Bending moment factor

k'	Transverse force factor
$K_{1,2,12}$	Thermoelastic constants in principal material direction
$K^{p}{}_{1,2,12}$	Thermoelastic constants in principal stress direction
l	Overlap length
N	Number of pixels in subset/image
P	Applied load to joint
$\overline{P}$	Force per unit length
$p(x_i)$	Shannon entropy probability mass function
$[Q]_{12}$	Principal material stiffness matrix
s	DIC shape function parameter vector
$t_{1,2}$	Adherend thickness
t_a	Adhesive thickness
T	Temperature
ΔT	Change in temperature
u, v	Horizontal and vertical translation
[T]	Transformation matrix
W	Width of overlap
W	Pixels across width of image

1. Introduction

1.1 Background

The use of polymer composites in the marine industry is rapidly increasing due to their beneficial specific material properties [1], [2]. The utilisation of composites offers significant structural weight savings, without reducing the overall strength or integrity of the structure. The improved design, fabrication and structural performance of low cost composite structures has been exploited in a wide range of applications such as control surfaces, bulkheads, hull and secondary structure in naval, commercial, rescue and leisure vessels. In naval applications weight savings up to 36% are possible when using composite materials instead of comparable steel vessels [3]. The weight reduction resulting from the implementation of composites in the manufacture of vessels has achieved operational and financial gains such as increased payload capacity and improved fuel consumption.

However, the increasing size and geometric complexity of marine structures makes it impractical and expensive for the composite structure to be manufactured in a single shot continuous moulding process. Therefore there is a requirement to assemble the composite structure from many smaller component pieces to form the required geometry, using the attachment of secondary strengthening structure such as ribs and stiffeners to provide structural integrity. In composite structures these components must be connected using mechanical or adhesive bonded joints. In this thesis analysis is focused on the application of adhesively bonded composite joints, which result in lighter assemblies than mechanically fastened alternatives. An example of a typical composite marine structural arrangement is shown in Figure 1, highlighting components bonded to the hull skin such as bulkheads, longitudinal and transverse stiffeners and secondary structures.

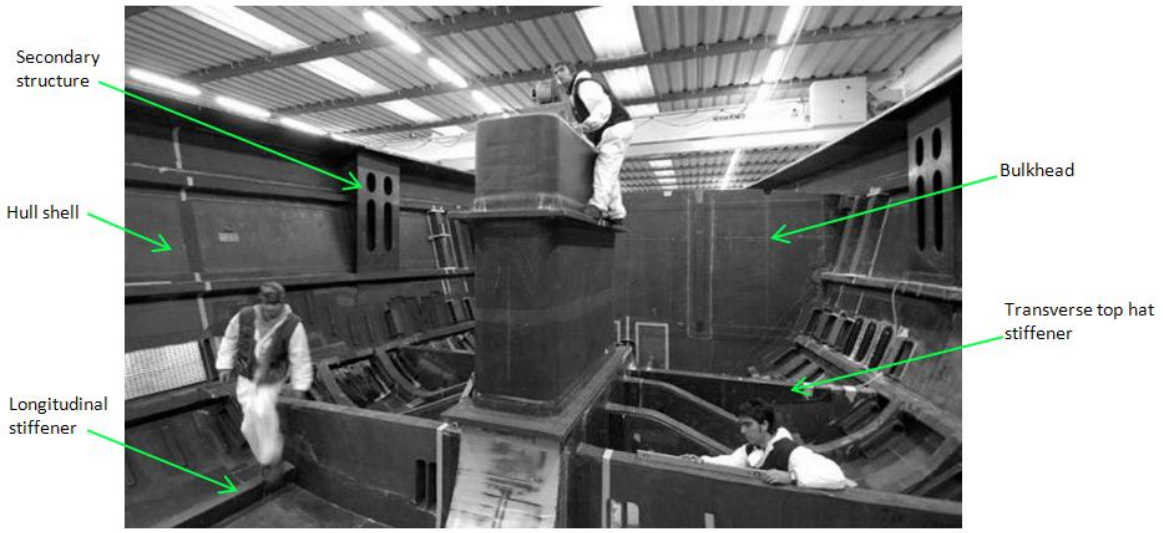

Figure 1: Typical composite structure in yacht hull [4]

In general, joints present a significant design challenge as they inherently contain discontinuities in geometry and material properties, generating complex stress and strain distributions. Such discontinuities act as stress raisers in the joint, resulting in complex localised stress and strain concentrations, which can result in catastrophic and/or unexpected failures in service. Epoxy matrix ccomposite joints provide additional difficulties; though strong in the in plane fibre direction, composites are weak normal to the plane of the laminate. Their strength is dominated by the mechanical properties of the epoxy matrix which is brittle compared to the fracture toughness of the laminate [5], [6]. This is due to the heavily cross linked molecular structure and lack of crack arresting mechanisms [7]. Unfortunately, the discontinuous nature of joints necessitates load transfer in the through-thickness direction between adherends across the adhesive layer. This makes the composite joints, particularly in the adhesively bonded configuration, susceptible to the initiation of interlaminar cracks in the laminate, leading to failure of the joint [8].

Analysis of the stress and strain distributions which develop in the joint under load are required to have a better understanding of damage initiation mechanisms in the structure. Developing better knowledge of the stresses and strains generated in complex jointed structures can be used to aid engineers in designing adhesive bonded joints which will perform more efficiently in service, withstanding higher service loading before failure. Increasing confidence in the behaviour of adhesively bonded joints is seen as an important step in increasing their acceptance in marine structures, capitalising on their advantageous properties.

1.2 Aims and objectives

It is of particular importance to assess the developing stress and strain fields within the joint to investigate failure within the through-thickness, particularly in the comparatively low strength, matrix dominated through-thickness direction.

Analysis is conducted on double butt strap (DBSJ) and single lap joints (SLJ). These configurations have been tested extensively in previous literature, providing a large library of data against which the observed joint behaviour can be referenced. This analysis is used to identify how the local strain distributions in the joint influence the initiation and propagation of damage. Increased understanding of the joint mechanics will result in greater confidence in the structural integrity of adhesively bonded joints and increase their usage; producing lighter, faster and more efficient marine structures. The primary aim of this research is to develop full-field experimental techniques capable of evaluating the local stress and strain distributions formed in adhesively bonded composite joints under quasi static and high strain rate loading. This will be achieved through the following objectives:

1. Generate reliable and accurate full-field non-contact experimental data using Digital Image Correlation (DIC), and quantitatively assess the strain fields generated in the bonded joint structure.
2. Develop a methodology to utilise high magnification optics to obtain high spatial resolution DIC strain data, and examine the initiation of damage at the root of the joint discontinuity.
3. Investigate sources of errors when conducting DIC under high magnification. Emphasis is placed particularly on the imaging and the appearance of the stochastic speckle pattern used in the analysis, providing a high degree of confidence in the experimental data.
4. Manipulate the strain field data to evaluate the material and principal stresses in the joint, and provide informative analysis on the initiation and development of damage and failure in the joint.
5. Develop a methodology for the validation of the DIC data against independent infra-red data collected from Thermoelastic Stress Analysis (TSA), to demonstrate the accuracy of the experimental mesoscopic DIC methodology and results. Use the validated experimental data to assess the performance of a 2D plane stress finite element modelling approach to evaluate the behaviour of the composite adhesively bonded joints.

6. Transfer the DIC methodology developed in 1 and 2 to testing at high strain rate and evaluate differences in the structural and material behaviour at quasi-static and high rate loading incidences, representative of in-service dynamic loading conditions in the marine environment.

These objectives follow a coherent narrative of experimentation, evaluation of measurement error, and validation of the methodologies and results. This structure delivers a high degree of confidence in the analysis of the experimental data presented in this thesis, and the subsequent use of the experimental results in the validation of a simplified finite element approach.

1.3 Novelty

A large proportion of the literature examining adhesively bonded composite joints, e.g. [9–11], analyses the effect of different joint geometries, materials and adhesive thicknesses. This analysis is presented at a global level, through comparisons of final failure strength and deformations. These global approaches do not identify the underlying changes in the material and structural mechanics responsible for changes in strength. Without experimental knowledge of the local joint responses around damage critical areas, leading up to and during failure, informed decisions on efficient joint designs cannot be made. Global measures also fail to fully validate finite element models, as localised yet critical material responses may be insufficiently represented. The work in this thesis focuses on the analysis of local response in the bonded joints, and the development of high resolution techniques which allow measurement of these small, yet critical, strains with high fidelity. The resolution of the data captures important localised concentrations that are otherwise missed by intrusive contact methods such as electrical resistance strain gauge rosettes, due to the size of the gauge, and the single point measurement which they afford. An evaluation of the role which local stress and strain distributions and the through-thickness material properties have on the development of damage is undertaken. Local through-thickness strains are seen to be critical in the initiation and growth of damage, the evaluation of which has not been presented before in literature as a continuum of the load history prior to damage initiation through to failure.

Measurement of the local strain in the joint is complicated by the small magnitude of the through-thickness strains in comparison to the components of shear and axial strain. This provides a significant measurement challenge, requiring new methodologies to conduct DIC. Spatial resolutions and accuracy usually only achievable using Moiré interferometry, [12], [13], are achieved using the DIC technique, removing the practical limitations of Moiré

interferometry caused by bonding a diffraction grating to the specimen surface. These are discussed in greater detail in the literature review in Chapter 2. In developing the mesoscopic DIC technique used in this thesis, a new method of assessing measurement errors and local morphometric analysis of the applied speckle pattern is developed, providing confidence in the accuracy of the DIC measurements.

Thermoelastic Stress Analysis is used to provide an independent high resolution infra-red measurement, against which the accuracy of the DIC strain results are assessed. The work illustrates the major well-known shortcomings of the TSA approach, i.e. the measured data are proportional to the sum of the principal stresses and hence are not able to identify the individual component stresses. In the neighbourhood of the discontinuity of the joint this is particularly important as the principal stress direction changes considerably. The usefulness of using TSA in the context of analysing bonded joints is therefore questionable. However TSA can generate information at high resolution very quickly. Therefore it was decided to use TSA to provide an independent validation of the DIC data. To this end, a new approach is presented that enables a presentation of the TSA stress metric from the DIC data. Using this new method the TSA and DIC data are manipulated into comparable forms so that the DIC data can be validated. The new analysis methods are seen to be vital in the accurate DIC analysis of complex composite structures such as adhesively bonded joints. This is because when high magnification optics are used in DIC the working distance is such that only one camera can be used hence parasitic effects due to out-of-plane displacements may have a significant effect on the data. TSA is not sensitive to these effects and hence can establish if the collected DIC data is representative. The application, and validation, of the TSA and DIC full-field measurement techniques provide complimentary analyse, showing DIC to be a powerful analytical tool to provide informative evaluation of complex composite structures and dynamic loading scenarios

Finally the developed mesoscopic full-field experimental methods are applied to examine full size adhesively bonded joint coupons at high loading rate. Similar tests have only ever examined the global response of the joint on smaller specimens, focusing on the shear response of the adhesive. DIC using high speed cameras is conducted to generate deformation and strain maps of the joint during the loading incidence with a high temporal resolution, identifying individual material, structural and damage initiation sensitivities under increased loading rate.

1.4 Thesis structure

The thesis describes the work which has been conducted since the start of the PhD project. An overview of different joining mechanisms common to the marine industry, and their respective

advantages are discussed in Chapter 2. This briefly explores the motivation behind the research described in the thesis; improving the understanding and ultimately utilisation of adhesively bonded composite joints in marine structures. A review of the literature surrounding the numerical and experimental analysis of the behaviour of joints under load proceeds this. A requirement for evaluation of localised effects, linked to the initiation of damage in the joint is identified, showing limits to the detail provided by numerical approaches. Subsequently, a review of experimental methods and their application to adhesively bonded joints is presented. Attention is focused on the use of full-field non-contact experimental methods, evaluating the through-thickness behaviour of composite bonded joint assemblies. Gaps and limitations in the current experimental methodologies are identified, developing the direction of the research in this thesis. A similar literature study discussing the behaviour of adhesively bonded joints under dynamic, high strain rate loading is also considered. Finally, a justification of the selection of DIC and TSA techniques for the experimental work conducted in this thesis is presented based upon the discussions of the literature.

The definition and characterisation of a suitable test specimen is undertaken in Chapter 3, initially using qualitative assessment of the high speed imaging of the failure incident and ultimate joint strength. A comprehensive evaluation of the material properties in the joint is also conducted. Chapter 4 addresses objective 1, undertaking evaluation of the strain fields in the joint at two increasing spatial resolutions using DIC. The complex localised behaviour observed with the DIC identifies a need for greater spatial resolution of data around the root of the discontinuity; requiring greater image magnification, and a robust methodology to conduct DIC at high magnification (objective 2). The increase in magnification and subsequent significant change in the appearance of the applied speckle pattern requires the error sources in the procedure due to the properties of the speckle pattern to be assessed. The investigations in Chapter 5 give confidence in the mesoscopic DIC technique and results, satisfying objective 3.

A methodology is developed in Chapter 6 using high magnification optics to perform DIC at the meso scale. Localised strain concentrations around the geometric discontinuity between the inner and outer adherend are identified up to failure with high fidelity (objective 2). The development of damage around the discontinuity is discussed through manipulation of the DIC strain data, extracting the individual stresses responsible for the initiation of damage in the structure as per objective 4.

Chapter 7 presents investigations covering objective 5, using high magnification TSA to validate the mesoscopic DIC analysis. The agreement between results also validates the conclusions in Chapter 7 on the selection of a speckle pattern application technique which minimises measurement errors. Limitations in the traditional TSA approach are identified and a

new methodology proposed for the analysis of complex composite structures. The DIC data is validated using the TSA data. The DIC data is used to evaluate the performance of 2D numerical modelling techniques through a comparison of the TSA and DIC stress metrics and the component DIC strains.

The work culminates in Chapter 8 with the application of the DIC technique to the analysis of the structural response of a composite single lap joint at high strain rate loading. The differences between strains in the joint at quasi static and high rate are measured, identifying strain rate sensitivities of the constituent materials and the damage critical joint responses, fulfilling objective 6.

Finally a summary and discussion of the work is presented, followed by conclusions and identification of areas for future work.

2. Literature review

2.1 Introduction

This chapter presents a review of the background and literature relating to the evaluation of adhesively bonded joints and is divided into four separate sections; analytical closed form solutions, finite element approaches, experimental methods and strain rate sensitivity. In each of these sections the current level of understanding is identified and limitations in the analysis discussed. Particular attention is paid to studies which assess full-field stress or strain fields in composite bonded joints leading up to failure. The benefits and disadvantages of the experimental techniques presented in the literature review are discussed, from which an informed decision is made regarding techniques employed in the present research.

2.2 Joining methods

There are two main methods that can be used to join a composite structure. The first, and most commonly used, is mechanical fastening, the second is adhesive bonding.

2.2.1 Mechanical fastening

Mechanical fastenings such as rivets, screws and bolts are widely used to join composite structures. The fasteners are straightforward to assemble, have low component costs, and are easy to inspect; all of which are important for construction, repair and maintenance [14–16]. A typical bolted assembly in a marine structure can be seen in Figure 2, showing the bolted attachment of a stiffener web to a secondary structure, and the bolted attachment of the secondary structure to the main component.

Figure 2: Typical marine bolted joint assembly [17]

In mechanically fastened composite joints, the strength of the joint is mainly provided by the bearing capability of the fastener, across which load is transferred. The clamping forces generated by the fastener also facilitate some load transfer through non-slip frictional forces between components. The weak through-thickness properties of the composite material however prevents the fasteners being highly tensioned without introducing damage, limiting this non-slip load transfer [18]. Metallic inserts can be used to prevent crushing damage, but are expensive and time consuming to manufacture. Mechanical fasteners have a number of advantageous properties. The metallic fastener provides through-thickness reinforcement to the joint, resisting highly destructive through-thickness forces in the joint. This promotes bearing failure of the joint, which occurs at higher loads, hence increasing the load efficiency of the joint. As the fastener and frictional forces provide the strength of the joint, little or no surface preparation of the joint is required, making the technique quick and easy to manufacture. Furthermore, mechanical fasteners allow for the dismantling of components and for the easy inspection, repair and replacement of damaged parts.

Although mechanical fasteners provide a reliable joining method, there are a number of disadvantages in composite applications. Firstly, mechanical fasteners are heavy, reducing the high strength, low weight advantage of using composite materials. The introduction of a hole in the material for the fastener generates large 3D stress concentrations around each hole location. These concentrations produce a non-uniform stress distribution in the joined components across the joint, promoting failure initiation [19]. The holes can also be exposed to damage sustained through delamination caused during drilling, or fretting between the bolt and the hole [20], which reduces both the strength and stiffness of bolted composite joints [21]. Furthermore the exposed edges of the holes create areas for moisture ingress, which is an important consideration in the marine environment, which can significantly reduce the load carrying

capability of bolted assemblies by up to 60% depending on the moisture absorption and exposure time of the laminate [22], [23]. The geometry of the composite bolted joint, such as hole size, hole position and the distance from the hole centre to the edge of the component, have a significant effect on the failure mode experienced, shear and bearing failure being the most common modes. Typical types of failure are shown in Figure 3.

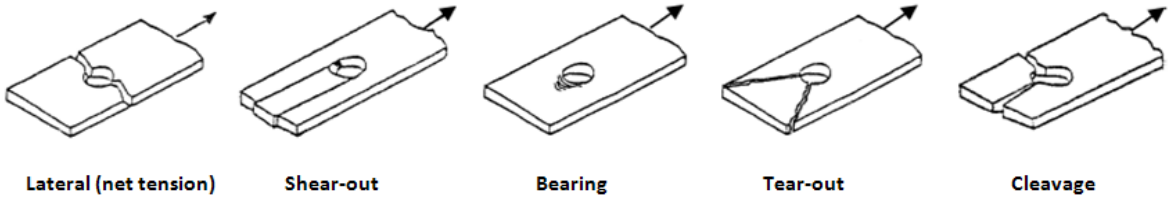

Figure 3: mechanically fastened failure modes [15]

2.2.2 Adhesive bonding

The alternative to mechanical fastening is using an adhesive to bond the components together. Epoxy based adhesives are most commonly used in the marine industry, due to their high strength and ease of application. The adhesive forms a coherent structural layer between surfaces across which load can be transferred as shown in Figure 4. The adhesion between the adhesive and substrate is typically formed by ionic, covalent or hydrogen bonds. In ionic bonding, electron transfer occurs between the adhesive and substrate molecules forming an electrostatic attraction between corresponding anions and cations. Covalent bonds form a stronger bond as electron pairs are shared between the adhesive and substrate molecules. The strength in hydrogen bonds is provided by the electromagnetic dipole-dipole attraction between hydrogen atoms to nitrogen, oxygen or fluorine atoms [24]. The strength of the bond is largely governed by the chemical compatibility between the adherend and the adhesive, which is improved when the bond surfaces are clean. This requires some surface preparation of the component before assembly to avoid contamination of the adhesive, adding some time to the manufacture process. In joints between epoxy adhesives and epoxy matrix composites hydrogen bonds are formed between the epoxide molecules.

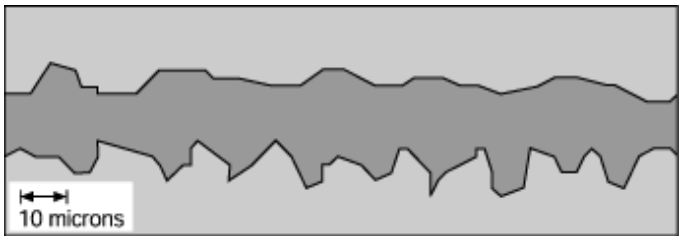

Figure 4: Adhesive layer between adherends [25]

One of the greatest benefits offered by adhesive bonding is a large weight saving over mechanical fasteners [3]. Due to the increased joint load transfer efficiency of adhesive joints, there are also secondary weight savings in the reduction of flange sizes between components. Importantly from a practical point of view, although adhesive joints require time for the adhesive to cure before full strength is reached, adhesively bonded joints greatly improve the ease of manufacturing of marine structures, reducing parts counts and manpower required for assembly, providing production efficiency benefits.

The realization of these benefits can only be achieved when there is a high degree of confidence in the behaviour of adhesively bonded joints. As a result, further investigation of their fundamental behaviour is required, providing the motivation behind this research.

2.3 Analytical models of adhesively bonded joints

Adhesively bonded joints have been studied for well over 70 years, during which a number of closed form numerical solutions have been presented to evaluate the stress and strain distributions in the joints. These closed form solutions offer a fast and convenient method to calculate the joint stresses. Throughout their development there has been an increasing requirement for analysis of the joint at increasing levels of detail, as the understanding of the joint mechanics has changed and new analysis methods developed. A number of anlaystical models are dicussed

The simplest representation of the stress in a single lap joint uses linear elastic analysis. Rigid adherends and constant deformation of the adhesive are assumed, expressing the shear stress, τ_a, in the adhesive as

$$\tau_a = \frac{P}{wl} \tag{1}$$

where P is the applied load, w is the width of the overlap and l is the overlap length.

In practice equation (1) provides a gross under estimation of the stress as it does not account for the behaviour of the adherends, the stress concentrating effect of the discontinuity or the contribution of through-thickness stresses. In 1938 Volkersen [26] published a model to represent the distributed shear stress $\bar{\tau}$ in the joint, taking into account both the shear of the adhesive layer and deformation of the adherends in tension, as given in equation (2) below

$$\bar{\tau} = \frac{\tau_x}{\tau_a} = \frac{\omega \cosh \omega\chi}{2 \sinh \omega/2} + \left(\frac{\psi - 1}{\psi + 1}\right) \frac{\omega \sinh \omega\chi}{2 \cosh \omega/2} \quad (2)$$

Where τ_x is the shear stress calculated at distance x from the centre of the joint, τ_a is the average shear stress as per equation (1), $t_{1,2}$ is the thickness of the adherends, t_a is the thickness of the adhesive and the parameters ω, ϕ, χ and ψ are given by

$$\omega^2 = (1 + \psi)\phi \quad (3)$$

$$\phi = \frac{Gl^2}{Et_1t_a} \quad (4)$$

$$\psi = \frac{t_1}{t_2} \quad (5)$$

$$\chi = \frac{x}{l} \quad (6)$$

This representation of the joint results in a shear-lag effect along the length of the joint, producing a non-uniform shear stress distribution in the adhesive layer as shown in Figure 5. Volkersen's analysis however does not include bending or rotation of the adherends, assuming through-thickness stresses generated by the eccentricity of the load path to be zero, which is a significant limitation of the model.

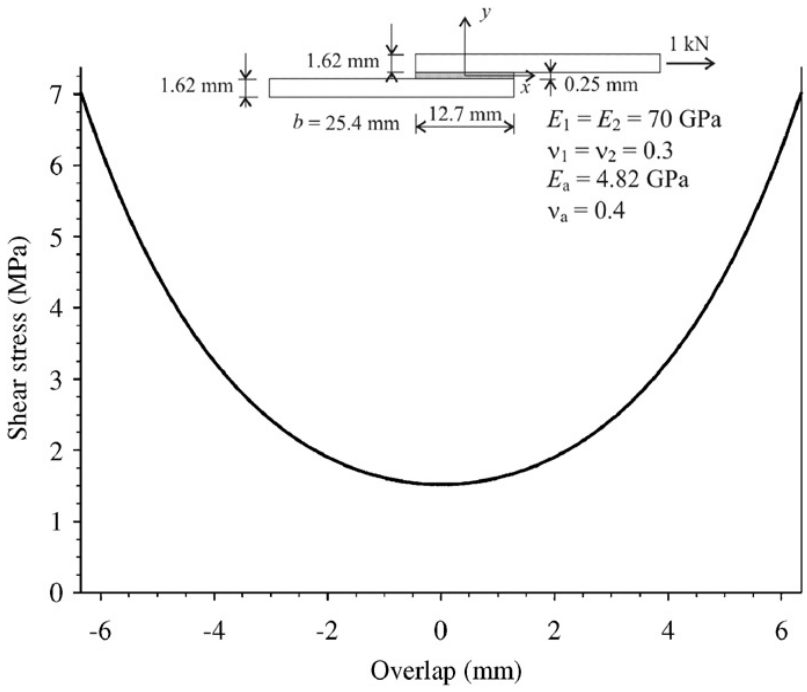

Figure 5: Volkersen's shear stress aproximation in adhesive [27]

Goland and Reissner [28] built upon Volkersen's model in 1944, including the effect of internal bending moments caused by eccentric loading paths in the joint, typical in single lap joints. The model introduces bending moment and transverse force factors, k and k' respectively, into the calculations of the adhesive shear stress and through-thickness stress distributions given as follows

$$\bar{\tau} = -\frac{1}{8}\frac{\bar{P}}{c}\left\{\frac{\beta c}{t}(1+3k)\frac{\cosh\left(\frac{\beta c}{t}\frac{x}{c}\right)}{\sinh(\beta c/t)} = 3(1-k)\right\} \tag{7}$$

$$\begin{aligned}\sigma_{peel} = \frac{1}{\Delta}\frac{\bar{P}t}{c^2}\Bigg[&\left(R_2\lambda^2\frac{k}{2} + \lambda k'\cosh(\lambda)\cos(\lambda)\right)\cosh\left(\frac{\lambda x}{c}\right)\cos\left(\frac{\lambda x}{c}\right) \\ &+ \left(R_1\lambda^2\frac{k}{2} + \lambda k'\sinh(\lambda)\sin(\lambda)\right)\sinh\left(\frac{\lambda x}{c}\right)\sin\left(\frac{\lambda x}{c}\right)\Bigg]\end{aligned} \tag{8}$$

Where the k and k' factors and parameters u_2, β, γ, λ and Δ are given by

$$k = \frac{\cosh(u_2 c)}{\cosh(u_2 c) + 2\sqrt{2}\sinh(u_2 c)} \tag{9}$$

$$k' = \frac{kc}{t}\sqrt{3(1-v^2)\frac{\bar{P}}{tE}} \tag{10}$$

$$u_2 = \sqrt{\frac{3(1-v^2)}{2}}\frac{1}{t}\sqrt{\frac{\bar{P}}{tE}} \tag{11}$$

$$\beta = \sqrt{8\,\frac{G}{E}\frac{t}{t_a}} \tag{12}$$

$$\gamma^4 = 6\frac{E_a}{E}\frac{t}{t_a} \tag{13}$$

$$\lambda = \gamma\frac{c}{t} \tag{14}$$

$$\Delta = \frac{1}{2}(\sin(2\lambda) + \sinh(2\lambda)) \tag{15}$$

The model allows for the calculation of through-thickness stresses induced in the adhesive layer. These stresses in the normal direction are given the term through-thickness stresses and

increase rapidly towards the end of the joint, resulting in a large influence on the joint behaviour. These through-thickness stresses are highly important for composite materials, which are weak in the through-thickness direction compared to their in-plane properties. The shear and through-thickness stress distributions predicted by Goland and Reissner's model for a typical single lap joint can be seen below in Figure 6.

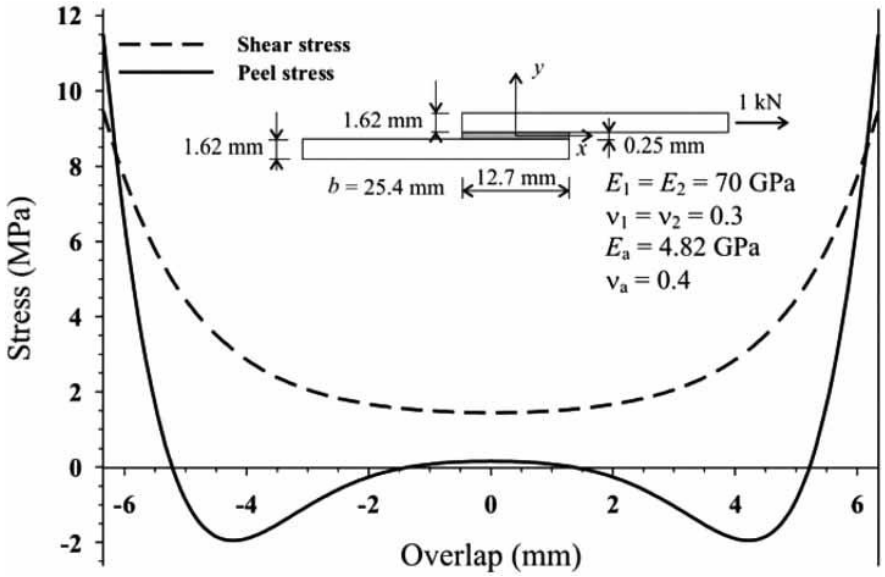

Figure 6: Goland and Reissner's stress distribution [27]

Goland and Reissner and Volkersen's models give a good indication of the stress states in adhesive joints. However there are still a number of limitations in the calculation of through-thickness stresses [27] as through-thickness shear stress and normal deformations of the adherends are not included in the models. Furthermore, the models by Volkersen and Goland and Reissner both violate the stress free conditions at discontinuities at the ends of the adherends.

When considering metallic adhesively bonded joints, neglecting the through-thickness contribution is a valid assumption, as the deformations in the longitudinal direction are significantly greater than through the thickness. However for materials with low transverse shear and through-thickness elastic moduli, such as laminated composite materials, this is not the case. Through-thickness stresses in composite materials cause large transverse shear and normal deformations in the adherends that must be included for an accurate prediction of the joint behaviour to be made. This requires considerably more complex models to analytically describe the localised effects in the laminate. Renton and Vinson [29] presented a model to include terms for the through-thickness shear deflections in the adherends, using first order shear theory in the adherends, which importantly satisfies the shear stress free boundary conditions. A higher order model was developed by Allman [30], which considered variation in

the through-thickness stresses through the adhesive and adherends. Further models have incorporated classical laminate plate theory into the model of the adhesive joint [31], or through the use of high order differential equations, which have the advantage of being able to model dissimilar materials and geometries [32].

A full evaluation of the numerous analytical joint models in the literature can be found in the review papers presented by Banea and Da Silva [8], and Da Silva et al. [27]. The models discussed in this section cover just a small selection of those in literature; however a clear progression in the development of models can be seen, improving the evaluation of localised effects in the joint. Ultimately the complexity required to be able to accurately describe these localised features yields them cumbersome and time consuming to use. The analytical solutions are relatively inflexible to changes in geometry and cannot fully represent variable local mechanics and boundary conditions experienced in the joints. Furthermore these analytical approaches all idealise the response of the joint. Three dimensional effects, which contribute to the stresses and strains in the joint, such as anticlastic bending and non-planar stress / strain fields are ignored. Therefore the models are severely limited in the localised detail that they can provide.

2.4 Finite element analysis approaches

Finite element approaches offer an advantageous alternative to analytical solutions, addressing many of the limitations previously discussed, and importantly providing flexibility in the analysis for a wide range of joint geometries [33] , [27] and applications [34]. Submodelling approaches are commonly utilised in analysis of bonded assemblies to maximise the density of the mesh, whilst keeping computational cost low [36]. Using these methods, a greater resolution of analysis can be achieved, capturing local analysis around damage critical features such as the root of the discontinuity between adherends.

2D models have been used in a number of parametric design studies due to their low computational cost. Modelling and optimisation techniques have been utilised to maximise the efficiency of the joint geometries, including adhesive fillets [33], marine steel/composite connections [34] and the through-thickness shape of double lap joints [37]. The ease of which new finite element models can be generated has led to a large number of different modelling approaches to be presented in the literature for a wide range of problems such as fracture and cohesive zone modelling, hygrothermal aging effects, fatigue and dynamic loading incidences.

Reviews of these models are presented in detail in the literature [38][39], however they lie outside the scope of this thesis.

Although there have been a large number of finite element models presented in the literature, model validation is typically demonstrated by comparison against joint deformation measurements recorded with strain gauges. These methodologies only confirm the global response of the joint and fail to identify the validity of the local stress and strain distributions in the model. Accurate analysis of localised effects was a key motivation behind the move from analytical to finite element solutions, negating much of the closed form solution's benefit.

Full-field experimental results can be used to provide data-rich validation of finite element models, delivering a high degree of confidence to the modelling of complex geometrical problems such as adhesive joints. Ruiz et al. [40] validated 2D plane element and 3D solid element models from the axial strain distributions on the surface and in the joint using Moiré interferometry and neutron diffraction respectively. Both showed good agreement against the finite element model, although a small difference was noted between the strain data obtained from the neutron diffraction in the centre of the joint and the results from the 3D model. This suggests that there is still a significant amount of complexity in modelling 3D adhesive bonded joints that is yet to be fully understood. This difference reinforces the need for accurate experimental results and validations, such as those presented in this thesis.

Moiré interferometry was again used by Ruiz [12] in the validation of a 3D model around the root of the discontinuity of a double lap joint between aluminium and CFRP adherends. Detailed comparison of the shear strain in the joint was shown, as well as qualitative visual comparison between the experimental and modelled components of strain in the joint.

However, both of these studies validate their models using just axial and shear strain components respectively, leaving some uncertainty in the accuracy of the modelling technique. Haghani [41] used a combination of both through-thickness strain and shear angle in the validation of a linear-elastic 3D model of a steel plate reinforced with bonded CFRP adherends. This validation identified the importance of the through-thickness behaviour in the load transfer between adherends, which would have not been considered otherwise. Tsai et al. [13] provides the best comparative validation of a 2D non-linear model around the discontinuity of a composite single lap joint. Validation is provided against all three components of strain across the thickness of the joint at varying locations along the bondline. The comparisons shown by Tsai et al. demonstrate the importance of considering all three strain components. The axial strains show good agreement between the experimental and numerical results, however the through-thickness and shear strain distributions show significant differences between the results close to the root of the discontinuity. These differences are particularly important for composite

adherends, where the through-thickness properties of the material are weak. This validation method ensures that the local model behaviour is representative of the real joint response, yet is not adequately employed in the validation of numerical models.

2.5 Experimental joint evaluation

There are a number of common composite joint designs used in the marine industry; testing of these joints has focused mainly on the behaviour of top-hat stiffeners [42–44] and T-joints [45–47]. Analysis of these joints is important, however due to their size and the complexity of applying representative loading and boundary conditions, which do not lend themselves to the analysis undertaken in this thesis. Repeatable specimens with consistent responses are required in order to confidently assess the capability of the developed experimental techniques. As a result, more common joint geometries such as single lap joints and double lap joints are typically assessed.

The majority of these experimental investigations have applied a parametric approach to testing, assessing joint behaviour on a global scale. Differences in the ultimate strength and deformation of the joint due to a series of geometry changes such as adhesive type [9], adhesive bondline thickness [10], joint overlap length [48], adherend geometry [11], and surface preparation [49] are typically assessed. Discussion of the underlying changes in the joint and material behaviours behind these results is seldom considered, and fails to improve the understanding of the behaviour of adhesively bonded joints. As such this broad category of experimental investigations will be largely ignored within this initial literature review as they provide only qualitative analysis of the joint against which the full-field stress and strain data collected in this thesis cannot be compared against.

Quantitative experimental studies of adhesively bonded joints which present analysis of the stress and strain distributions in adhesively bonded joints are presented below in sections relating to the different categories of experimental technique used.

2.5.1 Contact measurement techniques

Strain gauges

The simplest form of measurement of the joint response is through the use of electrical resistive strain gauges bonded to the surface of the adherends [10], [50], although have also been used attached along the bondline of the adherends [48]. Investigations using the strain gauges have shown good agreement with the trends seen in the closed form analytical solutions [48]; identifying the shear lag effect due to differential extension of the adherends, and deformation of the adherends as a result of through-thickness stresses close to the discontinuity. The through-thickness stresses formed at the discontinuity have been seen to be one of the major contributors towards composite joint failures, due to the low strength of composite materials in the through-thickness, matrix dominated, direction. Fibre tear and light fibre tear failures, as defined by ASTM D5573, are amongst the most commonly experienced for composite adherends [9], [48], [51–53]. Figure 7 shows the mechanisms behind the high through-thickness stresses at the discontinuity promoting fibre tear failure of the composite adherends.

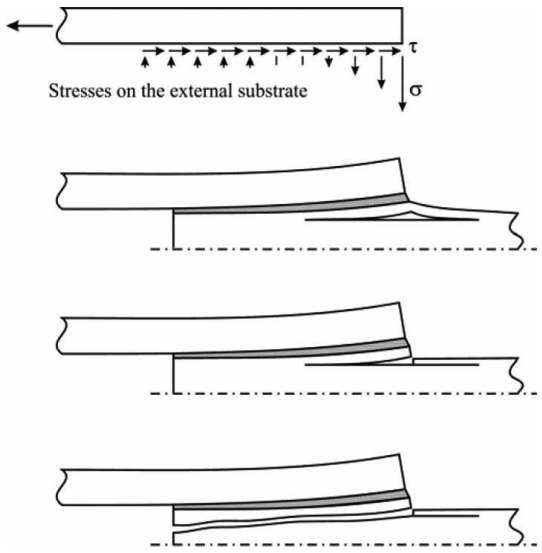

Figure 7: Through-thickness tensile failure [27]

Unfortunately, the use of strain gauges is limited by the single point measurements they provide, which unless using larger, more specialised strain gauge rosettes, can only provide strain measurements in one direction. The gauge length and size of the strain gauge, limit the spatial resolution of the analysis. As a result they cannot provide the resolution required to analyse local strain gradients and concentrations linked to the developments of damage at the root of the discontinuity.

The measurement from strain gauges is also dependent upon the quality of the bond of the gauge to the specimen surface, requiring careful preparation before testing. The attachment of the gauge can result in local stiffening of the specimen and also local heating due to the electric current passing through the sensor, which can both affect the readings.

Fibre Bragg gratings

Long gauge fibre Bragg gratings (FBGs) in optical fibres provide similar point measurement of strain, either bonded on the adherend surface, or embedded within the joint. The technique passes a laser beam down the optical fibre, which is then reflected from a grating etched into the fibre, and travels back to a receiver, and the differences between the wavelengths are measured. As the fibre is strained the spacing of the grating alters, changing the wavelength of the reflected light, from which the deformation and strain at the grating can be established. The gauge length of the FBGs are smaller than that of an electrical resistive strain gauges, providing slightly higher spatial resolution measurement, and multiple gratings can be placed along a single optical fibre, reducing interference with the specimen and increasing spatial resolution.

Murayama [54] used FBGs embedded along the length of the joint and within the adhesive layer to monitor the strain profiles along the joint under load, observing through-thickness strain concentrations at the end of the joint due to eccentricity of the load path. Residual strains in the joint due to post curing of the adhesive were also evaluated, forming compressive strains in the bondline. As FBGs can be embedded into the structure of the joint with relatively little interference, they are well suited to structural health monitoring applications for joints, clearly identifying strain changes in the material as a result of crack growth in the structure [19], or disbonding in adhesive joints [55–57].

The strain profiles created from the FBGs is an improvement on the point measurement of the electrical resistance strain gauges, but it still requires intrusive contact with the specimen, which in itself can alter the strain distributions. However, as the strain is established from the deformation of the grating spacing, only the strain in the direction of the FBG can be determined, heavily limiting analysis.

2.5.2 Non-Contact measurement techniques

The need for high resolution data in the evaluation of the joint requires different experimental techniques to be considered. Non-contact full-field experimental techniques have been in

development for over 50 years [58][59]. These techniques are capable of recording large amounts of data from a specimen's surface, without modifying the mechanical behaviour of the specimen. The application of these full-field techniques has become increasingly popular over the last 20 years as the availability of highly capable, low cost digital cameras and the desire to analyse more complex mechanical problems has increased. The resolution of data using these techniques is far greater than that possible with strain gauges or FBGs, making them well suited to the localised analysis of the developing stress and strain distributions in the joint specimen.

2.5.2.1 **White light techniques**

A number of different full-field techniques have been used to evaluate the stress and strain distributions in adhesively bonded joints. The main white light techniques are presented below in ascending order of spatial resolution of data, along with discussion of their use in the analysis of adhesively bonded joints.

Video extensometery

Video extensometery is a technique which allows non-contact measurement of the surface strains in a specimen as it is loaded. This technique is relatively cheap and quick to set up, requiring little specimen preparation, showing good accuracy relative to traditional contact strain measurement approaches [60]. The resolution of the data using video extensometry can be greater than that of electrical resistance strain gauges, but critically there is no interaction with the specimen surface that could affect the results. A high resolution digital camera is used to record a sequence of images of the specimen under load. The specimen is marked with high contrasting dots or lines, and the distance between which is calculated using an image tracking algorithm, based on the movement of grey level gradients in the image. From the displacement between the high contrast markers, the component strains in the specimen can be determined.

The technique has been used to image the side of the specimen, across the adhesive discontinuity, to assess the axial strains and derive joint stiffness values in composite double lap joints [61]. A similar methodology was also used to measure the relative movement between bonded adherends under tension and shear loading [62]. Multiple strain readings can be recorded from the images captured with the video extensometer, however full-field data cannot

be achieved, as the spatial resolution is limited by the large size of the markers, and the distance between markers required for the image tracking algorithm.

Photoelasticity

Photoelasticity is a simple and cheap full-field technique, which uses the principle of birefringence, or double refraction in white light. Stress or strain data is elicited from transparent materials which are isotropic when unstressed, and optically anisotropic when stressed. The birefringent effect results in the formation of a pattern of coloured fringes caused by interference of polarised light that is resolved along the directions of the principal strain axes in the component. Plane or circular polariscopes can be used to produce linear or circular polarized light. Plane polariscopes produce isoclinic fringes, where the stress is aligned with the axis of the polarisation of the polariser, and iscochromatic fringes to display contours of stress difference, whereas circular polariscopes are used to only produce isochromatic fringes. Stress/strain values are measured directly from the fringe pattern image. Modern photoelasticiy systems use digital measurement systems to analyse the observed fringes with high spatial resolution [63]. High levels of accuracy and sensitivity have been achieved using this method down to 0.005 fringe orders [64].

There are two techniques for photoelasticity. The first is transmission analysis, which creates a replica of the component geometry from a birefringent material. The replica is loaded and polarised light shone at the specimen, from which the intensity of the transmitted light is analysed. Transmission analysis of the composite joint cannot be undertaken due to the large variation in material properties in the composite joint. These cannot be represented by the birefringent material, and so another method must be used. The second technique for in-situ measurements uses a birefringent coating, with a reflective backing, bonded onto the surface of the desired specimen. A polarised light source is directed at the coating, and the fringes in the reflection from the specimen viewed through a linear polarizer to view the resulting fringes. This technique has been applied to evaluate shear transfer through the thickness of epoxy/aluminium joints [65] and verify predictions of stress distributions from Goland and Reissner's analytical model [66]. The technique has also been applied to quantify changes to the stress field in the joint due to the presence of defects in the adhesive bondline [67].

Although a highly informative and fast method of analysis, the presence of the birefringent coating restricts the analysis as it must remain coherently bonded to the specimen under loading. Therefore analysis of the damage initiation and growth in the joint during failure cannot be obtained.

Digital Image Correlation (DIC)

Originally developed in the 1980s, DIC is becoming an increasingly popular method to analyse solid mechanics problems. DIC is an optical technique that uses a correlation algorithm to measure the displacement of a specimen from a sequence of images recorded during loading. A stochastic speckle pattern is applied to the surface of the specimen providing a random grey level distribution that facilitates the correlation algorithm. The recorded images are split into smaller interrogation cells, producing a full-field array of data points across the specimen. At each interrogation cell the grey level distribution of the speckle pattern at time t is compared to the pattern in the subsequent image at $t+\Delta t$. A correlation function value is generated by the algorithm related to the similarity between patterns at time t and $t+\Delta t$. A number of different correlation algorithms have been developed, the core of which can be separated into cross correlation approaches, where the grey level intensities in the interrogation cell are multiplied together, or a sum of square of differences method, where the difference between the grey levels in interrogation cells is calculated. Although the mathematical operators are different, both functions determine a match between patterns when the correlation function they calculate are maximised, or minimised. The correlation function is maximised when there is a good match between the patterns in the two subsets. Areas of poor pattern match have low correlation coefficients. The location of the greatest correlation function corresponds to the location of the deformed subset relative to the reference, from which the image deformation is established. Adaptations of these correlation criteria have also been developed, introducing a degree of normalization into the calculation to correct for changes in lighting and exposure conditions between the images [68]. The technique can be used in either a 3D or 2D capacity. 3D DIC uses two cameras in a stereo vision set up to capture pairs of images of the specimen under deformation [69], from which out-of-plane deformations or 3D shape change under loading can be determined.

A detailed description of the algorithms behind the DIC technique is outside the scope of this review of its application to analysis of adhesively bonded joints, however detailed information on the processes behind DIC are provided in the book by Sutton et al. [69] or the review papers presented by Pan et al. [68] [70].

An overview of the correlation methodology is illustrated in Figure 8

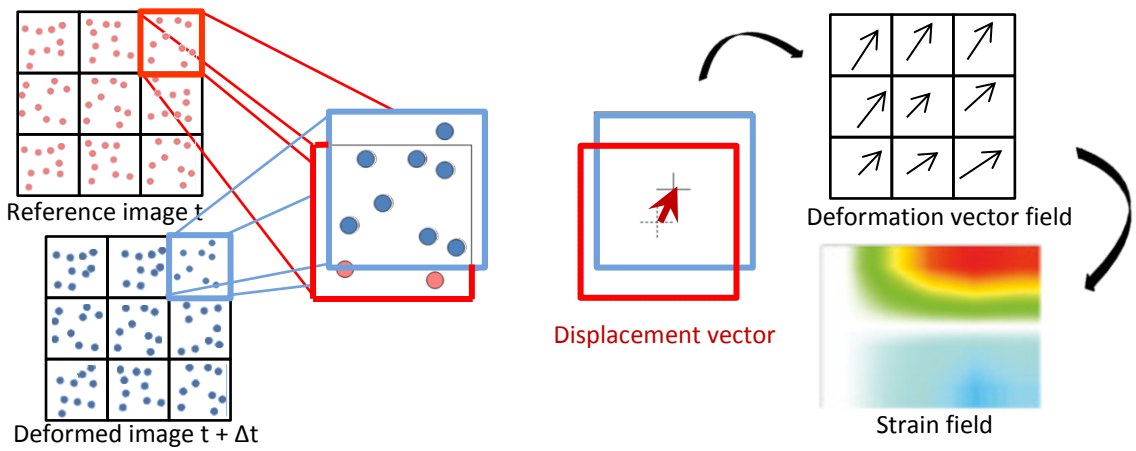

Figure 8: Schematic of Digital Image Correlation process

The accuracy of the strain measurement is increased as the number of pixels and speckles in the interrogation cells which are used to track the movement is increased [71]. Increasing the strain accuracy also has the undesirable effect of reducing the spatial resolution of the data, so a compromise must be found. Strain accuracy and spatial resolution can be improved either through increasing the resolution of the images or by using high magnification lenses to zoom in on the area of the specimen being analysed.

For accurate measurement of the displacements, sub-pixel measurement of the correlation function is required. The position of the correlation peak can be measured using a number of methods, including interpolation of the image grey level values [72], 2D Gaussian curve fitting methodologies [73], or through more popular iterative search methods [74]. These iterative search methods use shape function parameters which define the deformation of the subset. The shape functions are iteratively solved using numerical methods such as the Newton-Raphson approach or the Levenberg-Marquardt algorithm until the correlation coefficient is maximised. The application of appropriate subset functions is vital to DIC measurement accuracy [75].

Similarly, a number of different methodologies have been presented in the literature for the determination of the strains in the specimen from the calculated displacement fields. Numerical differentiation of the displacement fields provides the simplest method, however it is very sensitive to noise in the displacement signal [76]. Iterative search methodologies have also been presented to optimise a matrix of the DIC displacement gradients relative to a window of the neighbouring displacement results [77]. The optimisation of the gradients relative to the neighbours considers the strain fields as a continuum across the whole full-field array, reducing noise in the strain field.

The application of DIC is a popular tool for the analysis of adhesively bonded joints due to the ability to obtain a high spatial resolution of data. Investigations have focused on two main areas in the joint: shear behaviour of the adhesive between the adherends, and identification of the material response in the adherends under load. The latter addresses the limitations of the global joint strength investigations identified at the beginning of this section, by investigating the changes in the strain distributions resulting from geometry and material changes. Common to both of these sets of analyse is the underlying need for high resolution data.

The developing shear strains acting in the adhesive layer between adherends were evaluated by Nunes [78], extracting in-situ shear modulus values of rubber-elastic adhesives in a single lap joint. The interface behaviour between adhesives and the adherends has been examined by Guo et al. [79] at very high magnification lens to image a very small area, measuring approximately 0.4 mm x 0.49 mm, across the adhesive bondline in a single lap joint . Horizontal and vertical displacement fields were investigated in the lead up to fracture at the adhesive interfaces assessing the shear response of the adhesive. The adhesive interface has also been investigated by Goutianos and Drews [80] using high magnification optics to observe debonding of the adhesive/adherend interface with a displacement resolution of less than 1 micron. The DIC displacement data was used in the application of a J-integral approach to update cohesive zone models.

Moutrille et al. [81] used an image stitching technique to provide high spatial resolution analysis of the shear strain generated along the bondline. A number of high magnification images across the adhesive interface between an aluminium substrate and a composite strap in a DBSJ were joined together to form a single image across the bondline. Shear strain concentrations were identified at the interface between the adhesive and the composite material in all tests due to the low transverse stiffness of the composite material compared to the aluminium. The experimental data was heavily filtered due to the small thickness of the adhesive bondline, limiting the localised analysis, and also identifying the difficulty of performing DIC at high magnification levels as the sensitivity to camera movement and sensor noise is much higher. Colavito et al. [82], [83] used a similar image stitching technique to Moutrille et al. [81], mounting the camera on a computer controlled 3-axis table, and taking a series of images down the length of the adhesive bond. The slope of the displacement gradients through the thickness of the adhesive layer were analysed, giving a value of the through-thickness strains in the adhesive. Linear displacement gradients were seen in the adhesive, and an increase in through-thickness strain observed closer to the discontinuities in the joint. The through-thickness strain in the composite adherends, or the strain gradients in the adhesive layer, however were not evaluated.

The shear strain concentration at the root of the discontinuity between adherends in a composite single lap joint has been evaluated by Comer et al. [84]. Maximum principal strains in the adhesive spew fillet were analysed up to failure; cohesive damage propagation to corresponding to the locations of highest principal strain were observed. Katnam et al. [85] presented a similar evaluation of the root of the discontinuity of a SLJ to that of Comer et al. [84]. Maximum principal strains and maximum shear strains in the adhesive up to cohesive failure of the adhesive were evaluated, investigating the effect of adhesive ductility on damage initiation behaviour. These last studies begin to move away from pure analysis of the adhesive shear response by showing consideration of the structural response of the adherends in addition to the adhesive layer. The interaction between which is very important in the transfer of load and development of damage.

Wang et al. [86] observed the axial and shear strain distributions at the discontinuity between the inner and outer strap in an area of interest measuring approximately 1.2 mm x 1 mm. Varying types of spew fillet geometry and composite adherend bulges were evaluated, observing beneficial reductions in the axial and shear strain concentrations, due to the load bearing capacity of the adhesive fillets. Good agreement between the strain results and FE modelling was found, which were subsequently used to evaluate the through-thickness strains in the joint, however these were not independently validated. This analysis is much more informative than that presented by Kim et al. [87], who analysed a similar problem without DIC, demonstrating the power of the full-field analysis technique.

Haghani et al. [88] [41] investigated both the principal strain, and component shear and through-thickness strain distributions at the root of the discontinuity between carbon fibre reinforcements bonded onto a steel plate. Although not technically a joint, the specimens featured much the same geometric discontinuity and through-thickness local load transfer into the outer straps as seen in double lap joints. The presence of the adhesive fillet was observed to influence the location of the principal strain concentration [88], moving from the interface with the outer adherend to the inner interface when the fillet was removed. This shows the opposite result to that seen by Moutrille et al. [81], which may be due to the different loading conditions between the DBSJ and the reinforced steel plate. The through-thickness strain shows a very large localised concentration closest to the discontinuity between the adherends [41]. Peak through-thickness strains are twice that in joints with an adherend taper; however as little as 2 mm away from the discontinuity the strains in both geometries return to the same levels. Principal strains and shear strains are largely unaffected by the presence of the taper, yet a reduction of failure load greater than 10kN was recorded, highlighting the importance the through-thickness strains have in the intuition of joint failure.

The application of DIC has also been applied to analyse the principal strains at failure in a double butt strap joint with metallic inner adherends and composite straps [89]. High speed cameras, imaging at a frame rate of 3 kHz, were used to evaluate the formation of damage in the joint. Cracks were observed to initiate at the centre of the joint at the gap between the inner adherends, propagating outwards along the bondline towards the root of the discontinuity to final failure. The full-field strain data was only used to identify damage; global deformation data from strain gauges bonded to the specimen surface were used to validate the finite element model presented in the work.

The grid method

The grid method provides full-field deformation and strain measurement during loading from a bidirectional grid bonded onto the specimen surface [90]. A spatial phase shifting method is used to measure the changes in the phase of light reflected off the grid, due to a change in pitch under deformation. Using this method, displacements as small as 0.5 μm can be calculated [91], offering high precision measurement of the very small through-thickness strains generated in adhesively bonded joints. The grid used in this method can be created using a standard high dpi printer with pitches of up to 10 lines per mm, offering very high spatial resolution, low cost data. Higher pitch grids can be used but the printing method must change. The deformation of the specimen must not exceed that of the grid pitch between images, requiring a balance between the spatial resolution and the expected deformation.

The quality of the analysis is heavily dependent upon correct alignment of the grid on the specimen surface and the quality of the bond between the grid and the specimen. If the grid is damaged or through-thickness off the surface the analysis does not work. Out-of-plane deformations cannot be calculated using the grid method. These deformations result in erroneous in-plane displacements being measured as the image moves out of focus. Similarly the grid method is highly sensitive to rotations of the grid under load, which must be compensated for in order to obtain the phase shift and displacement data [90]. This is a large limitation in their application to adhesive joints, were rotation is expected due to the eccentricity of the load path.

2.5.2.2 **Coherent light techniques**

Moiré interferometry

Full-field strain measurements can be obtained from Moiré interferometry with high spatial resolution. The technique utilises the general concept of wave interference, whereby the superposition of two waves with a variation in frequency, either temporal or spatial, results in the formation of a fringe pattern. A high resolution two dimensional cross-line diffraction grating pattern is printed on a flexible transparent surface and bonded to the specimen surface, similar to the grid method. The fringe pattern is created from two beams of collimated coherent light, in the +1 and -1 diffraction order of the specimen grating. These beams diffract nominally perpendicular off the grid, as the grid deforms with the specimen under load. As the grating deforms, the diffracted beams are no longer collimated, and the wavefronts of the diffracted beams become warped, relating to the deformation of the grating. These warped wavefronts then interfere in the camera plane producing the Moiré pattern of light and dark fringes, Figure 9, which are used to calculate the deformations of the specimen [92].

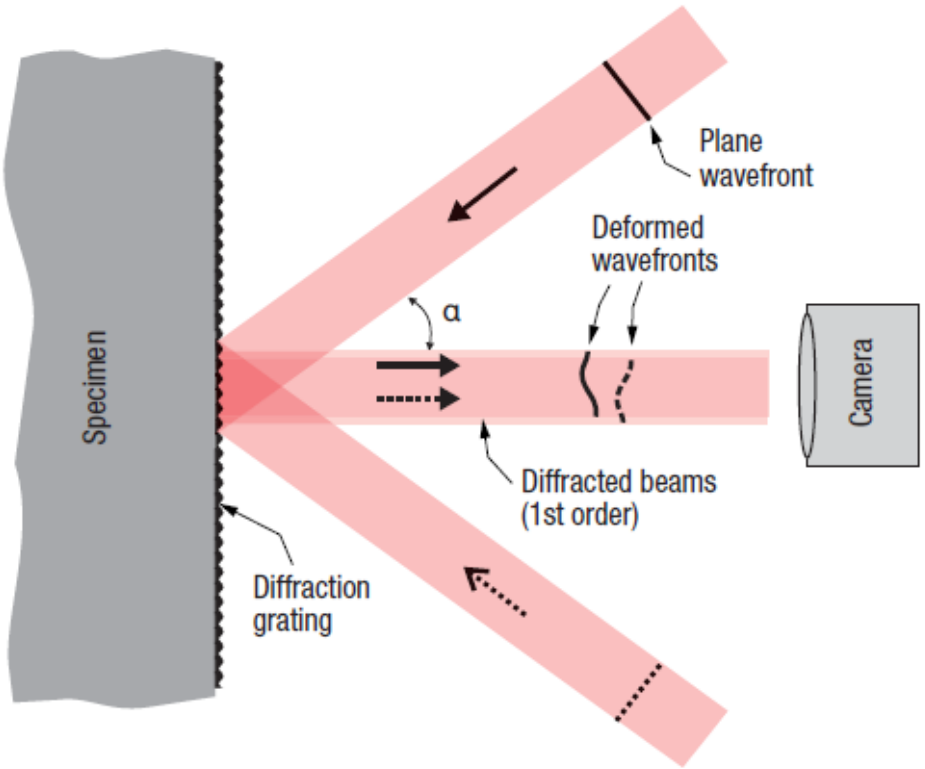

Figure 9: Plan view schematic of Moiré interferometry set up

The technique offers excellent spatial resolution, and a high signal to noise ratio, typically with a sensitivity of in-plane displacements of 0.417 μm per fringe order [93]. The advantage of Moiré interferometry over digital image correlation is the high strain accuracy and high spatial resolution of data possible as illustrated by Mollenhauer and Tyson [94] in a comparison between DIC and interferometry analysing a composite T-joint. Fringe spacing can be as little as 17nm per fringe when using microscopic Moiré interferometry systems. Large deformations can be analysed with this technique, but require a larger spacing of the lines in the diffraction grid pattern, reducing the spatial resolution of data.

The high spatial resolution of the measurement makes Moiré interferometry a very attractive experimental technique to analyse the behaviour of adhesively bonded joints. However the technique requires expensive experimental equipment such as laser sources, which are time consuming to set up. An optical table is also required to accurately align the lasers and the camera so that the diffracted laser beams are perpendicular to the specimen surface. The grating must stay coherently bonded to the specimen during loading, therefore analysis of failure initiation and damage behaviour is heavily limited. Measurement errors can be introduced through poor bonding of the grating to the specimen, which must be flat without any distortion prior to loading. The Moiré fringes can become less visible if the contrast of the grating is reduced due to lighting or poor bonding

The high spatial resolution of Moiré investigations make the technique popular for the analysis of geometric discontinuities in bonded joints. Asundi [95] used Moiré analysis to evaluate the shear behaviour of an adhesive layer between two metallic adherends, with varying overlap lengths. This work is similar to a number of studies presented earlier using DIC, however the high spatial resolution of the data is obtained from the fine pitch of the bonded grating, and not from the use of very high magnification lenses as is the requirement in the DIC studies. Tsai and Morton [96] used Moiré interferometry to analyse the effect of spew fillets at the discontinuity between adherends in a composite single lap joint. Analysis of the adhesive fillet showed a detailed redistribution of shear and through-thickness strains around the discontinuity, reducing peak through-thickness and shear strains significantly. Although this technique provided detailed full-field strain plots of the joint, comparison between the two geometries was conducted along the middle of the bondline. No analysis was shown of the strain changes in the composite adherends. This initial study was followed up in more detail in their following paper [13], presenting thorough analysis of the through-thickness behaviour in the adherends. Through-thickness strain concentrations are observed along the interface between the adherends and the adhesive, indicating local load transfer between adherends. The behaviour of the joint was evaluated from all three component strain terms, identifying strong interactions between the material responses in the adherends. The in-depth strain field analysis was used to validate

numerical modelling methods, as discussed earlier in section 2.4. The sensitivity of the Moiré results in this study identifies bend-twist coupling and anticlastic effects from the surface strain data. This is due to asymmetry of the laminate stacking sequence tested, and a large difference in the loading conditions experienced in the adherends either side of the discontinuity generating different Poisson's ratio effects.

A series of papers have also been published by Ruiz et al. [40] [12] to investigate the strain fields generated by metallic and composite adherends in double lap shear joints. A large field of view of 20 mm x 40 mm was investigated, viewing the strain distribution across the whole of the joint. The measurements of the surface strain data using Moiré interferometry were validated against axial strain measurements from within the centre of the joint under load using neutron diffraction [40]. Good agreement was seen in the analysis of aluminium/aluminium joints; however there was some disparity from the Moiré results for steel/steel joints reportedly due to edge effects. These are more commonly reported in Moiré analysis than DIC studies due to the increased sensitivity of the measurement. Evaluation of the strains was also used in the development and comparison of 3D and 2D finite element modelling methods, also discussed earlier in section 2.4.

A technique was developed in [97] to conduct the Moiré analysis at high magnification levels, focusing on a field of view of approximately 1 mm x 2 mm at the adhesive fillet between adherends. The high magnification increases the spatial resolution of the data, observing localised through-thickness and shear concentrations that were not visible at lower magnification levels. Full-field plots of the axial, through-thickness and shear strains distributions around the discontinuity for the aluminium/aluminium and aluminium/CFRP joint configurations are presented. In the aluminium/aluminium specimens a band of high through-thickness strain can be seen at the interface with the outer adherend at the end of the adherend due to the eccentricity of the load path between adherends. Results from testing of the aluminium/CFRP specimen show through-thickness strain concentrations at the same interface, although smaller and less well defined, due to high levels of noise in the data. The location of the strain concentration agrees with the principal strain concentrations observed by Haghani [41] and Katnam et al. [85], identifying this area to be very important in the development of damage in composite joints. The visual agreement between the studies in literature shows that further accurate, high resolution analysis of the strain concentrations around this discontinuity is required.

Electronic Speckle pattern interferometry

Electronic Speckle pattern interferometry (ESPI) uses the same wave interference principle as Moiré interferometry to form sets of light and dark fringes related to the deformation of the specimen. ESPI however does not use a diffraction grating bonded onto the surface. Instead the speckle pattern is created from the diffraction of a coherent light source off the surface of the specimen, which naturally alters as the specimen surface deforms. A Michelson interferometer is used to combine the speckle pattern diffracted from a rigid reference body with that of the pattern from the deforming specimen. The interference between these combined wavefronts creates a fringe pattern, from which displacement data is obtained.

The setup of this technique is simpler and cheaper than Moiré interferometry as less coherent light sources are required. Due to the use of a very fine natural diffraction pattern from the specimen, generated by the surface roughness, a very high spatial resolution of data, down to 1 pixel is possible. The ESPI technique is capable of measuring very small displacements down to 0.1 μm, but is not suitable for analysis of large displacements. Similar to Moiré interferometry, a steady optical table is required so that vibrations do not influence the speckle pattern from the reference body, limiting the types of structures and loading conditions which can be evaluated. The limitations of ESPI have resulted in very few references in literature where analysis of adhesive bonded joints has been conducted. Those which have used ESPI have typically been for wooden assemblies, due to the relatively low load levels required in the analysis. Investigations of finger joints in timber structures [98] and the shear strain distribution in a wooden single lap joint [99] both show very high spatial resolution of data clearly identifying the formation of localised strain concentrations in the wooden structures.

2.5.2.3 **Infra-red techniques**

Thermoelastic stress analysis

Thermoelastic stress analysis is a full-field experimental technique which uses the relationship between the material deformation and the thermal energy of a solid under loading based upon the thermoelastic effect [100]. Whereby at the same instance as a body experiences a stress change, a small temperature change also occurs. Loading is applied cyclically in the linear elastic region at such a speed that heat transfer is negligible [101], ensuring isentropic temperature change. A highly sensitive infra-red detector is used to measure the change in temperature experienced, ΔT, on the specimen surface due to the thermoelastic effect in addition

to the mean specimen temperature during testing, T. The relationship between the temperature measurements ΔT and T, and the change in the sum of principal stresses, σ^p_1, σ^p_2, is as follows for an orthotropic material [102]

$$\Delta T = -\frac{T}{\rho C_p}\Delta(\alpha^p{}_1\sigma^p{}_1 + \alpha^p{}_2\sigma^p{}_2) \tag{16}$$

$$K^p{}_{1,2} = \frac{\alpha^p{}_{1,2}}{\rho C_p} \tag{17}$$

where α^p_1 and α^p_2 are the coefficients of thermal expansion in the principal stress directions, ρ is the material density, and C_p is the specific heat capacity at constant pressure. These constants form the 'thermoelastic constants', K^p_1, K^p_2, in the principal stress directions. For orthotropic materials such as composites it is assumed that the principal stress and principal materials directions are coincidental [102], as discussed in greater detail in Chapter 7, forming two separate thermoelastic constants K_1 and K_2, which can be easily established from coupon tests of the material in the principal material directions. These values are substituted into equation (16) to form the following relationship between the infra-red data and the sum of the principal stresses.

$$\frac{\Delta T}{T} = -(K_1\Delta\sigma^p{}_1 + K_2\Delta\sigma^p{}_2) \tag{18}$$

A common expression of this relationship is the form of a 'stress metric' given below.

$$\text{Stress metric} = \frac{\Delta T}{K_1 T} = \Delta\sigma^p{}_1 + \frac{K_2}{K_1}\Delta\sigma^p{}_2 \tag{19}$$

The precision and spatial resolution of the temperature measurements makes TSA a powerful analysis tool for analysing areas of high stress gradients [103], and complex stress distributions [104]. TSA has been used in the analysis of a number of complex joint configurations such as finger joints in pultruded GRP materials [105] and GRP tee joints [106], both identifying localised stress distributions resulting from the geometric discontinuities in the joint. TSA has also being used as a successful damage monitoring technique, identifying areas of low stressed material associated with the evaluation of fatigue crack growth in bonded composite single lap joints [107].

The most detailed study of adhesively bonded joints using TSA was presented by Boyd et al. [108], [109]. TSA was used to create a map of the stress metric in a double butt strap joint constructed from pultruded composite material containing thick layers of greatly dissimilar roving and combination mat layers. Large stress concentrations were identified around the discontinuities between the inner and outer adherends, in addition to significant variation in the stresses relating to the material and stacking sequence in the joint. This analysis agrees with previous studies of adhesive joints discussed in sections 2.5.2.1 and 0, which identified large strain concentrations in the vicinity of the discontinuity. The TSA analysis provides a coupled stress metric, and as such a direct evaluation of the axial and through-thickness stresses could not be established. Therefore the experimental data cannot be used directly to evaluate the load transfer or damage initiation in the joint. A 2D finite element model was validated against the experimental stress sum, from which individual stress components could be identified. Good agreement between the stress metrics was obtained, although validation using the coupled stress metric prevents validation of the individual stress components in the model to be undertaken, limiting the analysis of the joint.

2.6 High strain rate behaviour

The literature studies discussed in sections 2.3-2.5 were all been conducted quasi statically. There have been few numerical or experimental investigations which identify the response of adhesively bonded composite joints subject to high strain rate loading. Dynamic loading incidences are common in the marine environment due to heavy seaways, ship motions, or impacts. These produce very fast impulse loading of the structure [110–112], which result in rapidly changing stresses [113], increasing the potential for significant damage to the structure [114]. Under high-rate loading incidences, both metallic and composite materials display rate-dependent material properties. Metallic structures exhibit an increase in stiffness and strength due to plasticity and dislocation dynamics [115]. Composites display an increase in strength due to viscoelastic effects in the polymer matrix. Under high rate load, energy is applied very quickly, activating only lower time and energy scale deformation mechanisms, such as stretching of the electronic bonding between atoms. This atomic deformation mechanism facilitates less deformation of the material, resulting in a stiffening of the material. Less energy is also absorbed over the short time scale, leading to a strengthening of the material before damage occurs [116–118].

Testing of adhesively bonded joints at high rate has focused on the adhesive response [119–121] in bonded assemblies, using Charpy impact rigs capable of strain rates up to 10 s^{-1}, and split

Hopkinson pressure bars, imparting strain rates of up to 10^4 s^{-1}. The structural dynamics of bonded assemblies have also been studied in tension [122–125], compression [126], impact [127] and shear [128], [129], seeing large increases in both the strength and stiffness of the assemblies during failure.

These investigations all assess the global response of the structure to the high rate loading, evaluating changes in failure load and joint extension. None of these studies have been able to isolate the mechanisms of change in the joint, identifying if the improvement in properties is due to the adhesive, adherend, or a complex interaction between the two. This is very similar to the qualitative parametric joint strength investigations discussed at the beginning of section 2.5. Therefore this is an area where considerable quantitative experimentation analysis is required using full-field methods.

Dynamic full-field analysis is becoming increasingly accessible due to significant improvements in the technology and cost of high speed digital cameras. Unfortunately the sensor hardware and memory writing speed are still the limiting factor in this analysis, as there are relatively few, low fill factor, pixels in the image [130]. The large quantities of data generated from the high speed imaging cannot be written to memory fast enough, requiring a trade-off between image resolution and temporal resolution to reduce the memory burden on the camera. This is especially noticeable in the use of high speed DIC where a smaller image size reduces the number of interrogation cells in the image, necessitating a reduction in the interrogation cell size, to the detriment of the strain measurement precision [130] [131]. As noted in section 2.5.2.1 high speed DIC has been previously conducted in the quasi-static analysis of adhesively bonded joints at frame rates of up to 3 kHz [89]. Principal strain field data was analysed from the images, but not constructively used to evaluate the failure behaviour of the joint. Adaptation of the methodology to higher rate loading was also not considered.

High speed imagery has also been used in conjunction with photoelasticity to analyse impact events, [132] however as stated earlier, this method is unsuitable for through-thickness analysis of composite adhesive joints. The temporal and spatial resolution trade-off also affects Moiré interferometry, which has been successfully implemented at 100kHz, however the sensitivity of the analysis is greatly reduced [133]. High-speed infrared thermography has been successfully used up to 15kHz by Crump et al. [134] to elicit the stress prior to failure in composite coupons subject to high speed loading. The use of the technique presents significant measurement challenges [135], requiring heavy windowing down of the field of view. The accuracy of the technique is also limited in high speed applications, as less photons are detected during the shorter interrogation time on the sensor, decreasing the sensitivity of the sensor.

2.7 Literature summary

A wide range of literature has been covered in this chapter. The fundamental differences between mechanically fastened and adhesively bonded joints were initially discussed, outlining the structural efficiency and cost benefits of adhesive joints over mechanically fastened solutions, and identifies the motivation for the evaluation of adhesively bonded composite joints in this thesis.

Sections 2.3 - 2.5 discuss very different analysis approaches; however they all share a common theme of evaluating the joint response at increasing spatial resolutions to capture localised effects occurring in the joint. In section 2.3 the development of analytical models is shown, identifying progression from linear elastic analysis through to the use of differential solutions and the incorporation of classical laminate plate theory as the mechanics of the bonded joint behaviour are better represented. Improving these methods delivers increasing analysis of the localised behaviours in the joint and provides evaluation of the responses in the through-thickness direction. Due to the variable local mechanics and boundary conditions in the joints however, the use of these closed form approaches is limited to simple geometries and loading scenarios.

The development of the finite element modelling methods presented in section 2.4 shows a clear improvement over the analytical methods in the analysis of localised joint behaviours. These models allow much greater flexibility in the geometry of the joints analysed, with the potential to generate highly detailed analysis of the component stress and strain fields in the joint. However the validation of these models is relatively poor, which is typically demonstrated though global deformation measurements. This approach fails to identify if the analysis of the local phenomena, which provides the motivation behind the use of these detailed models, are correct. The validation of finite element models is an area which requires improvement, in order to have confidence in the modelling solutions. The collection of accurate experimental data is an important part of this validation process which also needs to be addressed.

The review of experimental investigations in section 2.5 indicated a number of techniques used to examine the stress and strain distributions in adhesively bonded joints. A discussion of the different experimental methods was presented, demonstrating the limitations of contact methods such as strain gauges and FBGs due to their poor spatial resolution of data. Application of the experimental methods to the measurement of localised stress and strain distributions in

adhesively bonded joints is examined, identifying the potential of full-field measurement techniques

The two techniques which provide the most detailed analysis of adhesive joints are DIC and Moiré interferometry. Studies using these techniques have evaluated, at high resolution, the strains generated in the adhesive bondlines and at the damage initiation locations at the root of the discontinuity between adherends. The initiation of damage in the adhesive layer has been evaluated from plots of the principal strain. A strong correlation between the maximum principal strains and the development of cohesive damage in the adhesive is identified. A more common failure mode in composite adhesively bonded joints is fibre tear failure, where the development of damage is not restricted to the adhesive and occurs in the adherend due to through-thickness tensile failure of the adherend. The development of fibre tear failures are linked to the low through-thickness modulus of composite material, and high through-thickness strains generated around the discontinuity. Experimental measurement of the through-thickness strains around the root of the discontinuity has shown good agreement with both analytical and finite element solutions, observing localised through-thickness strain concentrations at the interfaces between the adhesive and the outer adherend. These interfacial concentrations are believed to form damage initiation sites in the joint and act as a major contributing factor to the joint. However the strain field analysis provided in the DIC and Moiré studies shows very little analysis of strain feature responses in relation to the development of damage in the joint. This demonstrates a need for a greater understanding of the developed stress and strain fields in the composite adherends of the joint, and their interaction with the failure behaviour of the composite material. This is an area of research which is currently greatly undervalued, but which appears critical to the joint failure, necessitating further investigation.

The literature discussed in sections 2.3 - 2.5 relates to investigations of joint strength under quasi-static loading conditions. Marine structures experience dynamic in-service loading conditions, resulting in high strain rate loading of the structure. The behaviour of adhesive joints during dynamic loading events is discussed in 2.6, where a large change in the behaviour of the joint is established. This testing is conducted on relatively small coupons in order to achieve constant strain rate loading. This limits the type of structure that can be tested, of which there is very little testing conducted at intermediate strain rates between 10 s^{-1} and 10^4 s^{-1}. The results from the experimental investigations have been presented as global measures of load and displacement, providing little quantitative analysis of the changes in material and structural responses. High speed full-field experimental techniques have not been applied to analysis of adhesively bonded joints at high strain rates. This is identified as a very novel and important development in analysing the strain rate dependencies of composite adhesively bonded joints.

2.8 Experimental technique choice

The literature summary identifies the need for better experimental analysis to generate better understanding of joint mechanics, and improve the validation of finite element modelling approaches. The use of full-field experimental techniques is required to deliver data-rich analysis of the component stresses/strains in the joint. Analysis and understanding of the through-thickness behaviour of adhesively bonded composite joints was identified from the literature summary to be weak. A suitable experimental technique must be selected to allow the evaluation of the small, yet highly important, through-thickness strains in the composite adherends in the lead up to damage and joint failure. The technique must also be adaptable to conduct high speed analysis of the joint as it is loaded at high strain rates.

Sections 2.5 and 2.6 have discussed a number of different techniques for the quasi-static and high speed analysis of adhesively bonded joints. Each technique has slightly different merits and drawbacks which affect the suitability of the technique in this thesis. From the overview of the techniques and literature described in the previous sections, a summary table with relative ranking values assigned out of 10 for each full-field technique based upon the author's interpretation of the literature review, is presented in Table 1.

When considering technical performance Table 1 identifies that Moiré interferometry would be the best technique to use for analysis of the through-thickness strains and local load transfer mechanisms in a bonded joint due to the very high spatial resolution of the data. The technique has also been proven to work well when applied to analysis of dynamic events using high speed cameras. Practically though Moiré is an expensive and labour intensive procedure to use. Critically affecting the performance of Moiré interferometry is the use of the diffraction grating. The sensitivity of the deformation measurements and the maximum deformation measurements are both limited by the pitch of the diffraction grating used in the analysis. Furthermore, the grating must remain coherently bonded to the specimen surface during analysis, preventing evaluation of displacements during failure events.

The next best alternative is DIC, which has proved to be a very versatile technique in the analysis of adhesively bonded joints. The use of macro lenses and microscope stages offers a cost effective method to provide high resolution analysis using this technique, well suited to analyse the through-thickness strain distributions in the joint. The experimental setup of the technique is relatively simple and low cost, which can be easily adapted to high speed analysis using a high speed camera and increased illumination. Importantly, as the speckle pattern used for correlation is painted directly onto the surface of the specimen, analysis of the specimen deformation during failure can be undertaken without detriment to the full-field results.

Thermoelastic stress analysis provides very accurate, high spatial resolution data, which is well suited to analysis of the localised features present in the adhesive joint. Although not well suited to high speed applications, the TSA method is the only approach discussed which uses infra-red temperature data, which is independent of the white light and coherent light techniques mentioned in this review. Conducting analysis with TSA therefore, will compliment analysis from DIC, allowing the validation of finite element models from two independent data sources. Agreement between these two sets of experimental data will provide large confidence in the accuracy of the finite element solutions.

The conclusion of the choice of experimental technique identifies that a combination of DIC and TSA will be used in this thesis to conduct data-rich analysis of the stress and strain distributions in adhesively bonded joints.

	Technique	Measurement	Spatial resolution	Measurement precision	Cost	Ease of use	Application to high speed imaging
Digital Image Correlation	White light	Displacement	7	8	6	8	9
Moiré Interferometry	Coherent light	Displacement	9	9	9	6	7
Thermoelastic Stress Analysis	Infra-red	Temperature	8	8	7	8	5
Photoelasticity	White light	Light intensity	5	7	2	9	8
Speckle Interferometry	Coherent light	Displacement	8	8	7	7	2
Grid Method	White light	Light intensity	7	8	4	7	7
Video Extensometry	White light	Displacement	3	8	4	9	6

Table 1: Summary of common full-field experimental techniques

3. Initial bonded joint testing and material characterisation

3.1 Introduction

This Chapter presents the materials, manufacture and geometry of the adhesively bonded joint used in the present research. In addition global behaviour of the joint under load is assessed. Methods and results from the evaluation of the constitutive material properties, used extensively throughout this research, are also presented.

3.2 Joint design and construction

The research in this thesis builds upon work conducted at the University of Southampton investigating a Double Butt Strap Joint (DBSJ) between pultruded, and quasi-pultruded glass fibre laminates [108], [109]. In the present research a similar DBSJ configuration is chosen for the experimental work. A schematic of the joint geometry can be seen in Figure 10(a), presented in the material coordinate system which is used throughout this thesis.

The laminate architecture has been designed to form a 7mm thick laminate containing 300 g/m^2 glass fibre chopped strand mat (CSM) and Gurit UT-E800 unidirectional glass fibre layers. A $[CSM_3,0_4,CSM_2]_s$ stacking sequence is used, mimicking the pultruded structures seen in references [108], [109] and [2], which provides a distinctive banded structure for analysis. A magnified image of the specimen laminate construction can be seen in Figure 10(b) identifying the definitive structure of the laminate and the visual differences between the materials in the laminate.

Although not replicating the geometry or layup of typical in service joints, the double butt strap joint in this study has a number of advantages. The joint represents an extensively researched design with a severe discontinuity from which a baseline understanding of the stress and strain responses in the joint can be evaluated. The symmetry of the DBSJ generates a symmetrical deformation of the outer adherends about the centre of the joint. This is important as it minimises sideways movement and rotation of the joint during loading, which have implications

on the complexity of the experimental set up, due to the changing orientation of the through-

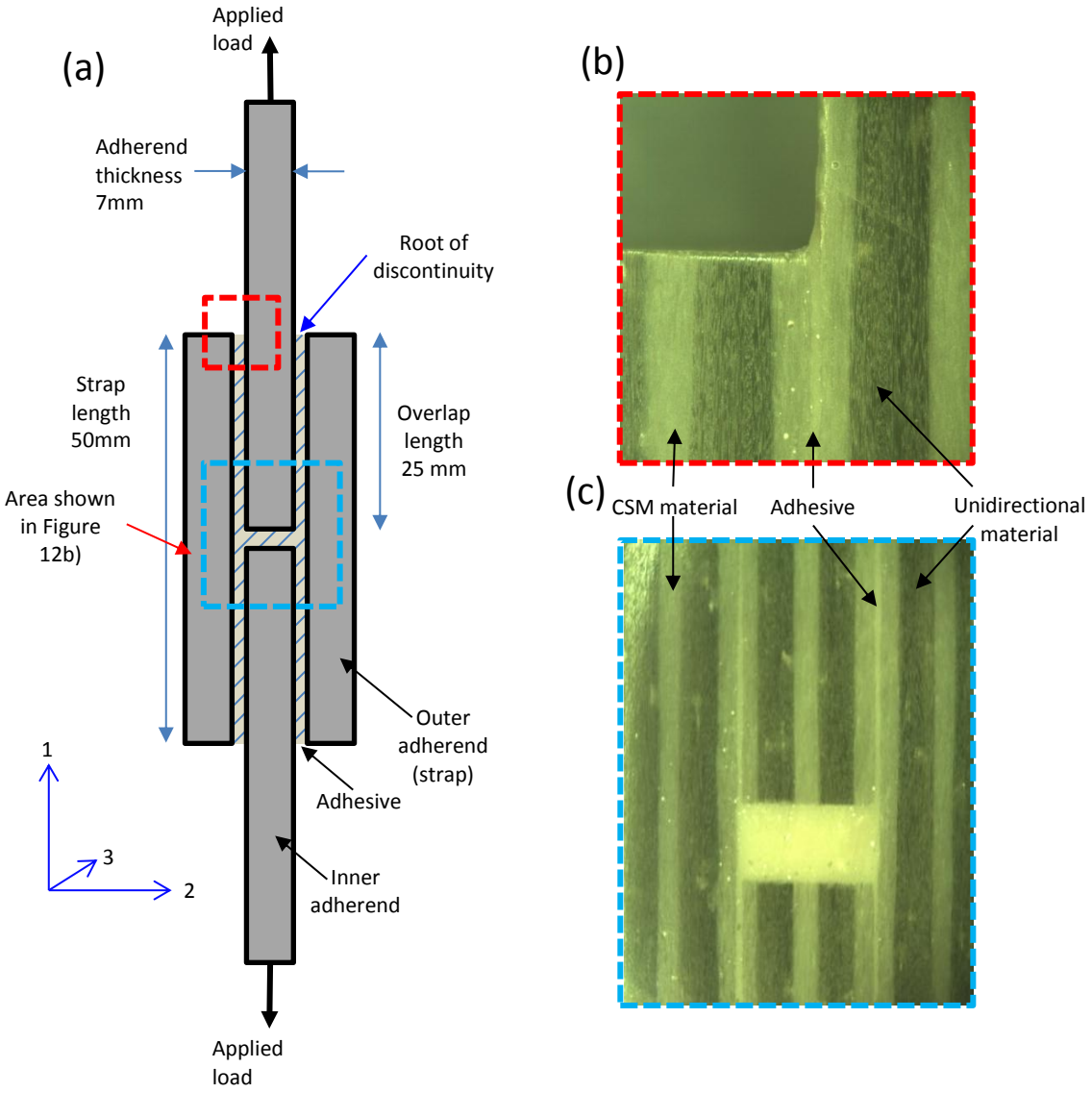

Figure 10: (a) Schematic of the double butt strap joint used in this project, Microscope image of the laminated structure of the joint at (b) the root of the discontinutiy and (c) centre of the joint

thickness direction.

In Chapter 5, 6 and 8 a DBSJ with an outer strap length of 50 mm and overlap length of 25 mm is used. The overall length of the joint is 200 mm and width 25mm. The joint is manufactured using Gurit Prime 20LV epoxy resin using a resin infusion process, best replicating typical closed mould manufacturing methods commonly implemented in the marine industry. The outer straps and inner adherends were cut from the laminate with a width of approximately 350mm and bonded together to form one very wide joint. The wide joint was then cut to form the

separate joints for testing with a width 25mm. This method minimises misalignment of the straps relative to the inner adherends during assembly and provides greater control over the symmetry of the joint, both of which create more repeatable joints for testing.

The surfaces of the adherends were prepared for bonding by abrading the bonding areas with P120 sandpaper to remove the resin rich surface layers of the material and generate a flat, clean surface for bonding. The abraded surfaces were cleaned with acetone to remove any dirt or grease. The joint was bonded together using the structural epoxy adhesive Araldite 2015. The joint was bonded in a two-step process, bonding each outer strap to the inner adherends separately, and waiting for the adhesive to cure between operations. This minimised the risk of movement of the adherends when the adhesive had not fully set. A mass of 25kg was evenly distributed on top of the bond area between the adherends during curing; ensuring good contact between the adherends and the adhesive. Once both sides were bonded the whole joint assembly was post cured at 80^{o}C for 1hr as per the manufacture's data sheet instructions to maximise the shear strength of the adhesive. This post cure cycle is less than that recommended for the Prime 20LV epoxy resin, however the investigations in this thesis are not concerned with maximum strength, rather the stress and strain distributions generated in the joint up to failure, so not reaching the maximum resin properties is not a concern.

The spew fillet that results from the assembly of the joints between the outer strap and the inner adherend is removed. The removal of the spew fillet aims to make the measurements in the through-thickness direction easier to obtain with DIC by increasing the local eccentricity of the load path between the inner and outer adherend. Higher load path eccentricity increases the internal bending moments developed at the end of the outer adherends, generating higher through-thickness stresses and deformations in the joint. Relatively thick adherends are required to provide sufficient measurement area for the DIC and TSA techniques used in this research. The thick, stiff adherends reduce contributions of anticlastic bend-twist coupling, providing surface responses which are representative of the stress and strain states found across the width of the joint. Conversely these thick adherends strongly resist the through-thickness stresses created in the joint; reducing the measurable response. This arrangement provides a significant measurement challenge, pushing the capability of the DIC system to measure the small through-thickness strains. Successful measurement of these small values however demonstrates the potential of the DIC technique to conduct measurements cheaply and accurately at small length scales, usually only possible in analysis with Moiré interferometry as discussed in Chapter 2.

A similar DBSJ joint with a different arrangement of the outer adherend overlap is used in Chapter 7, where it is discussed in more detail. In Chapter 8 a single lap joint arrangement is used due to practical experimental limitations in the high speed joint testing discussed in that

chapter. These alternative joints, although different, share the same construction techniques, adhesive material and parent laminate structure as used in Chapter 6. For all of the joints tested in this thesis the CSM material forms the adherend facesheet interfacing with the adhesive. This is a remnant of the pultruded material structure tested by Boyd et al [108], [109] and a response to the increased use of CSM material in structural applications as a damage propagation inhibitor [136], [137], absorbing the energy of the crack front through local cracking of the matrix and debonding of the fibres.

3.3 Global joint properties

It is important to characterise the global behaviour of the DBSJ before the local strain distributors are examined in further detail. Of particular importance is the ultimate failure load and global deformation of the joint such that suitable experimental procedures are used in future tests. Evaluation of the joint up to failure will also give a qualitative assessment of the primary damage modes experienced in the joint.

Seven DBSJ specimens were tested using an Instron 5569 servo-mechanical test machine fitted with a ±50 kN load cell, and loaded at a constant displacement rate of 2 mm/min. Displacement data was measured from the crosshead displacement. It is recognised that machine crosshead displacement is less accurate than a clip on or electrical resistance strain gauge [60]. However, as the data is only used to quickly understand the joint behaviour and obtain initial limits which will be used during later tests, a less precise extension measurement technique is deemed acceptable.

The load / extension plot for the seven specimens is presented in Figure 12, and the results summarised in Table 2. A typical example of a failed joint specimen is shown in Figure 11 indicating that all specimens fail due to fibre-tear in the CSM face sheet in the outer adherend. This failure mode explains the relatively large variation between failure loads, due to the different failure crack propagation paths experienced through the heterogeneously orientated fibres in the CSM layer. Although there is a large variation in the final joint failure loads, observation of the load / extension curves show very similar linear joint responses prior to failure. The loading curves give very little indication of the onset of damage, or the likelihood of failure. Instead sudden catastrophic failure is observed. The small response from the joint attributable to the development of damage highlights the need for better understanding of how failure initiates in the joint. The spread of the results does not indicate if the damage behaviour is a stress or strain critical event. Knowledge of this is important for engineers when designing joints, reinforcing the need for local analysis of the joint conducted in the following chapters.

Figure 11: Typical joint failure indicating light fibre tear

A change in the joint stiffness above 0.1% strain may also be identified from Figure 12. This change is a result of parasitic machine compliance at the beginning of the specimen loading attributed to settling of the machine grips. Unfortunately this cannot be completely removed, and is identified later in Chapter 8 as one of the many experimental challenges faced in the experimental DIC analyse conducted in this report.

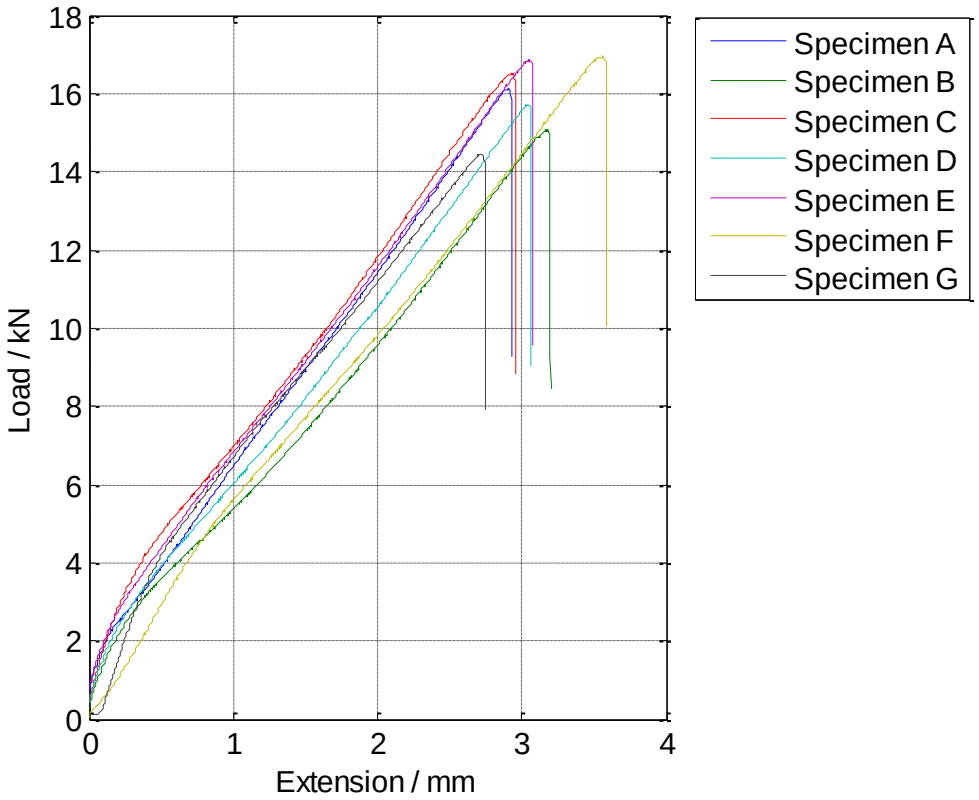

Figure 12: Load / extension response of double butt strap joint

	Ultimate Tensile extension (mm)	Ultimate tensile load (kN)
Mean value	3.09	15.84
Coefficient of variation / %	8.05	5.79

Table 2: Tensile testing evaluation

3.4 High speed video of failure incidence

The catastrophic DBSJ failure events presented in Figure 12 show a considerable, and rapid, change in the joint behaviour. This change necessitates further analysis of the failure incident using high speed imaging to identify how the crack growth in the CSM layers changes from stable to unstable behaviour leading to failure.

An 8 bit Motion Pro X3 plus high speed camera with a 1 Mp CMOS sensor was used to capture the failure incidence of the joint using the same experimental procedure as used in the ultimate failure load analysis. As with all high speed cameras there is a trade-off between the spatial and temporal resolution. The full 1280 x 1024 pixel array of the Motion Pro X can only be used with a maximum frame rate of 2 kHz due to limits in the on board camera memory and hardware buffering speeds, which is too low for analysis of the failure event. Therefore, to reach higher temporal resolutions, the image is windowed down, reducing the number of pixels used in the array, and hence reducing the file size and memory buffering requirements of each image. In this investigation a temporal resolution of 6.6 kHz was used, providing an image resolution of approximately 15 pixels / mm across the 21 mm x 49 mm field of view of the joint face. In addition to the hardware limits, illumination provides a significant physical limitation to high speed imaging. As the camera frame rate increases, the exposure time of the sensor reduces, capturing less light producing a darker image, from which concise evaluation of the image is very difficult. To overcome this, two Das Licht 5W halogen lights are used to illuminate the specimen during testing. High illumination also allows a small aperture to be used, which provides a large depth of field, accommodating out of plane motion without reducing focus quality.

Figure 13 shows 8 images taken at 1.51×10^{-4}s intervals over a 1.21×10^{-3}s time period at the end of the loading curve, capturing the initiation and growth of cracks leading to the final failure of the joint. Discussion of the images must be considered in unison of the load transfer mechanisms occurring in the joint under load.

Load in the joint must be transmitted between the inner adherends via the outer strap due to the discontinuous nature of the joint. The load is transferred between the adherends through shear of

the adhesive layer between the adherends. The transfer of load in the joint generates differential tensile extension along the length of the adherends, with little extension of the inner adherends close to the butt in the centres, where most of the load has been transferred to the outer strap, and vice versa for the outer strap which deforms more in the centre of the joint and experiences no deformation at the free end by the root of the discontinuity. This leads to a non-uniform shear stress distribution as discussed by Volkersen [26] shown in Figure 5. The eccentricity of the load path generated by the transfer of load between the inner and outer adherends creates an internal bending moment localised around the discontinuity where the eccentricity is largest. These bending moments peel the outer adherend away from the inner adherend, imparting through-thickness stresses along the bondline and in the strap. A crack can be seen to develop in Figure 13, image 1, in the CSM layer in the outer strap next to the adhesive layer at the root of the discontinuity between adherends generated by these through-thickness stresses. The internal bending moment feeds the propagation of the crack front shown in images 2 and 3 as there is less material to resist the through-thickness stresses. The growing crack front also increases the eccentricity of the load path between the adherends, further increasing the internal bending moment and peel stresses acting on opening the crack. As the length of the crack grows the joint loading becomes asymmetric, introducing a large external bending moment. This bending moment adds to the propagation of the crack resulting in larger deformations of the outer strap seen in images 4, 5 and 6. The external moment causes rotation of the joint leading to the crack propagating through the adhesive butt between the inner adherends, image 7 and 8, and catastrophically propagating into the opposite outer strap up to failure.

Although on a macro scale the randomness of the CSM layer can be assumed to be equal for all specimens, at the meso scale at which the crack initiates and propagates, the randomness and orientation of the fibres is vastly different. The random orientation of the CSM fibres result in extensive fibre bridging across crack faces, which absorbs fracture energy and produces resistance to the crack opening. The high speed imaging shows the damage in the CSM layers reaches a critical level between image 2 and 3, whereby the joint failure is self-perpetuated by the deformation of the outer strap; accentuated by the asymmetry of the load path resulting from the crack front. As such, the variation in the ultimate strength and strain to failure observed in Figure 12 is most likely to be due to differences in the localised initiation of the damage at the root of the discontinuity, rather than the subsequent and much more destructive rapid crack growth and joint deformation. Therefore the material response at the root of the discontinuity is of considerable interest for further analysis using the full-field measurement techniques, in order to evaluate the behaviour of the joint before critical damage levels are reached.

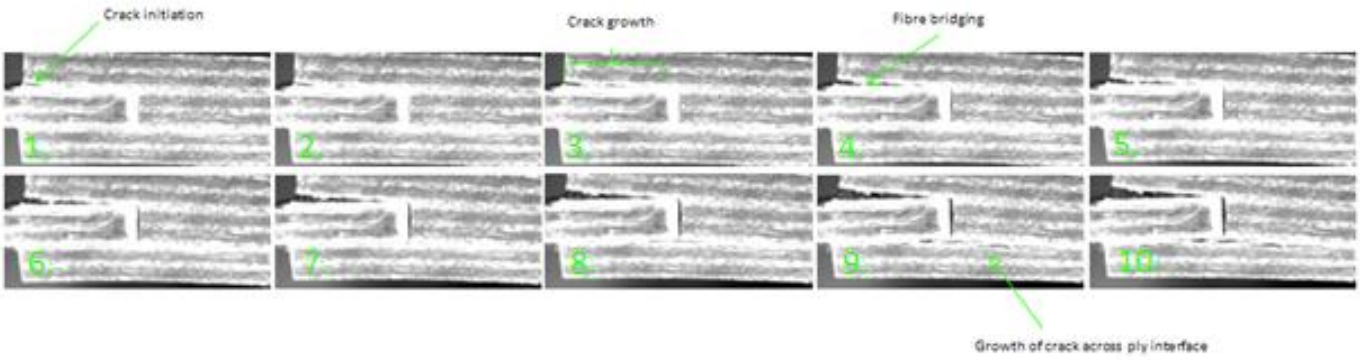

Figure 13: Joint failure sequence at 6.6kHz

3.5 Material characterisation

In addition to recording the global response of the DBSJ it is important to characterise the properties of the materials used in the joint. The material properties of the component materials in the joint are important for the analyses conducted in Chapters 6-7. Of particular importance are the properties of the CSM material in the through-thickness direction to resist the peel stresses which contribute to the initiation and propagation of cracks. In Figure 13 the CSM face sheets were observed as being critical in the initiation and propagation of damage. As such, all properties for the CSM material were experimentally obtained. Properties of the unidirectional material are evaluated from a mixture of experimental and literature values. Properties from the adhesive are taken from tests conducted using ISO 527 and DIN 53445 given in the manufacturers data sheet [138].

An overview of the experimental methods used to establish the properties are provided in the following sections, accompanied by a summary of the established material properties in Table 3 and the relevant coefficients of variation from the experimental testing. Schematics of the test specimens used in the testing are shown in Figure 14

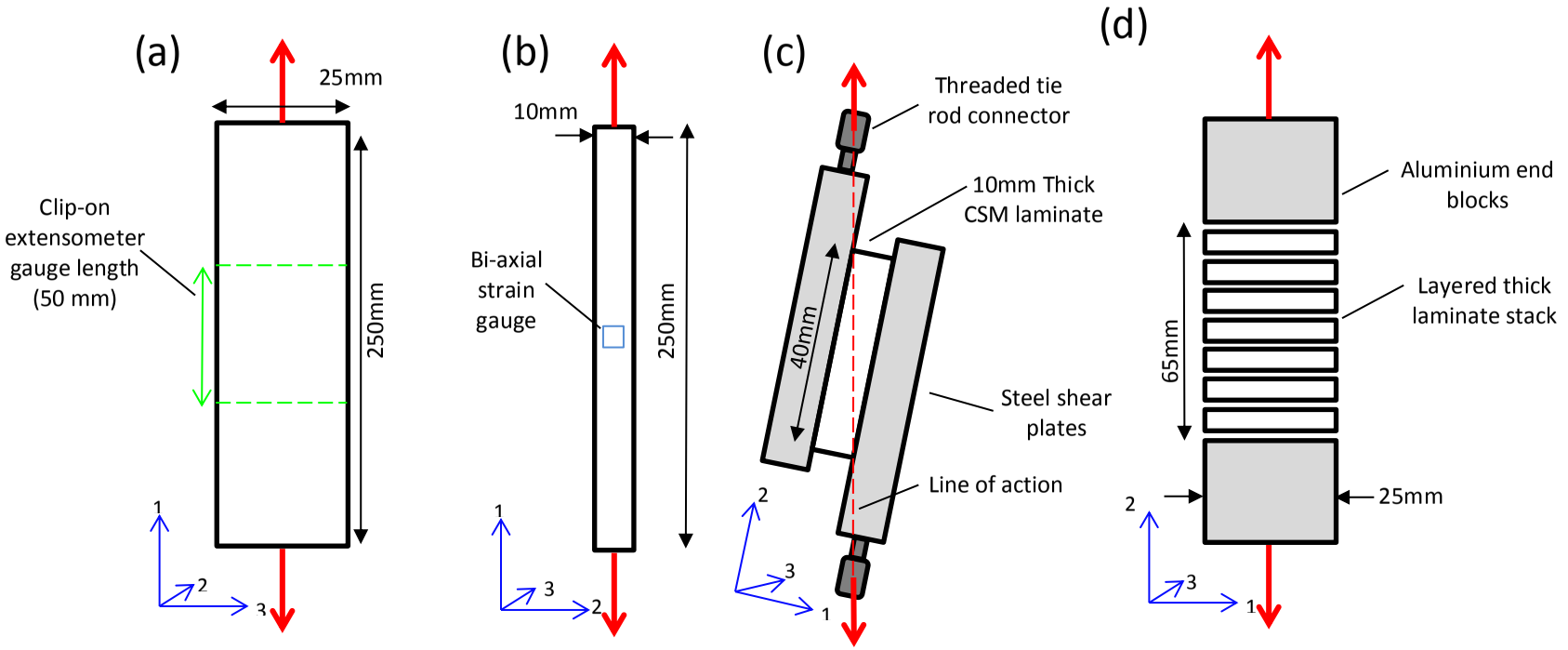

Figure 14: Schematic of the material properties test coupons

3.5.1 In-plane materials characterisation

The in-plane moduli E_1 and E_3 for the CSM material and unidirectional materials were calculated from ASTM D3039 coupon specimens shown in Figure 14 (a), loaded at 2mm/min in an Instron 5569. The specimens were manufactured from 4 layers of 450 g/m^2 CSM material, and 4 layers of 800g/m^2 UT-E800 glass fibre, using Gurit Prime 20LV epoxy resin and the resin infusion method as per the method used to manufacture the joints. In-plane strains were recorded using an Instron 2630-113 clip gauge extensometer with a 50mm gauge length.

3.5.2 Chopped strand mat through-thickness Poisson's ratio

The through-thickness Poisson's ratio ν_{12} for the CSM material were obtained from testing of modified, 8mm thick, ASTM D3039 coupons manufactured with 16 layers of CSM material. A Tokyo Sokki Kenkyujo Co FCA-3-32 biaxial strain gauge was bonded onto the side of each thick specimen to measure the in-plane and through-thickness strains. A schematic of the test coupon is shown in Figure 14(b).

3.5.3 Chopped strand mat shear modulus

The G_{12} shear modulus was obtained from analysis of six shear specimens constructed from 8mm thick CSM laminate coupons measuring 40 mm x 40 mm bonded between two steel shear plates using Araldite 2015, as shown in Figure 14(c). Evaluation of the through-thickness shear modulus had to be undertaken experimentally as it is not suitable to be calculated analytically. The specimens were fixed to an Instron 5569 test machine using a threaded tie rod with a universal end joint, such that the line of action of the load passes through opposing corners of the specimen, loading the specimen in pure shear. The specimen shear strains were recorded using 2D DIC providing a large number of data points across the specimen, which could not be obtained using strain gauges due to the geometry of the specimen. The specimen was imaged with a spatial resolution of 38 pixels /mm, and the strain fields calculated with a subset size of 79 x 79 pixels in DaVis 8.0. The coefficient of variance between these six specimens is relatively high, but not unexpected, due to variations across the full-field strain data for each specimen resulting from the random orientation of the CSM fibres in both the through-thickness and in-plane directions. The shear modulus of the unidirectional material was not experimentally obtained, as in much of the analysis discussed in this thesis, the unidirectional material is out of the field of view and not analysed.

3.5.4 Through-thickness specimen design

As identified by Ferguson [139], the majority of polymer composite testing has been conducted on relatively thin coupons, which are unsuitable to determine the through-thickness properties of thick composite laminates. As a result suitable candidate specimen geometry is required, from which accurate measurement of the through-thickness material properties is possible. A number of thick specimen designs have been used in literature [139–142] many requiring heavy machining and preparation to achieve the desired geometries. The thickness of these specimens also provides a significant challenge during manufacturing to achieve a completely parallel stack of fibres with an even distribution of resin through the thickness. Boyd et al. [109] constructed through-thickness test specimens from four laminate coupons measuring 50 x 50mm wide bonded together into a 24.8mm high stack between two aluminium blocks in a study of the thermoelastic response of composite materials in the through-thickness direction. The simple design and manufacture of these specimens is very advantageous, and will be used in the following testing. Due to the very low aspect ratio of these specimens it is suspected that the strain field in the laminate stack is highly non-uniform. This non-uniformity is also visible in the full-field temperature data presented in reference [109] from the specimen surface, supporting the concerns about the specimen geometry. Therefore the geometry of the specimen was re-evaluated to give confidence in the accurate measurement of the through-thickness properties.

A finite element investigation was undertaken to examine the effect of aspect ratio on the uniformity of the strain field in the through-thickness specimens. A 3D solid model was created in ANSYS using eight node, quadrilateral, Solid45 elements to represent the aluminium and adhesive components. Higher order, 20 node, Solid95 quadrilateral elements were used to model the composite material. The extra node through the midplane of the Solid95 element makes it well suited to capture the stresses and strains through the thickness of the element. The linear 8 node Solid45 volumes were meshed first followed by meshing of the 20 node Solid95 composite volume, automatically dropping the midside node in the Solid 95 elements at the interface with the Solid45 elements, thus ensuring continuity between the elements [143].

A unidirectional glass fibre composite was modelled between the aluminium blocks using material properties from literature [144]. A quarter of the test specimen was modelled, applying appropriate symmetrical boundary conditions to maximise the number of elements in the model and minimise computational effort. The base of the model was constrained with zero displacement and a tensile load of 0.8 kN applied at the top, as used in reference [109]. A

schematic of the modelled specimen structure, and the positions at which data samples were evaluated, can be seen in Figure 15. Initially a model with an aspect ratio of 0.49 was tested, similar to that used by Boyd et al [109].

This modelling is not designed to establish absolute values of stress or strain in the specimen as there is imperfect knowledge of the material properties in the through-thickness direction. Rather this investigation is used as a tool to identify the relative difference in uniformity in the specimen as a result of different aspect ratios, and ensure that the specimen used will produce results which are representative of the bulk material response.

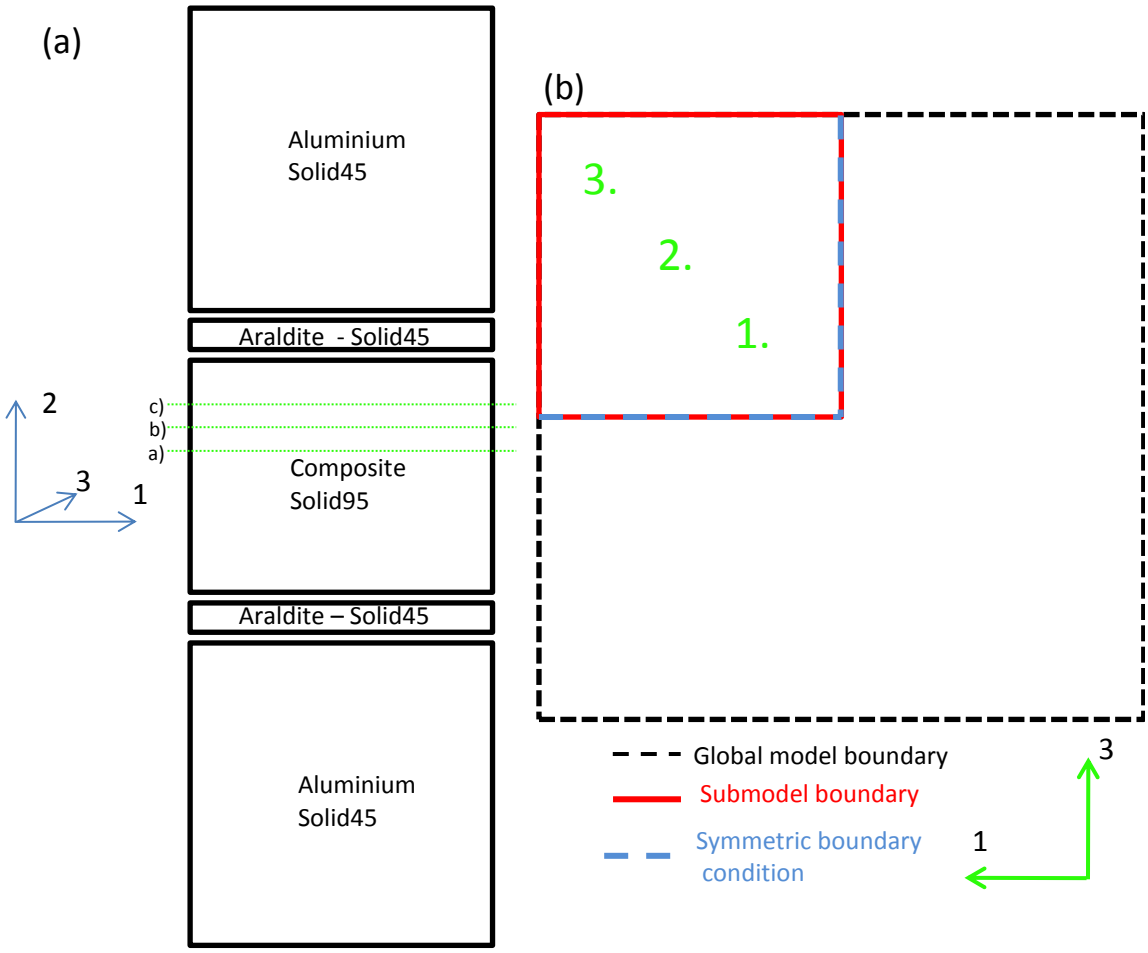

Figure 15: Schematic of the FE model (a) side view of model (b) section through global model

Figure 16 show plots of the strain in the through-thickness, 2, direction taken at three evenly spaced cross sections away from the centre of the specimen, marked (a)-(c) on Figure 15. Large variations in strain up to 17% can be seen across the cross sections. The response across section (a) is very different to that in section (c), showing less uniformity across the section and lower surface strains, which are unrepresentative of the bulk material behaviour.

A study to reduce the non-uniformity of the strain field throughout the composite was undertaken by altering the dimensions and aspect ratio of the model. Figure 17 and Figure 18 shows a comparison of the strains at points 1, 2 and 3 from Figure 15 at varying distances from the aluminium end blocks. These plots show a convergence of the strain values through the thickness and across the width of the specimen as the aspect ratio is increased. The increased uniformity seen in Figure 17 and Figure 18 is also evidenced by Figure 19, which shows the through-thickness strain map at an aspect ratio of 2.45 as per Figure 16. The high aspect ratio specimens show greater strain uniformity, providing confidence in the accuracy of surface measurements taken from the specimens to establish the through-thickness material properties. This analysis also identifies that there is low confidence in the surface measurement taken by Boyd et al [109] from the low aspect ratio specimens.

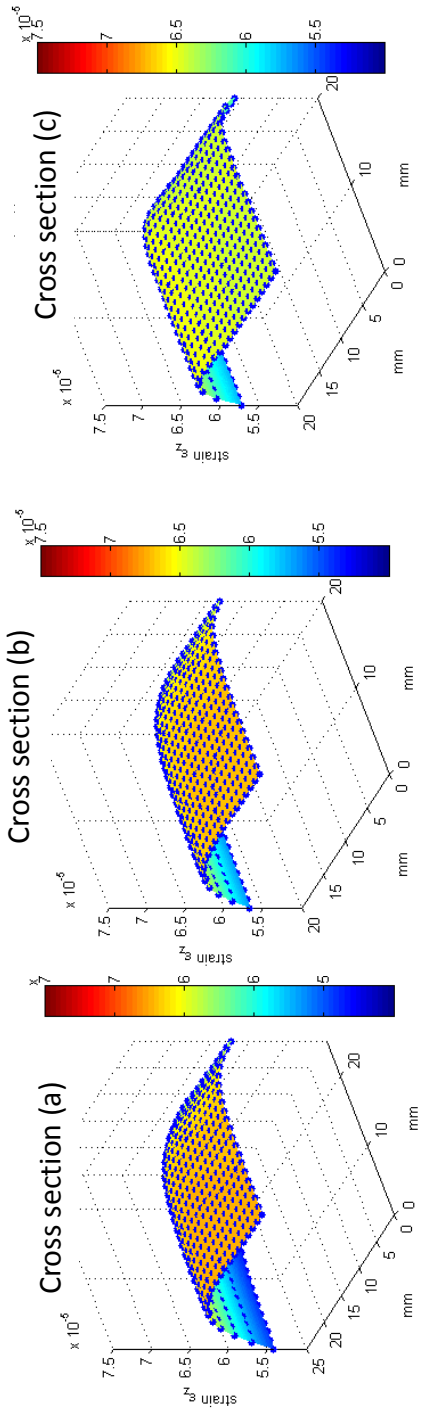

Figure 16: Strain map through the thickness of the composite aspect ratio 0.49

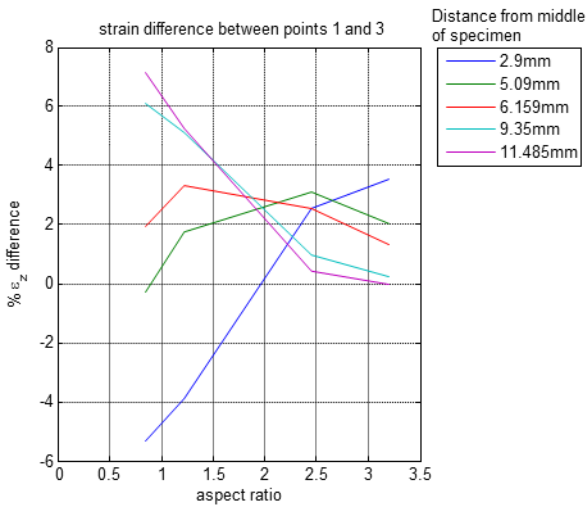

Figure 17: $\%\varepsilon_z$ strain difference between location 1 & 3

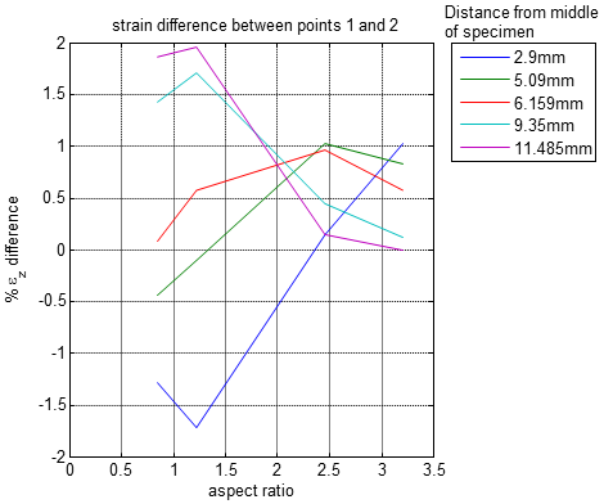

Figure 18: $\%\varepsilon_z$ strain difference between location 1 & 2

Practically, the aspect ratio cannot be too high due to the difficulty in manufacturing very thick composites with consistently parallel fibre layers using the resin infusion process. Also the width of the specimen cannot be too small, as it must have sufficient through-thickness strength to withstand the applied loading. The convergence of the strain uniformity and distribution observed in Figure 17 and Figure 18 suggest that there is little additional benefit to increasing the aspect ratio above 2.45. As such a specimen with an aspect ratio of 2.5 will be used for future investigations.

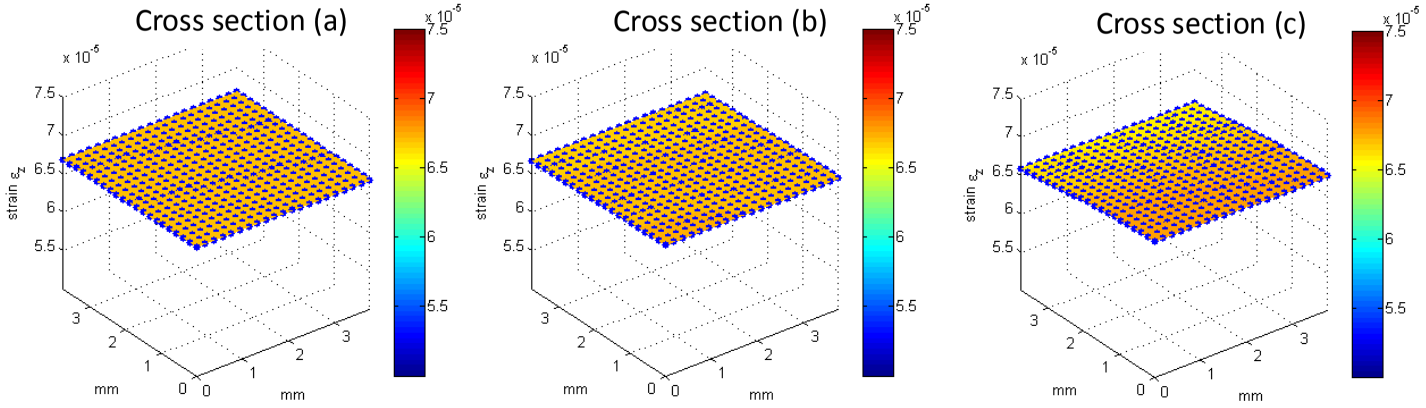

Figure 19: Strain map through the thickness of the composite aspect ratio 2.45

3.5.5 Through-thickness experimental evaluation

The conclusions of the FE investigation give confidence in the measurement of the through-thickness material properties from the new high aspect ratio specimens. Confidence in these values is vital to this thesis to accurately determine the stress and strain distributions in the joint from the subsequent experimental and numerical investigations.

High aspect ratio specimens with a target ratio of 2.5 were manufactured by bonding thick 30mm x 30mm laminate sections together between a 25 mm x 25mm x 25mm aluminium end tab fitting using Araldite 2015. Specimens of CSM and unidirectional material were manufactured. Figure 20 shows a photograph of the bonding and alignment jig. The overlap between the laminate and the aluminium end tabs were machined flush with the grips to ensure flat, adhesive free measurement surfaces. Four specimens of both unidirectional and CSM material were tested, with average aspect ratios of 2.61 and 2.64 respectively.

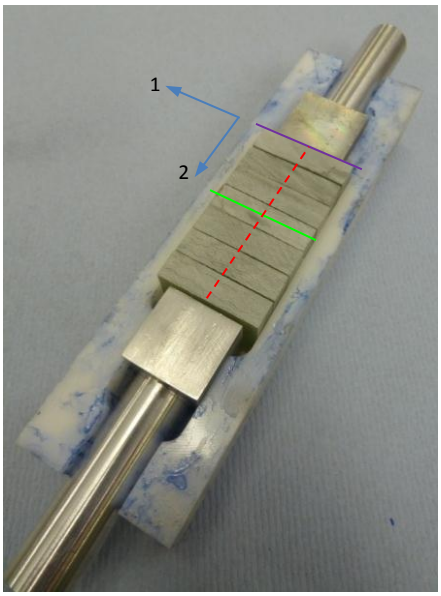

Figure 20: Manufacture of high aspect specimen

The material properties were established from the surface strains measured using Digital Image Correlation. Speckle patterns with a white background and black speckles were applied using a spray can, before being placed in an Instron 5569 mechanical test machine and loaded at 2 mm/min up to 4 MPa. Images were recorded during the loading sequence using a LaVision E-lite 5 Mp camera imaged at 59 pixels / mm resolution. In order to produce a high spatial resolution of strain data across the specimen, only half of the specimen was imaged. 2D DIC was conducted using the LaVision Davis 7.4 correlation software to analyse the strain distribution present in the specimens using a subset size of 128 x 128 pixels with an overlap of 50%.

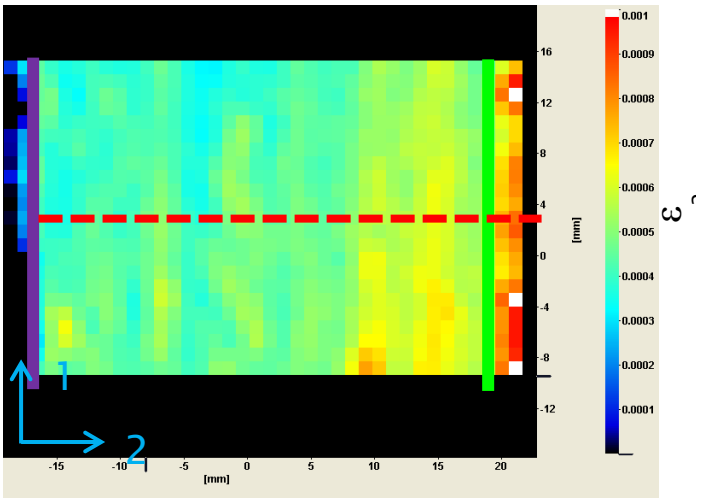

Figure 21: Through-thickenss, ε_2,strain in high aspect ratio specimen at 4MPa

Figure 21 shows the strain in the through-thickness material direction in the specimens loaded at 4MPa. The purple line represents the edges of the aluminium block between which the specimens are glued; the green line represents the horizontal midplane of the specimen, and the red dotted line the vertical midplane. Figure 21 shows consistent through-thickness ε_2, strains across the width of the specimen, with a slight increase along the specimen length towards the middle (green line).

DIC of low aspect ratio specimens as per the dimensions used by Boyd et al. [2] was also conducted using the same correlation parameters and an image resolution of 259 pixels / mm. Figure 22 shows a plot of the axial strain across the horizontal midplane of the specimens clearly identifying the non-uniformity of the strain distribution due to the low aspect ratio. The axial strain in the low aspect specimens shows a 50% difference in strain from the edge of the specimen to the centre for both the CSM and unidirectional materials. The high aspect ratio specimens show much less variation across their width, producing a constant level of strain and suggesting a more uniform response of the material. Along the middle of the gauge length of the specimen (the red line in Figure 21), the new, high aspect ratio specimens show a uniform strain distribution in the through-thickness material direction. Strain data corresponding to the compliant adhesive layers between the specimens have been removed from the plots in Figure 22 and Figure 23 for clarity, and is ignored in the derivation of the through-thickness material property data for the two materials. The DIC strain distributions agree with the trends identified in the FE investigations, providing confidence that the surface strain measurements of the high aspect ratio specimen are representative of the bulk material response.

The through-thickness modulus for the CSM and unidirectional materials evaluated from the surface strain readings are presented in Table 3 along with the rest of the experimental testing results.

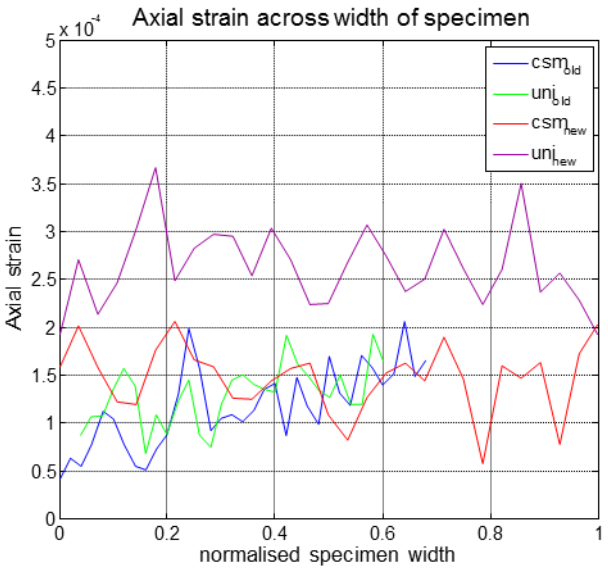

Figure 22: Axial strain across width of specimen

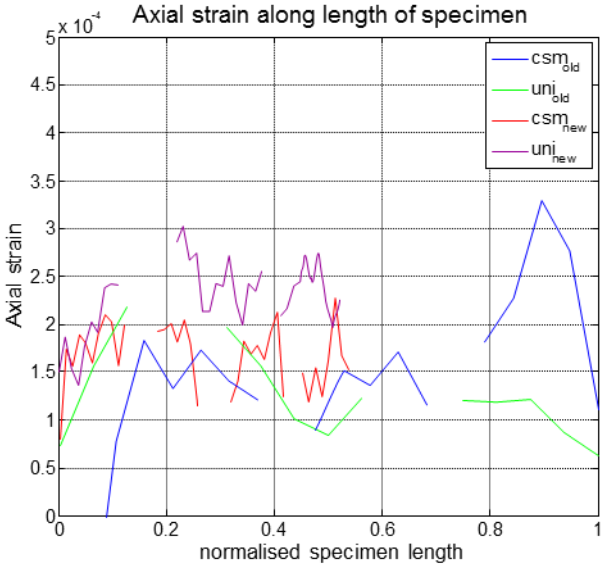

Figure 23: Axial strain across the length of specimen

3.5.6 Unidirectional material Poisson's ratio

The experimental in-plane E_1, and through-thickness E_2 Young's modulus values for the unidirectional material show good agreement with those presented in literature of very similar materials [144], [145]. In the majority of the investigations in this thesis, the area of interest does not feature the unidirectional material. Therefore, the decision was made to use the ν_{12} and ν_{21} Poisson's ratios from literature, in order to maximise testing time of the CSM face sheet material. It is most important to characterise the CSM material, as the analysis presented in this thesis shows the CSM to be highly important to the initiation of damage in the joint.

3.5.7 Summary of material properties

A summary of the material properties from the experimental testing outlined above, and the relevant coefficients of variation from the experimental testing are shown in Table 3.

	CSM	Unidirectional glass	Araldite 2015
E_1 (GPa)	11.27 6.43%	50.20 2.42%	2 [138]
E_2 (GPa)	7.63 7.43%	15.43 8.23%	2 [138]
ν_{12}	0.34 3.43%	0.34 [144]	0.36
ν_{21}	0.23[a]	0.25 [144]	0.36
G_{12} (GPa)	2.42 17.7%	9 [144]	0.9 [138]

Table 3: Materials properties values for CSM and unidirectional material

[a] Established from constituent relations between E_1, E_2 and ν_{12} [5]

3.6 Conclusion

The global analysis of the joint in this chapter forms a good basis for understanding the joint response under load, failure behaviour and the constituent material properties. The ultimate failure loads can be used to design test protocols for the more detailed analysis conducted in the following chapters. Visual identifications of the failure modes with the high speed imaging show the failure mechanisms in the joint to be complex, requiring high spatial resolution analysis to observe the localised initiation of damage at the root of the discontinuity. Finally the material properties characterised in this section are core to the manipulation and validation of the DIC strain data into the stresses in the joint, as discussed in Chapters 6 and 7.

4. Full-field analysis of strain distributions in an adhesively bonded composite joint

4.1 Introduction

Evaluation of strain components generated across the thickness of double butt joints up to failure is conducted using DIC and is used to address the global measurement shortcomings of the qualitative measurements conducted in Chapter 3. Particular attention is given to the behaviour in the through-thickness direction, which has a significant influence in the initiation of damage in the composite structure. The strain fields are examined at increasing levels of magnification, providing high resolution measurement of the developing strain distributions. Complex localised strain features are identified, and experimental challenges related to conducting DIC at high magnification are discussed

4.2 Global response of joint

Analysis was performed using a 3D stereo DIC configuration [69] to measure both the in-plane and out of plane displacements and strains. The 3D DIC analysis uses two synchronised LaVision 12 bit 5 megapixel Imager E-lite cameras fitted with 50 mm lenses, to image the specimen. The two cameras are mounted on a beam supported on a tripod, such that they are positioned at a similar distance and angle of incidence to the specimen face. A calibration procedure is undertaken using a type 7 LaVision calibration plate bespoke to the DaVis software. Using this calibration process the relative position of the cameras and specimen in 3D space by the correlation software [69] allowing both in-plane and out-of-plane displacements of the specimen can be analysed. The load cell output and the camera signals are processed through an analogue/digital converter into the DIC software for analysis. Illumination was provided by a 72 W CREE XR-E Q3 LED floodlight with 1310Lm illumination at 2m. The CREE XR-E Q3 LEDs used in the floodlight emit most of their light in the 450 and 550nm wavelengths. This matches well with the Sony ICX625 sensor which peaks in sensitivity around the 500nm wavelength, ensuring maximum image signal and reduces noise in the image signal. A schematic of the 3D DIC setup can be seen in Figure 24, showing the image capture, illumination and data acquisition systems used.

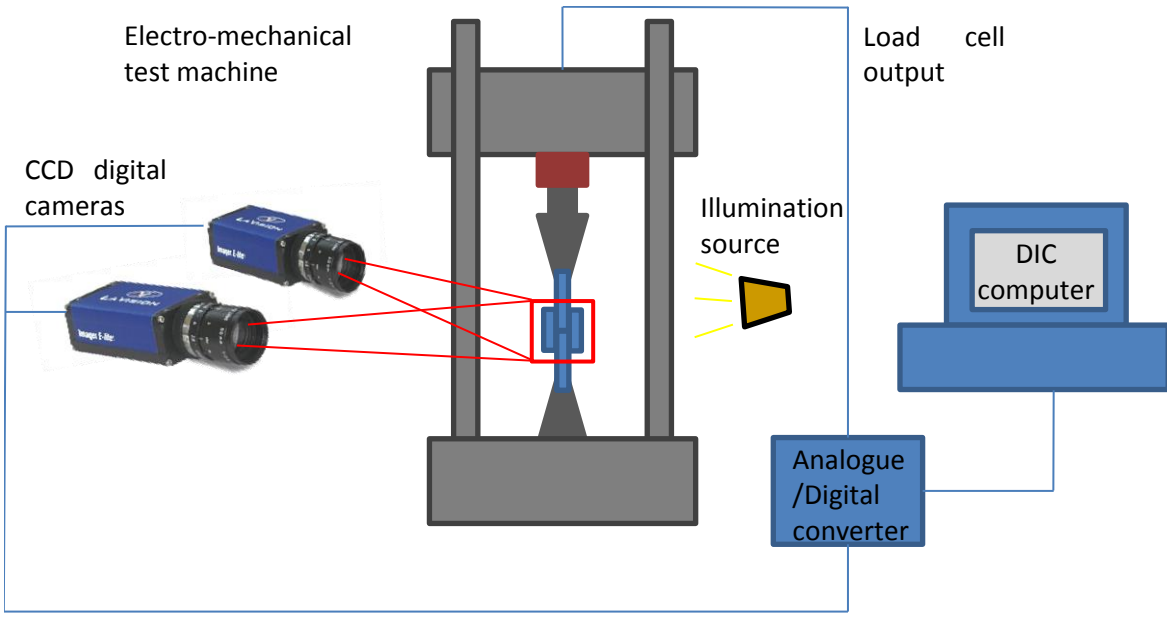

Figure 24: Schematic of 3D DIC experimental set up

3D analysis was initially undertaken, as although the double butt strap joint has been designed to minimise out-of-plane deformation, any out-of-plane deformations must first be quantified before a 2D configuration can be used with confidence. The synchronised cameras imaged the joint at 1 Hz as it was loaded at 2 mm/min up to failure in an Instron 5569 servo mechanical test machine. The specimen was viewed edge on, capturing the response of the axial and through-thickness strains through the thickness of the joint. The data was processed using a subset size of 64 x 64 pixels and a subset overlap of 50%, producing a spatial resolution of 1.04 mm between each processed strain data point, generating 22 data points across the 23 mm width of the joint.

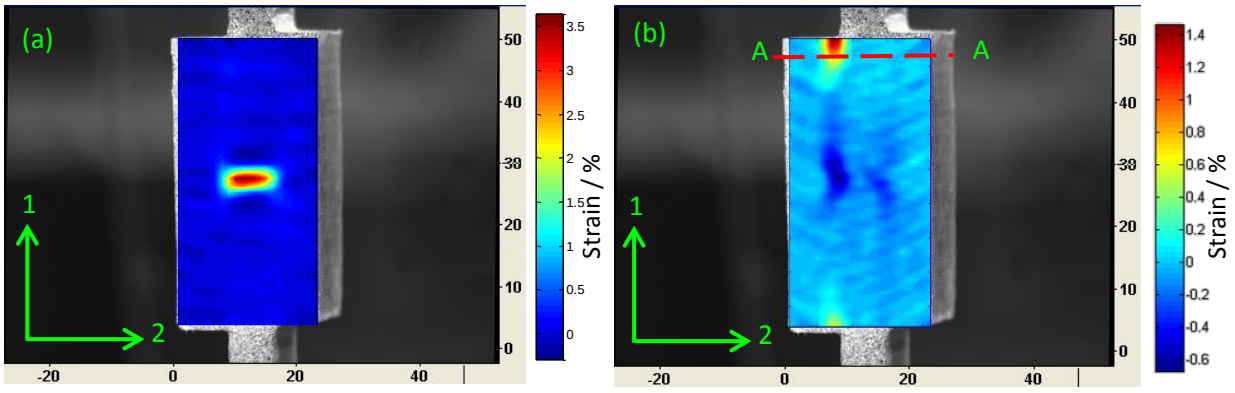

Figure 25: (a) axial (ε_1) (b) through-thickness (ε_2) strain distribution in joint loaded at 16kN

Figure 25(a) and Figure 25(b) show the axial and through-thickness strains (denoted with axes 1 and 2) in the DBSJ specimen at 16 kN which is 95% of the specimen failure load. Analysis of the loading sequence shows a widely uniform axial strain field throughout the joint. Figure 25(a) demonstrates large shearing of the adhesive between adherends, facilitating load transfer between the inner adherend and outer straps, distributing the axial load across the joint. A high axial strain concentration is visible in the centre of the joint in Figure 25(a) corresponding to the area of compliant adhesive at the butt between inner adherends. Two large through-thickness strain concentrations can be identified at the discontinuity between the inner adherend and the outer strap in Figure 25(b). Above 14.8kN asymmetry in these distributions appears, with larger strains observed in the concentration at the top of the joint. Maximum through-thickness strain of 2.6% is recorded at 16kN in the concentration at the top of the joint near to section A-A, before the joint eventually fails catastrophically in this area.

Analysis of the through-thickness displacements bisecting section A-A reveals a step change in the displacements through the high through-thickness strain concentration. The loads at which the step change occurs corresponds to the visual asymmetry of the through-thickness, $\varepsilon_{2,}$ stain distributions. The discontinuity in displacement suggests that the recorded strain values in this area are generated by rigid displacement of the adherends caused by the growth of a crack, and not true strain in the material. No discontinuities in the through-thickness displacement were observed through the concentration at the bottom of the joint, indicating a true material response.

It is interesting to note the analysis captures two very different responses at the discontinuity regions between the inner and outer adherends. This indicates that the mechanisms occurring are very unstable and have a large impact on the global strength of the joint. Clearly, at this spatial resolution, the location of the crack initiation and subsequent propagation cannot be accurately assessed, only providing a qualitative indication of the failure initiation site in the joint. This severely limits the analysis, and needs to be improved for quantitative analysis of the material responses in this damage initiation area.

The analysis has shown the DIC technique is capable of successfully capturing the axial strains in the joint under load, but that greater spatial resolution is required before a full understanding of through-thickness strain behaviour in the joint can be made around the critical failure initiation sites. The spatial resolution severely limits the analysis, and must be improved for any quantitative analysis of the damage initiation area to be carried out. The limitation of using DIC is the inherent trade-off between spatial resolution and strain precision. Figure 26 shows schematically, how to achieve a high degree of strain precision, large subset sizes are needed, increasing the accuracy due to the increased number of features in the subset. The effect of this

though, is to reduce the spatial resolution of the images, as fewer subsets can be fitted into the size of the image. In this study it is desired to have both high strain precision and high spatial resolution to have confidence in the analysis of the local strain distributions. Figure 26 illustrates that these two regions of high resolution and precision, identified in the green highlighted circles, cannot be satisfied simultaneously using the DIC processing parameters available. As a result, it is proposed to use magnifying optics to increase the spatial resolution of the data, whilst using large subsets to maintain high strain accuracy, overcoming the trade-off in the processing parameters.

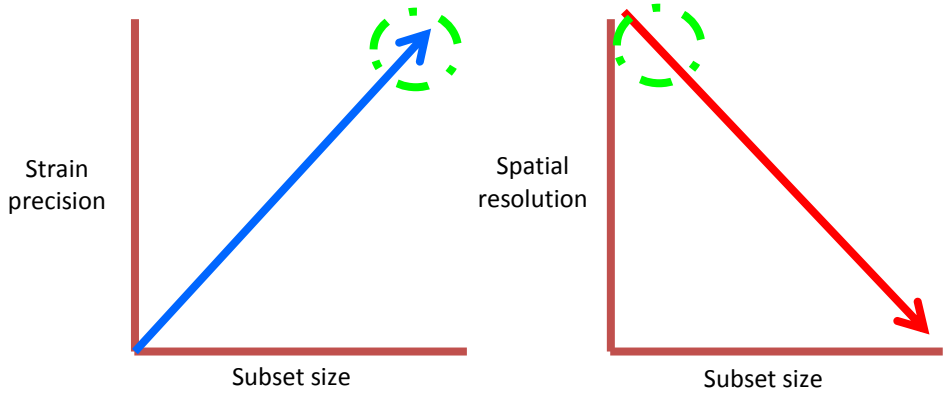

Figure 26: schematic of the trade-offs in DIC processing parameters

4.3 High magnification DIC

Images with greater spatial resolution are required to address the limitations in the analysis identified from the 3D DIC investigation. Greater spatial resolution, i.e. increasing the number of pixels per millimetre, can be achieved using a camera with a larger sensor array, containing a greater number of pixels, and hence increasing the number of interrogation cells in the analysis. However, these cameras are expensive. An alternative approach is to use magnifying optics providing an image with a high spatial resolution at the expense of reducing the size of the area of interest for analysis. Using this technique there is no need to compromise on the size of the subsets in the analysis, as a large spatial resolution of data points/mm is obtained. This provides a high level of strain precision whilst retaining a high spatial resolution of data, both of which are essential for the accurate analysis of the joint.

The short focal length and large dimensions of the macro lenses required for the magnified imaging limits analysis to a 2D system, i.e. one camera aligned perpendicular to the joint face. The disadvantage of the 2D set up is that it is unable to determine out of plane movements,

instead manifesting the motion as erroneous in-plane deformation. The maximum out-of-plane displacements of the joint recorded from the 3D analysis was 0.2 mm, which results in an out of plane strain of around 0.4% which is about the same size as the measured strain shown in Figure 25(b). However it was observed that this displacement occurred at the beginning of the testing when loading between 0 and 200 N, above which the out of plane displacement remained constant. This infers that the motion originates from settling of the machine grips under load, and not deformations from the loaded joint. Unfortunately this parasitic test machine compliance cannot be completely eliminated as the compliance is within the grips of the test machine. To minimise its effect, small aperture sizes are selected to maximise depth of field, and the camera was mounted on an X-Y- ϕ micro adjustable stage to ensure perpendicular alignment of the camera to the specimen surface, reducing optical distortions. A LED ring flash light was used to provide consistent cold lighting for the data collection.

An area of interest measuring approximately 9.84 mm x 8.24 mm with an image resolution of 250 pixels/mm was imaged around the geometric discontinuity between the inner and outer strap at the top left hand side of the joint in the area of high through-thickness activity seen in the global DIC analysis as indicated in Figure 27. The joint was loaded in an Instron 5569 servo mechanical test machine at 2 mm/min until failure and images recorded at 5 Hz. The same correlation settings as those used for the global joint DIC study, were used as they produced a good compromise between the noise of the strain data and the spatial resolution of the data, delivering a spatial resolution of 7.8 data points per millimetre.

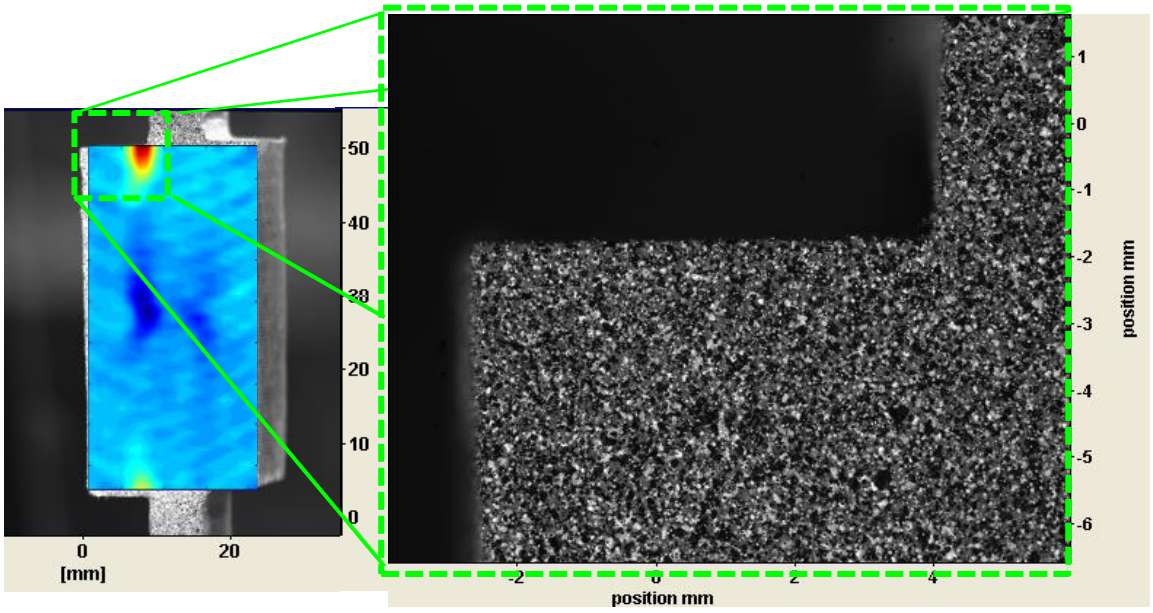

Figure 27: Area under macro DIC investigation

Figure 28 shows a plot of the through-thickness strain in a DBSJ specimen at 17 kN (80% of the specimen failure loa(d), with an image resolution of 250 pixels / mm. Increasing the magnification improves the resolution and structure of the data compared with the initial global joint DIC, Figure 27. A more detailed image of the through-thickness strain distribution is shown developing around the geometric discontinuity. A number of localised features can be identified at the root of the discontinuity, in the CSM layers in the inner and outer adherend, and at the interfaces between the adherends and the adhesive layer. The through-thickness strain in the inner adherend is concentrated in a small region at the root of the discontinuity circled in red, where the load path eccentricity is greatest, reaching a maximum of 0.5% strain, reducing rapidly away from the discontinuity. An area of high through-thickness strain approximately 2 mm x 2 mm is visible in the outer adherend next to the discontinuity circled in blue, reaching a maximum of 0.8% strain where the discontinuity is greatest, extending downwards along the adhesive interface with the outer adherend. An area of compression is also visible below the root of the discontinuity in the inner adherend circled in the red dashed line, formed as a result of the rotation of the outer adherend, peeling away under load, compressing the inner adherend. Figure 28 identifies unique features, which were not visible at 30.8 pixels / mm, revealing a complex distribution of through-thickness strain concentrations and damage initiation sites in the joint. The generation of the two through-thickness strain concentrations either side of the discontinuity provides an indication of the local load path around the discontinuity, bisecting the high through-thickness strain areas either side of the adhesive. Furthermore, the proximity of these concentrations next to each other indicates a coupling between the material responses experienced either side of the adhesive due to load transfer occurring across the adhesive discontinuity between adherends, and their interaction with the adhesive layer. Analysis of these strain concentrations shows lower through-thickness strain at a higher load compared to the testing undertaken at 30.8 pixels / mm indicating no damage in joint. This is also seen from evaluation of the displacement fields near the discontinuity.

Evaluation of the shear strain in the joint at the same loading level is shown in Figure 29. A distinct band of shear strain can be seen in the adhesive. This identifies significant shear loading of the adhesive between the adherends, suggesting that the main load transfer mechanism across the discontinuity between the adherends is enabled through shear of the adhesive. Elevated shear strains are visible in the facesheet layers of the adherends, compared to the rest of the adherends in Figure 29, demonstrating the interaction between the shear loading of the adhesive. The shear response of these areas shows the interfacial layers of material to be very important in the transition from axial load in the inner adherend, through the adhesive, and into axial and through-thickness loading of the outer adherends.

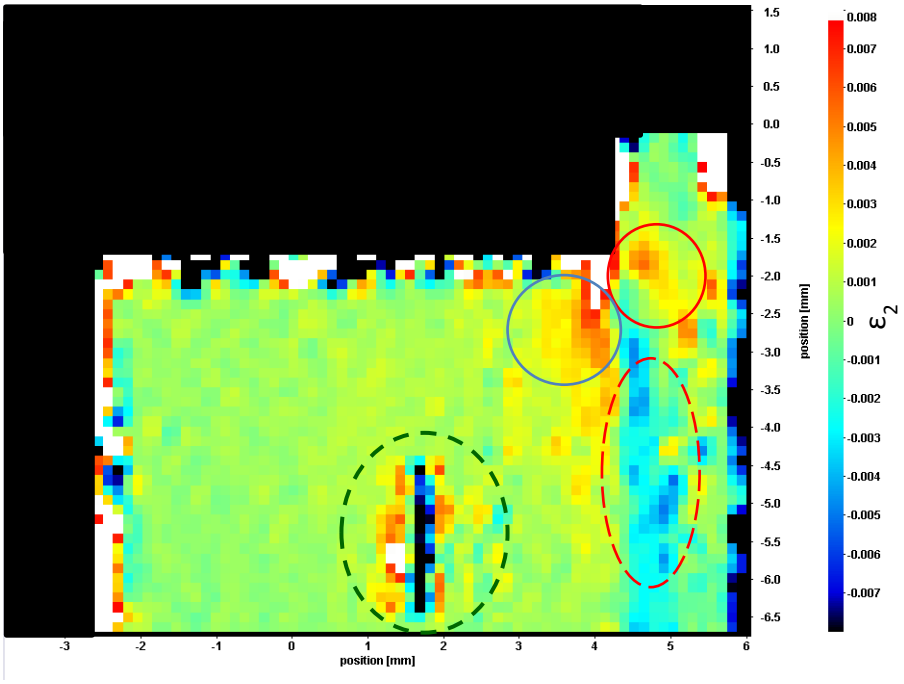

Figure 28: ε_2 in joint loaded at 17 kN under 250 pixels / mm

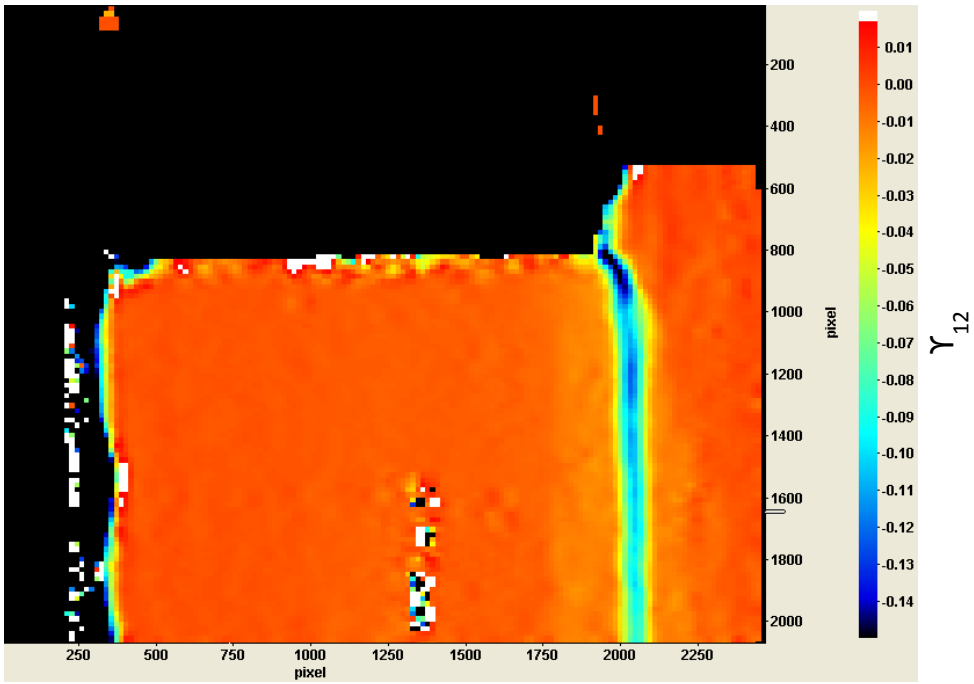

Figure 29: γ_{12} in joint loaded at 17kN under increased magnification

4.4 Shortcomings of current DIC setup

Increasing the magnification has allowed analysis of the strain concentration at the geometric discontinuity at a greatly improved resolution compared with the initial global joint DIC study. Features which were not visible using the 50 mm lens are now observed in increased detail, particularly around the root of the geometric discontinuity, where through-thickness strains are greatest and from where failure initiates, giving a better indication of the material responses in the joint.

Unfortunately, as identified in the discussion there are still a number of barriers which prohibit the DIC strain data to be effectively used to evaluate the complex strain fields in the joint. The analysis has also shown that a degree of caution is required when looking at the results due to the complex nature of the laminate structure and the overlapping of many of the key strain features in the joint, particularly across the adhesive interface. The quality of the data is an improvement over that seen at 30.8 pixels / mm, however strain data is relatively noisy, particularly away from the root of the discontinuity in the outer strap where there is little straining of the material. This noise is a function of the small deformations being measured, which generate changes to the pixel grey levels from the deformation that are very similar to the fluctuations caused by noise on the camera sensor, producing poorly correlated results. This explanation is evident in Figure 29 which has a better signal to noise ratio compared to Figure 28 due to the greater deformation of the joint through shear, which is well above the fluctuations in greylevel produced from the camera sensor. Improvements in the signal to noise ratio are required to give a higher degree of confidence in the results. Furthermore an area of poorly correlated results appears in the outer strap, circled by the green dashed line, which can be attributed to dust on the camera lens.

The options for improving the experimental set up however are limited by a number of compromises which have had to be adopted, affecting the quality of the results, such as the use of a symmetrical double butt strap joint geometry. The use of a symmetrical joint reduces the internal bending moments in the joint that generate the through-thickness stresses, due to a reduction in the eccentricity of the load path between adherends. The effect of reducing eccentricity reduces the through-thickness stresses, and hence low through-thickness strains are formed in the joint, producing little deformation of the joint in the images. This in turn increases the uncertainty of the strain measurements and decreases the signal to noise ratio of the data. Thinner straps could be used to increase the through-thickness strain in the joint, whilst keeping it symmetrical. However reducing the area around the discontinuity is likely to make the localised strain distributions smaller and harder to observe.

These geometrical issues are also compounded by the compromise between the spatial resolution and strain precision which still remains, even though the magnification has been increased from 30.8 pixels / mm up to 250 pixels / mm. A smoothing method could be used to reduce the noise levels in the image, but the definition and detail of the strain concentrations size and magnitude, which are needed to be able to analyse the through-thickness joint response adequately, will be lost. In order to combat these deficiencies in the analysis it is proposed to increase the magnification of the images further. This will have a number of beneficial effects. Firstly, for the same strain levels there will be an increased pixel movement in the image, which should improve the quality of the correlation as the uncertainty associated with the joint movement will be decreased. Secondly, increased magnification will allow for a higher degree of spatial resolution in terms of data per millimetre, whilst keeping the subset sizes large enough to ensure high levels of strain accuracy.

Increasing the magnification however is not a simple solution, as it creates a number of difficult practical issues with the experimental and analytical set up which must be overcome. These issues are principally related to the optic, generating a reduced depth of field, increased sensitivity to vibration/movement, and darker images due to a reduced effective aperture size. A major and often unconsidered, additional barrier to conducting DIC at higher magnifications are the large changes to the appearance of the applied speckle pattern used by the correlation algorithm. The fundamental changes in the pattern properties have wide implications of the performance of the DIC measurement, requiring further analysis to have certainty in the accuracy of the small and complex strain distributions observed around the discontinuity of the joint. This analysis will be addressed in Chapter 5.

4.5 Conclusion

Further analysis of the adhesively bonded joint has been provided through the use of Digital Image Correlation. This technique has allowed quantitative evaluation of the individual components of strain in the joint as it is loaded. Analysis was initially conducted with an image resolution of 30.8 pixels / mm, observing the whole joint loaded up to failure. A region of high axial strain could be seen in the low modulus, compliant adhesive region between the two inner adherends, in addition to the formation of two large through-thickness strain concentrations around the geometric discontinuity in the joint. The analysis provides a broad picture of the global strain distributions in the joint, which is heavily limited by the spatial resolution of the data.

Magnifying optics were used to increase the spatial resolution of the data, imaging at 250 pixels / mm. The macro imaging was focused on the geometric discontinuity between the inner and outer strap identified in the global joint analysis to have the greatest through-thickness response. Increasing the magnification shows a large improvement in the quality and detail of the analysis. Local through-thickness strain concentrations are identified in the adherends either side of the geometric discontinuity, demonstrating the behaviour of the composite adherends due to the high through-thickness load transfer across the adhesive between adherends in this region. Unfortunately analysis is still limited by a low signal to noise ratio, preventing confidence in the experimental results, and the spatial resolution of the data is not sufficient to evaluate with the through-thickness material response prior to failure.

It is proposed to increase the magnification further to increase the spatial resolution and accuracy of the data at lower strain levels. Increasing the magnification produces a number of experimental challenges, of which the appearance of the applied speckle pattern requires further investigation to assess the sources and contributions of error in the DIC measurement that can be attributed to the higher magnification of the pattern.

5. Speckle pattern assessment

5.1 Introduction

Analysis of the strain fields in the adhesively bonded joint up to this point has shown to be limited by the trade-off between spatial resolution and strain precision. Chapter 4 showed that magnifying optics could be used as a low cost method of overcoming this limitation and improving the spatial resolution of the data. Before further investigation is undertaken using high magnification optics it is very important that a solid understanding of the DIC process and the sources of error in the measurement is obtained. Of particular interest is the role of the random speckle pattern and its effect on the measurement error due to the fundamental changes in its appearance with increased magnification.

When using magnifying optics, the observed shape, size and distribution of the applied speckle pattern is very different to lower magnification images. This results in significantly different properties for the correlation algorithm to track, and ultimately heavily influences the accuracy of the measurement. To achieve confidence in the repeatability and reproducibility of the measurements at high magnification levels, it is important to ensure the applied speckle pattern properties, in terms of the size, shape and distribution of the speckles, are suitable for analysis at these high magnification levels.

The aim of this chapter is to identify that the morphometric properties, such as size, shape and distribution of the speckle, in the pattern are an important indicator of pattern quality. An image processing approach is developed to analyse the properties of a number of speckle patterns, showing fundamental changes to the pattern as magnification levels and spatial resolution are increased. This method is used to identify the most suitable pattern application method when conducting 2D DIC at the mesoscopic scale using magnifying optics, and quantify the anticipated measurement uncertainty from the pattern. Analysis is conducted on four different pattern types, varying application method and pattern colour, at two different magnification levels. Analysis of numerically generated patterns is also used to show a relationship between the size and density of the speckles locally within an interrogation cell, linking the errors and trends from the morphometric analysis to the DIC correlation algorithm.

5.2 DIC method and measurement accuracy

A detailed discussion of the DIC process is presented in the earlier literature review in Chapter 2, however as this chapter deals specifically with the concepts of DIC, it is apt to present a brief reminder of the approach before further analysis.

Digital image correlation is a white light technique based on the comparison of images of the specimen before and after deformation, typically acquired using a monochromatic CCD camera. A stochastic speckle pattern is applied to the specimen surface to provide random grey level fluctuation, which is tracked using the correlation algorithm. The images are divided into a grid of interrogation cells (subsets) and movement of pixels within the cells between images detected by searching for areas of matching grey scale values between the deformed and undeformed images. The resolution and accuracy of the displacements calculated using DIC are limited by the number of pixels within the image. If a high degree of spatial resolution is required, such as in areas of complex strain distributions, smaller interrogation cells must be used, but as the interrogation cell size is decreased, the uncertainty in the strain measurement increases [71], due to a reduction in the number of features to track within the subset. The use of magnifying optics, such as macro lenses or microscope stages, is an option to achieve a high spatial resolution of data within a small region of interest, whilst using large interrogation cell sizes to minimise the strain measurement uncertainty.

The majority of research into the accuracy of the DIC technique has focused on the many different correlation algorithms and processing parameters, such as subset size [146], shape function selection [75] and methods of obtaining sub-pixel accuracy [147]. Less attention has been paid to the effect of the quality of the speckle pattern on the measurement accuracy of the DIC technique, particularly, differences due to changes in the spatial resolution of the image. It is also important for the speckle pattern to be matched to the expected displacement field to maximise measurement accuracy, as speckles can be both too large and too small for accurate measurement [148]. In references [149] and [150] patterns with a range of speckle sizes, applied using different methods were examined. Haddadi and Belhabib [149] identified that finer patterns with more speckles and more ‘randomness’ performed better in comparison to larger ‘dotted’ patterns in rigid body motion tests. Barranger et al. [150] noted the importance of matching the pattern to the expected deformation, with differences between pattern types becoming greater at larger levels of strain. The reasons behind the performance differences for the patterns were not assessed, nor were the suitability of the patterns tested for different applied strain levels, allowing only qualitative conclusions to be made which cannot be used to benchmark pattern quality.

A number of pattern assessment criteria have been presented in the literature, generating a range of different pattern quality measurement parameters. These parameters do not provide the definition of a perfect pattern to be used, as there is insufficient control in the application of the speckle pattern or imaging methods to consistently achieve the same quality of pattern from user to user. Rather the parameters are best used as comparative assessment tools to inform application methods and inform error analyses of DIC measurements. Broadly these metrics can be separated into global and local assessments. Measures such as the Sum of Squared Subset Intensity Gradients [151] and Mean Intensity Gradient [152] have both been developed directly from an understanding of the Sum of Squared Differences correlation algorithm, measuring pattern quality locally at each pixel location. However these two parameters are presented as a summation and a mean of the image intensity gradients at each pixel location within the entire image. This approach provides global measures from local criteria. The summation and mean values are not considered to be appropriate as the speckle pattern is stochastic across the region of interest and unrepresentative of the pattern quality, as there is no indication of the variation in quality across the image. This is important as the values can be significantly biased by areas with anomalously high or low intensity gradient values. The Mean Subset Fluctuation [153] and Subset Entropy [146] provide metrics which assess the difference between the grey level of each pixel within the image to the mean grey level value of each subset, and the grey level values of the eight surrounding pixels at each location. These metrics are also calculated locally within the subset, and then presented as a mean, global, value for the whole of the image, ignoring variation between subsets in the pattern.

Morphological approaches have been used to apply local analysis of pattern quality based upon the physical properties of the pattern, such as the size and frequency of the speckles within the pattern [148], [154]. Typically this is undertaken using an image thresholding technique, converting all pixels with grey levels above / below a certain threshold value into black and white values to form a binary image of the pattern. The thresholding method is a fast and practical solution, but can fail to identify the true edge of shapes in patterns. Alexander [155] noted that the size and shape of the generated binary speckles are highly dependent upon the chosen grey level threshold value, which can result in the edge of the speckles being poorly defined and not representative of the actual speckle size or shape. The threshold method also prevents the identification of discrete speckles below/above the threshold values, which is especially evident where there is a very broad grey level distribution, or where the edges of the speckles are very soft. These local measures are more adept at quantifying differences between patterns due to changes in application method or pattern style i.e. black paint on white back ground and vice versa, both of which are important considerations for experiments with different materials and scales. Importantly, using these morphometric techniques, the local

information from within the pattern is not lost or masked in the attempt to form a global parameter from what are highly variable and complex analysis problems. As a result the local, morphometric, pattern analysis approach is used in this paper. For completeness a summary of recently used global and local pattern assessment criteria is provided in Table 4.

Table 4: Review of recent pattern assessment criteria

	Pattern assessment criteria	Global	Local	Pros	Cons
Sum of Square of Subset Intensity Gradients [151]	$SSSIG = \sum_{i=1}^{N}\sum_{j=1}^{N}\left[f_{x,y}(x_{ij})\right]^2$	x		Intensity gradients directly used in the Sum of Squared Differences correlation procedure Provides a direct measure between the pattern and correlation process	Total value for image does not show variability within the pattern SSSIG does not describe how or why patterns are different to each other – difficult to comparatively analyse application methods
Mean Intensity Gradient 147]	$\delta_f = \sum_{i=1}^{N}\sum_{j=1}^{N}\frac{\sqrt{f_x(x_{ij})^2 + f_y(x_{ij})^2}}{W\ x\ H}$	x		Intensity gradients directly used in the Sum of Squared Differences correlation procedure	Mean value for image introduces bias as the calculation as it does not show variability within the pattern
Mean Subset Fluctuation [153]	$S_f = \frac{\sum_{P\in F}\sum_{i=1}^{3}\sum_{j=1}^{3}\lvert a_{ij} - \bar{a}\rvert}{W\ x\ H}$	x		Compares pixel grey level values to the mean grey level value of each subset Provides a measure of contrast within the pattern	Mean value for image does not show variability within the pattern Bias towards patterns with very high contrast where $\lvert a\_ij\text{-}\bar{a}\rvert$ is maximised Cannot distinguish influence of speckle size i.e. one large speckle of size 50 pixels in the subset will yield same results as 10 speckles each with an area of 5 pixels distributed within the subset
Subset Entropy [146]	$S_f = \frac{\sum_{P\in F}\sum_{i=1}^{3}\sum_{j=1}^{3}\lvert a_{ij} - \bar{a}\rvert}{W\ x\ H}$	x		Identifies differences between each pixel to its surrounding 8 pixels grey levels giving an indication of the fluctuation, or 'randomness' of the pattern	Mean value for image does not show variability within the pattern
Speckle radius distribution [154]	Image thresholding		x	Fast and easy to implement	Speckle Radius does not account for speckle shape which influences speckle size Threshold method inaccurate
Average speckle size [148]	Image thresholding			Fast and easy to implement	Average size doesn't show variability within pattern Threshold method inaccurate

5.3 Speckle pattern generation

A variety of speckle patterns, application methods and pattern colours are typically used in digital image correlation. In this study two different pattern application methods are investigated; spray paint and airbrush. A Clarke Wiz air compressor and airbrush kit was used to apply the airbrush patterns using Createx opaque paints for the speckles. High quality RS components matt black and white aerosols were used for the spray paint patterns. These two application methods were each tested with two different background colour combinations. The four different pattern types are each tested at two high magnification levels of 296 pixels /mm and 705 pixels /mm. Four samples of each pattern type were produced and analysed providing a sufficient sample for general trends between pattern application methods to be analysed. A summary of the pattern application methods and magnification levels used is given in Table 2.

Pattern type	Area of interest	Pixels/mm	Spray can	Airbrush	Background colour	Speckle colour
A_{b_296}	8.3 x 6.94	296		X	Black	White
A_{w_296}	8.3 x 6.94	296		X	White	Black
S_{b_296}	8.3 x 6.94	296	X		Black	White
S_{w_296}	8.3 x 6.94	296	X		White	Black
A_{b_705}	3.45 x 2.88	705		X	Black	White
A_{w_705}	3.45 x 2.88	705		X	White	Black
S_{b_705}	3.45 x 2.88	705	X		Black	White
S_{w_705}	3.45 x 2.88	705	X		White	Black

Table 5: Speckle pattern properties

The patterns were painted on a flat plate of glass fibre epoxy composite material, which was sanded smooth to prevent the substrate texture influencing the quality of the applied patterns. To achieve a consistent pattern application methodology the paint was sprayed from a similar distance, with the same number of spray passes. A 5Mp 12 bit monochromatic LaVision E-lite camera fitted with a Canon MP-e65 lens was used to image the speckle patterns. The visual change in the speckle patterns due to application method and magnification can be seen in Figure 30, imaging an area of interest of 8.3 mm x 6.94 mm and 3.45 mm x 2.88 mm.

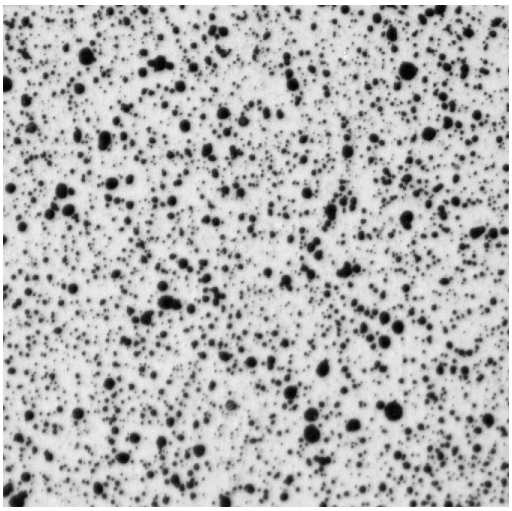

A_{W_296} (Airbrush, 296 pixel / mm)

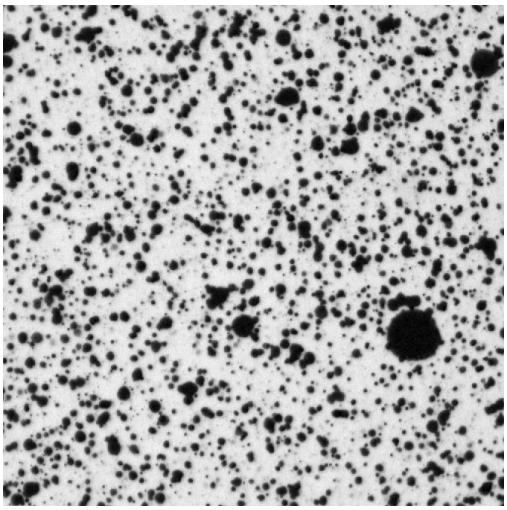

S_{W_296} (Spray can, 296 pixel / mm)

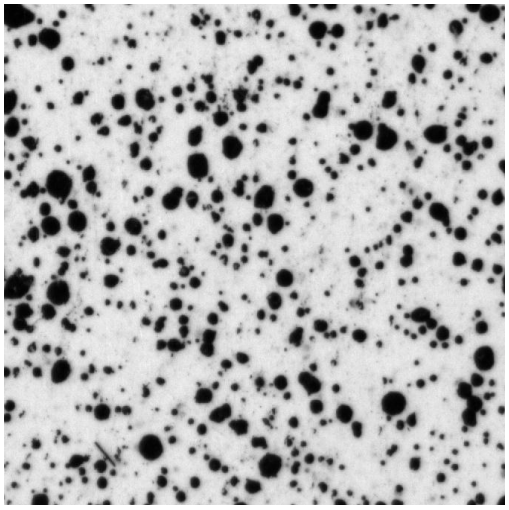

A_{W_705} (Airbrush, 705 pixel / mm)

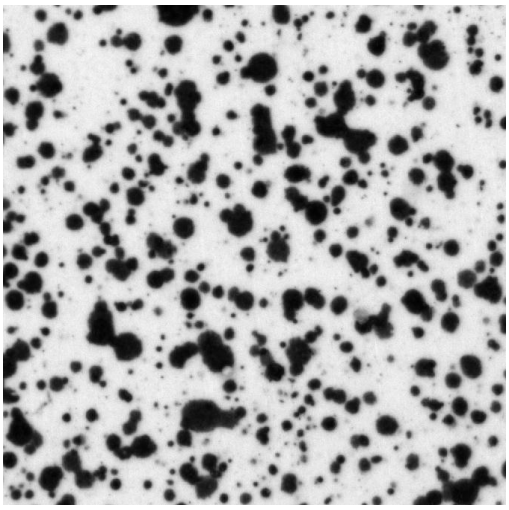

S_{W_705} (Spray can, 705 pixel / mm)

Figure 30: Physical differences between speckle patterns under increased magnification and different application methods.

The patterns were imaged under lighting levels which maximised the grey level distribution of the image over as much of the 12 bit dynamic range as possible available from the camera CCD without resulting in saturation of the image. The exposure time and lighting levels used for the images were adjusted for the two magnification levels so that the histograms of the images remained as similar as possible. Histograms of speckle patterns S_{B_296}, S_{W_296}, S_{B_705} and S_{W_705} are provided in Figure 31 and demonstrate the similarity between patterns at the different magnification levels. This similarity ensures that any measurement errors evaluated in this study are a result of the physical changes to the pattern as opposed to reductions of the dynamic range of the image, which are known to influence the accuracy of DIC measurements [150].

Evaluation of the image histograms can be used as an initial assessment of the properties of the speckle patterns. The histograms show the frequency distribution of the available grey levels, from 0 (black) to 4096 (white), within the image, identifying very different properties between patterns with a white or black background. Figure 31 shows patterns with a black background (S_{B_296}, S_{B_705}) containing a narrow, high frequency peak of black grey levels, representing the large amount of black background colour. There is little distribution of mid-range or white grey level values, identifying a small and poorly contrasted number of white speckles in the image. In contrast, the patterns with a white background (S_{W_296}, S_{W_705}) show a lower, but broader peak of white grey levels. The width of the peak shows that the background colour is not as monochromatically biased as that of the patterns with a black background, rather that there is a larger degree of grey level variation within the background, generating greater mid-range grey levels. The greater breadth of the grey level distributions identifies the possibility for greater pattern uniqueness compared to the darker patterns.

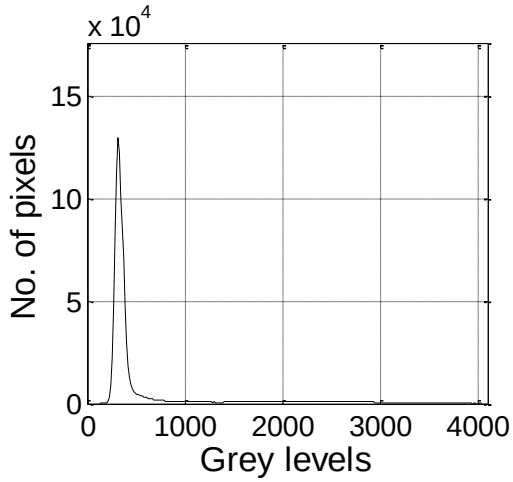

Pattern S_{B_296} (Spray can, black background, 296 pixel / mm)

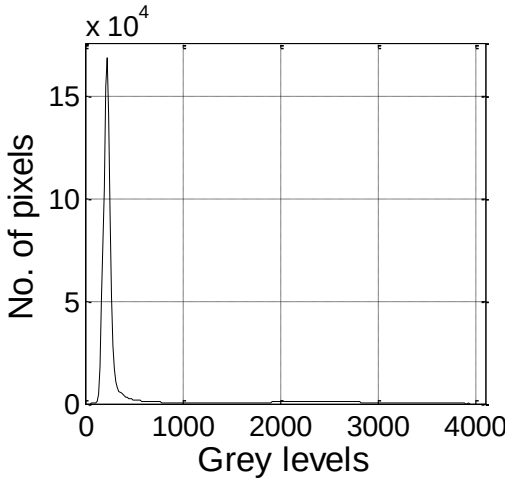

Pattern S_{B_705} (Spray can, black background, 705 pixel / mm)

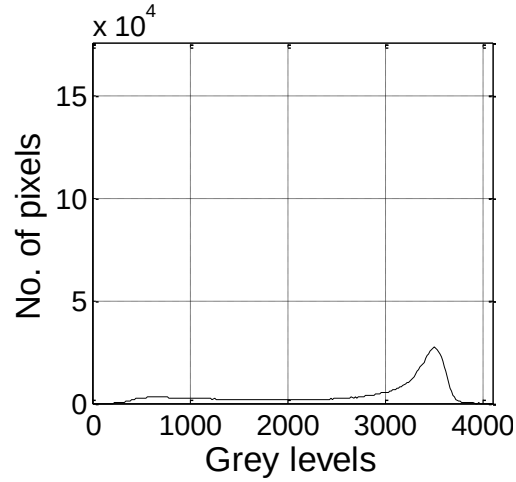

Pattern S_{W_296} (Spray can, white background, 296 pixel / mm)

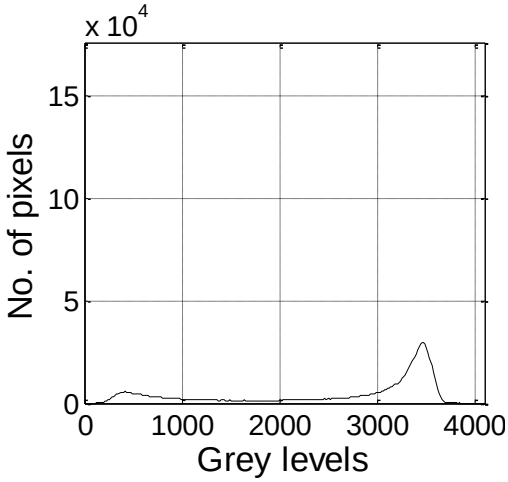

Pattern S_{W_705} (Spray can, white background, 705 pixel / mm)

Figure 31: Histograms of speckle patterns with black and white backgrounds at both magnifications

Further analysis of the image histograms can be conducted using a simple global image assessment parameter from information theory known as Shannon entropy [156]. Shannon entropy provides a measure of the information content of an image that is used for evaluating the randomness, or texture, of a form or pattern. An image with high entropy requires a large number of 'bits' to create an adequate representation of the form in a digital image. Hence a pattern with a high Shannon entropy value indicates a high level of texture, or broadness in the

grey scale distribution of the image, both of which are beneficial for maximising the correlation function peak when a correct match has been found. The Shannon entropy is defined as [14]:

$$Shannon\ entropy = \sum_{i=1}^{N} p(x_i) \log\big(p(x_i)\big) \tag{20}$$

where N is the grey level value and $p(x_i)$ is the probability of the given grey level in the image.

Figure 32 shows a plot of the mean entropy of the four specimens for each pattern type. A large difference is visible between the patterns created with a black and white background, with white background patterns showing constantly higher entropy at both magnification levels. This supports the initial visual histogram assessment, which saw white backgrounds delivering an image with a broader dynamic range. Under increased magnification, patterns with white backgrounds maintain similar entropy levels as the low magnification, whereas patterns with a black background experience a reduction in entropy due to the more uniform and narrower dynamic range of the background grey level. The difference between the Shannon entropy values for patterns produced with the spraycan (S_{b/w_296}, S_{b/w_705}) and the airbursh (A_{b/w_296}, A_{b/w_705}) is small, with higher entropy values produced by patterns with a spraycan suggesting better pattern quality.

Image histogram and Shannon entropy values are useful initial pattern selection parameters, as they give an overview of the global properties of different patterns. The main limitation of these measures is that they are only based upon the global image attributes. They do not distinguish between important factors such as the size or distribution of the speckles in the image and are also heavily influenced by the speckle coverage and lighting levels. Moreover, they do not describe any of the physical or morphological characteristics of the pattern within the image, which are needed to make a full assessment of the pattern quality. As such absolute measurements of the quality of the patterns cannot be made reliably using image histograms and Shannon entropy and they act only as a coarse measure of the relative difference between different patterning techniques or magnification levels. A more quantitative method is required to compare the properties and performance of different speckle patterns with a high degree of confidence.

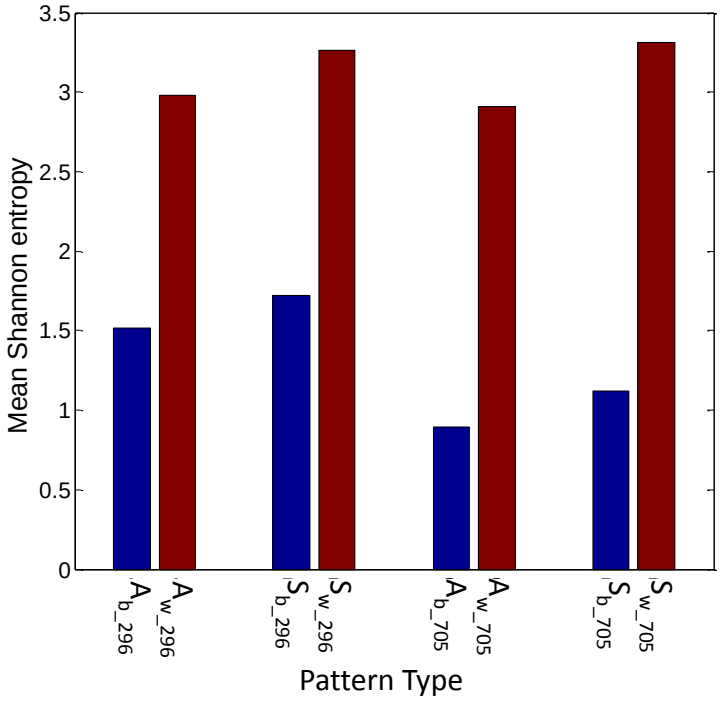

Figure 32: Shannon image entropy

5.4 Morphological assessment of speckle characteristics

Assessment of the histogram and Shannon entropy analysis illustrates how global pattern parameters related to the image quality and information content can mask important local details of a pattern, which contribute significantly towards its suitability for use as a DIC pattern. This is seen in the similarity between the results for vastly different pattern appearances, as identified by Figure 30. It is therefore very important to develop a methodology for pattern assessment based also upon local analysis of the pattern, which can determine changes in fundamental features of the stochastic pattern.

To provide a versatile tool to identify speckles in the images the Laplacian of Gaussian edge detection method is used to analyse the patterns. Application of this method aims to remove the ambiguity of edge detection using the thresholding method by producing more accurate representations of the speckle size and shape. Firstly a Gaussian filter is applied to reduce noise from the image, and then the Laplacian operator is used to calculate the second spatial derivative of the image. From this, regions of rapid intensity change can be detected, that enables the identification of the edges of speckles. Accurate edge detection is controlled by careful adjustment of the Laplacian gradient value and standard deviation of the Gaussian filter. The process is shown in Figure 33. In Figure 33(a) a typical speckle pattern is shown and in Figure 33(b) the edges detected by the Laplacian of Gaussian method is shown. It can be seen in

Figure 33(b) that some edges are detected that do not form a closed contour around the speckle, so a 2D alpha shape technique is employed to reconstruct a closed contour from the pixels along the boundary. The alpha shape method formalises the intuitive notion of the 'shape' of a set of points. A generalisation of a 'convex hull' from the point set is created which describes the space enclosed by a set of points based on the outer most points [157]. The alpha shape generalisation to the convex hull allows concave as well as convex shapes to be mapped, creating a realistic border profile, better matching the actual shape of the pattern. From these closed contours a binary image of the speckle pattern is created for analysis as shown in Figure 33(c).

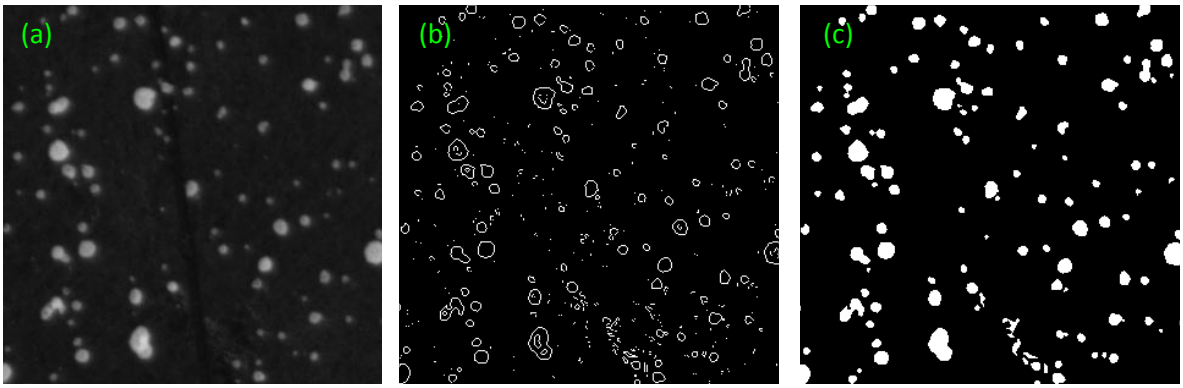

Figure 33: (a) Speckle pattern image (b) Edge detection image (c) Binary speckle pattern

Using the edge detection method the size and number of the speckles in the patterns are analysed. Figure 34 & Figure 35 shows the distributions of speckle sizes up to speckles with an area of 300 pixels in the pattern. The distribution of speckle sizes is expressed as a cumulative percentage of the total number of speckles in the pattern, identifying the frequency distribution of the speckle sizes present within the pattern. For example, a distribution with a straight diagonal line from 0% to 100% would indicate an even distribution of speckle sizes within the pattern, such that each of the speckles in the pattern was a different size. Conversely, a distribution which showed a step change from 0% to 100% at the speckle size of 10 pixels would indicate that all the speckles within the pattern had a size of 10 pixels. The distributions have all been normalised by dividing by the coverage ratio of the pattern, (i.e. the total number of pixels defining the speckles divided by the total number of pixels in the image for each pattern). This removes any bias in the results caused by different speckle densities as opposed to morphometric differences due to the change in spatial resolution. From this the relative differences between the distributions of speckle sizes within the speckle patterns can be seen.

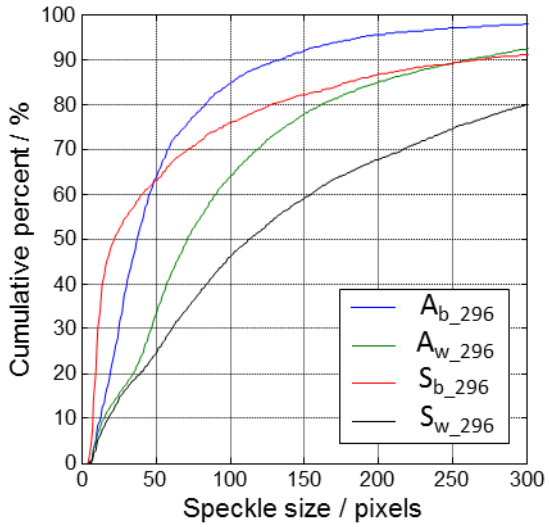

Figure 34: Speckle size distribution – 287pixel/mm

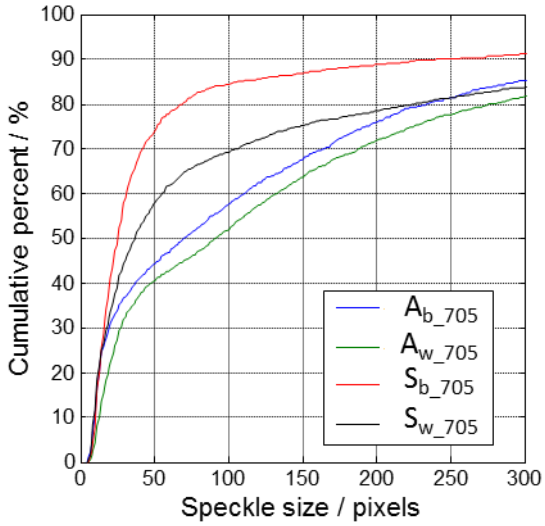

Figure 35: Speckle size distribution – 705 pixel/mm

Figure 34 & Figure 35 show a number of differences between the distributions of speckles at low and high magnification levels due to physical changes to the patterns. At the lower magnification level, Figure 34, the distributions of speckle sizes can be identified to form two different responses depending on the colour of the pattern background. This shows dark background patterns (A_{B_296}, S_{B_296}) to have a higher proportion of small speckles than patterns with a lighter background colour (A_{W_296}, S_{W_296}). Interestingly, a similar distribution of speckles is produced for each background colour below a speckle size of 50 pixels. This identifies both application methods to apply similar distribution of speckle below a size of 50 pixels. Above 50 pixels the differences between application methods becomes more pronounced. Particularly in the case of S_{W_296}, the spraycan exhibits a distribution with a lower gradient compared to the airbrush. This indicates a slightly more even distribution of speckle sizes within the pattern. The larger variation between the pattern distributions is most likely due to the high number of speckles at this magnification, creating a more varied and random distribution within the pattern.

When the magnification increases, the distributions of the speckle patterns appear to change significantly. As shown in Figure 35 the distribution of the patterns can be seen to separate into two different distributions depending on application method; the opposite of the trend identified in Figure 34. The distribution of spray paint patterns S_{B_705}, S_{W_705} have a steep gradient up to approximately 50 pixels, showing a high proportion, 60-80%, of speckles in the pattern below 50 pixels. Above 50 pixels the gradient decreases, showing a lower proportion of large speckles in the pattern. In contrast, the airbrush patterns show approximately 40-45% of speckles below 50 pixels, after which the gradient decreases and the proportion of speckles increases almost

linearly with size up to 80% of the total speckles in the pattern. This indicates that the pattern possesses a more uniform distribution of speckle sizes greater than 50 pixels, within the pattern. The greater distribution of larger size speckles, indicated by the flatter gradient, decreases the randomness of the speckle positions as the larger speckles occupy more space in the finite interrogation cell. However, larger speckles have a greater number of shape permutations, creating more uniquely defined individual speckles within the pattern. Larger speckles also register across more pixels, so there is less relative fluctuation and uncertainty in the speckle shape and size resulting from noise from the camera. In contrast, the distributions created by the spray paint are composed of predominantly small speckles. Speckles of very small size are registered on only a small number of pixels on the camera sensor. This increases the similarity in shape and size of speckles in the pattern, reducing the uniqueness of the pattern. Additionally because of camera noise and grey level fluctuations, small speckles produce large variations in the identification of their size, shape and position relative to their original features, which is detrimental to the accuracy of the measurement. At the higher magnification the difference in pattern distributions resulting from background colours are much less than the differences created by changing the application method. The identification of fewer small speckles may be due to better contrast of the black speckles on the white background and the narrower dynamic range of the background colour in the images, which possess less natural variation in background grey level compared to the white background.

The morphometric Laplacian of Gaussian and alpha shape reconstruction image processing parameters used in the methodology presented in this paper provide a large degree of control and flexibility to adapt to a wide range of speckle patterns, application methods and scales. This includes patterns where the grey level fluctuation provided by the painted speckle pattern is provided by the natural texture of the material, such as in the analysis of polymer bonded explosives [158] or the grain structure of metallics [159]. Natural patterns with a flat texture i.e. possessing very little contrast between features in the pattern, such as bare metallic surfaces [160][161] are less suitable for this methodology. However inconsistent illumination and reflections from these untreated surfaces are highly detrimental to the correlation so the application of a painted stochastic pattern is always strongly advised.

The analysis suggests that patterns applied with an airbrush will perform better than those made with spray paint during correlation at the higher magnification. This can be attributed to the broader, more even distribution of speckle sizes above 25 pixels. This is expected to create a pattern not only with a high degree of uniqueness in speckle position within the pattern, but also high uniqueness between speckles size and shape. A pattern with a large number of unique features for the DIC algorithm to track should reduce the measurement errors by increasing the size of the correlation function peak when a pattern match is made during the calculation. The

spray paint patterns show a higher distribution of predominantly small speckles, which may increase the uniqueness of the pattern. conversely small speckles defined by less pixels have a larger uncertainty of their position, which may increase the error levels [71]. Furthermore, small speckle patterns have been shown to result in phase errors and amplitude attenuation due to their high spectral content when using sub-pixel interpolation methods [162]. At the lower magnification it is difficult to predict the measurement error between patterns as there is a much larger degree of variation in the distributions between the patterns.

5.5 Evaluation of displacements obtained with different speckle patterns

To determine the effect of different speckle pattern characteristics on the quality of the DIC, a known displacement field was imposed on the images. The error was assessed by calculating the standard deviation between the strain fields from the measured DIC result and the imposed deformation. A linear displacement field in the x-direction was applied in strain increments of 0.1% up to 1% maximum strain. The image deformation was undertaken in the Fourier domain by upsampling the transform of the image then downsampling to achieve accurate sub pixel displacements. A low pass filter was applied to the images before manipulation to remove high frequency components and minimise errors caused by image aliasing during the scaling process. Gaussian noise was added to the deformed images to best replicate the experimental variation in pattern intensity due to noise on the camera CCD. The deformed speckle patterns were imported back into the LaVision correlation software DaVis 7.4, which uses a cross correlation algorithm using Fourier transforms to analyse the strain in the x-direction. Sub-pixel accuracy is achieved through a 2D Gaussian peak fitting function, as opposed to interpolation of grey levels in the image. The images are deformed numerically so that errors from lighting and optical aberration effects are removed. Strains are obtained by numerical differentiation of the displacement vectors. Due to the uniform linear displacement field imposed on the image, minimal measurement errors are anticipated from this calculation approach. Errors are being assessed from the difference between the strain and not displacement data as in engineering applications it is the strain data which is of most importance when analysing structures. It is important therefore to analyse the strain error so that an end user of DIC software can have confidence that the speckle pattern being used will result in high fidelity strain measurements. Large interrogation cells of 128 x 128 pixels are used in this study as the use of large interrogation cells produces measurements with a high degree of fidelity [71]. As a result, when using these large subsets, any differences in the strain derived from the DIC can be attributed to changes in

the pattern properties, and not uncertainties resulting from poor quality correlation due to insufficient features in the interrogation cell. Gaussian noise was added to the deformed images to best replicate the experimental variation in pattern intensity due to noise from the camera CCD.

The standard deviation, *SD*, between the imposed strain field, $\varepsilon_{imposed}$, and the measured strain field, $\varepsilon_{measured}$, in the x-direction was calculated for all of the measurement points, *n*, to give a value of the error due to the speckle pattern properties using the following equation

$$SD_{\varepsilon} = \sqrt{\frac{n\sum(\varepsilon_{measured} - \varepsilon_{imposed})^2 - \left(\sum(\varepsilon_{measured} - \varepsilon_{imposed})\right)^2}{n(n-1)}} \quad (21)$$

Figure 36(a) shows that at the lower magnification there appears to be very little difference in the measured error between patterns A_{B_296} and A_{W_296}, whereas the difference between patterns S_{B_296} and S_{W_296} is much larger. In Figure 34 it was seen that within pattern S_{B_296} almost 50% of the speckles in the pattern were below 25 pixels large, and S_{B_296} can also be seen to be the pattern with the highest error values in Figure 36(a). This suggests that a high proportion of small speckles may not be as beneficial as suspected. It is interesting that the errors for A_{B_296}, A_{W_296} & S_{W_296}, which had smaller proportions of small speckles, are very similar, suggesting that the cross correlation algorithm used in the DaVis software is relatively insensitive to the differences in the physical characteristics of these speckle patterns seen in the speckle distributions and histograms at this magnification.

As the magnification increases from 296 pixel/mm to 705 pixel/mm, Figure 36(b), the errors in the strain measurement triple. Very high standard deviation values are recorded for all patterns due to the sparseness of the patterns providing little grey level fluctuation to facilitate the correlation. This is shown in the clear distinction between the errors from the patterns created with an airbrush and spray paint. The airbrush patterns produce approximately half the error compared to those created with the spray paint, as its finer nozzle allows a more even coverage of speckles in the pattern, leaving less bare invariable background colour exposed within the subset. This shows good agreement with the predictions from the morphological analysis in Figure 35, that more even distribution of speckle sizes in the airbrush patterns results in lower strain measurement errors. The spray paint patterns, which show a distribution of predominantly small speckles, appear to result in higher strain measurement error. These results also appear to support the findings of the initial numerical deformation study regarding the relationship between the speckle size, shape and error. The high error values illustrates the importance of examining the role of the speckle pattern in greater detail, showing that small changes in the pattern properties identified using the morphological approach yield large changes in the

measured strain error. Figure 35 shows that the background colour of the speckle pattern had little effect on changing the shape of the speckle pattern distributions for the airbrush patterns, with white backgrounds having slightly lower distribution curve gradients. Figure 36(b) shows there to be little difference between the measurement errors for the two background colours for the airbrush, with the white background producing slightly lower error. However, for the spray painted specimens, the white background appears to produce almost half the error compared to patterns with a black background. This reflects the larger difference between the speckle distribution curves observed for pattern A_{b/w_705} & S_{b/w_705} in Figure 35. This result also suggests that there is more natural variation in the grey level of the white background between the sparse speckles compared to in the black background, improving the correlation between images and lowering the contribution of the anomalous results on the standard deviation error measurement.

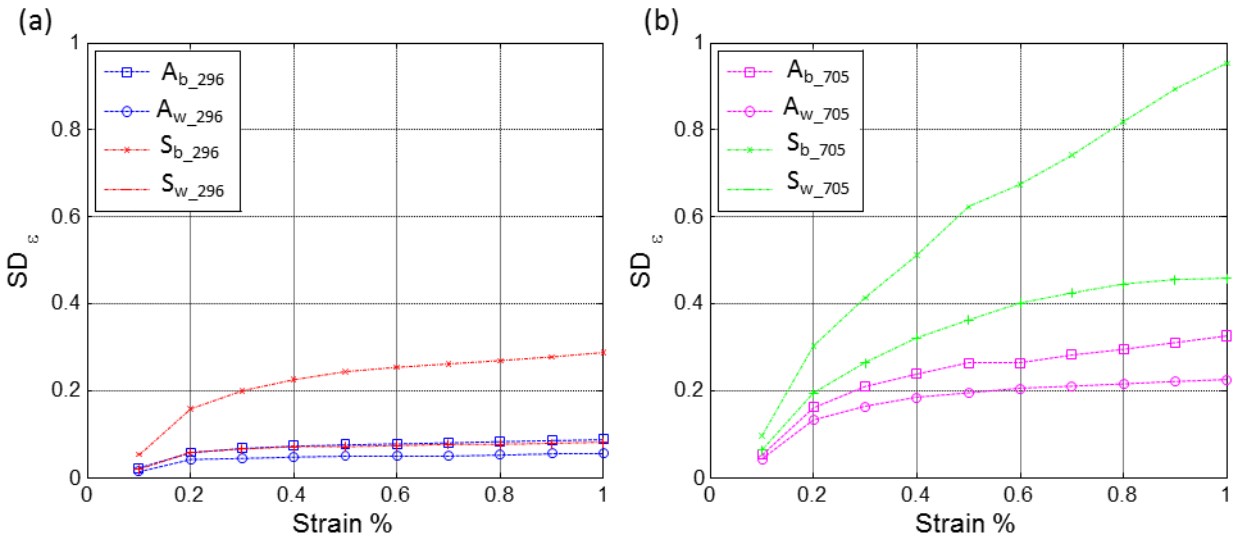

Figure 36: Standard deviation of strain data at (a) 296 pixel/mm (b) 705 pixel/mm

5.6 Experimental pattern analysis

The results appear to show that analysis of the speckle pattern distribution using the morphological methodology is a good indicator of pattern quality. Validation of the morphological and numerical analysis was conducted by comparing experimental DIC and strain gauge results, evaluating the errors caused by the speckle pattern. 2D DIC was conducted on four 25 mm wide x 250 mm long x 1 mm thick rectangular aluminium specimens. Vishay CEA-06-240UZ-120 strain gauges with a 6 mm gauge length were bonded on to the surface of

the specimens and a speckle pattern was applied over the surface of the specimen and strain gauge as shown in Figure 37. Two specimens were painted using the airbrush and two with the spray paint. All specimens were painted with a black background with white speckles. Although it was shown above (see Figure 36) that patterns with a white background produced less measurement error, the difference in error between the airbrush and spray paint is the largest for patterns with a black background. As such a black background is used to maximise the measurable difference in the DIC strain results between the patterns tested. The specimens were loaded in tension in an Instron servo-mechanical test machine up to 2 kN; giving an approximate applied strain of around 110 micro strain. Images were captured at 0.25 kN intervals using a 12 bit 5 Mp LaVision digital camera with image spatial resolutions very similar to the earlier analysis of 712 pixels/mm. The camera was mounted on an X-Y-ϕ stage, to allow fine adjustment of the focal plane. This ensured as practically as possible that the camera was parallel to the specimen surface during the test, minimising errors from misalignment of the optical setup. Some out-of-plane displacement is inevitable in this set-up however but it was not possible to conduct 3D DIC using the microscope stage due to the lens size and short focal distance. The experimental setup is shown in Figure 38. DIC was performed using the LaVision DaVis 7.4 software, with the area of interest directly over the strain gauge, once again using 128 x 128 subset sizes to remain consistent in the analysis of the patterns conducted in this chapter. The data from the strain gauge were compared to the average of the DIC data from the interrogation cells covering the strain gauge.

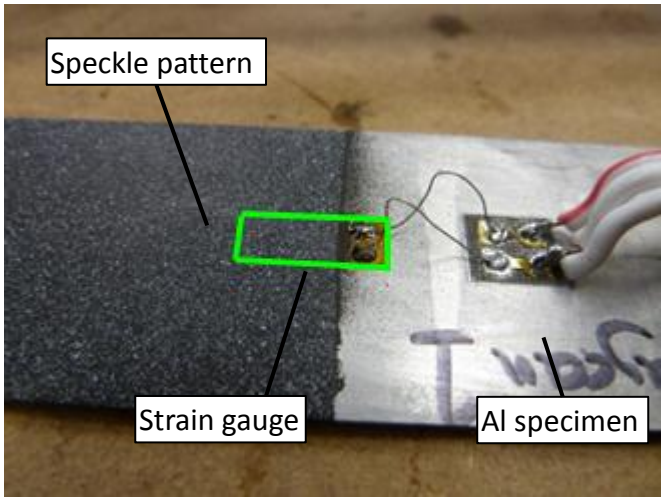

Figure 37: Detail view of strain gauge with speckle pattern applied on top

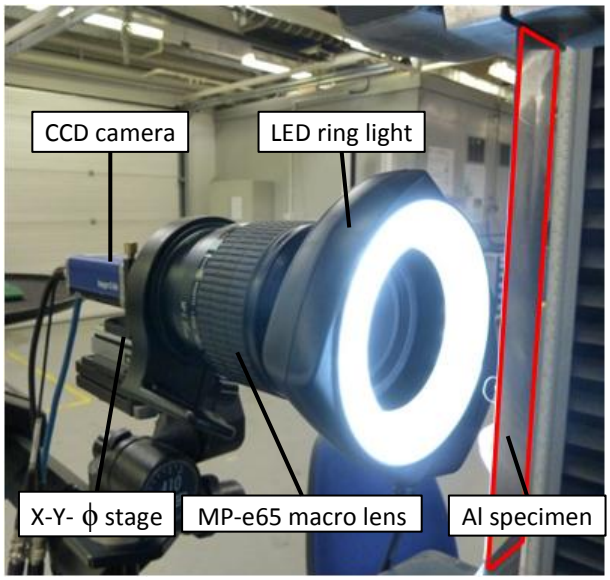

Figure 38: Experimental test setup

Figure 39 & Figure 40 show a comparison between the strain measurements recorded using the strain gauge and the DIC methods. It can be seen at the lower magnification, Figure 39, that below 1 kN there is a large variation in the results obtained and a high deviation between the recorded strain gauge and DIC results. It is suspected that at the lower load levels there is a small amount of settling of the grips as load is applied resulting in some out of plane movement. At high magnification levels the depth of field of the lens is very small, so these parasitic loading effects appear to have a large influence on the quality of the correlation results, including the spike in Airbrush 2 and the step change in strain seen for Spray can 1. Above 1 kN the DIC results appear to increase in line with the strain gauge data and are very similar in result to the strain gauge for 3 of the specimens above 1.5 kN. The convergence of the results at the high strains agrees with the earlier analysis which showed very little difference in measurement error between different application methods at 295 pixel / mm.

At the increased magnification, Figure 40, the DIC strain data for the airbrush pattern and the strain gauge show good agreement in comparison to the agreement between the strain gauge and spraycan pattern. Perfect agreement between the DIC strain data for the airbrush pattern is not shown; exhibiting some variability in the strain data, however the same trend and gradient of the data is visible, which is sufficient for the analysis being undertaken. In addition, as shown in Figure 36(b) the pattern used in this testing is of low quality, up to three times greater than patterns with a white background, which overall gives confidence in the accuracy of the DIC data relative to the strain gauge results. The large difference between the DIC results using the spray paint pattern and the strain gauge data confirms the numerical deformation analysis in Figure 36, which identified less strain measurement error from patterns painted using an airbrush as opposed to a spray paint when conducting DIC at high magnification. Under the higher magnification the airbrush specimens also appear to be less sensitive to the parasitic effects of the test machine, which are seen to greatly affect the lower magnification images. This may be due to the wider distribution of speckle sizes within the pattern, reducing the uncertainty of the speckle position between images. The sparsity of the pattern may also help to reduce the visible effect of the out of plane motion of the specimen. Furthermore, at the increased magnification, the pixel motion of the speckles at the same strain levels relative to the lower magnification is greater. This may increase the fidelity of the measurement and result in a larger, more accurate peak in the correlation function.

This result confirms the numerical deformation analysis and the use of the morphological assessment of the speckle size distribution which had both identified the airbrush pattern as producing the least measurement error due to the more even distribution of speckle sizes within the pattern. This also validates the analysis of the speckle pattern distribution using the morphological method as a good initial identifier of pattern quality. From the pattern assessment

methodology it has been shown that the distribution of larger speckles appears to have a beneficial effect, providing patterns with a high degree of uniqueness between the speckles in the pattern, and also producing patterns which are more resistant to the uncertainties in speckle location created from of image noise. In this case, as shown in Figure 36b), the best quality pattern, delivering the least measurement error is created using a black pattern on a white background produced from an airbrush.

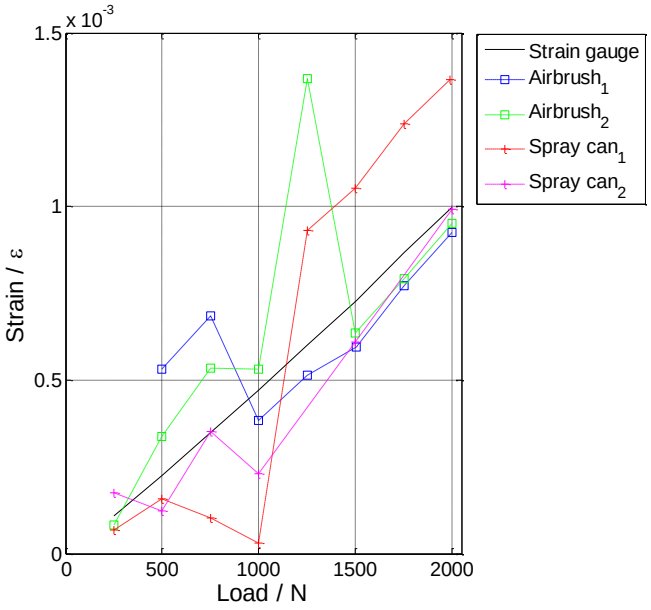

Figure 39: Strain gauge/DIC comparison at 287 pixel/mm

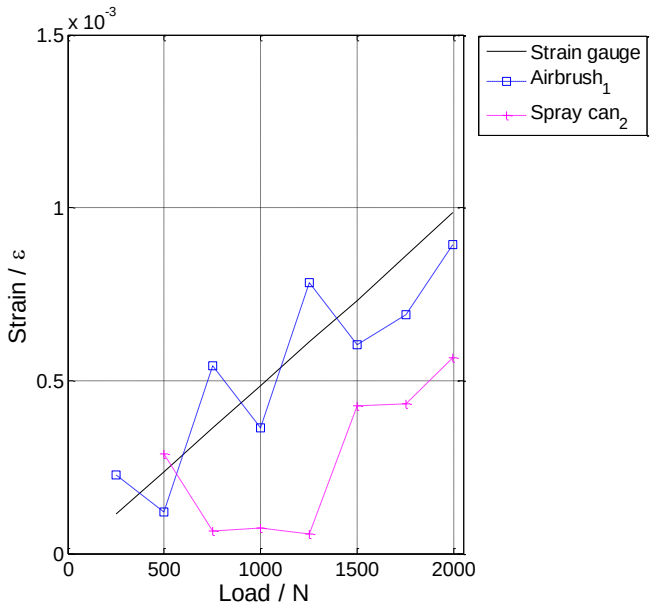

Figure 40: Strain gauge/DIC comparison at 712 pixel/mm

5.7 Evaluation of simulated speckle pattern variations

It has been seen that the properties and distributions of the speckle patterns change dramatically when viewed under increasing magnification. The quality of the speckle pattern has a large influence on the correlation function used to determine displacements between images. It is desirable to have a pattern with high levels of unique features and randomness in order to maximise the correlation function response when a match is found, and hence the accuracy of the calculated displacements. The results from the earlier sections show that patterns with an even distribution of speckle sizes result in greater measurement accuracy. Here it is investigated if the accuracy of the DIC strain measurement is related to the relationship between the relative size and density of the speckles in each interrogation cell, i.e. the relationship between the

coverage and the uniqueness of the pattern that can be created within a given number of pixels. This investigation is used to help interpret the speckle size distribution plots from Figure 34 and Figure 35, providing a structured link between the morphological analysis and the performance of the correlation algorithm.

To investigate this constrained relationship between the available pixels within the images, the number and size of the speckles within each interrogation cell and the resulting effect on the measurement accuracy, a pattern generation program was developed. The program generated a test matrix of 64 unique 12 bit patterns with differing combinations of speckle radii, from 2 – 9 pixels radius, and number of speckles present within each subset measuring 128 x 128 pixels within the image, from 4 – 18 speckles in intervals of 2. Each generated image was 1408 x 1408 pixels and contained 121 subsets. The generation program allows a degree of random variation of the radius of speckle around its circumference, replicating the characteristic random shape of each speckle in a real pattern. The program is such that the variation is linked to the speckle radius, so smaller speckles have less variation in shape, whilst larger speckles have more shape variation. Two examples patterns from the test matrix of 64 individually generated images can be seen in Figure 41(a) and (b). The patterns were deformed in 0.1% intervals up to 2% maximum strain, with errors evaluated between the measured and calculated strain measurements using interrogation cell sizes of 128 x 128 pixels, with no overlap between subsets. The pattern deformation was undertaken using the same Fourier domain methodology discussed in section 5.5. The x-direction displacements were derived by importing the speckle patterns into the LaVision correlation software DaVis 7.4. The location of the subsets analysed by the correlation software correspond to those defined in the pattern generation program, ensuring that each DIC interrogation cell has speckles of the same size and density. Errors between the imposed and measured strain fields were calculated as per the methodology described in section 5.5 and equation (21).

Figure 42(a) and Figure 42(b) show an array of the mean error in the strain measurements from each of the 121 interrogation cells calculated within each of the 64 different generated images tested at 1% and 2% strain respectively. A clear gradient of error across both plots is visible, primarily running from left to right. This gradient shows greater mean measurement errors when there are fewer speckles per subset within the image. The error reduces when there are more speckles and a greater number of features in the pattern to track (i.e. from left to right in the plots the error reduces). A secondary gradient can also observed diagonally from bottom left to top right of the figures. This diagonal gradient indicates that for the same number of speckles per subset, patterns with larger speckles appear to produce a lower amount of error within the measurement, compared to patterns with smaller radius speckles. Hence increasing the size of the speckle has an impact on the quality of the speckle pattern because the larger speckles have

a greater variation in shape, creating very unique patterns. Figure 42(a) and Figure 42(b) also show that the pattern is not improved by simply increasing the number of smaller speckles within the pattern to produce more features to track, and that there are a number of factors affecting pattern quality which must be considered.

Examination of the correlation function provides more explanation of the error trends. Figure 44 shows (a) 2D and (b) 3D views of the correlation function in a typical interrogation cell with 8 speckles per subset and a speckle radius of 3 pixels. Figure 41 shows similar results for a pattern with a speckle radius of 8 pixels. It can be seen in Figure 43 that patterns with smaller radius speckles the correlation peak is very small, creating a very concentrated area where the pattern matches. Patterns with larger radii, such as that shown in Figure 41(b), produce a correlation function peak with a larger diameter to the footprint due to the increased coverage and shape definition of the pattern, Figure 44(b). The large footprint of the correlation peak in Figure 44 is defined by a greater number of points than Figure 44 so that the sub-pixel accuracy is increased because the Gaussian distribution used to define the correlation peak has more points, producing a better fit. When the speckle size is small, the peak is defined by fewer points, making an accurate fit to the correlation peak difficult to achieve, resulting in larger errors. When conducting sub-pixel interpolations small speckles have also been shown to result in phase errors and amplitude attenuation due to their high spectral content [162]. Similar results are expected from other DIC systems which use different methods of interpolation or curve fitting of the correlation function to achieve subpixel accuracy as increasing the footprint of the correlation peak provides a greater number of points to inform any interpolation of the correlation function.

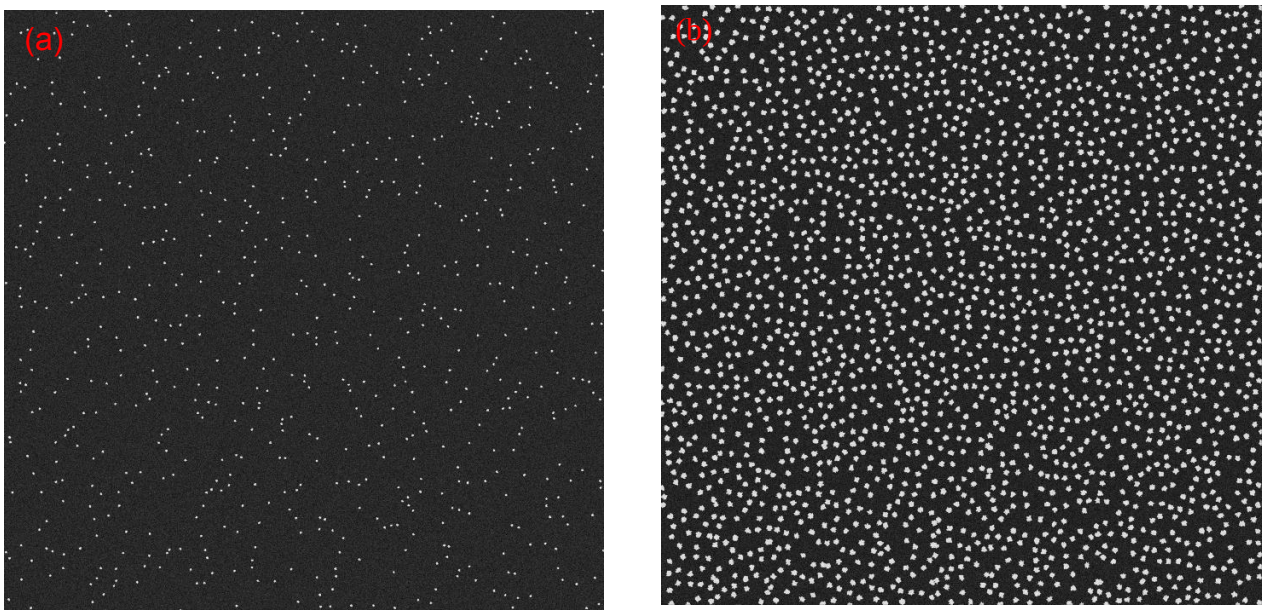

Figure 41: Generated patterns with (a) 6 speckles per subset, speckle radius 3 pixels (b) 6 speckles per subset, speckle radius 3 pixels

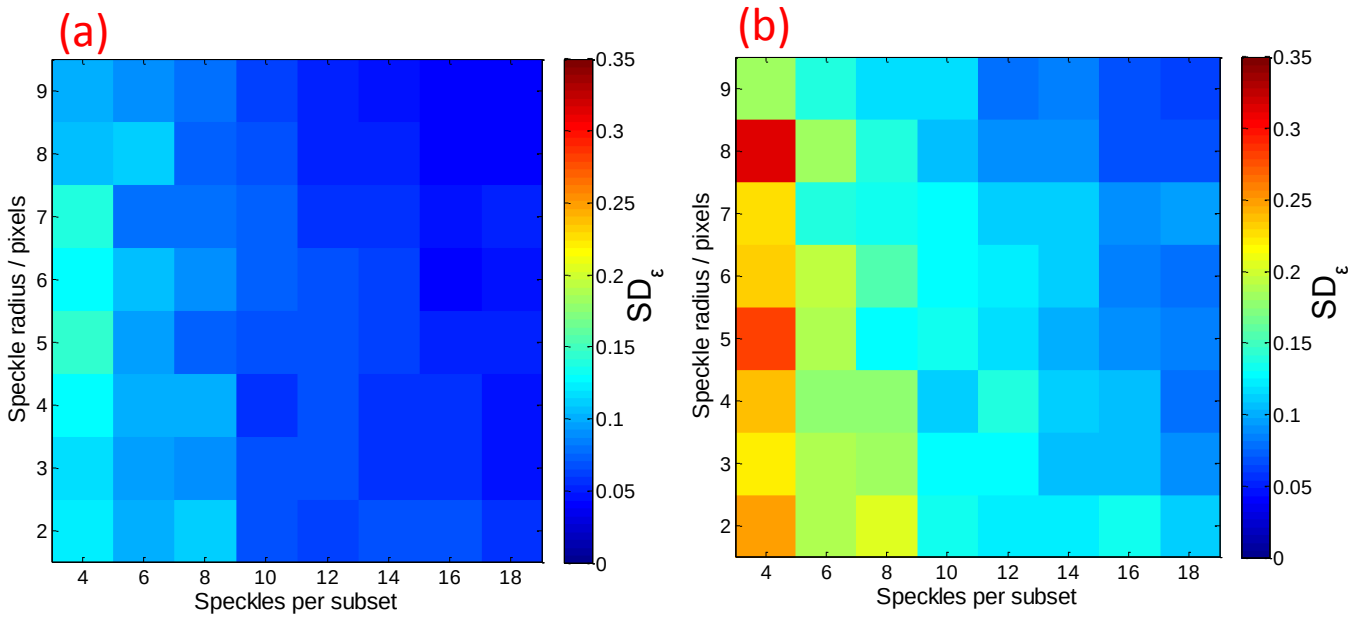

Figure 42: (a) Error levels for speckle patterns at 1% strain (b) 2% strain

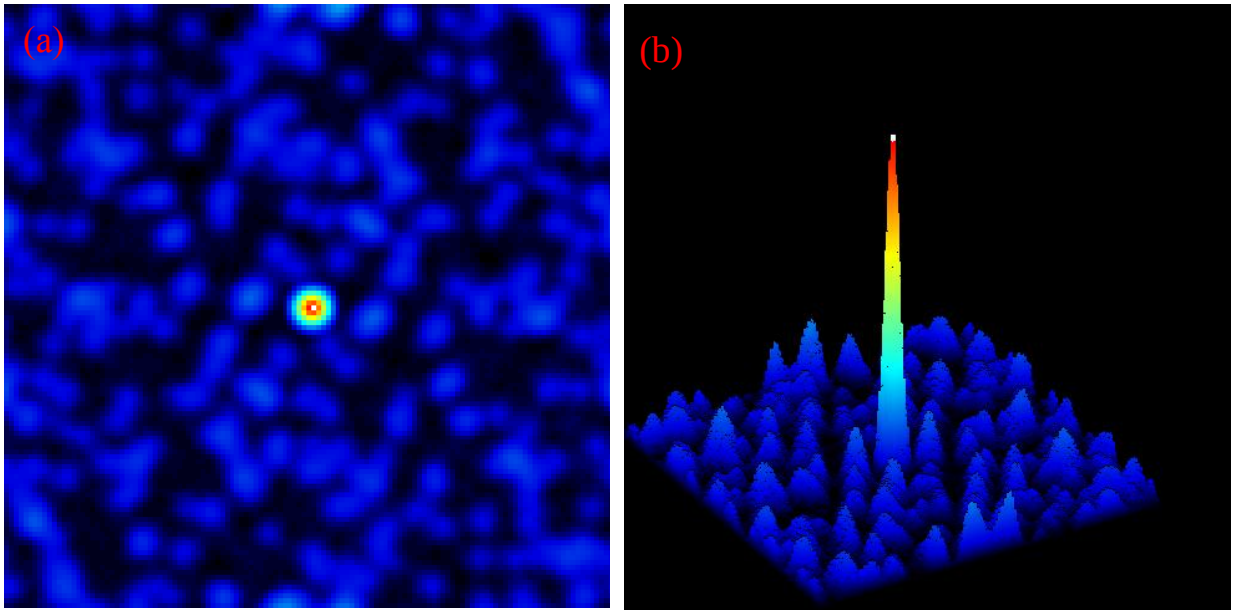

Figure 43: Typical correlation function peak for pattern with speckle radius of 3 pixels (a) plan view (b) 3D

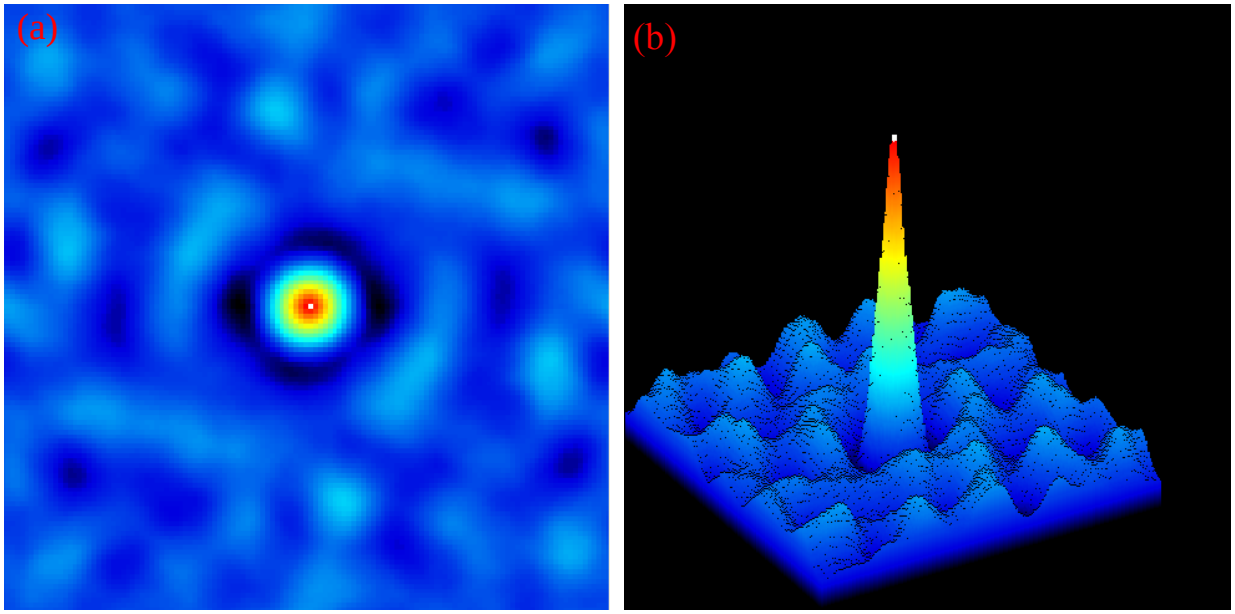

Figure 44: Typical correlation function peak for pattern with speckle radius of 8 pixels (a) plan view (b) 3D view

In practice it is highly impractical to create a speckle pattern with an optimised distribution, size and shape when applying the pattern from an aerosol nozzle due to the random behaviour of the paint in the airflow. However, this investigation helps to explain the differences in error seen between patterns at the higher magnification of 705 pixels/mm in Figure 36, and the speckle size distribution plot identified in Figure 35. Patterns generated with the airbrush which had a more even distribution of speckle sizes throughout the pattern, and hence a greater number of larger, more unique, speckles more adept to the 2D Gaussian sub-pixel accuracy method. In contrast, patterns created with a spray can were seen to have a greater distribution of smaller speckles, which as shown in Figure 43 have worse sub-pixel accuracy due to the very narrow correlation peak. The numerical pattern analysis delivers a quantitative interpretation of the speckle size distribution plots output from the morphological analysis, based upon an understanding of the mathematical processes occurring within the correlation algorithm. This quantitative link also provides confidence that conclusions on pattern quality using the morphological approach are transferable to the analysis of any pattern.

5.8 Conclusion

The work described in this chapter has demonstrated the use of image processing techniques to evaluate the effect of physical changes of speckle patterns on image correlation. The suitability of different pattern application methods and pattern colours has been assessed to minimise measurement errors originating from the speckle pattern during high magnification DIC analysis.

Global pattern quality parameters were discussed and Shannon Entropy was used to demonstrate that the global measures are not sufficient to assess the quality and properties of the pattern. As a result a morphological approach is presented using the Laplacian of Gaussian edge detection method, successfully identifying the edges of speckles and overcoming some of the shortfalls of image thresholding techniques previously used in literature. This method identified large changes to the distribution of the speckle sizes with increasing spatial resolution of image which could not be established when using the global Shannon image entropy parameter or histogram assessment. Clear links were identified between the levels of measurement error due to the pattern and the evenness of the speckle size distribution in the applied speckle pattern. Numerical deformation and experimental comparison of 2D DIC against strain gauge readings were used to validate this assessment approach, identifying patterns which showed the most even distribution of speckle sizes in the morphological assessment to result in the lowest errors.

A random pattern generation program was created to evaluate the effect of speckle size and coverage in speckle patterns using numerically deformed images. A relationship between the measurement error and the uniqueness of a pattern resulting from the speckle size and shape was seen. Errors reduced as the size of speckles increased, which provide a greater variation of shape. This relationship is identified to be linked to the specific sub-pixel displacement method used in the DaVis correlation software, which is more suitable to accurate measurement of the broader correlation function peak formed by the larger speckles. This conclusion helps to explain why the performance of patterns with a more even distribution of speckle sizes, and hence a greater number of larger speckles, perform better than those with a greater number of smaller speckles.

Overall it was shown that speckle patterns made using a white background and black speckles applied with an airbrush, with an even distribution of speckle sizes and shapes, have the greatest chance of producing a pattern with low measurement errors, when conducting DIC at high magnification. This conclusion will be implemented in all further work presented in this thesis, and provides confidence in the DIC measurements undertaken at high magnification levels.

6. Mesoscopic strain field analysis

6.1 Introduction

Previous testing in Chapter 4 had limited success identifying the strain distributions in the joint at two increasing image spatial resolutions. Increased magnification had produced data with a higher spatial resolution, showing more detail of the complex strain distributions. However it was concluded in Chapter 4 that there is a requirement for greater resolution data, necessitating testing at greater magnification levels.

The testing in Chapter 4 raised a number of shortcomings and difficulties in the high magnification DIC process when evaluating the strain fields in the joint. These difficulties centre on the inherent trade-off between spatial resolution and strain accuracy when conducting the analysis, and practical issues such as fundamental changes to the appearance of the applied speckle pattern when viewed at increased magnification. This resulted in a thorough investigation discussed in Chapter 5 into the behaviour of the speckle pattern under high magnification and its contribution to the total errors in the DIC process.

Using the knowledge gained in Chapter 5 an experimental methodology is established to perform DIC at the mesoscopic scale, enabling accurate, high spatial resolution analysis of the small through-thickness strains around the discontinuity. The mesoscopic scale enables the strains to be analysed to establish their contribution to the failure process. Pertinent strain data allows the full-field stresses in the joint to be determined, complimenting the analysis of damage initiation and load transfer in the joint.

6.2 Experimental procedure

Analysis of the speckle patterns in Chapter 5 had concluded that black patterns created with an airbrush on a white background are most likely to produce the least level of measurement error, and will be used exclusively for all further testing at high magnification. Throughout the work described in this chapter a 5MP 12 bit monochromatic LaVision E-lite camera and Canon MP-e65 macro lenses were used. The short depth of field of the image had also been cited as one of the practical issues when using high magnification optics, reducing the quality of the imaging when subjected to vibrations or out of plane motions. The camera was mounted on an X-Y- ϕ micro adjustable stage, similar to the setup used in the high magnification analysis in Chapter 5, improving the quality of the image focus and ensuring that the camera is perpendicular to the specimen surface, reducing errors due to the optical setup [163]. A LED ring flash was also

attached to the lens to produce a repeatable and consistent level of lighting throughout the testing, and also minimising image noise from flicker of the lights. The standoff distance between the lens and the specimen was approximately 50mm, of which 20mm is taken up by the thickness of the ring flash. The test setup can be seen in Figure 45.

The camera was focused on the geometric discontinuity between the inner and the outer strap, which was seen in Chapter 4 to be the area of largest through-thickness strain concentration in the joint. An area measuring 3.1 mm x 2.6 mm was imaged, as shown in Figure 46; delivering a spatial resolution of 769 pixels / mm. Increasing the magnification to this level has the effect of increasing the observed pixel movement of the stochastic speckle pattern in the image for any given strain. As such when observing small deformations there is a large ratio between the speckle movement and sensor noise, giving more certainty to the correlated results. This level of magnification remains consistent with the levels of magnification used in the speckle pattern analysis of Chapter 5, providing good confidence in the performance of the speckle pattern and measurement accuracy.

The specimen was mounted in an Instron 6600 servo mechanical test machine and loaded at a loading rate of 1 mm/min. This loading rate is lower than that used in Chapter 4, as this was seen to minimise the effect of the parasitic movement of the grips and out-of-plane movement of the specimen as it is initially loaded. This was very important due to the narrow depth of field of the high magnification lens. Images were recorded at 0.5 kN intervals until final failure of the specimen. The recorded images were post processed into 3195 x 2456 pixel images padded with blank data, to form a sequence which removed any contributions of rigid body motion of the joint as it passes through the small field of view of the camera for ease of visual analysis. The contributions of the image which show the joint moving in, or out of the camera field of view were discounted in the strain field analysis to produce a continuum of analysis around the discontinuity.

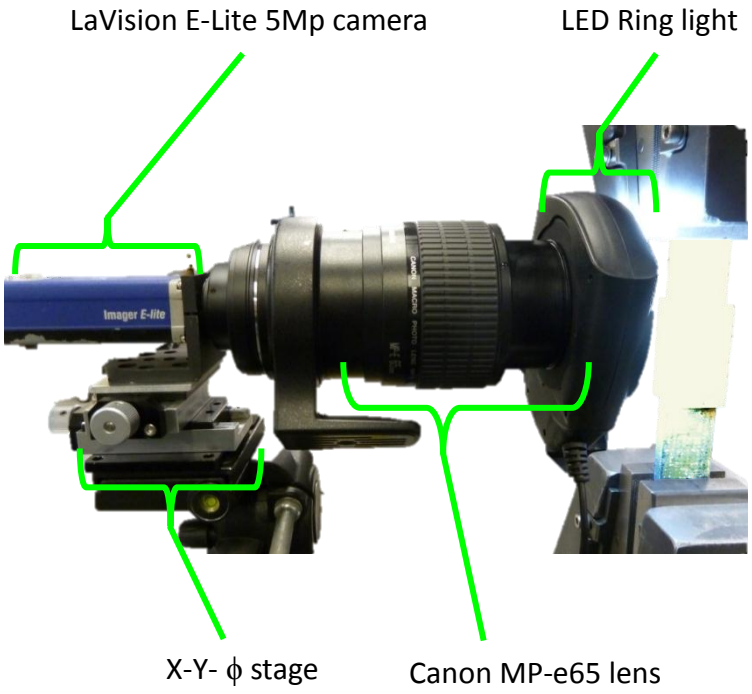

Figure 45: High magnification DIC experimental setup

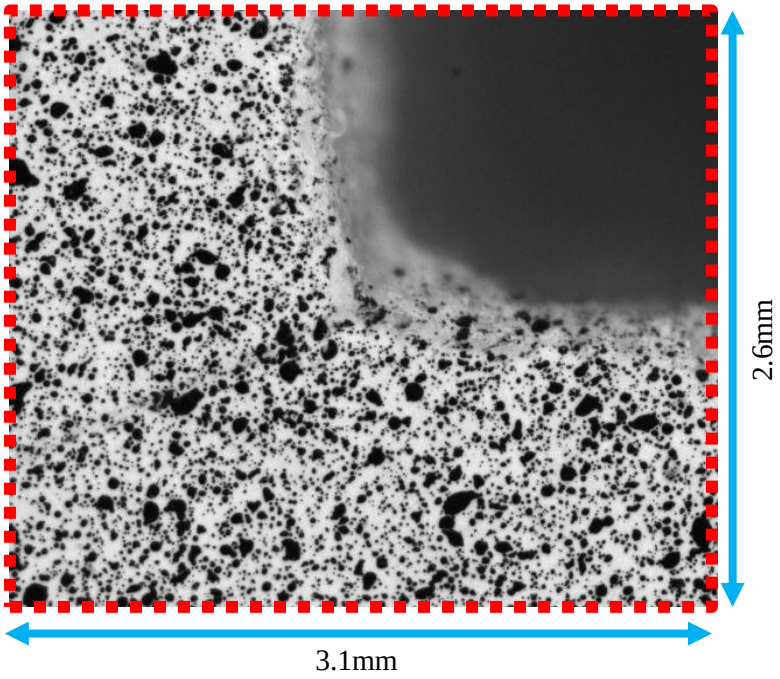

Figure 46: High magnification image of the geometric discontinuity between inner and outer strap adherend at 769 pixels / mm

6.3 Meso scale strain field analysis

Figure 47 shows full-field plots of the axial, through-thickness, and shear strains in the principal material directions evaluated at 13 kN. An immediate improvement can be seen in the quality of the data in comparison to that shown in Chapter 4. At this magnification, a spatial resolution of 24 data points per millimetre is achieved, allowing data rich analysis of the complex strain distributions observed in the joint. The axial strain plot in Figure 47(a) shows considerable axial strain in the heavily loaded inner adherend. The axial strains reduce in the inner adherend away from the discontinuity demonstrating load being transferred into outer straps. The axial strain gradient running diagonally from the inner adherend, past the root of the discontinuity and into the outer strap identifies the load transfer across the adhesive layer between the adherends. Two prominent through-thickness strain concentrations are identified in Figure 47(b), peaking at 0.3% strain either side of the root of the discontinuity. The first through-thickness strain concentration is located at the root of the discontinuity in the inner adherend, adjacent to the interface with the adhesive layer. The second strain concentration forms in the outer adherend adjacent to the root of the discontinuity. This location identifies a substantial through-thickness deformation of the outer adherend due to the eccentricity of the load path around the geometric discontinuity between adherends. A region of compression in the adhesive is generated by deformation of the outer strap peeling away from the inner adherend. Figure 47(c) shows a line plot of the through-thickness strain 0.25 mm below the root of the discontinuity indicated by the red broken line in Figure 47(b). A large increase in through-thickness strain can be seen between the inner and outer adherends, with the strain in the outer adherend over four times greater than that in the inner adherend.

The shear strain distribution shown in Figure 47(d) shows high shear strains isolated in the compliant adhesive layer between adherends, as identified form the material properties shown earlier in Table 3. The shear strain peaks just below the root of the discontinuity, showing a decrease in strain towards the unloaded horizontal free edge of the outer adherend. The high shear in the adhesive corresponds to the area of load transfer identified from the axial strain gradient in Figure 47(a). This result importantly demonstrates that the load is transferred across the discontinuity through shear of the adhesive layer. The shear strain distribution in the adhesive layer is not uniform across the thickness of the bond layer. Figure 47(b) and Figure 47(d) both show the location of the maximum shear strains correspond with the location of the greatest through-thickness strains at the interface with the outer adherend. This indicates a strong interaction between the adhesive layer and outer adherend due to load transfer between the inner and outer adherends through shear of the adhesive. Therefore, the behaviour at this highly loaded interface area between the compliant adhesive and the relatively stiff CSM material in the outer adherend is seen as critical in the control and initiation of damage.

The strain distributions in Figure 47 show good agreement to the results in literature observed by Haghani [88] and Ruiz [12]. This gives confidence in the experimental methodology, showing that the observed strains are representative of typical joint structural behaviour, and not an observation resulting from the highly heterogeneous fibre / matrix bundles of the CSM material.

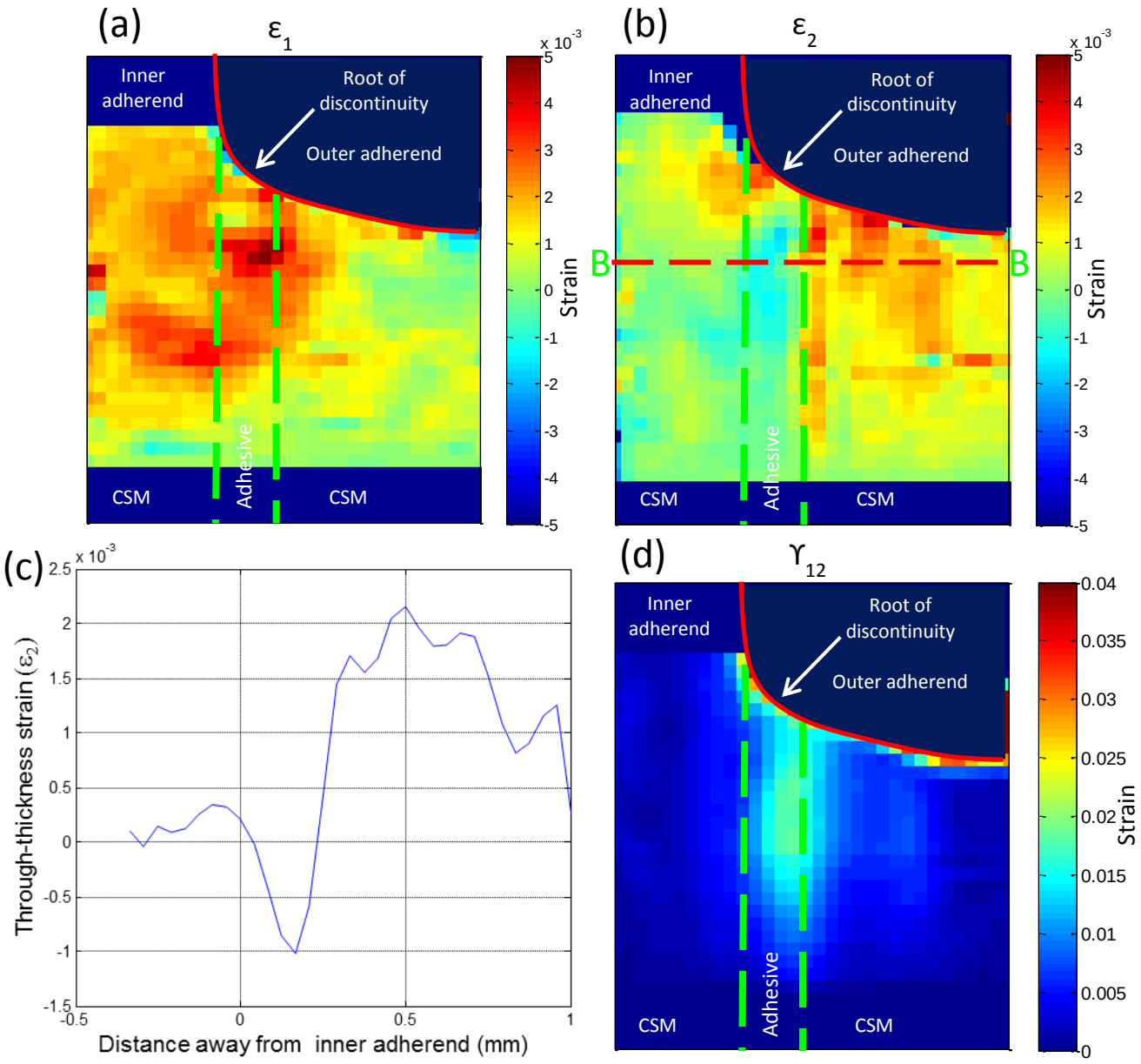

Figure 47: (a) Axial (ε_1) strain field (b) Through-thickness (ε_2) strain field (c) Line plot of ε_2 along section B (d) Shear strain (γ_{12}) distributions around joint discontinuity at 13 kN

Damage is observed to occur in Figure 48 when the specimen is loaded to 17 kN, identified at the location of the blue dotted circle in Figure 48(a). Noticeably there is a large reduction in the axial strain in the outer adherend, shown in Figure 48(a). This discontinuity in the axial strain

field indicates that load is no longer being transferred between adherends across the damaged region. The through-thickness and shear strains at the interface area between the adhesive and outer adherend also become very large at this load, shown in Figure 48(b) and Figure 48(c). These large strains are produced as a result of rigid body displacement of the adherend due to the presence of damage at this interface. This damaged interface provides a preferential route for damage to propagate. However, the final failure of the joint initiates from the small localised through-thickness strain concentration at the root of the discontinuity in the inner adherend identified in Figure 47(b). A crack propagates quickly along the interface between the inner adherend and the adhesive, resulting in light fibre-tear failure as categorised by ASTM D5573.

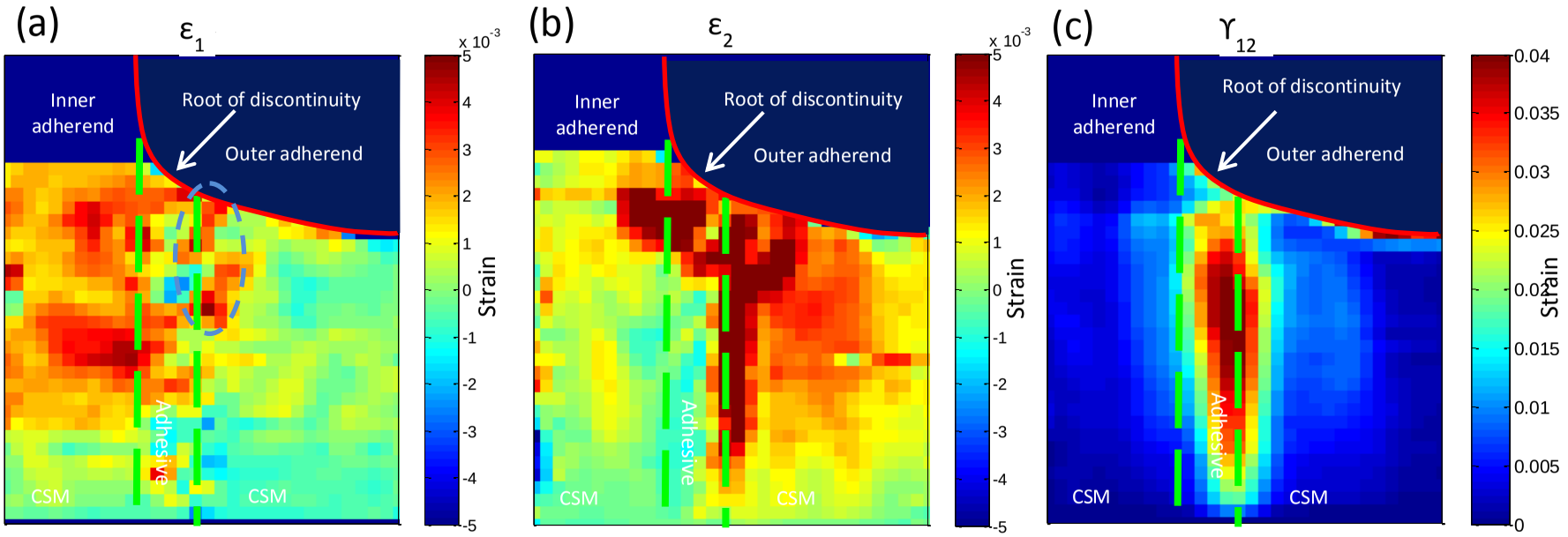

Figure 48: (a) Axial (ε_1) (b)Through-thickness (ε_2) (c) Shear strain (γ_{12}) distributions around joint discontinuity at 17 kN

6.4 Deriving stresses from the strain data

Figure 47 and Figure 48 provide a quantitative analysis of the strain fields generated around the root of the discontinuity in the joint. However from this analysis it is not possible to directly relate the strains to the development of damage in the joint. To provide full analysis of the load transfer and damage mechanisms, it is necessary to derive the stresses in the composite structure.

In the evaluation of the DIC strain fields only in-plane loading is considered, hence a plane stress assumption is applied. The stresses in the principal material directions (i.e. the 1 and 2 directions) can be obtained from strains derived from the DIC presented in Figure 47 and Figure 48, and the material stiffness matrix, $[Q]_{12}$, using the following relationship [5]

$$\begin{bmatrix} \sigma_1 \\ \sigma_2 \\ \tau_{12} \end{bmatrix} = [Q]_{12} \begin{bmatrix} \varepsilon_1 \\ \varepsilon_2 \\ \gamma_{12} \end{bmatrix} \tag{22}$$

The linear elastic assumptions of equation (22) are acceptable for the analysis due to the small deformations around the root of the discontinuity and the linear behaviours of the adhesive [164] and composite materials.

The material stiffness matrix was obtained from the experimentally established constitutive material properties shown in Table 6, collected from the experiment methodologies outlined in Chapter 3.

Material	E_1 (GPa)	E_2 (GPa)	v_{12}	v_{21}	G_{12} (GPa)
CSM	11.27	7.63	0.344	0.233	2.484
Araldite 2015	2 [138]	2 [138]	0.36 [108]	0.36 [108]	0.9 [138]

Table 6: Materials properties values for CSM and Araldite 2015 materials

A Gaussian filter, with a small kernel size of 3 x 3 data points and relatively low standard deviation of 1.5 was applied to the DIC strain data. This filter minimised noise in the strain data without homogenising the strain distribution across the discontinuity; retaining the critical local features. Filtering reduces the fluctuations in the data, ensuring better continuity between the strain fields. These fluctuations can be large and highly detrimental due to the large magnitude of the shear stress relative to the axial and through-thickness components, which causes

difficulty in the subsequent manipulation into principal stresses using Mohr's circle, discussed in a later section.

Figure 49 shows the stresses in the principal material directions derived from the strain data given in Figure 47 and the material properties given in Table 6 using equation (1). The stress distributions closely match the strain fields observed in Figure 47. The main difference is identified in the adhesive layer where, due to the compliant material properties of the Araldite 2015 adhesive, the stresses are low. The shear modulus of the CSM material which interfaces with the adhesive is over 2.5 times greater than that of the adhesive, and as a result, large interfacial shear stresses are observed in the composite adherends.

Analysis of the stresses in the principal material directions at 16 kN, i.e. prior to damage occurring at 17 kN, shows the maximum axial, through-thickness and shear stresses in the damage initiation region to be 70 MPa, 45 MPa and 77 MPa respectively. This results in a significant mixed-mode loading at the interface. Therefore it is very difficult to succinctly evaluate the individual influence on each of these stresses towards the initiation of damage. It is the principal stresses which govern failure in the brittle matrix leading to interlaminar cracks which promote damage propagation. Therefore, when assessing the damage development and initiation in the joint it is important to consider the principal stresses and not the stresses in the principal material directions.

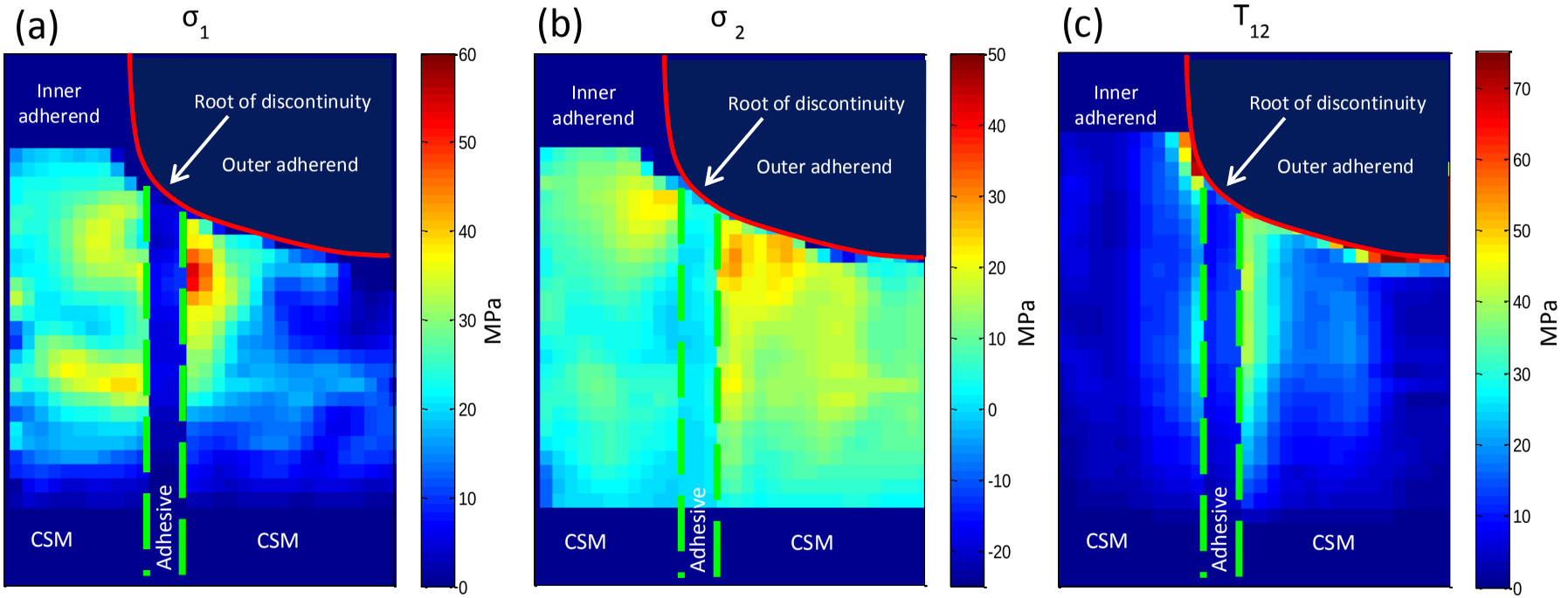

Figure 49: (a) Axial (σ_1) (b)Through-thickness (σ_1) (c) Shear stress (τ_{12}) distributions around joint discontinuity at 13 kN

The principal stresses, $\sigma^{p}{}_{1}, \sigma^{p}{}_{2}$, are obtained using a simple Mohr's circle analysis. It is important to note that due to the discontinuous nature of the joint geometry the direction of the principal vectors are different at every location around the discontinuity. Therefore the Mohr's circle transformation of stresses was conducted on a point by point basis. Figure 50 shows plots of the principal stresses and maximum shear stress derived from the data given in Figure 49. The very high maximum principle stress in the interface region where the damage initiates is clearly identified in Figure 50(a). The average maximum principal stress at the interface is 60 MPa, increasing close to 80 MPa nearer to the discontinuity. This is greater than the maximum tensile and shear strengths reported for the adhesive in the manufacturer's data sheet of 30MPa and 9MPa [138] respectively. This is also greater than the through-thickness and shear failure stresses for CSM material reported in the literature of 8.9MPa and 15.9 MPa [142].

The discontinuity between the adherends, and high shear strains around the adhesive, result in a rotation of the principal stress direction of between 35^{o} and 45^{o} from the vertical. This means that the maximum principal stresses are approximately one and a half times that of the peak axial stress recorded in Figure 49(a). Minimum principal stresses of -20MPa are recorded in Figure 50(b) along the adhesive interfaces in the inner and outer adherends. The maximum shear stresses are located in the relatively stiff CSM material at the adhesive interface with the outer strap, corresponding to the high shear strain areas identified in Figure 47(d).

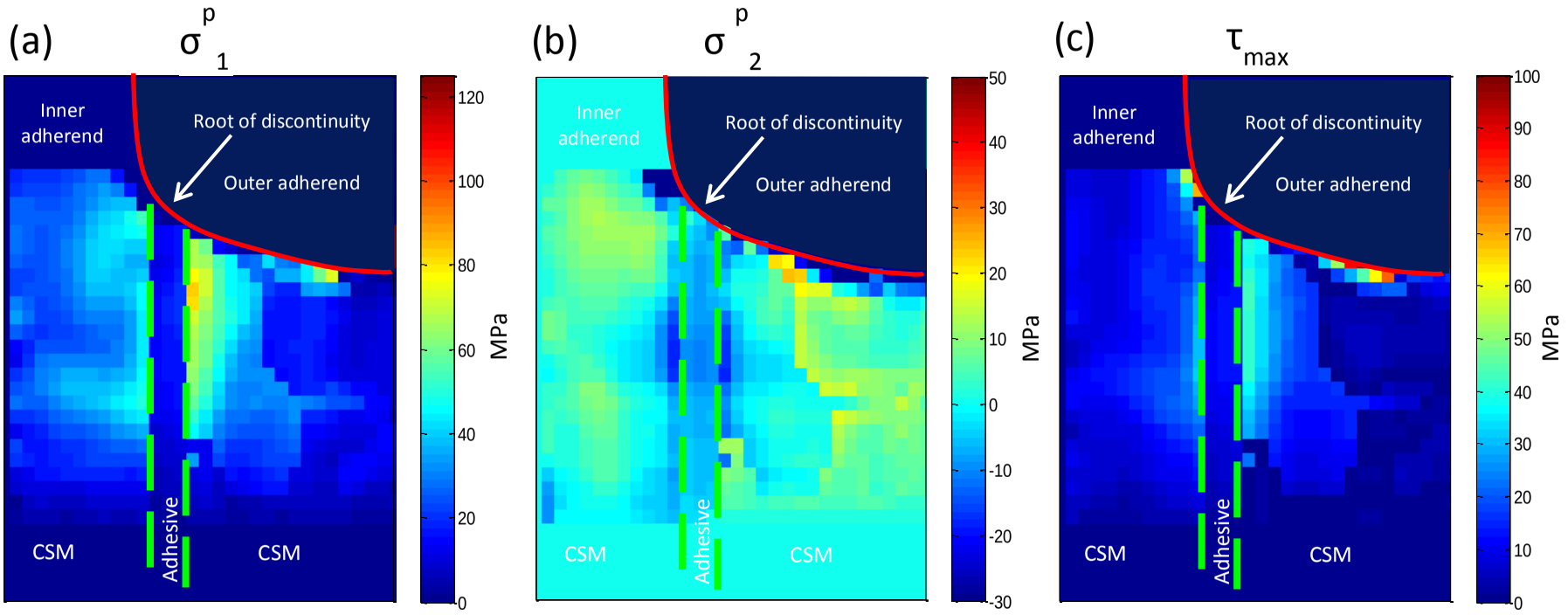

Figure 50: (a) Maximum principal stress (σ^{p}_{1}) (b) Minimum principal stress (σ^{p}_{2}) (c) Maximum shear stress (τ_{max}) at 13 kN

As the load increases up to 15 kN the maximum principal stresses in Figure 51(a) remain concentrated along the adhesive interface with the outer adherend, increasing up to 115 MPa at the root of the discontinuity. Stresses in the inner adherend show little increase in stress at this higher load level, showing the stress concentrating effect of the geometric discontinuity to have greatest effect in the outer adherend. The shape and size of the maximum shear stress distributions in Figure 51(c) show a high degree of similarity to the maximum principal stress distribution, identifying considerable rotation of the principal stress direction and load transfer between the adherends.

At 16 kN there is a large change in the shape and magnitude of the maximum principal stress concentration as shown in Figure 52(a). A maximum change in stress of 50 MPa is observed, reaching a maximum of 150 MPa along the interface region. This high stress region is highly localised, with a large stress gradient to the surrounding stress values at the interface. The sharp isolated change in the stresses suggests that they are a result of localised damage in the material, and are not representative of the intact material response. A similar breakdown in the continuity of the analysis can also be seen in the analysis of the minimum principal and maximum shear fields.

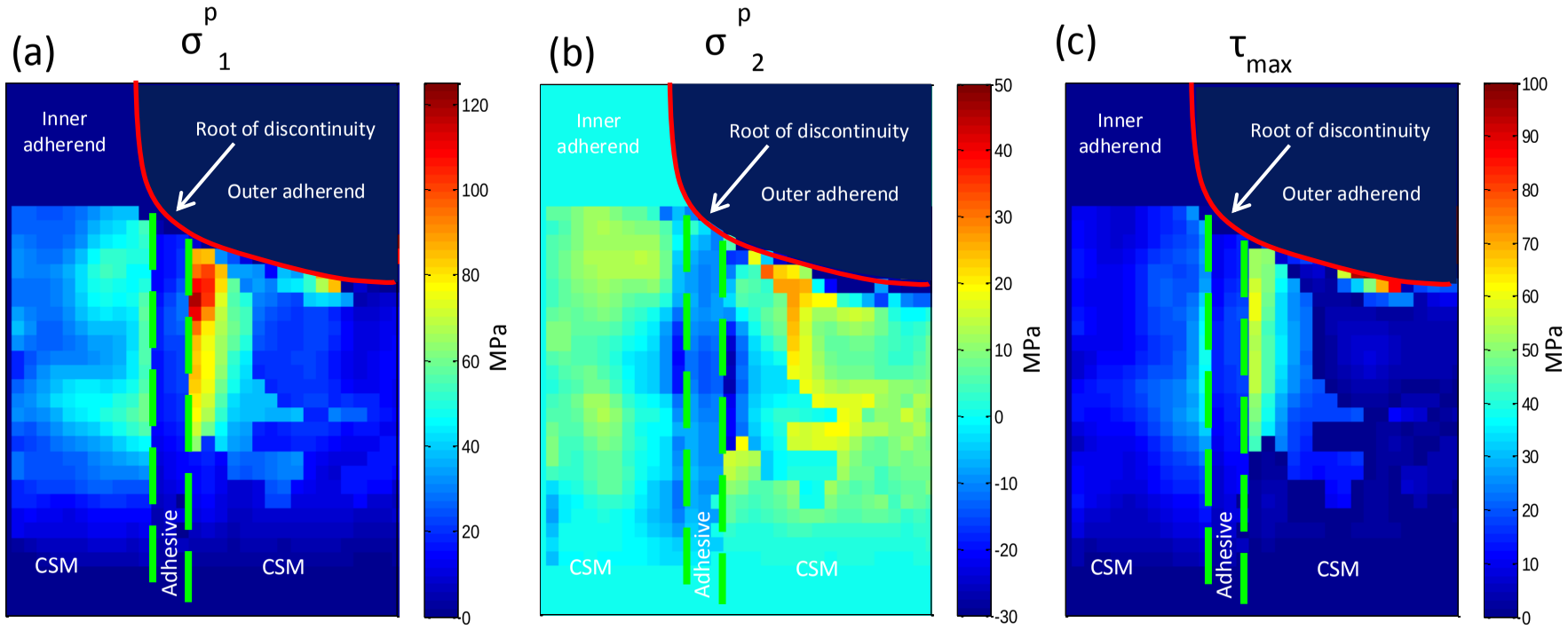

Figure 51: (a) Maximum principal stress (σ^{p}_{1}) (b) Minimum principal stress (σ^{p}_{2}) (c) Maximum shear stress (τ_{max}) at 15 kN

Figure 52(b) shows a magnified view of the raw image used to conduct the DIC in the highlighted area in Figure 52(a). Three very small thin cracks are visible along the interface with the outer adherend in the region where the very high maximum principal stress was recorded. These very small cracks were overlooked in the strain analysis as the axial strain field had shown the load transfer between the inner and outer adherends to still be intact, suggesting load transfer through fibre bridging across the damage. The high interfacial through-thickness and shear strains recorded in this region also masked the significance of the strain changes in this area due to the small size of the cracks. Figure 52(b) shows these cracks are aligned close to 45^{o} clockwise from the vertical. Analysis of the principal stress direction at 15 kN in the undamaged joint condition shown in Figure 52(c) show good agreement between the principal stress and crack directions, indicating failure due to a mainly mode 1 opening of the crack in the adhesive at the adhesive interface.

Unfortunately there is insufficient temporal resolution to capture the initiation of failure in the inner adherend, though it is strongly suspected from all of the stress and strain field analyses undertaken that the localised damage at the outer adherend interface provides relief of the stresses concentrated in the outer adherend. Unable to transfer load across the damaged region to the outer adherend, the root of the discontinuity in the inner adherend quickly becomes highly stressed, and interlaminar cracking of the CSM laminate occurs in the region of the through-thickness stress concentration observed in Figure 47(b).

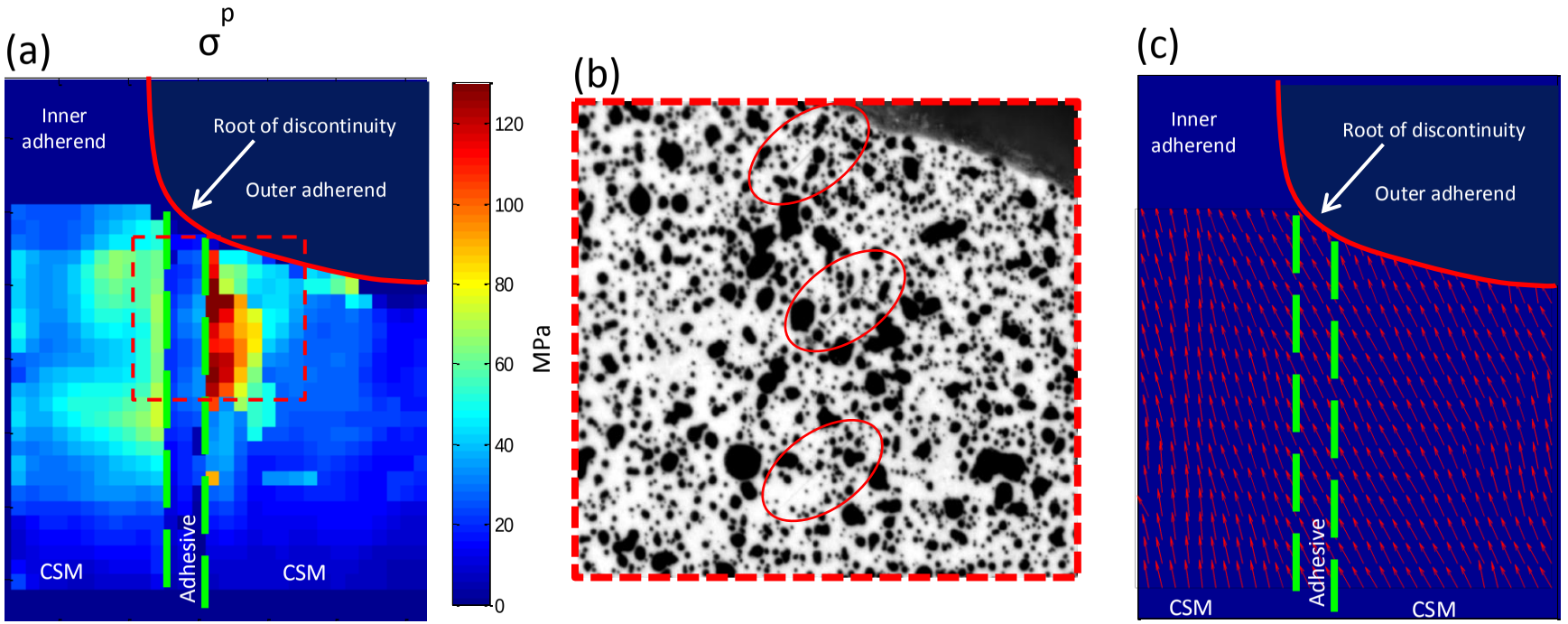

Figure 52: (a) Maximum principal stress (σ^{p}_{1}) at 16 kN (b) Raw image of joint at 16 kN (c) Maximum principal stress direction at 15 kN

Analysis of the principal stresses delivers a comprehensive evaluation of the development of damage in the joint. The stress fields compliment the strain analysis and provide clear analysis of the load transfer and damage initiation process in the joints. Using analysis of the principal stresses, the location of damage initiation becomes very clear. Importantly, damage is identified 1 kN earlier than from analysis of the principal material strains, providing a clearer understanding of the critical stresses in the initiation of damage, and the subsequent behaviour of the joint as it fails. The maximum failure stress criteria is shown to be a much more effective damage assessment criteria for the analysis of the composite bonded assembly, due to the large mixed-mode loading in the component between adherends. Damage critical behaviour is observed above a maximum principal stress value of 115 MPa in the joint. Only through analysis of the principal stresses were the very small, yet highly critical, interfacial cracks in the outer adherend identified.

6.5 Conclusion

DIC is shown to be a powerful experimental technique, providing high resolution analysis of the complex, localised strain distributions generated around the geometric discontinuity between adherends in a DBSJ up to failure. The results show vastly different strain distributions to those seen in the initial global joint analysis in Chapter 4 when using the revised experimental setup and procedures. Analysis of the strain fields in the joint is used to evaluate the load transfer between adherends and investigate the role of the strain components on the initiation of damage in the joint. The improvement in quality of the results also justifies the time and effort spent developing a solid understanding of the correlation process and developing the experimental setup, such as the analysis of the speckle patterns in Chapter 5.

The full-field strain data was manipulated to provide analysis of the accompanying stress states in the principal material and principal stress directions around the discontinuity of the joint. Analysis of the stresses in the principal stress direction, which govern failure in the brittle matrix material, provide a full evaluation of the development of damage and failure in the joint. The analysis identifies that evaluating the stress or strain fields in the principal material directions do not provide accurate information of damage initiation in the joint. Using the principal stress analysis approach the first occurrence of damage is identified at a lower load and in a different location compared to analysis of the principal material strain fields. This result demonstrates the importance of examining both the stress and strain distributions in complex structures to evaluate the structural and damage behaviours with the different metrics.

Through this analysis a greater understanding of the material behaviour in the highly complex stress and strain fields generated around the geometric discontinuity was obtained. The full-field results show good agreement with previous experimental investigations in literature, generating confidence in the results and methodology. Although efforts have been made to mitigate out sources of error in the 2D DIC methodology, validation of the results is not presented, and uncertainty in the measurement accuracy still remains.

7. Independent validation of mesoscopic DIC strain data using thermoelastic stress analysis

7.1 Introduction

Evaluation of the DBSJ using DIC presented in Chapter 6 provides high resolution analysis of the local stress and strain fields and damage development in the complex structure. The data collected satisfied objectives 2 and 4 from Chapter 1, greatly improving the understanding of the joint mechanics. However as identified in Chapter 6, no validation of the results is presented other than visual agreement with studies in literature. It is imperative that validation of the results is undertaken, as although efforts have been taken to mitigate for potential error sources in the experimental analysis, a number of underlying uncertainties still remain. These include the effect of the parasitic out of plane movement of the test specimen during loading noted in Chapter 4, and optical distortions associated with non-perpendicular alignment of the 2D camera set-up to the specimen face. Both uncertainties can greatly affect the measurement accuracy. In addition to these error sources, there are also difficulties in the analysis due to the highly localised strain concentrations generated around the discontinuity, requiring a compromise in the correlation settings.

In this chapter the white light strain data obtained using DIC is validated against independent experimental data collected from Thermoelastic Stress Analysis (TSA) of the joint. The validation generates high confidence in the measurement of the individual stress and strain components in the joint, and importantly confirms the accuracy of the high magnification 2D DIC methodology and the investigations conducted in Chapter 6.

Limitations in the TSA methodology are identified in the region of the geometric discontinuity due to the variation of the principal stress direction away from the principal material direction. A new analysis approach is developed to address these concerns. The strain data from the DIC analysis of the discontinuity is used to inform the transformation of the thermoelastic constants from the principal material axis, in which they are obtained experimentally, to the principal stress direction. The two validated independent TSA and DIC data sets are also used to assess the accuracy of a 2D finite element approach to model the complex 3D bonded joint problem. An inverse approach is used to improve the agreement between experimental and numerical results, showing the in-situ properties of the adhesive at the discontinuity to be very different from those reported on the manufactures data sheet [138].

7.2 Validation approach

The highly localised strain fields seen in Chapter 6 create a significant challenge in validating the experimental measurements. Traditional approaches, such as comparison against electrical resistive strain gauge measurements do not provide the spatial resolution to confidently assess the accuracy of the DIC results. Therefore validation must be undertaken using data from another high resolution full-field non-contact measurement technique. Of the experimental techniques discussed in Chapter 2, only DIC, Moiré interferometry and TSA were identified as having sufficient spatial resolution to be applied to the analysis of the adhesively bonded joint. In this chapter experimental data from TSA is selected to provide the validation of the DIC data, as there is very high confidence in the infra-red measurements [165] obtained in TSA, with few sources of error [166] [167]. Critically the TSA technique generates an independent infrared, as opposed to white light, experimental dataset for the validation, giving a very high degree of confidence in the results if a match between techniques is shown.

Validation will be shown through manipulation of the DIC strain terms into a similar comparable stress metric as that produced by the TSA. Few studies have presented TSA and DIC data in a single comparable metric for analysis or validation purposes. Good agreement between the techniques was found in the analysis of steel test coupons containing a hole [168]. The single stress metric was used to provide a validated experimental assessment of the performance of DIC strain measurement methods against the independent, high accuracy TSA data. Fair agreement was seen in the similar evaluation of the stress around a hole in a CSM laminate [169]. However, the DIC stress metric was relatively noisy due to the random architecture of the fibres in the CSM material and the isotropic material assumption used by the author. Even when presented in a comparable metric, the coupled nature of the TSA stress metric limits analysis of complex structures, as the individual components of stress cannot be separated. To address this, investigations have been attempted using the manipulation of the different stress metrics obtained from TSA and Photoelasticity [170], [171] to separate the stress components contained in the TSA stress sum.

The work undertaken in this chapter using both TSA and DIC techniques shares a very similar motivation to the studies discussed above. Assessing the performance of the DIC experimental method against the low error TSA technique as a single stress metric validates the individual DIC strain results. This gives confidence to the manipulation of these strain terms into individual stresses, which cannot be extracted from the TSA signal alone. Evaluation of the individual stress terms provides a much more detailed analysis of the material behaviours around the discontinuity in this complex composite assembly. The resulting validated individual

stress and strain components therefore deliver an extensive data set against which the accuracy of numerical modelling methods can be evaluated.

7.3 Joint structure

As noted in Chapter 3, the DBSJ used in this chapter is different to that used previously in the strain analysis in Chapter 6. The materials in the DBSJ were kept constant, however the stacking sequence of the joint was altered to a $[CSM_8\ 90_4]_s$ sequence. This produced a slightly thinner, more flexible outer strap, designed to increase the measurable deformation, and through-thickness strains generated in the outer strap using DIC. This change is anticipated to produce a better signal to noise ratio of the through-thickness strain data, as the ratio between the pixel movement from the specimen deformation to the random movement caused by camera noise is increased; providing more certainty to the deformation measurement. Similarly, an alteration was made to the joint geometry; increasing the length of the outer adherends to 75mm, producing an asymmetric joint with overlap lengths of 25 and 50mm, as shown in Figure 53. This geometry ensures that failure initiation occurs at the discontinuity with the smaller overlap, providing certainty that the stress and strain states observed at the small length scales by the DIC and TSA are leading up to and associated with the initiation of damage in the joint. The DBSJ was constructed with a width of 25 mm. The inner adherends were 150 mm long separated by a 2 mm gap at the butt between the adherends. For consistency in the analysis, Araldite 2015 was used to bond the adherends, and adhesive spew fillets were removing during construction.

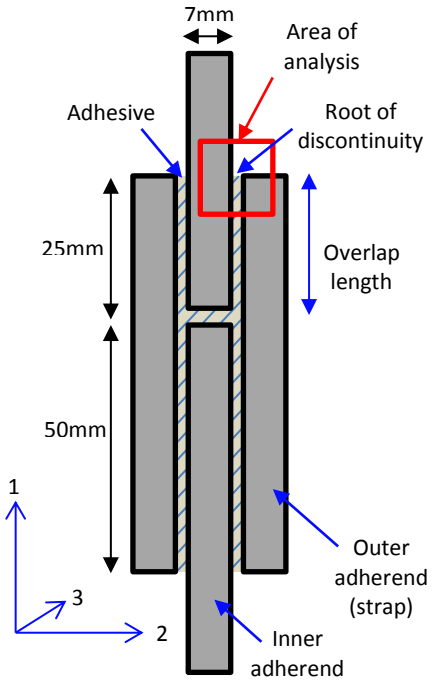

Figure 53: Schematic of Double butt strap joint

7.4 Meso scale DIC analysis

As the geometry of the specimen has been altered, re-evaluation of the strain fields in the joint are required. A similar meso scale 2D DIC methodology to that in Chapter 6 is used to image an area around the discontinuity between the inner adherend and the shorter overlapping adherend shown in Figure 53 with a 5Mp LaVision E-Lite camera mounted on and X-Y- ϕ adjustable mount. The region around this discontinuity experiences the largest through-thickness strains due to the severity of the discontinuity, which are critical in the initiation of damage and failure initiation in the joint. A high magnification Canon MP-E65 macro lens was paired to the camera to image a 3.1mm x 2.6mm area of interest at the root of the discontinuity; producing an image resolution of 684 pixels / mm. Images were recorded at 5Hz as the joint was loaded at 2 mm/min in an Instron 5569 test machine. Analysis of the strain fields was conducted using the DaVis 7.4 correlation software, using a subset size of 128 x 128 pixels with a 50% subset overlap. A spatial resolution of approximately 3 data points per millimetre was produced using these settings.

The localised strain distributions around the discontinuity at 6 kN are shown in Figure 54(a)-(c). The largest axial strains are identified in the inner adherend, which bears the whole of the joint load prior to the discontinuity. An axial strain gradient can be seen diagonally from the inner adherend, past the root of the discontinuity and into the outer adherend as load is transferred across the adhesive between adherends. The rise in the outer adherend axial strains is associated with a similar magnitude decrease in axial strains in the inner adherend away from the discontinuity towards the centre of the joint due to the load transfer. The low axial strain in the outer adherend close to the free end observed in Figure 54(a) clearly demonstrate the differential shear effect described by Volkersen [26]. At this low load level the through-thickness deformations are relatively small Figure 54(b). Nevertheless two concentrations around the discontinuity in the inner, and more noticeably, outer adherends can be identified. These concentrations are generated by the internal bending moment from the eccentricity of the load path around the discontinuity. The through-thickness strain in the inner adherend is lower, as there is less loading eccentricity. The shear strains in Figure 54(c) are heavily concentrated in the compliant, shear loaded adhesive layer. The shear strain decreases close to the root of the discontinuity showing a satisfaction of the shear free boundary conditions at the end of the adherend. The band of shear strain in the adhesive identifies the load transfer between adherends via shear of the adhesive layer, which is linked to the increase in axial strains in the outer adherend identified in Figure 54(a).

The strain fields in Figure 54 provide similar insight of the highly heterogeneous strain distributions generated in the structure to those in Chapter 6. The region around the geometric

discontinuity can again be identified from these localised strains to be a critical area in the development of damage, requiring accurate analysis of this area and validation of the data.

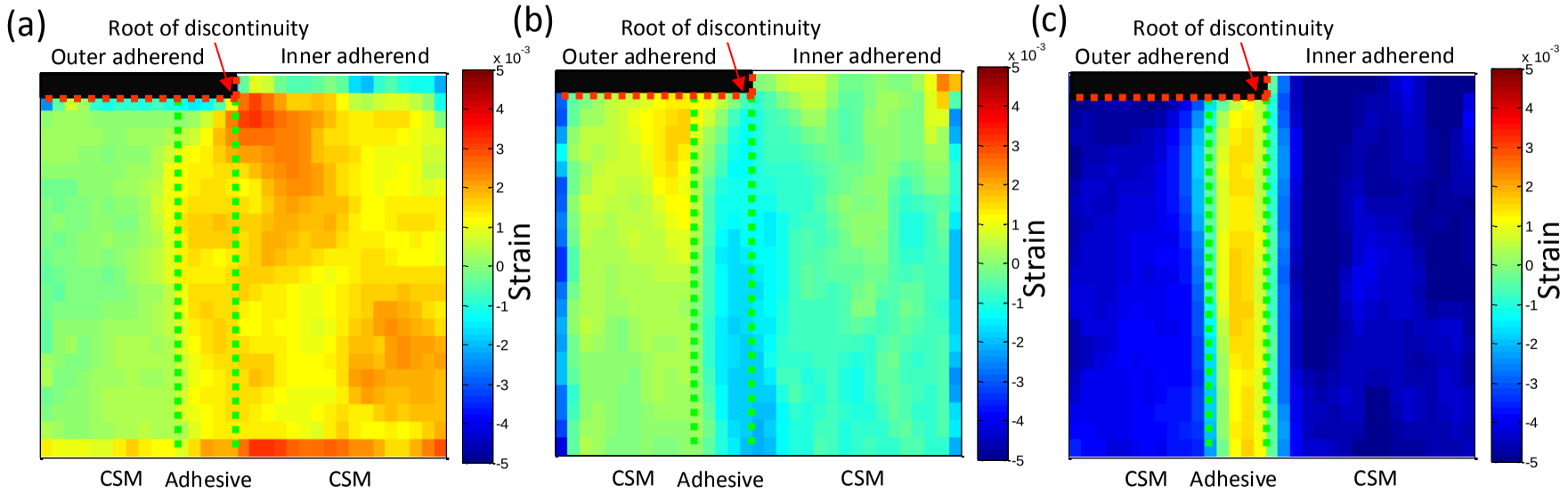

Figure 54: (a) Axial (b) Through-thickness (c) Shear strain around the geometric discontinuity at 6kN

7.5 Thermoelastic stress analysis

Visually, the concentrations of strain around the root of the discontinuity in Figure 54 show good agreement with the strain concentrations observed by Ruiz using Moiré interferometry [12] and the stress concentration identified in TSA of pultruded composite double butt strap joints [108]. Unfortunately this visual agreement provides only qualitative validation of the data. To demonstrate full validation of the DIC strain data set, TSA around the root of the discontinuity of the joint is undertaken; producing independent data with a high spatial resolution against which the accuracy of the DIC results can be assessed.

A detailed explanation of the TSA technique has been presented in the literature review presented in Chapter 2 detailing the thermoelastic relationship between the infra-red data and the stresses given in equation (18)

$$\frac{\Delta T}{T} = -(K_1 \Delta \sigma^p{}_1 + K_2 \Delta \sigma^p{}_2) \tag{18}$$

It is important to note that equation (18) is non-dimensional; furthermore T and ΔT on the left hand side of the equation are scalar quantities. Therefore the right hand side is also a scalar; this means the thermoelastic response itself is not a function of the material directions. A more useful form of equation (18) is to manipulate it into the form of a 'stress metric' and hence the following tensor quantity [172]:

$$\text{Stress metric} = \frac{\Delta T}{K_1 T} = \Delta \sigma^p{}_1 + \frac{K_2}{K_1} \Delta \sigma^p{}_2 \tag{19}$$

7.5.1 Analysis methodology

TSA was conducted analysing the root of the discontinuity of the joint using a highly sensitive Flir Silver SC5000 infra-red detector. A G1 macro lens with a short focal length was fitted to enable the detector to be placed very close to the specimen, maximising the spatial resolution of the 320 x 256 pixel array of indium antimonide detectors. The joint was loaded at 20 Hz with a mean load of 6kN, and loading amplitude of 3kN in an Instron 8800 servo hydraulic test machine, generating a stress change of 6kN, the same load level as used to evaluate the strains using the DIC in Figure 54. The data was sampled at 283Hz, such that data was recorded over all points of the loading cycle. The load output of the test machine and the signal from the infra-red detector are connected to a lock-in amplifier which filters the thermoelastic data such that

only the change in temperature and mean temperature data at the loading frequency are measured. This reduces the noise in the data and allows high accuracy measurement of very small temperatures changes. A schematic of the experimental thermoelastic stress analysis set up can be seen in Figure 55.

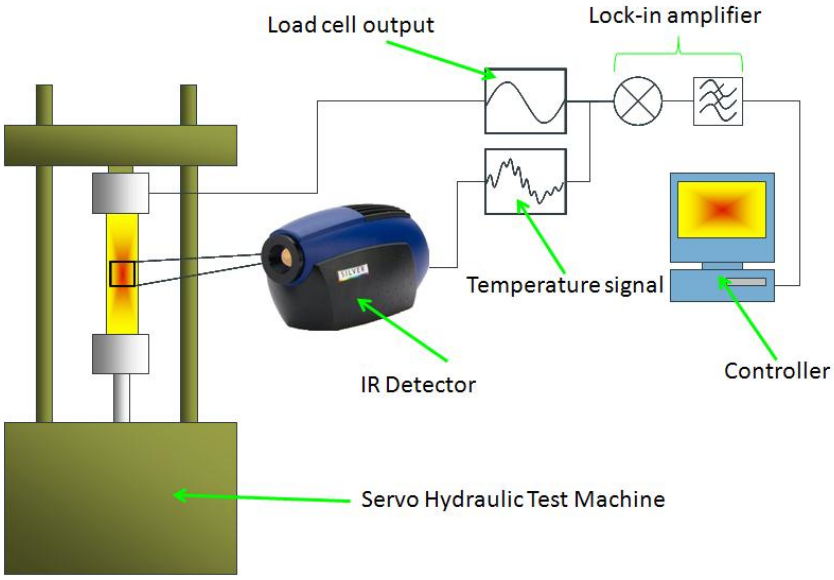

Figure 55: Schematic of TSA experimental setup

The detector imaged an area 7 x 5.7 mm around the geometric discontinuity between the inner and outer straps with a spatial resolution of 45 pixels / mm. This resolution captured the complex behaviour around the root of the discontinuity at a similar mesoscopic length scale as the DIC. Due to the small field of view of the G1 macro lens there is a large motion of the specimen through the frame during the loading cycle. The Flir Random Motion software was used to correlate the movement of data points analysed during the loading cycle, compensating for the movement of the specimen during analysis which has been shown to remove erroneous data from the lockin temperature signal [173].

A plot of the raw $\Delta T/T$ infra-red data around the discontinuity can be seen in Figure 56. The texture of the temperature plot shows the effect of analysing across the thickness of the joint, identifying the variable orientation of the CSM fibres aligned out of the page and rough surface finish from preparing the specimen. An area of high temperature change is seen at the root of the discontinuity concentrated in the CSM layer of the inner adherend. This temperature change is greatest in the adhesive layer where the geometric discontinuity is most severe. A high response is also observed in the 90^{o} fibres at the centre of the inner adherend, where axial loads are very high.

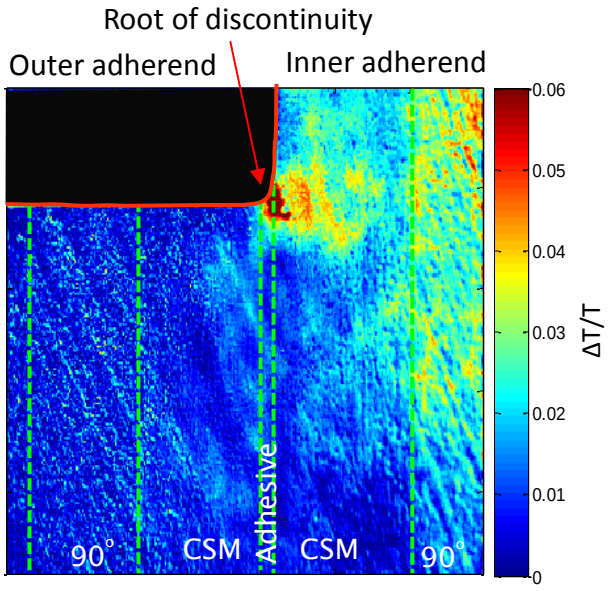

Figure 56: Raw ΔT/T infra red data at a load amplitude of 6kN

7.5.2 Thermoelastic constants

As detailed in the description of TSA, thermoelastic constants are required for the manipulation of the raw infra-red temperature data into the informative stress metric shown in equation (19). The thermoelastic constants are established from uniaxial testing of material coupon specimens in the principal material directions, axially (1) and through-thickness (2), as per the convention used throughout this thesis. Testing was conducted using the Flir Silver SC5000 infra-red, imaging at 283Hz, with very similar methodologies to that outline in Section 1.5.1.

The K_1 thermoelastic constant for the CSM material was evaluated from four 8 mm thick modified ASTM D3039 coupons, as per the coupons used in Chapter 3 for the derivation of the through-thickness Poisson's ratio shown in Figure 14. The specimens measured 200 mm x 25 mm cut from a $[CSM]_{16}$ laminate. They were loaded with a mean load of 8kN with an amplitude of 4kN at 20 Hz in an Instron 8800. Measurements were recorded from the side of the specimen, replicating the measurement surface of the joint. Measurements were taken from 2 areas along the length of each specimen, collecting a large number of data points for analysis. The specimens were subjected to a uniaxial stress change in the 1 material direction. Therefore the thermoelastic relationship given in equation (18) can be rearranged to determine the K_1 thermoelastic constant from the applied load level and the recorded temperature data as follows:

$$K_1 = \frac{\Delta T}{T\Delta\sigma_1} \tag{23}$$

Due to the orientation of the material axis in the 90° material, both K_1 and K_2 thermoelastic constants were established from the K_2 through-thickness testing procedure discussed in the following section.

The K_2 through-thickness constant for the CSM and 90° material was evaluated from four 25 x 25 x 70 mm, high aspect ratio, specimens loaded transverse to the fibre layers. The same specimen design and construction methodology was used as presented in Chapter 3 for the evaluation of the through-thickness material properties shown in Figure 14. The specimens were assembled from a number of thick $[CSM]_{16}$ and $[90]_{10}$ specimens bonded together using Araldite 2015 into a stack between two aluminium end blocks. Resin rich surface layers and residual adhesive material was removed from the specimen with light abrasion to improve the accuracy of the measurement [174] and provide representative surface measurements of the joint. The specimens were loaded in the through-thickness material direction with a mean load of 3kN with an amplitude of 2.5kN at 20 Hz in an Instron 8800 test machine via a set of universal joints to minimise specimen bending. A picture of the specimens and experimental set up can be seen in Figure 57 and Figure 58 respectively.

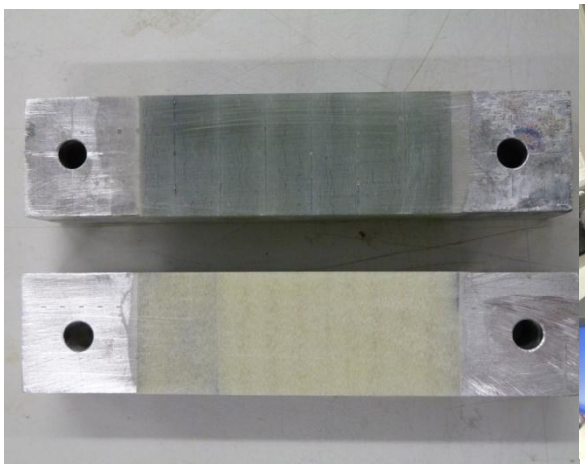

Figure 57: K_2 specimens

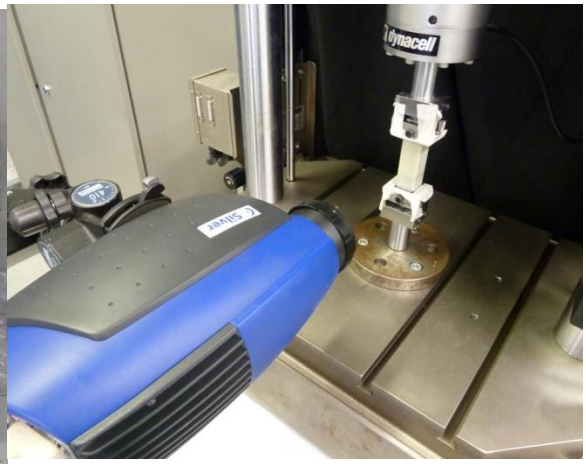

Figure 58: Experimental K_2 test set up

Analysis was conducted with a spatial resolution of 5.75 data points / mm, measuring 275 x 115 data points across the specimen surface. Figure 59(a) and Figure 59(b) show the raw temperature change recorded by the detector. Bands of high temperature change relating to the compliant adhesive regions between the composite laminates can be clearly identified. The texture to the image in Figure 59(a) identifies the highly random nature of the CSM material, which delivers a greater temperature response compared to that of the 90° material, Figure 59

b), where resin rich areas around fibre bundles can also be identified. The measurement area used in the derivation of the K_2 thermoelastic constants are outlined in red in both images. The adhesive regions of the specimens were discarded during the derivation of the K_2 thermoelastic constants, and only the thermal response of the constitutive composite material considered.

As it can be assumed that the specimens are being loaded solely in the σ^p_2 direction, the thermoelastic equation can be rearranged to evaluate the K_2 thermoelastic constant as follows

$$K_2 = \frac{\Delta T}{T \Delta \sigma_2} \tag{24}$$

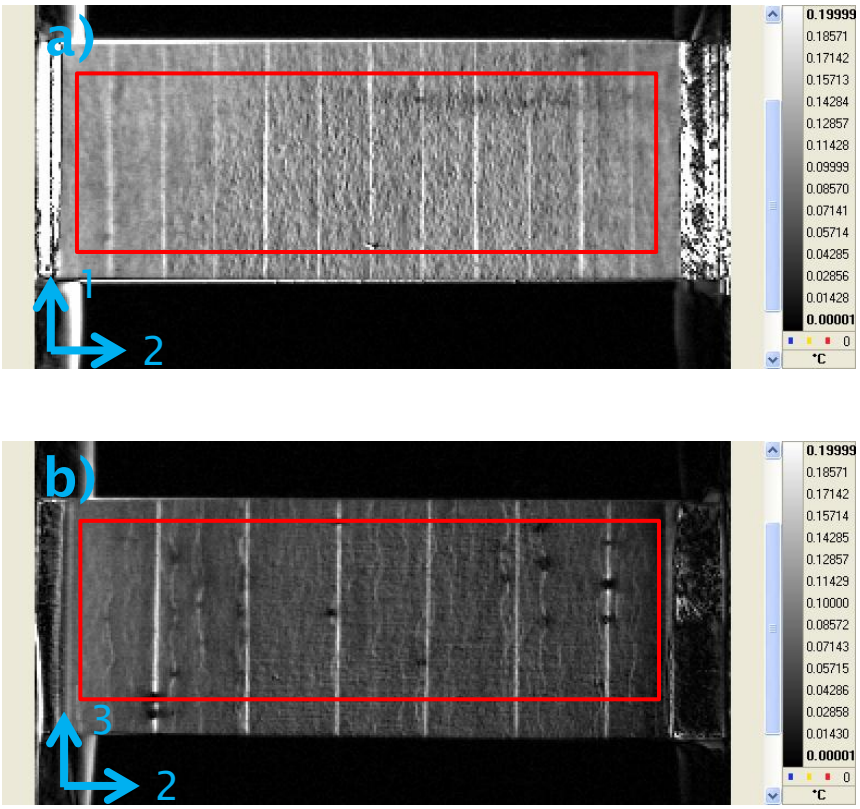

Figure 59: Raw ΔT data obtained from testing of (a) CSM and (b) unidirectional materials

A summary of the experimentally obtained K_1 and K_2 thermoelastic constants for the CSM and 90^o material can be found in Table 7.

Material	K_1 (MPa^{-1})	K_2 (MPa^{-1})
CSM	$9.83x10^{-6}$	$4.47x10^{-5}$
90^o	$2.17x10^{-5}$	$2.17x10^{-5}$
Araldite 2015	$2.88x10^{-5}$ [108]	$2.88x10^{-5}$ [108]

Table 7: Summary of thermoelastic constants

7.5.3 Derivation of the stress metric

A more common expression of the raw temperature data shown in Figure 56 is to use the 'stress metric' measure presented in equation (19). This metric accounts for the different thermal responses of the materials in the joint under load, distinguishing areas of high and low stress around the discontinuity. The full-field plot of the stress metric is obtained by multiplying the raw temperature data in Figure 56 by the $1/K_1$ thermoelastic values for each of the material layers in the joint, shown in Figure 60. Applying the thermoelastic constant significantly changes the appearance of the full-field data. The large K_1 value for the 90^o and the adhesive materials produce markedly different areas of low stress compared to the signal from Figure 60. The concentration around the discontinuity in the CSM layer shows very high stresses up to 110MPa localised in a very small area at the geometric discontinuity between adherends. The severity of this stress concentration, paired with the complex strain distributions observed in Figure 54, begin to show why this region is often found to be the location of failure initiation in the joint.

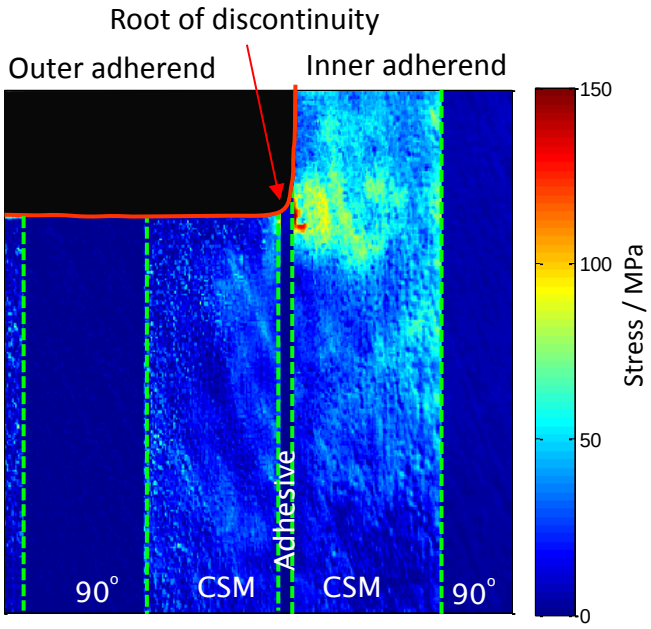

Figure 60: Process TSA stress metric

It is important to note that the TSA stress metric presented in Figure 60 is a calibrated expression related to the sum of the principal stresses in the joint. This coupled metric, although not producing individual stress components, does provide a high resolution, high accuracy measure against which the 2D DIC methodology can be validated. Validation of the DIC methodology therefore allows subsequent high confidence analysis of the individual stresses and strains in this region directly from the DIC data. This can be used for in depth evaluation of the stress components and damage initiation behaviour in the complex structure.

7.6 Validation of DIC strains using Thermoelastic Stress Analysis

The DIC and TSA experimental techniques produce two different metrics, stress and strain. Therefore manipulation of the two data sets is required to bring the techniques together into a single, directly comparable metric. The infra-red temperature data from TSA creates a coupled stress measure, as previously discussed, from which individual stress or strain components cannot be easily extracted for comparison against the DIC strain results. Accordingly, the strain components calculated from the DIC data must be manipulated into the principal stress metric which is used in the TSA data, expressed in equation (19).

Firstly the DIC strains in the principal material direction of the joint are manipulated into the stress terms in the equivalent principal material direction, using the following constitutive relationship presented in Equation 5.

$$\begin{bmatrix} \sigma_1 \\ \sigma_2 \\ \tau_{12} \end{bmatrix} = [Q]_{12} \begin{bmatrix} \varepsilon_1 \\ \varepsilon_2 \\ \gamma_{12} \end{bmatrix} \tag{22}$$

where $[Q]_{12}$ is the stiffness matrix in the principal material directions for the materials in the joint, taken from the experimental material characterisation undertaken in Chapter 3, shown in Table 8.

	CSM	90°	Araldite 2015
E_1 GPa	11.27	15.43	2
E_2 GPa	7.63	15.43	2
v_{12}	0.34	0.34[144]	0.36
v_{21}	0.23	0.28 [145]	0.36
G_{12} GPa	2.42	9[144]	0.9

Table 8: Materials properties values for CSM and 90° material

The principal material stresses are evaluated using Mohr's circle analysis to determine the direction, θ, and magnitude of the principal stresses, $\sigma^p{}_1, \sigma^p{}_2$, in the joint, which are required to form the TSA stress metric given in equation (19). This was conducted on a point by point basis for each point in the full-field array around the discontinuity. Evaluation of the principal stress direction from the analysis and manipulation of the component strains at 6kN in Figure 54 using this methodology are shown in the quiver plot in Figure 61. The vector length in Figure 61 is not proportional to stress magnitude, only direction. From this plot a significant variation in the principal stress direction away from the principal material axis around the discontinuity region can be identified. The greatest rotations are found in the outer adherend, deviating further from the material axes closer towards the root of the discontinuity, where the load path eccentricity is at its greatest. In the adhesive layer the stress direction is between 35°-45° indicating a large component of shear between adherends, also identified by the significant shear strains in Figure 54. The inner adherend indicates little rotation of the principal stress direction, showing the stresses to be predominantly aligned axially in line with the main loading direction.

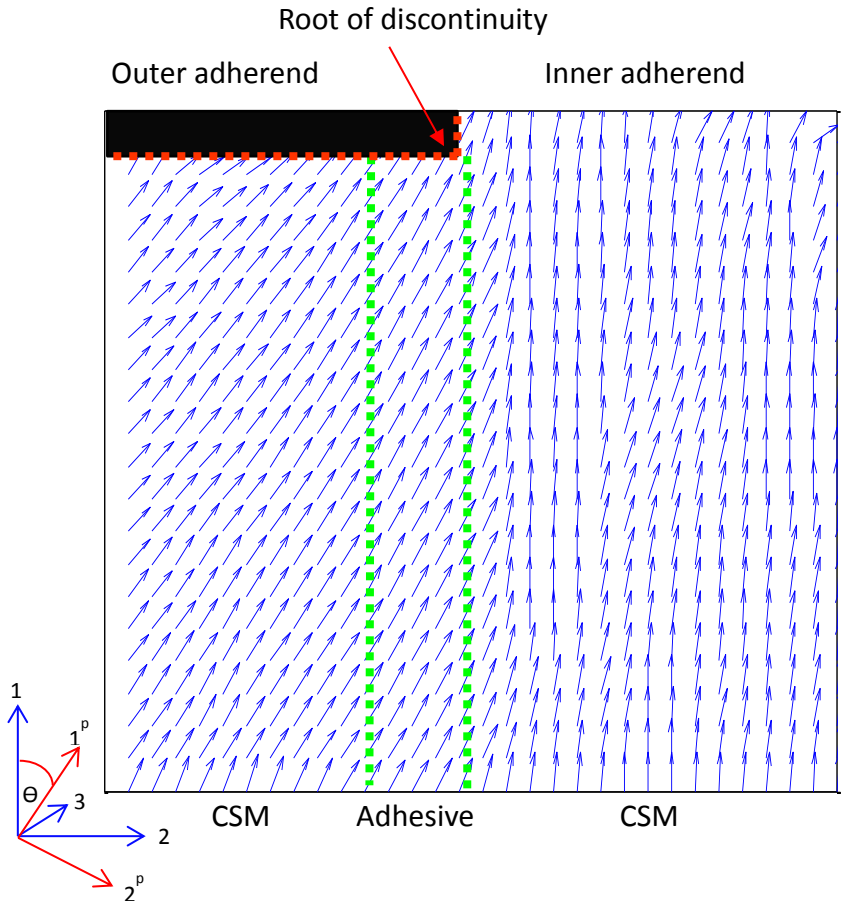

Figure 61: Principal stress direction around the discontinuity evaluated from DIC material stresses

In previous analysis of composite structures using TSA the assumption is made that the thermoelastic constants in the principal material directions K_1 and K_2 are coincidental to those in the principal stress directions, K^P_1 and K^P_2, shown in equation (19). However, the principal stress directions shown in Figure 61, evaluated from the DIC data in Figure 54 clearly show the directions of the principal stress axes, 1^p,2^p, to significantly differ away from the principal material axes, 1,2, due to the presence of the geometric discontinuity between the adherends. This has a significant effect on the manipulation of the infra-red data into the stress metric shown in equation (19), as the metric is a tensorial quantity dependent upon the thermoelastic constant in the principal direction. As the directions are not coincident with each other; the assumption about the thermoelastic constants no longer holds true requiring a new analysis methodology to be developed.

A new approach is proposed which transforms the experimentally obtained K_1 and K_2 values, point by point into the thermoelastic constant values associated with the principal stress

directions around the geometric discontinuity. Transformation of the thermoelastic constants is executed using the principal stress directions established from the earlier Mohr's circle analysis of the principal material stresses in the joint, derived from the DIC strain data. A similar transformation methodology was used by Dulieu-Smith [175] to analyse a filament wound composite cylinder with +/- 15^o winding angle, loaded in pure shear, whereby the stresses where transformed from the global cylinder coordinates into the material directions. The method in this thesis applied the transformation to the thermoelastic constant and not the stresses, differing from that of Dulieu-Smith.

Transformation of the constants is undertaken using the transformation matrix, T [5], [175], as follows:

$$\begin{bmatrix} K^p{}_1 \\ K^p{}_2 \\ K^p{}_{12} \end{bmatrix} = [T]^{-1} \begin{bmatrix} K_1 \\ K_2 \\ K_{12} \end{bmatrix} \tag{25}$$

The importance of transforming the thermoelastic constants is shown in Figure 62, and shows the sensitivity of (a) $1/K^p{}_1$ and (b) $K^p{}_2/K^p{}_1$ ratios for the CSM material as the principal stress direction rotates away from the principal material direction. The greatest effect is seen between 0^o-15^o, where small changes in the principal direction angle away from the material axis yield large reductions in the $1/K^p{}_1$ and $K^p{}_2/K^p{}_1$ ratios, heavily influencing the associated calculation of the stress metric. The rate of decrease slows as the rotation angle increases to 45^o, above which the thermoelastic responses see little change. The rate and shape of the changes in the thermoelastic ratio is heavily dependent upon the relative difference between the experimentally obtained K_1 and K_2 values. Materials which are highly orthotropic such as unidirectional materials will exhibit a very steep and large reduction, whereas materials where the K_1 and K_2 values are more similar, such as the in-plane directions for CSM materials, less reduction will be observed.

This analysis shows large limitations in the assumptions used in conventional TSA. The consideration of the principal stress direction is vital when using TSA to analyse complex composite structures, such as in the previous analysis of a composite tee-joint by Dulieu-Barton [106], or the analysis of a pultruded joint by Boyd et al [108], [109] which the present work is a continuation of. The effect of the principal stress direction rotation is especially important when analysing structures where the principal stress direction is very close to that of the materials axis. This may be a possible explanation for the large differences in calibrated stress metric between numerical and experimental analysis of a carbon cross ply material seen by Crump [176], which had been suspected to be due to non-adiabatic behaviour of the surface ply.

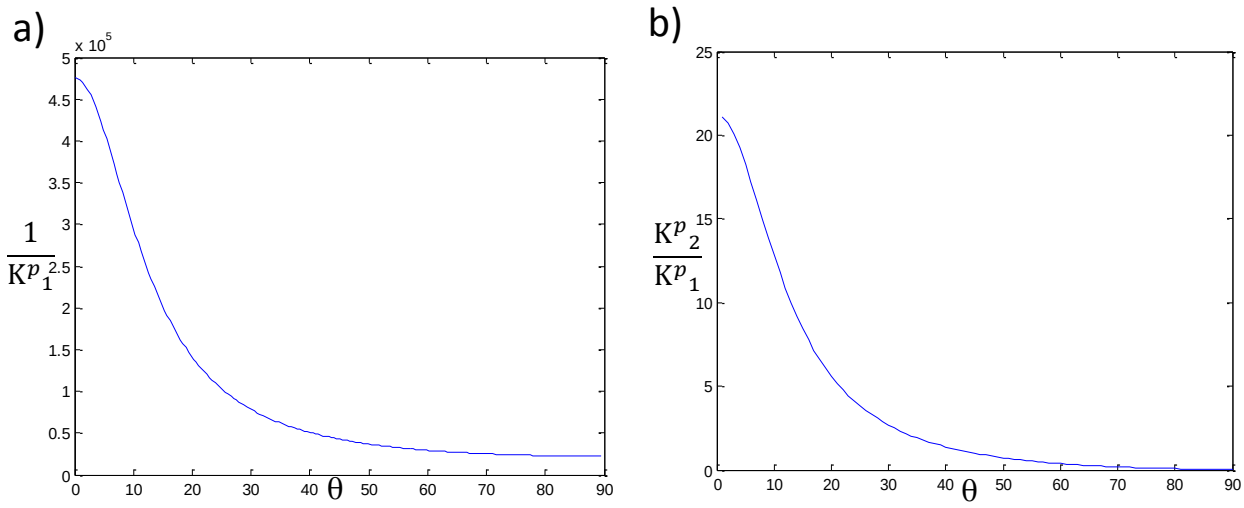

Figure 62: Response of (a) $1/K^{p}_{1}$ and (b) K^{p}_{2}/K^{p}_{1} thermoelastic constants transformed away from the material axis

Transformation of the $K_{1,2}$ thermoelastic constants in the new methodology is dependent on the principal stress direction angle θ, which is provided from Mohr's circle analysis of the component stresses calculated from the DIC strain data. The area of interest and spatial resolution of the TSA data is greater than that of the DIC, therefore the TSA area is cropped and downsampled by an integer factor of 3 to approximately the same spatial resolution and area of interest as the DIC data. This ensures that the principal stress direction and transformed thermoelastic constants correspond very closely to the same location between the two sets of data. The revised TSA stress metric is established by multiplying the ΔT/T infra-red data by the transformed thermoelastic constant value $1/K^{P}_{1}$ for each infra-red data point, forming the directionally sensitive quantity in equation (19), shown in Figure 63(a).

The minimum principal stresses established from the DIC data are manipulated by the transformed thermoelastic constant quantity K^{P}_{2}/K^{P}_{1} and added to the maximum principal stress on a point by point basis as per equation (19), forming the full-field DIC stress metric shown in Figure 63(b), which is directly comparable to that in Figure 63(a).

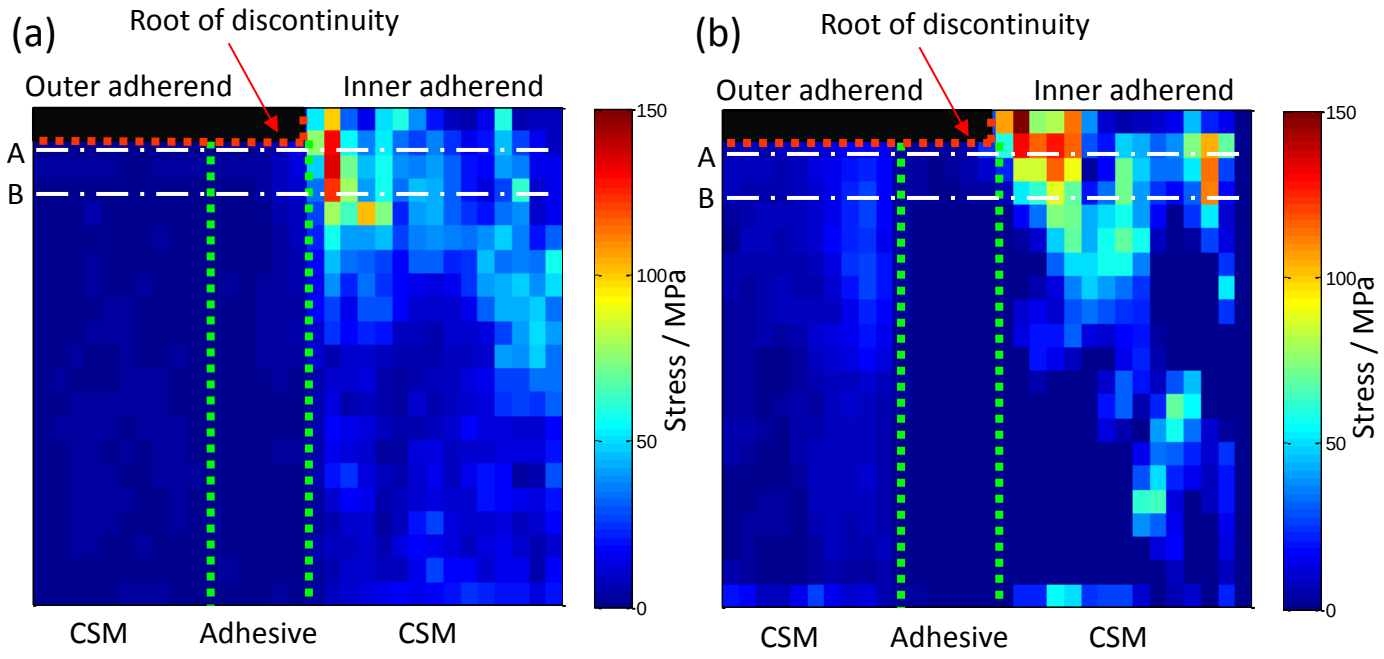

Figure 63: Directly comparable (a) TSA and (b) DIC stress metrics around geometric discontinuity

Although the two techniques use independent data sources, it should be noted that the manipulation and validation of the independent techniques is dependent on the measurement of the principal stress direction. This is derived from analysis of the principal material stresses established from the DIC white light strain measurement. As such, the use of the DIC strains to establish the principal stress directions inevitably has an influence on both stress metrics. Errors in the calculation of θ, due to inaccuracies in the measurement of the stresses from the DIC strains, are also introduced into the TSA stress metric through the transformation of the thermoelastic constants; and hence are no longer truly independent quantities. This is unavoidable due to the non-dimensional nature of equation (18), and the coupled stress term it represents, from which the direction of the principal stresses cannot be established to transform the constants.

With this in mind, Figure 63(a) and Figure 63(b) show very good visual agreement between the two comparable DIC and TSA stress metrics, capturing the location and magnitude of the stress around the complex geometry well in both figures. The greatest stresses are located in the inner adherend at the root of the discontinuity, similar to that seen in Figure 60, concentrated in and area measuring approximately 0.5 mm x 0.5 mm. The size of the stress concentration in the inner adherend is very similar between both techniques, reducing quickly away from the discontinuity towards the centre of the joint, identifying the powerful stress concentrating influence of the geometric discontinuity. Low stresses are observed in the outer strap due to the

large rotation of the principal stress direction, reducing the influence of the $1/K^P_1$ and K^P_2/K^P_1 thermoelastic constant terms on the data.

The DIC stress metric identifies a smaller secondary stress concentration in the outer adherend adjacent to the adhesive layer at the root of the discontinuity. This is not observed by the TSA data, although it can be clearly linked to the area of high axial, through-thickness and shear strains recorded in the DIC analysis in Figure 54. It is suspected that some of the high axial and shear strains observed in Figure 54 between the outer adherend and the adhesive are facets of the large subset size and overlap used in the analysis, which subsequently result in the elevated interfacial stresses in the outer adherend at this low load level. This is also evidenced by the highly localised $\Delta T/T$ concentrations observed in the inner adherend shown in Figure 56, where there is little response at the outer adherend interface. Local differences in the geometry around the discontinuity due to the removal of the adhesive fillet between specimens used for the TSA and DIC specimens may also have an influence on the DIC measurement at this interface.

The agreement between the two data sets is best shown in Figure 64(a) and Figure 64(b) which show a line plot through the two data sets along lines A and B in Figure 63, 0.03mm and 0.093mm from the end of the outer adherend, bisecting the stress concentration generated around the root of the discontinuity. Along lines A and B low stresses are observed in the outer adherend for both stress metrics due to the rotation of the thermoelastic constants and high localisation of the stresses around the discontinuity. An increase in the DIC stress metric is seen at the adhesive interface with the outer adherend as previously mentioned, due to the influence of the high through-thickness and interfacial axial/shear strains. The stress metrics across the adhesive layer are low due to the low elastic modulus of the adhesive and the pure shear deformation of the adhesive such that the sum of the principal stresses is very low. The sharp increase in stress around the discontinuity in the inner adherend is captured very well; both plots show comparable maximum stress values and display a similar decrease in stress away from the discontinuity towards the middle of the joint.

The agreement between the two datasets, both visually and through the line plots, provides confidence in the validation of both experimental methodologies. Importantly this agreement gives assurance that the measurement of the individual strain components using the magnified 2D DIC are accurate. With confidence in their measurement, the strains can thereafter be manipulated to establish the individual material and principal stresses providing further analysis of the load transfer in the joint. This addresses the major limitation in analysis of the joint using TSA due to the coupled stress metric. In addition to the validation of the two techniques, the agreement also provides confidence in the measured elastic properties of the materials in Table 8. These are extensively used in the calculation of the principal material stresses from the DIC

strain data, and fundamental to the methodology. Without accurate material properties, the transformation of the strains, the resulting analysis of the principal stress direction and transformation of the thermoelastic constants would be incorrect. This agreement also removes the uncertainty over the shear modulus value for the CSM material obtained in 3.5.3 using DIC, which had a high coefficient of variation.

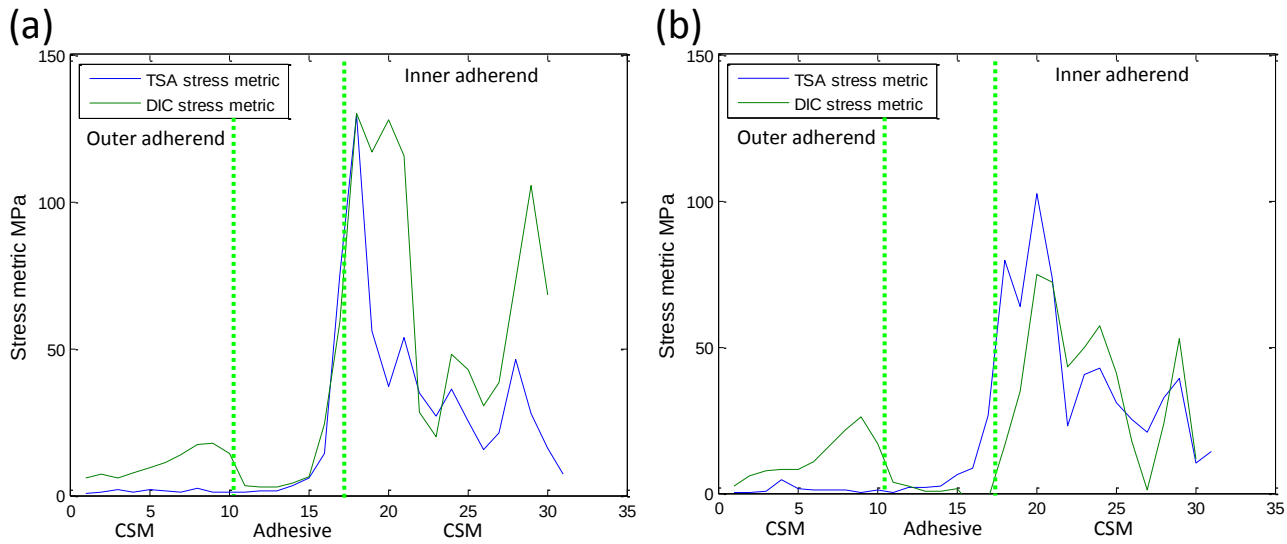

Figure 64: Stress plots through line (a) A and (b) B shown in Figure 63

The importance of using the new informed point-wise TSA methodology is observed in Figure 65. The stress metrics calculated using the two different thermoelastic constant approaches are shown along line A, 0.09mm below the end of the outer adherend. The main difference between the two approaches is visible in the outer adherend, where Figure 61 had shown a large rotation in the principal stress direction away from the principal material direction. The stress metric calculated using the traditional approach is up to 10 times greater than those from the new TSA methodology closest to the root of the discontinuity due to the influence of the transformation of the thermoelastic constants. At the root of the discontinuity there is good agreement in the peak stresses recorded with both approaches. However the stresses in the inner adherend using the new method reduce to a lower level away from the discontinuity due to the small rotation of the principal stress direction shown in Figure 61 from the strain data. This demonstrates the local severity of the stress concentration to be greater using the new approach.

Without the new methodology the TSA technique does not accurately capture the material responses in the region of varying principal stress direction around the geometric discontinuity. It is clear from Figure 65 that without using the new approach developed in this chapter that the analysis of the stresses in the outer adherend are over predicted and the local severity of the stress concentration under represented. Incorrect interpretation of the TSA data may lead to the

unsuitable validation of numerical models in the damage critical region around the geometric discontinuity, stressing the importance of this new informed methodology.

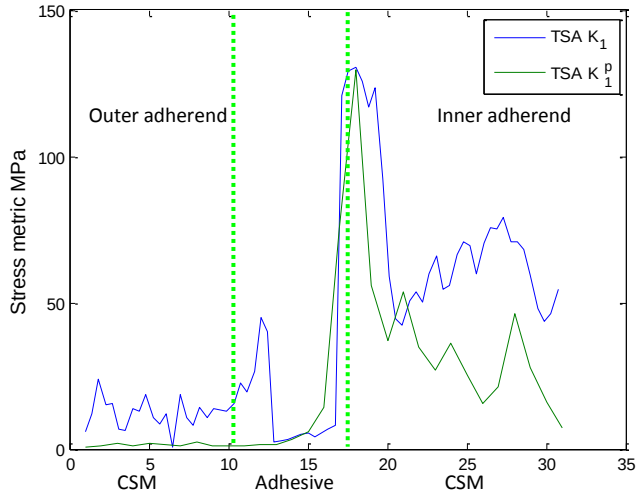

Figure 65: Comparison between the traditional, K_1, and new transformed, K^P_1, thermoelastic constants in the TSA methodolgoies along line A in Figure 63

7.7 Numerical model evaluation

The validation of the experimental techniques gives confidence to their use in the accurate evaluation of complex composite structures. For designers and engineers however, experimental testing of candidate structures or joint designs is time consuming and expensive. Finite element analysis provides a time efficient method of designing, analysing and optimising composites structures. It is greatly important that these models capture the complex physics and material behaviour occurring in the joint in an accurate and computationally efficient manner.

An outcome from the experimental investigations is a comprehensive set of validated experimental data, which can be used in the assessment of different numerical modelling methods. In this work the performance of a 2D finite element approach using ANSYS 12.0 is examined, with the aim to determine if the 2D approach adequately captures the stress and strain distributions with in the complex three dimensional composite adhesive joint problem.

A global model with the same dimensions of the joint was generated using 8 node, PLANE82 elements under the plane strain condition. This condition has shown good agreement with in-plane full-field surface measurement in previous experimental investigations [177]. The geometry of the laminate layers was established from measurements of the joint using vernier calipers, and micrograph inspection of the joint structure. A structured mesh containing 205

elements through the thickness of the joint was generated and 6kN load applied to the end of the inner adherend. A zero displacement boundary condition applied to the opposing end of the joint, replicating the experimental loading scenario. A submodelling approach was utilised to generate a 693934 node, plane 82 element, quarter model of the discontinuity. The submodeling method allows a highly refined mesh around the geometric discontinuity between adherends without the considerable computational expense associated with using a mesh of this density on a global model. Figure 66 shows a schematic of the submodel. The element divisions along each of the lines which form the mesh are indicated on Figure 66. In total there are 445 elements across the half width of the joint, increasing the density of elements in each material layer closer to the root of the discontinuity. Elements along the length of the joint were weighted towards the discontinuity to give greater mesh refinement as seen from the insert in Figure 66. Nodal displacements through the thickness of the joint, 11.9mm above and 13.28mm below the discontinuity, were extracted from the global model and applied to the corresponding locations in the submodel to provide the loading and boundary conditions. A symmetrical boundary condition is applied along the vertical centreline of the joint.

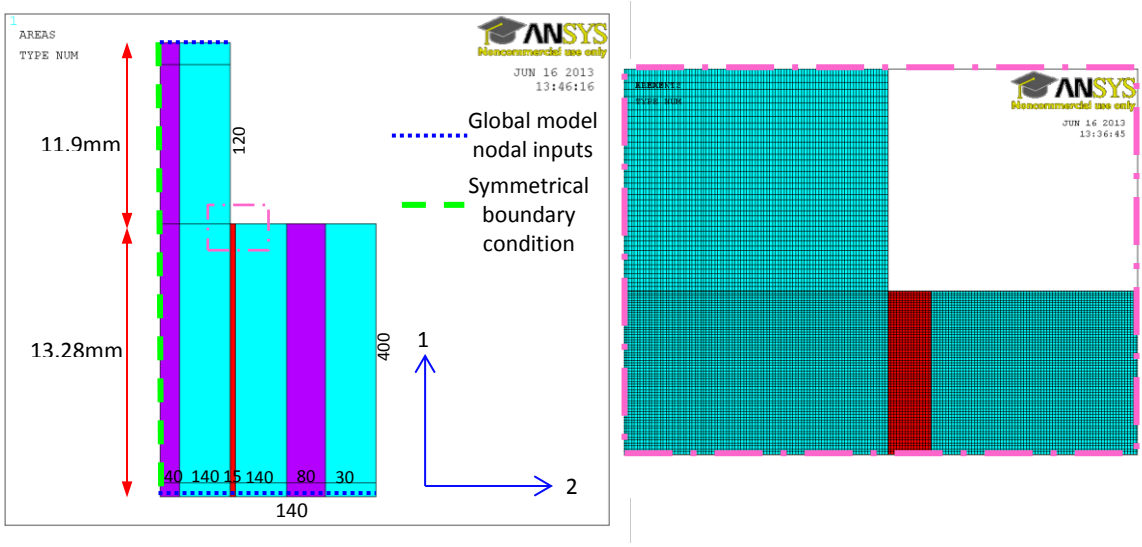

Figure 66 : Schematic of the submodel and structured mesh

Full convergence studies for both global and submodels were undertaken at 6kN, shown in Figure 67, identifying the global model to be heavily limited by the extent of the mesh refinement around the discontinuity in comparison to the submodel. Maximum axial stresses in the submodel were up to twice those seen in the global model, justifying the importance of this high resolution submodelling approach, and identify the difficulties caused by the severe geometric discontinuity and localised stress concentration effect. The material properties used for the model are the same as those presented in Table 8.

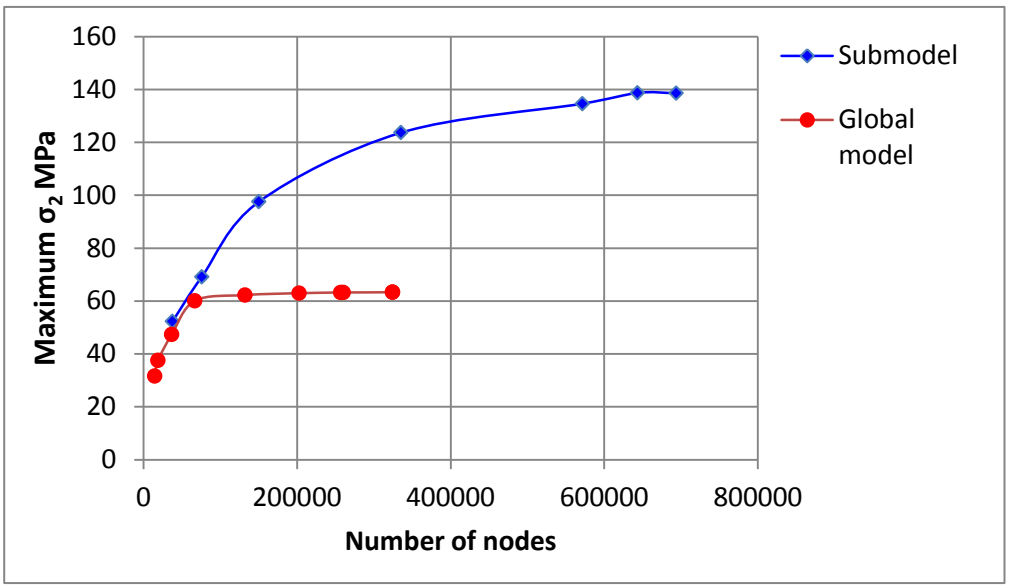

Figure 67: FE mesh convergence studies for global model and sub modelling approaches

Principal material stresses were extracted from the sub model solution and evaluated using Mohr's circle to establish the principal stresses and their orientations at each data point on the specimen surface as per the methodology used for earlier analysis of the DIC strains. The principal stresses were manipulated into the single stress metric form derived for the TSA and DIC data giving in equation (19) as per the methodology for the manipulation of the DIC strains, using the principal stress direction obtained from Mohr's circle analysis to inform the transformation of the K^{P}_{1} and K^{P}_{2} thermoelastic constants.

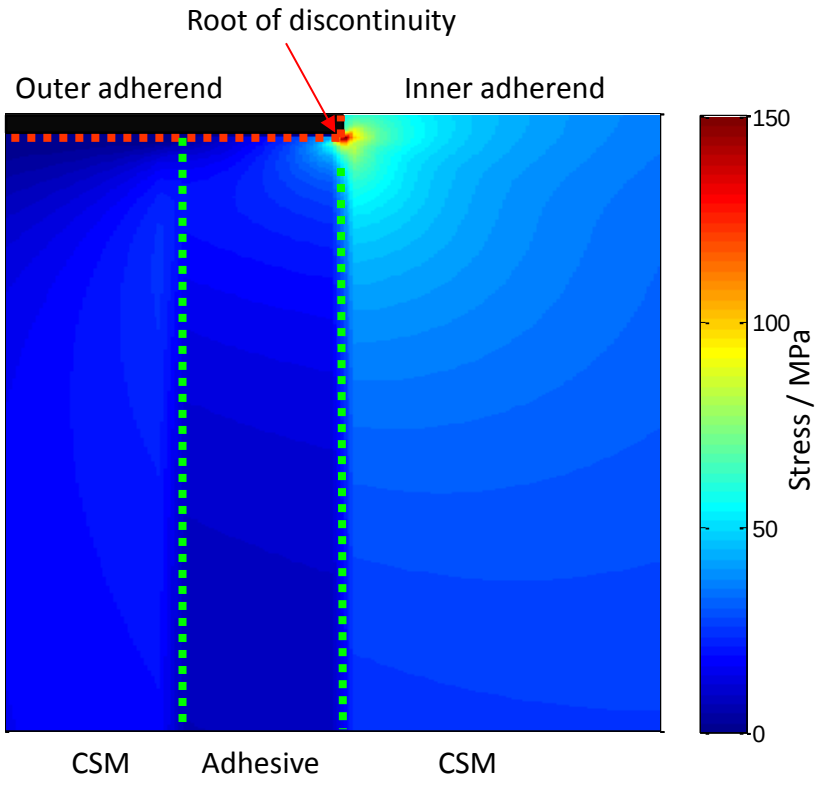

Figure 68: FE stress metric around the discontinuity at 6 kN

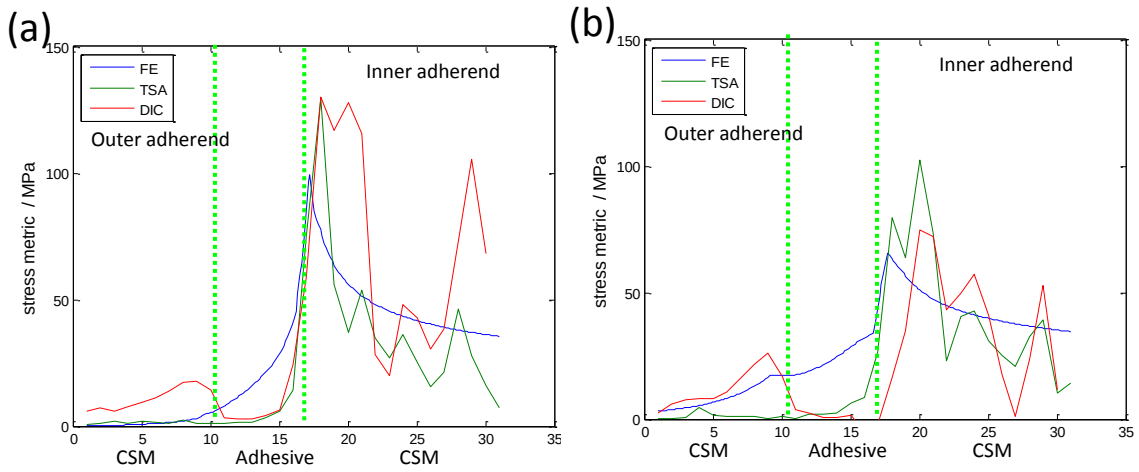

Figure 69: Comparison of DIC, TSA and FE stress metrics through line (a) A and (b) B shown in Figure 63

Figure 69(a) and Figure 69(b) show line plots across the thickness of the joint along lines A and B in Figure 63 identifying good agreement between the numerical model data and the validated TSA and DIC stress metrics along both line plots. The distribution of stress in the joint matches well to those observed from the experimental data, peaking in the inner adherend close to the discontinuity, before falling rapidly across the adhesive layer and into the outer strap, where the

principal stress directions are furthest away from the principal material axes. The line plots appear to give good confidence in the validity of the 2D numerical modelling approach. The agreement between the plane strain FE model and the plane stress experimental results also provides confidence that the 2D surface measurement techniques produce data which is representative of the response within the 3D structure. However evaluation of the accuracy of the modelling method using only the coupled stress metric does not deliver full validation of the model, as the accuracy of the individual stress and strain components, which have a significant effect on the behaviour of the structure, cannot be assessed. Earlier validation of the DIC methodology provide a highly informative dataset of individual stress and strain components in the joint against which full validation of the numerical modelling method can be established.

Plots of the axial, through-thickness and shear strains evaluated from the numerical model and validated DIC analysis, along lines A and B are shown in Figure 70 and Figure 71. There is a good match between the strain in the CSM layers either side of the adhesive layer between the numerical solution and experimental strains in both plots. The plots show that the resolution of the DIC data is unable to capture the large localised peak strains recorded from the highly refined FE model at the interface with the adhesive layer. Unfortunately, this is a result of the large strain gradients in this region and the large size of the subset necessary in the correlation due to the requirement for high accuracy measurement. These large subsets provide an 'average' displacement in the subset, effectively smoothing the deformation and strain fields, and failing to capture the large strain gradients at the interfaces. The method of displacement differentiation, or shape functions, used to establish the strains from the displacement data, of which the DaVis 7.4 method is very simple, has also been shown to have an effect on the measurement of large inhomogeneous strain gradients using DIC[178], [179] .

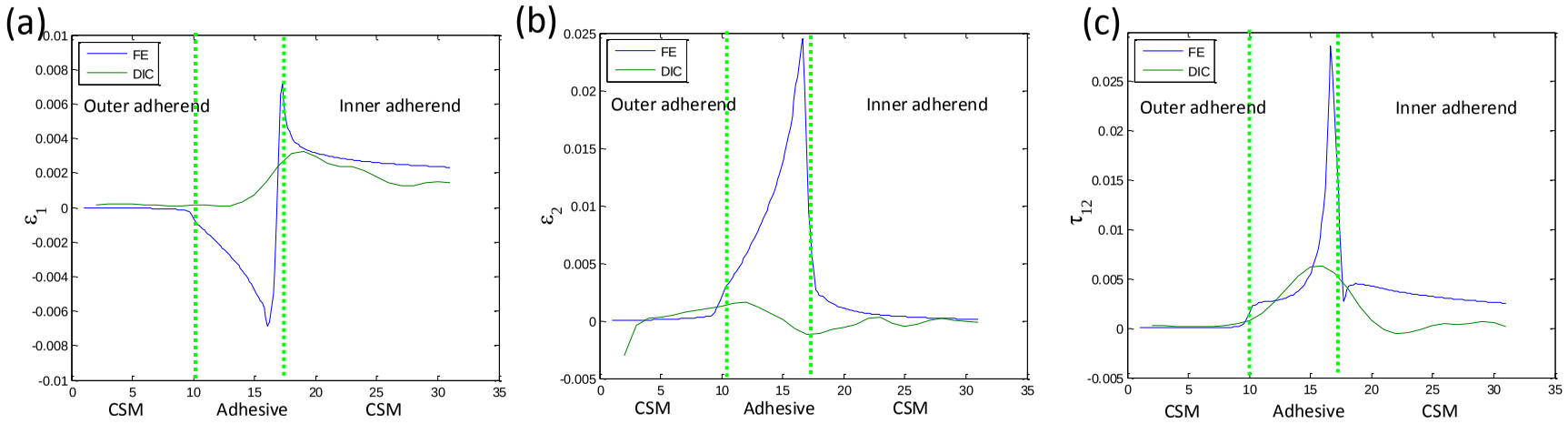

Figure 70: (a) Axial, (b) Through-thickness and (c) Shear strain plot comparison of DIC and FE data through line A shown in Figure 63

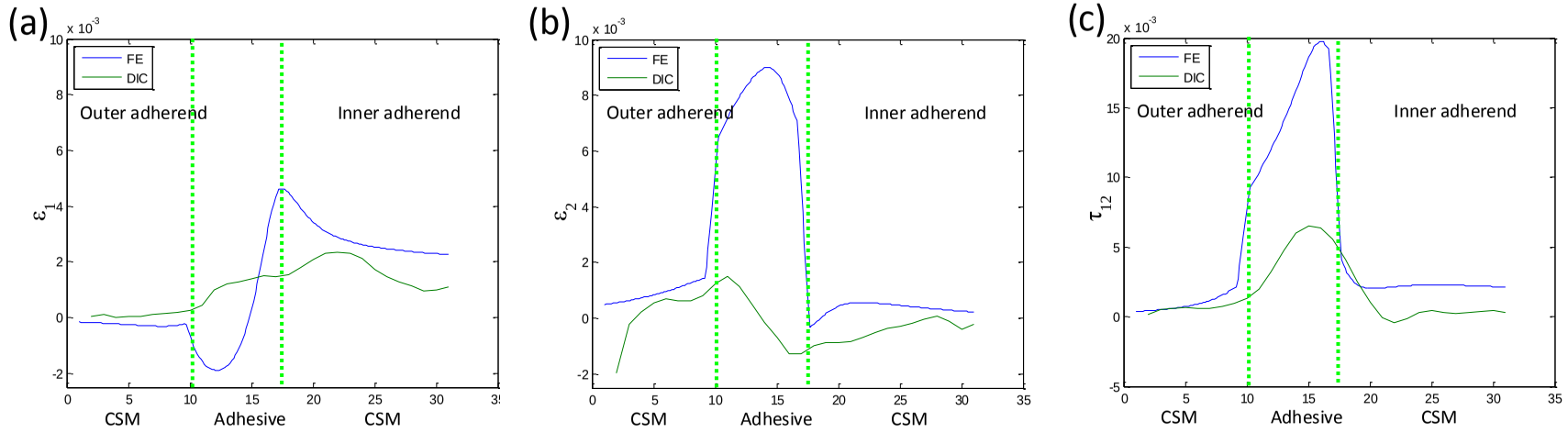

Figure 71: (a) Axial, (b) Through-thickness and (c) Shear strain plot comparison of DIC and FE data through line B shown in Figure 63

In contrast to the adherends, the strains in the adhesive layer show poor agreement between the numerical and experimental results. The large difference between the experimental and numerical measures of the shear strain in Figure 70 and Figure 71, and the isolation of this disagreement to the adhesive layer suggest that this disagreement is due to incorrect modelling of the material properties of the adhesive layer in the triaxial stress state around the discontinuity in the joint and not an inherent consequence of the 2D modelling approach. The adhesive material properties data were taken from the reported values on the manufactures datasheet [138], tested using ISO 527 and DIN 53445 international standards. Agreement between the TSA and DIC data sets in the previous analysis was proven to validate the material properties used in the manipulation of the strain terms into stresses. However, in the isotropic adhesive the principal stress direction is very close to 45^{o}, therefore the maximum and minimum principal stresses established from the DIC strains are almost exact opposites of each other, producing a very small output when summed. The opposing nature of the stress values dominates this calculation, whereby the values of the material properties used to establish the principal materials stress become almost inconsequential. Hence, although agreement between the TSA and DIC data is found, the result does not necessarily validate the in-situ material properties of the adhesive layer in the joint due to the coupled nature of the stress metric.

To demonstrate significant differences between the reported and in-situ adhesive properties, an inverse methods approach is undertaken to iteratively alter the adhesive material properties until better agreement between the numerical and experimental strain response across the adhesive is observed. The quality of the agreement from the new material properties was evaluated against both the coupled stress metric, and the individual strain plots. This provides validation of the new material's properties against both the white light DIC data and the infra-red TSA data, delivering high confidence in the new values and ensures that the alteration of the adhesive properties does not have a detrimental effect on the agreement witnessed in the adherends.

The large deviation of the FE strains away from the DIC data in the adhesive layer infers that the in-situ adhesive properties are markedly different from those quoted on the manufacture's data sheet. Figure 72 and Figure 73 show revised plots of the stress metric plots of the axial, through-thickness and shear strains along lines A and B with the revised adhesive material properties shown in Table 9. The values in Table 9 were converged towards from an iterative cycle of 15 simulations using trial and improvement until good agreement between the numerical and experimental data was observed. Altering the adhesive properties shows strong improvements with the axial, through-thickness and shear strain agreements in the adhesive layer. A noticeable improvement can also be seen at the interface between the adhesive and the outer adherend, particularly along line B. The improvement in strains in the outer adherend illustrates the coupled strain response between the materials at the adhesive interface due to the

load transfer in the through-thickness across the adhesive layer. Strains in the inner adherend remain largely unchanged, indicating that the response in the inner adherend is dominated by the axial loading, with little influence of the shear response. This is also identified by the plot of the principal stress directions from the DIC analysis in Figure 61, where there is little deviation away from the principal material direction. The large improvements in the strain distributions, particularly in Figure 73 (b), show that the supplied data sheet values may be very different from the in-situ values in the joint. An improvement can also be seen in the agreement between the stress metrics in the inner and outer adherends in Figure 74, making the peak stresses closer to the experimental results. The agreement between the stress metrics in the adhesive layer in Figure 74 however is worse than in Figure 69. This suggests that the adhesive properties are still not correct, and that there is scope for further iterations and improvements. This is also suggested by the very high material properties which have been produced from the current iterations, which are now more similar to the properties of the CSM material than a typical adhesive.

	Manufacturer's datasheet adhesive properties [138]	Revised inverse method material properties
E GPa	2	10
v	0.36	0.25
G GPa	0.735	4

Table 9: Adhesive properties from material datasheet and inverse approach

The agreement along line A in Figure 72(a), although improved, is not as good as that along line B in Figure 73(b), where the through-thickness and shear strains along line A continue to show a large difference between the experimental and numerical results. Strains in the inner adherend are over predicted and the distribution across the adhesive interface close to the discontinuity is appreciably different. These differences may be due to the low spatial resolution of data and high strain gradients around the discontinuity, which is a major limitation of the DIC technique when analysing discontinuous structures with large subsets observing localised material behaviours. The accuracy of the strain distribution generated by the finite element model is also questionable, due to the difficulty in modelling the severe numerical singularity created by the discontinuity at this small length scale. This is apparent from the highly localised deviation between results at the discontinuity, affecting only the distributions along line A and not line B. Geometrical differences also exist between the modelled and experimental geometry, which still features a very small adhesive fillet despite best attempts to remove this during manufacture, reducing the stress concentration effect. As such, the inverse methods approach used in this investigation does not try to generate an exact solution to these parameters as there is still too much uncertainty in the measurements around the critical discontinuity area. Rather this

investigation is used to identify large limitations in the current 2D modelling technique due to fundamental insufficiencies in the in-situ adhesive properties and challenges in modelling the behaviour of the discontinuity.

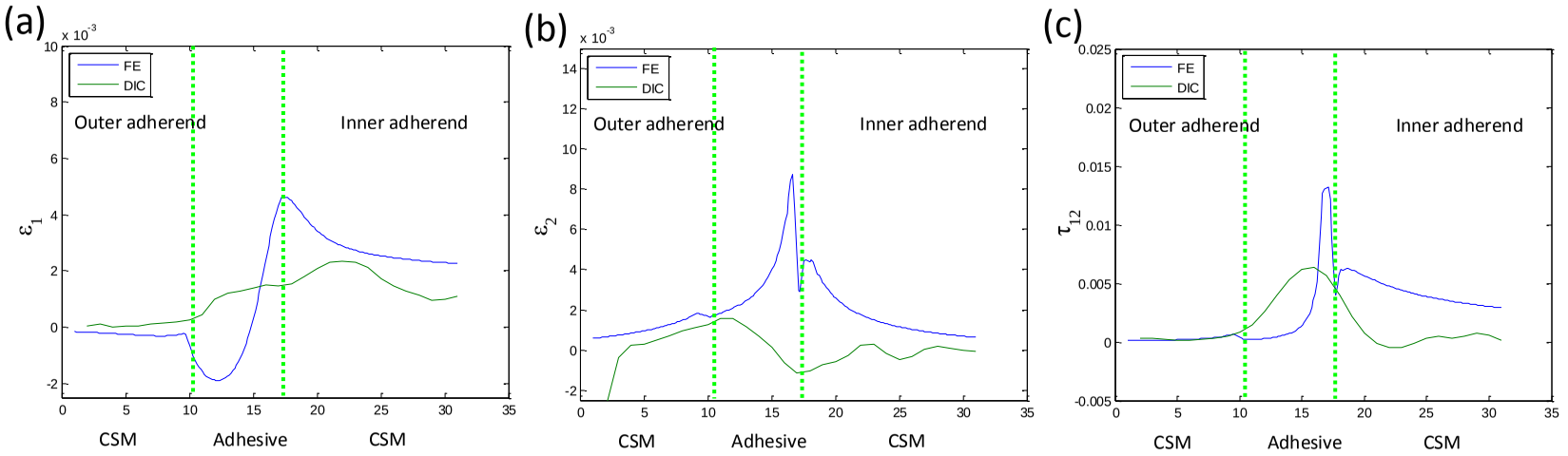

Figure 72: (a) Axial, (b) Through-thickness and (c) Shear strain plot comparison of DIC and FE data through line A shown in Figure 63 using new adhesive properties

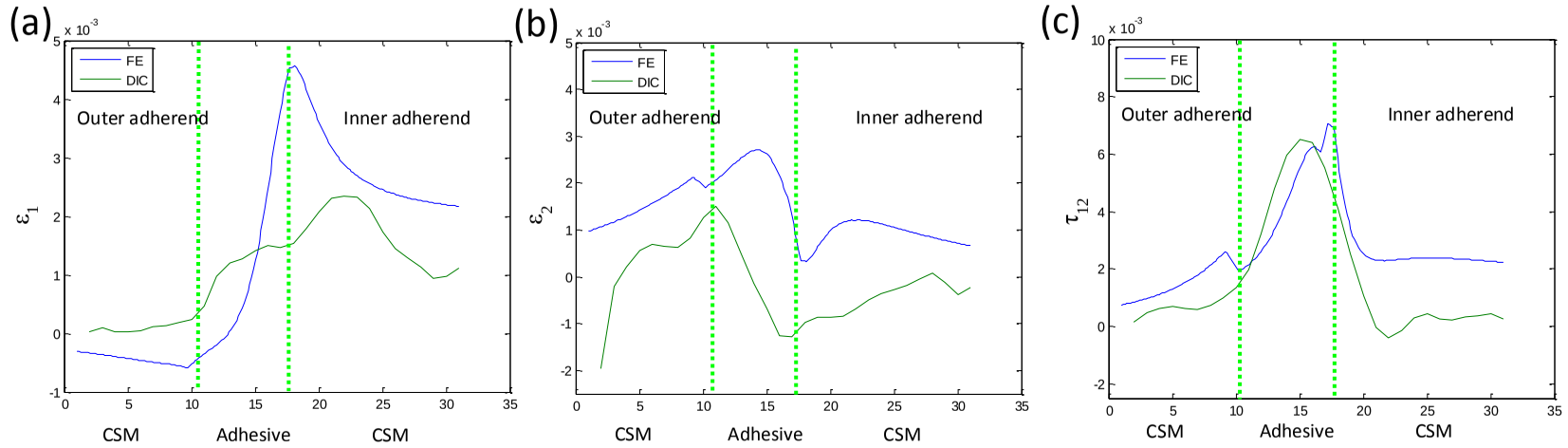

Figure 73: (a) Axial, (b) Through-thickness and (c) Shear strain plot comparison of DIC and FE data through line B shown in Figure 63using new adhesive properties

Overall the 2D modelling method appears to perform very well, capturing complicated strain responses around the severe discontinuity with a relatively low computational cost. As discussed in literature, the 2D plane element model is not capable of modelling 3D effects such as anticlastic bending of the adherends [36], [38], [39] but the agreement with the two experimental sets of data shows that this does not degrade the quality of the simulated results. Platitudinously the model is only as good as the input parameters, of which the adhesive properties supplied by the manufacturer's data sheet are shown to be unsatisfactory. Small changes in the adhesive parameters are observed to yield large changes in the peak strain values observed at the interfaces. Importantly it is the peak strains, and stresses, which are responsible for damage in the structure. Further in-situ testing of the adhesive properties and higher spatial resolution DIC data is required before there is full confidence in the model results, especially at critical material interfaces, and the model performance be fully assessed.

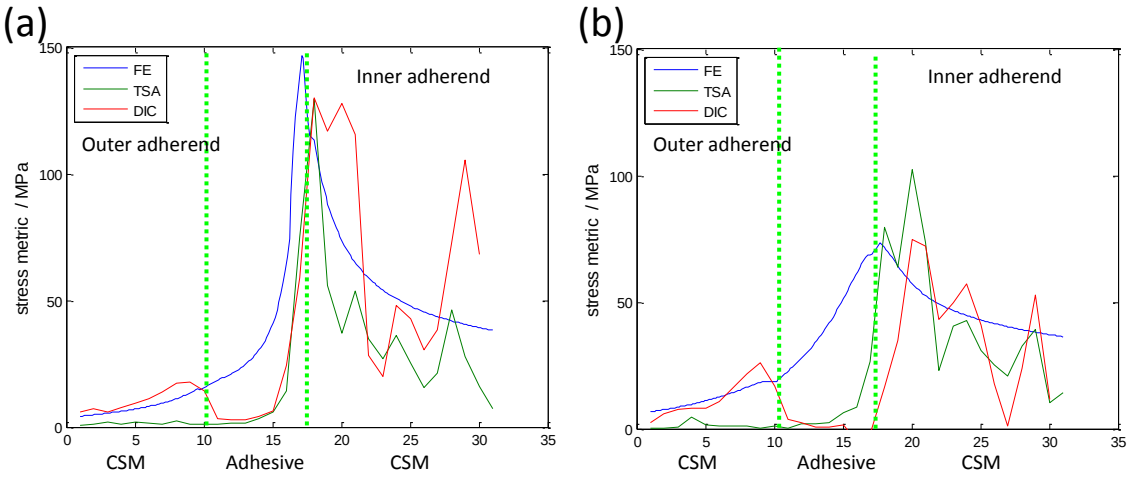

Figure 74: Stress plots through line (a) A and (b) B shown in Figure 63 using new adhesive properties

7.8 Conclusions

In this chapter TSA is used to independently validate the accuracy of the 2D mesoscopic DIC methodology used extensively in this thesis.

Validation is provided through the manipulation of the white light strain data into the same coupled stress metric as TSA data collected around the discontinuity. During this process it is noted that there is a significant variation in the principal stress direction around the discontinuity away from the material axes. Subsequently this invalidates one of the main assumptions regarding determination of the thermoelastic constants used in TSA of composite structures.

A new methodology was developed to address this issue, calculating the TSA stress metric using thermoelastic constants transformed to the principal stress direction in the joint on a point by point basis. The new methodology is identified to be highly important when evaluating complex composite structures, as small changes in the principal stress direction away from the material axes can yield large changes in the measured stress metric. The direction of the principal stress used in the transformation is informed by Mohr's circle analysis of the material stresses evaluated from the DIC strain data. Comparison of the DIC and TSA stress metrics calculated using this methodology show very good agreement, validating the independent experimental infra-red and white light measurements and methodologies. The agreement against the highly accurate TSA data shows the DIC technique to be a powerful and versatile tool for the analysis of composite structures featuring small, yet critical localised stress and strain concentrations at the mesoscopic scale. Importantly, this agreement also retrospectively provides confidence in the methodology used to evaluate the principal stresses in the joint conducted in Chapter 6. From the studies in this chapter a maturity in the experimental measurement and data processing techniques are demonstrated; providing the experimental mechanics community with a robust methodology which may be used in future investigations.

The validated datasets are used to evaluate the performance of a computationally inexpensive 2D finite element modeling approach. Good agreement was seen between the experimental stress metrics, but a significant difference in results was identifying in the adhesive layer when evaluated against the validated high confidence DIC material strain data. An inverse approach is used to demonstrate that this is due to a large difference between the reported and in-situ adhesive materials properties, and not due to insufficiencies in the 2D modeling approach.

The analysis in the preceding chapters has shown a structured development of the 2D mesoscopic DIC methodology. Shortcomings in the analysis have been identified and addressed through in depth evaluation of error sources and revised experimentation. Validation of the methodology against the independent TSA results is the final step in the methodology reaching maturity, demonstrating high confidence in the DIC measurement of the bonded joints. This methodology will now be adapted to analysis of high strain rate loading events using high speed cameras to provide novel quantitative analysis of the strengthening mechanisms experienced in bonded joints at high strain rates. As discussed in the literature review in Chapter 2, this form of analysis has not been conducted before, and the application of the DIC methodology has great potential in developing the understanding of the structural and material dynamics.

8. High strain rate testing of adhesively bonded composite joints

8.1 Introduction

The literature review in Chapter 2 identified significant gaps in the understanding of material behaviours in adhesively bonded joints loaded at high strain rates. Large increases in both global strength and stiffness of bonded assemblies have been observed in literature, however no research has been presented which measures changes to the local material responses in the joint during the failure incident. The work undertaken in the previous chapters using DIC and TSA has identified that these local effects in the joint are critical to the development of the strain field in the joint and the initiation of damage, both of which ultimately influence joint strength. It is therefore very important that measurement of these local features is applied to the dynamic loading event in order to develop a quantitative understanding of the material and structural mechanics.

In this chapter comparative analysis is undertaken of a composite single lap joint (SLJ) tested both quasi-statically and at high rate, representative of in-service marine loads. The high magnification DIC methodology developed for quasi-static loading is adapted to incorporate high speed cameras to provide high temporal resolution DIC analysis of the developing strain fields in the joint structure. Changes in the joint strength and strain distribution are identified between the loading conditions, providing a better understanding of the dynamic behaviour of bonded composite joints. Analysis of the strain fields addresses the shortcomings in literature, where local material responses are never considered. Knowledge of the dynamic material and failure behaviour can be used to improve joint designs; maximising in-service performance whilst minimising the initiation of damage.

8.2 Joint structure

The change in testing apparatus and imaging equipment require a change in specimen geometry. The DBSJ used in the previous chapters provided a highly stable platform for analysis; however the symmetry of the joint reduces the eccentricity of the load path making accurate analysis of the joint very difficult. Therefore a different specimen design was required which would generate greater measurable through-thickness strain. The SLJ was selected for analysis due to its simple construction, large geometric discontinuity and high through-thickness loading

between adherends. The SLJ layup and overlap length were designed to ensure that the response of the joint in the through-thickness direction is adequately captured using the optics and cameras available. This is especially important due to limitations in the spatial resolution of the high speed images, which as shown in the previous analysis greatly influences the quality of the DIC measurements. As discussed in the literature review, the limited spatial resolution is a function of the current high speed camera technology, where spatial resolution is sacrificed in order to gain temporal resolution. The single lap joint has been extensively tested and modelled in literature, providing a large database against which the experimental strain results can be compared, providing confidence in the experimental methodology.

The joint was constructed with a [CSM_7 90_4 CSM_7] layup from 800g/m^2 unidirectional and 450g/m^2 chopped strand mat (CSM) glass fibre using Gurit Prime 20 LV epoxy resin and the resin infusion process. The SLJ specimen is shown Figure 75(a); it is 25 mm wide with an adherend overlap length of 25 mm. The adherends had a total length of 150 mm with a 50 mm tapered end tab design. Araldite 2015, a toughened structural epoxy adhesive, was used to bond the adherends together. An image of the layered joint structure is shown in Figure 75(b). Adhesive spew fillets were removing during construction to artificially increase the through-thickness strain in the thick, stiff adherends.

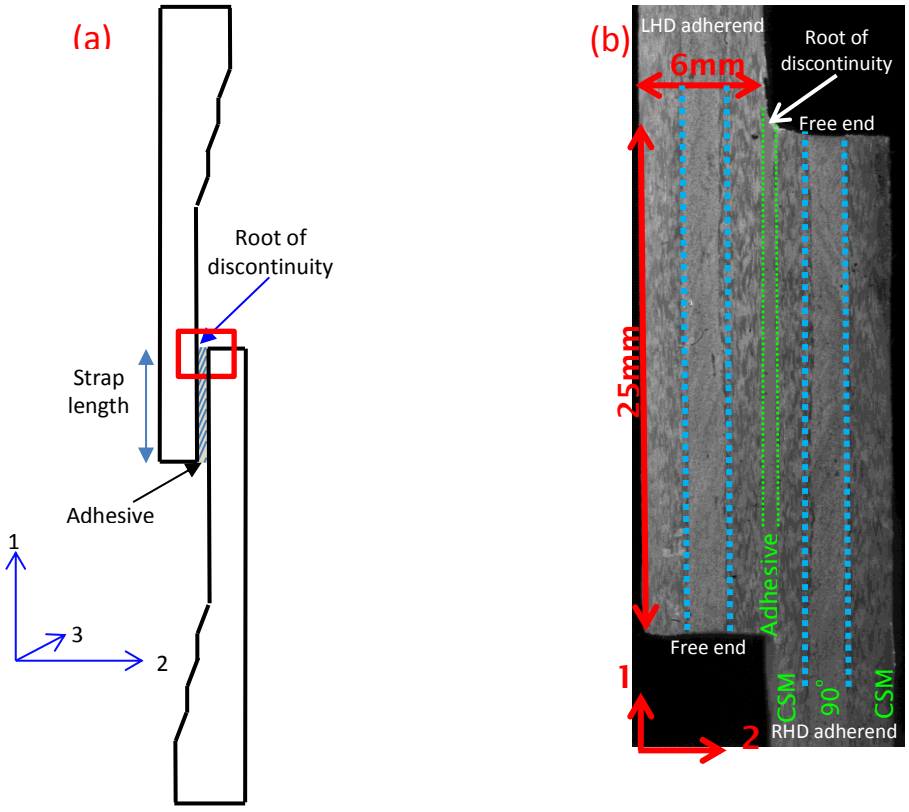

Figure 75:(a) Schematic of the single lap joint (b) image of the layered composite structure of the joint

8.3 SLJ quasi-static analysis

The SLJ was initially tested quasi-statically to establish a baseline joint response, against which the effects of dynamic loading are compared. The joint was mounted in an Instron 5569 electromechanical test machine and loaded at 2 mm / min up to failure. A 16 MP 14 bit monochromatic LaVision Imager pro X camera fitted with a Sigma 105 mm macro lens was used to image the specimen with an image resolution of 142 pixels / mm at 5 Hz. Illumination was provided by a LED ring flash light mounted onto the lens, delivering consistent cold lighting of the specimen. The stochastic speckle pattern was applied using RS components matt black aerosol, onto a white background painted onto the specimen. A needle cap was used to provide a larger aperture nozzle from the black aerosol, matching the pattern properties to the resolution of the image, minimising errors in the correlation. The sequence of images was processed using the LaVision DaVis 8.0 correlation software, with a subset size of 75 x 75

pixels and a step size of 25 pixels, delivering a spatial resolution of approximately 5 data points / mm.

Figure 76(a)-(c) show a detailed view of the evolving through-thickness strains, ε_x, in the joint loaded at 1.5, 3 and 4.7 kN respectively. Through-thickness strain concentrations form at the root of the geometric discontinuities in the CSM layers either side of the adhesive layer between adherends. These concentrations form due to the external bending moments created from the load path eccentricity and become larger with greater applied load. The through-thickness strain is greatest at the free end of the adherends, where the structure is least constrained, experiencing the greatest deformations. The bending and rotation of the joint during deformation generates a band of high interfacial through-thickness strain between the CSM and 90° materials around the discontinuity in the adherend adjacent to the free end. The localised strains, generated at the discontinuity, result in the initiation of a crack and the propagation of damage downwards into the joint, (see Figure 76©), and final joint failure at 4.8N.

Figure 77(a)-(c) show the development of the shear strains in the joint at the same load intervals as Figure 76. As expected, the largest shear strain is experienced in the adhesive layer, as shear is the primary load transfer mechanism between the inner and outer adherends. A symmetrical shear strain distribution is observed, peaking towards the discontinuity. The bending of the adherends is observed to generate greater shear strains in the face sheet CSM material compared to the central 90^o material, contributing to the high, damage inducing, strain field at the root of the discontinuity.

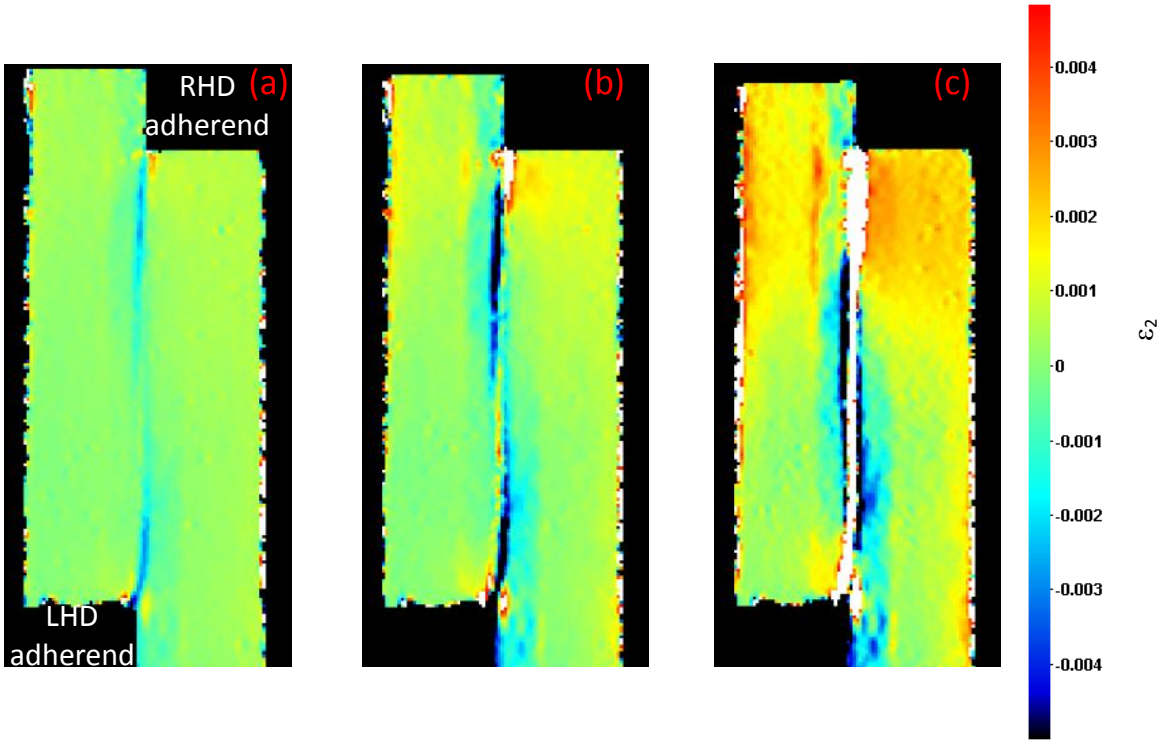

Figure 76: Through-thickness (ε_2) strain in the SLJ at (a) 1.5kN (b) 3kN (c) 4.7kN

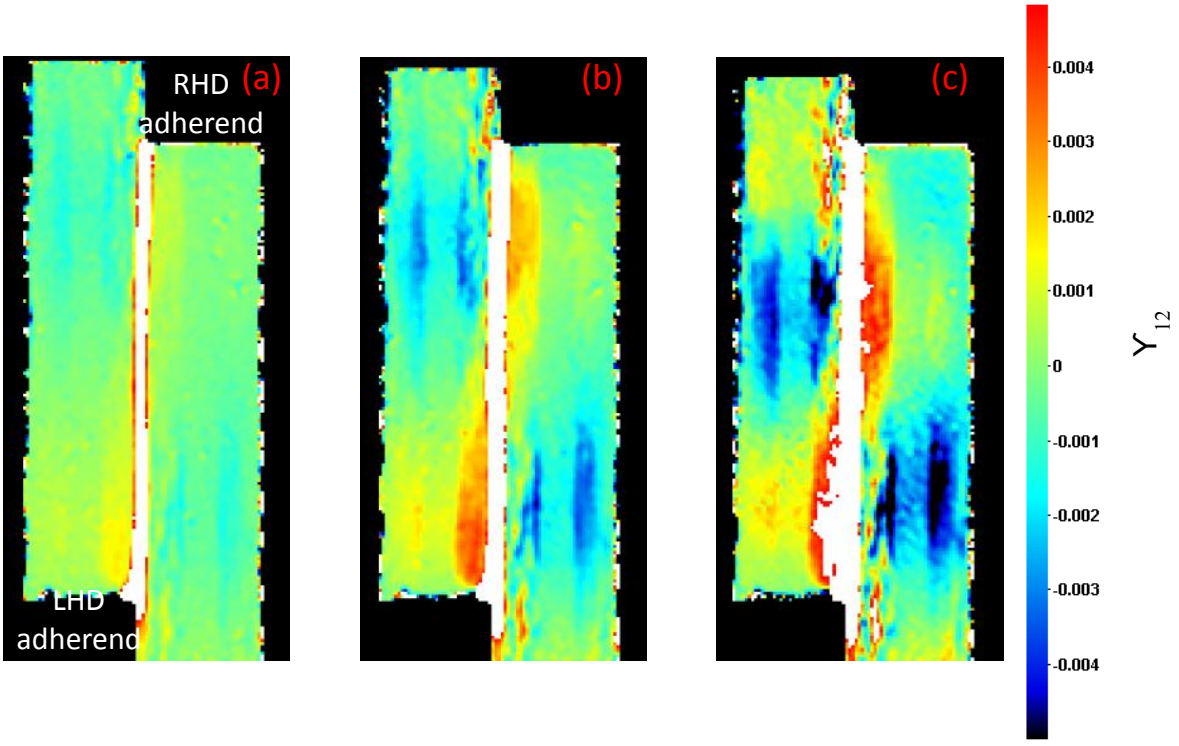

Figure 77: Shear (γ_{12}) strain in the SLJ at (a) 1.5kN (b) 3kN (c) 4.7kN

An improvement in the quality of the data is observed over the results in Chapter 4 at similar image resolutions, producing localised analysis comparable to that in Chapter 6. The improvement in data is a result of the geometry change to a single lap joint, generating greater through-thickness strains. The improvement can also be attributed to the use of DaVis 8.0 instead of DaVis 7.4, which was used in the analysis in the previous Chapters. This new version of the software changes from an inverse FFT method in DaVis 7.4 to a least squares method correlation function, allowing greater flexibility in the processing parameters. Importantly the methods for determining strain from the displacement fields are also changed in DaVis 8.0. A basic central differences approach is used in DaVis 7.4, comparing the displacements of neighbouring subset pairs in isolation. This approach accentuates errors in the displacement field, as small differences in displacement can lead to large strain gradients, producing a rippled 'texture' to the strain fields. In DaVis 8.0 the strain fields are obtained through an optimisation of the DIC gradients, which are determined using a 5^{th} order shape parameter function. This method produces a smoother continuum of strain, as the strain value at each subset is determined with consideration of the surrounding subsets, as discussed in the literature review.

Analysis using the DIC technique provides a detailed and complementary view of the localised through-thickness and shear strain distributions generated in the joint. Good agreement is seen between the through-thickness strain results and those obtained from Moiré interferometry by Tsai and Morton [13], providing confidence in the experimental results and methodology. High spatial resolution full-field data is gathered, identifying the global and local material behaviours in the joint, assessing their contribution to the initiation of failure, similar to the work undertaken in Chapter 4 and Chapter 6. The strain distributions in Figure 76 and Figure 77 demonstrate that the relatively simple discontinuity between components results in very complex, inter-dependent strain distributions in the joint. The localised through-thickness and shear strains identified at the root of the discontinuity play a significant role in the development of damage and the control of ultimate joint failure, providing an initiation site for damage in the strain critical brittle epoxy matrix leading to ultimate joint failure. The detail of these critical localised strain distributions would not be obtained using traditional single point measurement techniques, such as strain gauges; demonstrating the need for full-field measurement. With the current spatial, and temporal, resolutions there is insufficient detail to resolve the initiation and propagation behaviour around this damage critical region and needs to be investigated further.

To improve the temporal resolution of the data, quasi-static tests were conducted using the same test procedure with a 10 bit Photron SA5 high speed camera. The high speed camera provides the capability to capture the fast initiation and development of damage in the joint up to an including failure. Images were recorded at 1000 Hz with an image resolution of 464 x 384 pixels. The image size is much smaller than achieved previously with the 16 MP LaVision

Imager pro-x camera due to limits in the on board camera memory and the high speed imaging technology. To compensate, optics are used to increase the magnification of the image, increasing the number of pixels per millimetre in the image. This provides an image with a high spatial resolution at the expense of reducing the size of the area of interest for the analysis. An area of interest 6.2 mm x 5.1 mm was imaged at the root of the discontinuity between the adherends, where damage was observed in Figure 76(b) and Figure 76(c) to initiate and propagate. A Sigma 105 mm macro lens was attached to the Photron SA5 producing an image resolution of 75 pixels / mm, approximately half that of the initial analysis shown in Figure 76 and Figure 77 due to the smaller sensor size of the high speed camera. The image sequence was analysed with a subset size of 69 x 69 pixels and step size of 20 pixels, producing a spatial resolution of approximately 4 data points / mm. The high magnification Canon MP-e65 macro lens used in Chapter 6 and 7 was not used in this investigation, as the size and short focal depth of the lens preventing adequate illumination for the high speed imaging.

Figure 78 shows (a) axial, (b) shear and (c) through-thickness strain distributions in the joint at 2.7 kN. Although the image resolution with the high speed camera is lower than the previous analysis, analysing the joint with a high temporal resolution is very important in establishing an understanding of the rapid crack growth behaviour in the joint. These two high spatial and temporal resolution data sets complement each other, providing a reference against which the high rate testing results can be evaluated. Figure 78(a) shows higher axial strain in the constrained adherend on the left compared to the free adherend on the right, identifying the free adherend to be lightly loaded. The axial strain field provides a quantitative visualisation of the differential extension between adherends in the single lap joint due to the different boundary conditions in the free end of the adherend on the right and the highly loaded adherend on the left. As seen in Figure 78b), in the joint the shear strains are greatest in the adhesive layer between adherends at the discontinuity, decreasing rapidly away from the adhesive into the surrounding CSM material. Through-thickness strains shown in Figure 78c), are concentrated in the right hand adherend close to the free end, where load eccentricity is at its greatest, reducing quickly away from the discontinuity.

Figure 79 shows data for an increased load of 3.1 kN; here the through-thickness and shear strain distributions develop into distinct, yet inter-dependent features very similar to those identified in Chapters 6 and 7. Analysis of the shear strains identifies a non-uniform distribution across the thickness of the adhesive layer, generating higher shear strains closer to the interface between the adhesive and the adherend on the right, propagating into the CSM face sheets, Figure 79(b). The through-thickness strain in Figure 79(c) is greatest adjacent to the region of high shear strain at the interface between the adhesive and right hand adherend. The position of these concentrations indicates a coupling between the through-thickness and shear material

responses at the interface resulting from the load transfer across the adhesive into the adherend, similar to that noted in Chapter 4, 6 and 7. The high strain along the interface is comparable to that identified in Chapter 6, which was linked to the initiation and propagation of damage. As per the previous descriptions of the strain fields in Chapters 4, 6 and 7, the load transfer between the adherends can be identified through shear of the adhesive. A greater through-thickness response can be observed as a result of the increased load path eccentricity between the adherends caused by the asymmetry of the joint. This leads to a generation of a large external bending moment which imparts larger through-thickness stresses at the end of the adherends. Subsequently the through-thickness strain field can be clearly identified despite the lower spatial resolution of the images compared to previous chapters.

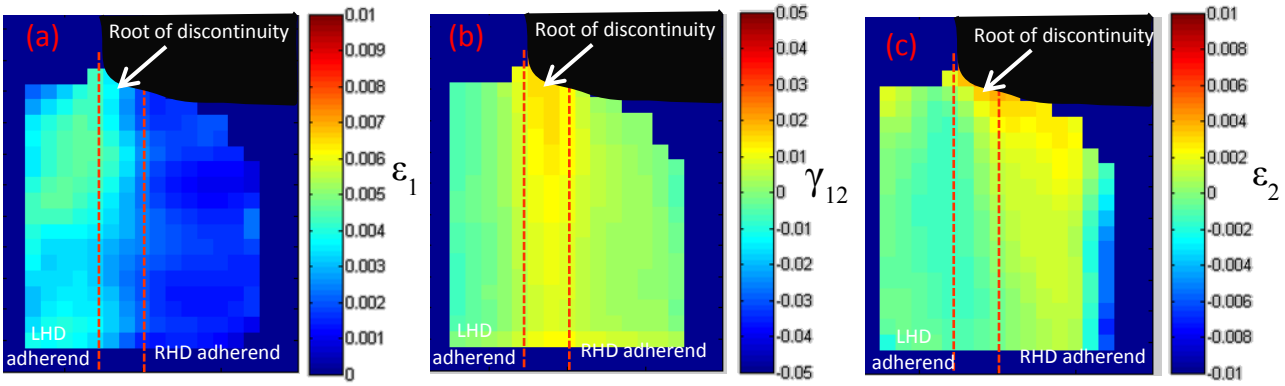

Figure 78: (a) Axial (ε_1) b) Shear (γ_{12}) (c)Through-thickness (ε_2) strain fields developed around the discontinuity at 2.7 kN

The first visual signs of damage in the joint can be observed at 3.1kN from the raw images. A very small 0.13 mm crack forms at the root of the discontinuity at the interface between the adhesive and the left hand, constrained, adherend, close to the white arrowheads in the images. Shear strains in the adhesive layer are 1.8% just prior to the crack initiation. The through-thickness strain is much lower; between 0.15-0.2% and 0.5% axial strain in the left hand adherend. The failure site is located in the left hand adherend, where the local through-thickness and shear strains are lower than along the interface as identified in Figure 76(c). This suggests that the initiation of damage is dominated by through-thickness and not shear strain. The severe geometric discontinuity at this location is also suspected to influence this damage in the high axially loaded adherend.

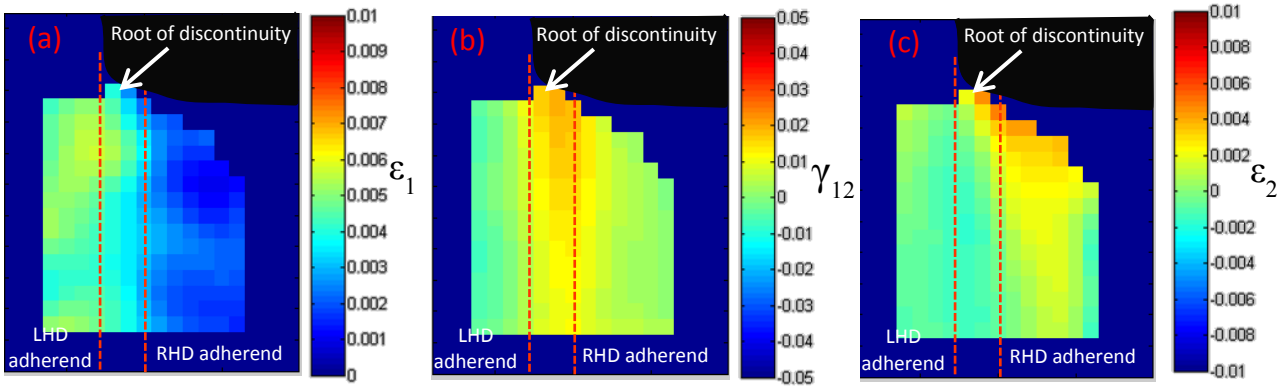

Figure 79: (a) Axial (ε_1) (b) Shear (γ_{12}) (c) Through-thickness (ε_2) strain fields developed around the discontinuity at 3.1 kN

The joint demonstrates significant residual strength and damage tolerance, with the load trace largely unaffected by the steadily growing crack up to a length of 0.4 mm at 4.5 kN Figure 80(a). Shortly after exceeding 4.5 kN a critical crack length is reached and the crack growth becomes rapid and unsteady leading to the final failure of the joint. The evolution of the crack from stable to unstable behaviour is aided by high through-thickness and shear strains which form ahead of the crack tip. These high strains generate micro cracks ahead of the crack tip in the adhesive layer. Above 4.5 kN these micro cracks coalesce, forming a large single crack, rapidly increasing the crack growth speed, up to a maximum crack length of 3.2 mm after which joint failure occurs, as shown in Figure 80(b).

The strain distributions obtained from this investigation form a comprehensive baseline, against which testing at high speed, representative of dynamic marine loading conditions, are evaluated. Full-field analysis of the initiation of damage in adhesively bonded composite joints is not presented in literature with comparable spatial or temporal resolutions. Although the geometry used in this test is very simple, analysis from the high speed DIC show the strain distributions and crack dynamics in the laminate to be very complicated due to the mixed mode loading around the discontinuity.

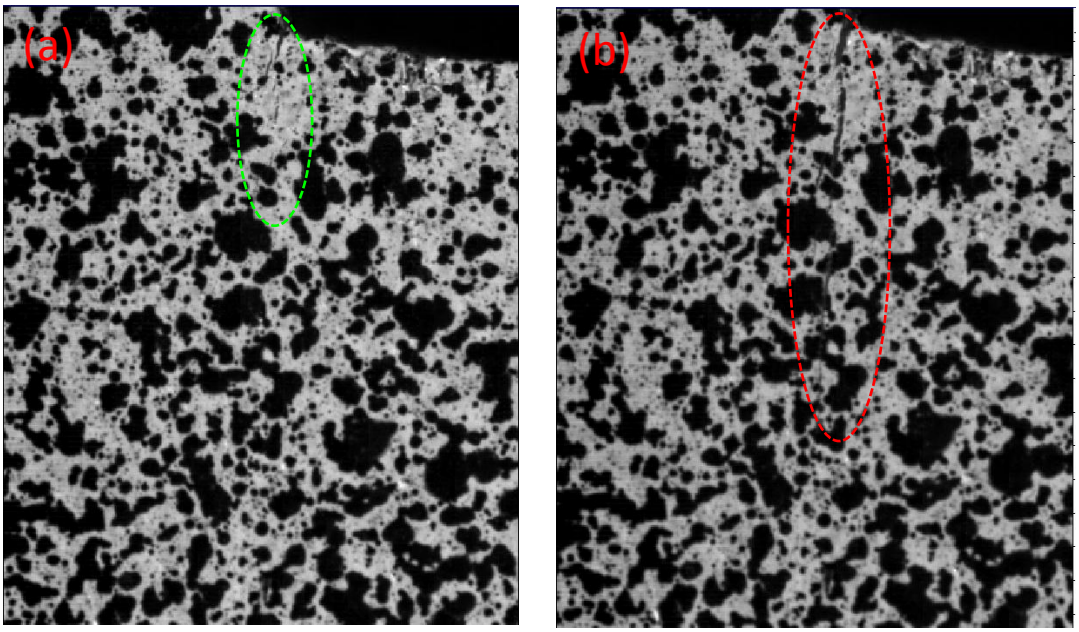

Figure 80: (a) Formation of micro cracks formed ahead of crack tip at 3.8kN (steady crack growth (b) Coalescence of micro cracks at 4.5 kN into single crack (unsteady crack growth)

8.4 SLJ High strain rate analysis

To date, the majority of high strain rate testing of composite materials and bonded components have used a split Hopkinson pressure bar, imparting strain rates of up to 10^4 s^{-1}. Unfortunately, to achieve a constant strain rate loading it is usually the case that test coupon is relatively small, hence limiting the type of structure and material that can be tested. Drop test rigs and Charpy impact test rigs have also been used to assess strain rate sensitivity of adhesively bonded coupons under impact [127] and tension [124], [125], but are only capable of strain rates up to 10 s^{-1}. In this work an Instron VHS 80/20 servo hydraulic test machine, capable of actuator speeds up to 20 m/s, specially adapted for composite materials, is utilised. The geometry of the specimens used in this machine are of similar size as those as defined by British (BS), International (ISO) and American (ASTM) standards at quasi-static rates. The set-up of this machine provides results which are directly comparable between the high speed and quasi-static test cases. There is a large enclosure around the machine allowing good optical access of the specimen with high speed cameras as it is loaded. The machine operates by the controlled single shot release of an oil reservoir held at 280 bar through a control valve. The first 100 mm of the actuator displacement takes place in a hollow ‘slack adapter’ system attached to the bottom of

the specimen, see Figure 81. This allows the acceleration of the actuator up to constant velocity, removing any inertial loading from the specimen. At the end of this initial displacement the actuator engages the end of the slack adapter tube, loading the specimen, as shown in Figure 81. The speed and travel of the actuator allows for testing at strain rates up to approximately $2x10^2$ s^{-1}. The load is measured using a 100 kN Kistler piezo-electric load cell sampled at 3 MHz. A TTL pulse generator is used to synchronise the data and image capture between the test machine and the Photron SA5 high speed camera during the failure event, triggered from the displacement of the slack adapter system just prior to engaging the loading mechanism. A schematic of the data acquisition and synchronisation system can be seen in Figure 82.

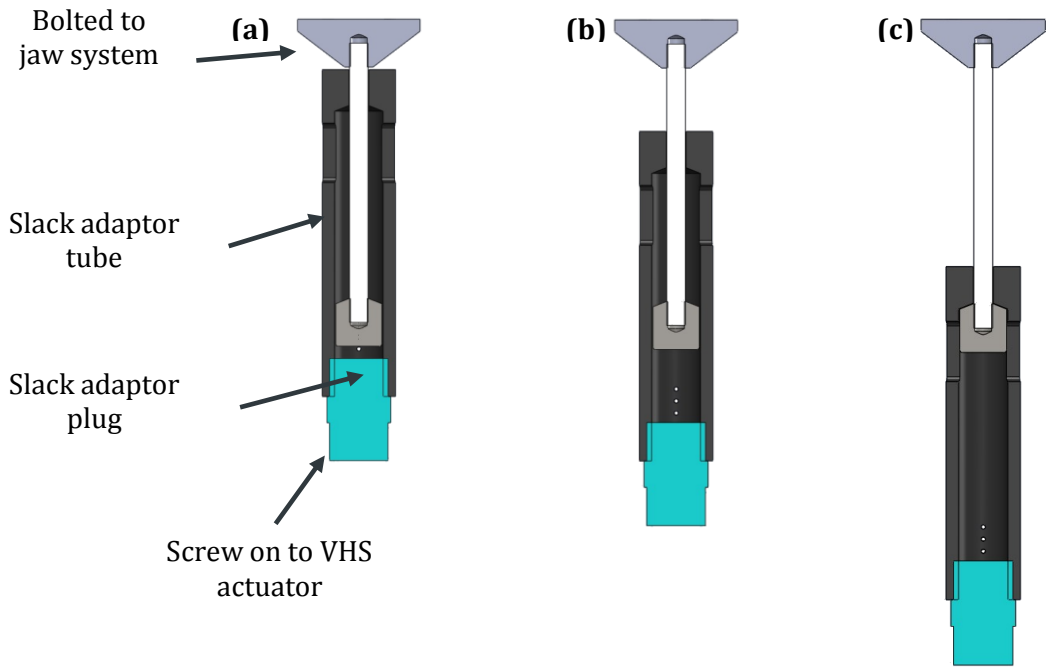

Figure 81: Schematic of the slack adapter system, (a) prior to actuator movement, (b) during acceleration of the actuator, (c) engagement between stack adapter and specimen loading at constant velocity

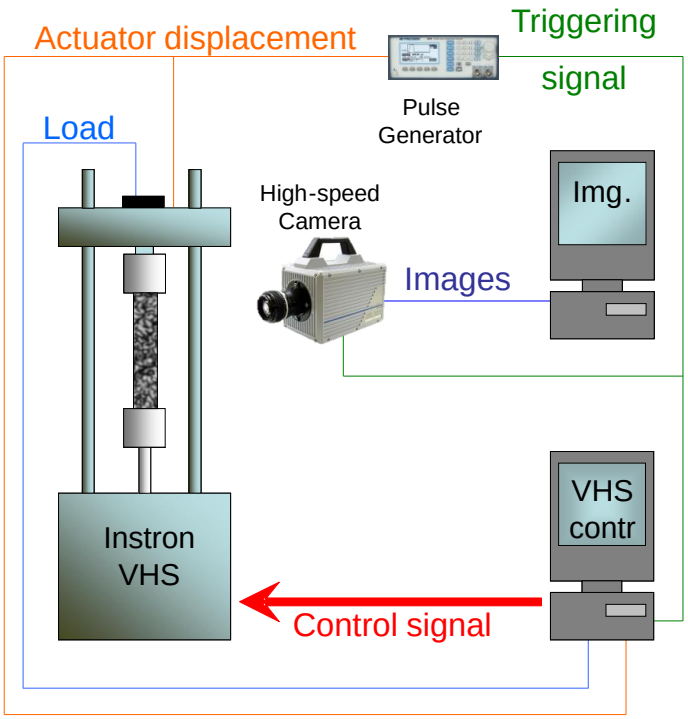

Figure 82: Schematic of the data acquisition and camera synchronisation equipment

High speed testing was conducted with an actuator velocity of 2.5 m/s, which sits in the range of common slamming impact velocities found by Manganelli for a 50 foot racing yacht during a circumnavigation of the globe [112]. At this speed the specimen is loaded at a strain rate of approximately 100 s^{-1} across the overlap length, however locally the strain rate will be much greater. An area measuring 12 mm x 8.9 mm around the root of the discontinuity was imaged using the Photron SA5 camera. Images were recorded with a temporal resolution of 25 kHz and an image resolution of 600 x 448 pixels. The failure of the joint occurs rapidly, approximately 1 millisecond, presenting a significant challenge in observing the development of the strain fields and damage in the joint up to failure, as very few images are recorded during the loading and failure event.

Figure 83 shows the load trace from 4 specimens tested in the Instron VHS machine. The joints load steadily up to 6 kN, above which there are small fluctuations in the load trace associated with the growth of damage up to final failure at 9 kN. The failure load during the quasi-static analysis was 4.5 kN, showing a 100% increase in the failure load of the joints due to the increased loading rate. This is a significant change in joint strength, and is greater than reported previously in similar testing of adhesives [180], composite double butt strap joints [122] or single lap joints [125], which used composite layups with 0^o, 90^o, 45^o and woven $0/90^o$ adherend

face sheets. This suggests that the increase in strength may be due to the behaviour of the CSM face sheet material and its influence on the failure mechanisms in the joint. A noticeable change in the failure surfaces for the joint is observed between the two different loading regimes. At the quasi-static rate the failure surface shows the crack growth to occur along the interface between the adhesive and the composite adherend, with practically no crack growth into the composite adherend, as shown in Figure 84(a). At the elevated loading rate a different failure surface is observed; see Figure 84(b), which shows fibre-tear failure between adherends. This indicates that the crack has grown in the adherend rather than just at the adhesive interface, resulting in the heavily damaged failure surface observed. The consistent and dramatic change in the failure surfaces at the high loading rate suggests a change in the behaviour associated with the increase in ultimate joint strength through greater interaction between the CSM face sheet and the crack front. This crack/fibre interaction is apparent from the variation in the load trace above 5.2 kN in Figure 83, indicating the variable development of damage in the joint.

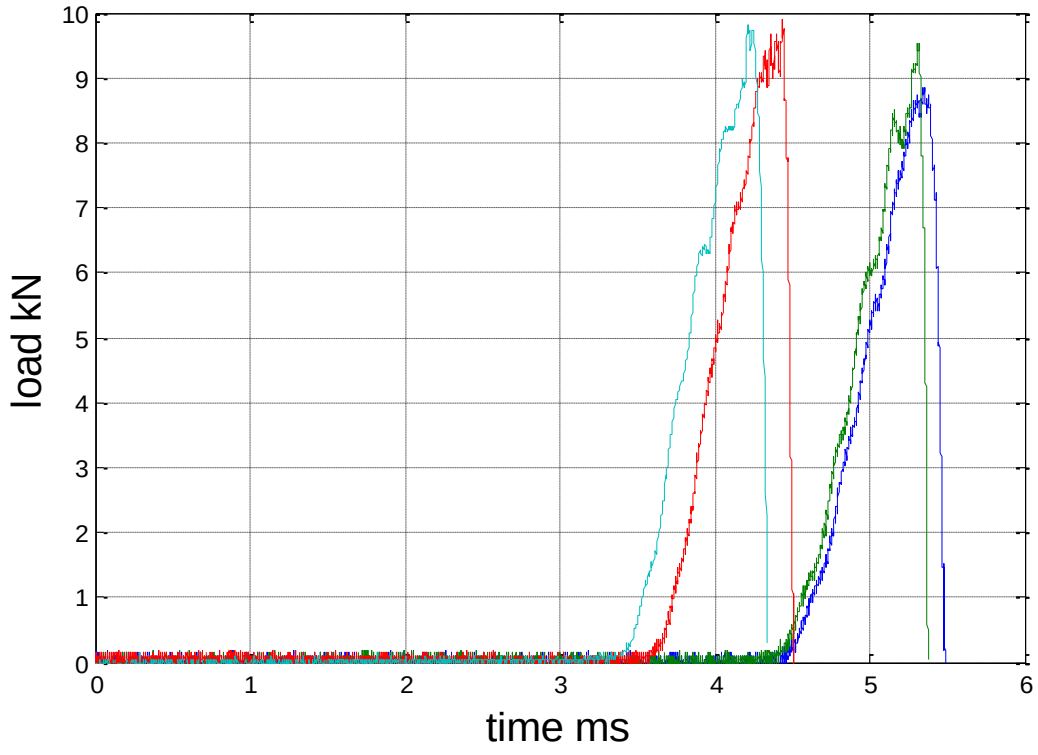

Figure 83: SLJ loading curves at 2.5 m/s

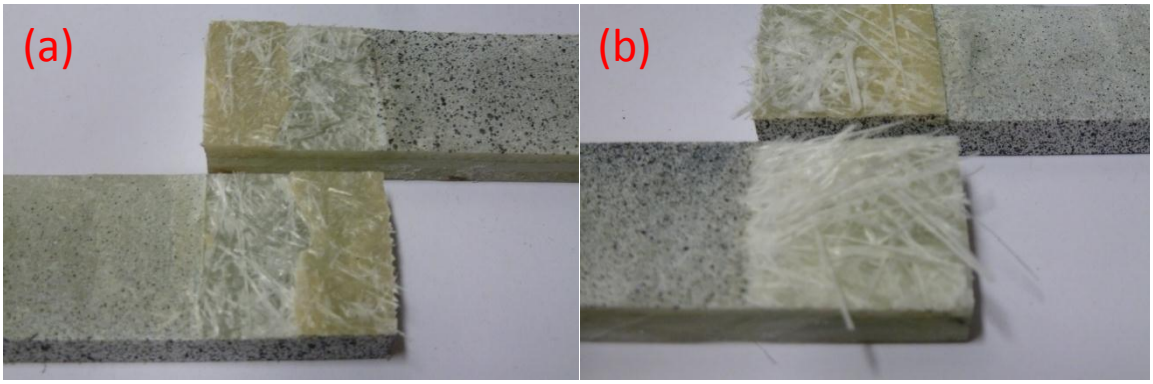

Figure 84: Specimen failure surfaces at (a) 2 mm/min (b) 2.5 m/s

Analysis of the developing strain fields using DIC from the high speed imaging was used to evaluate the behaviour responsible for the changes in joint strength. The high speed images were processed with a subset size of 49 x 49 pixels and a step size of 15 pixels, producing a spatial resolution of 3.3 data points / mm. this produces data with a very similar spatial resolution to that of the magnified quasi-static failure analysis in Figure 78. Inspection of the high speed images, Figure 85, shows damage to occur at the interface between the right hand adherend and the adhesive layer at the root of the discontinuity, the same location in the joint as observed in the quasi-static analysis using the high speed camera. The initial damage occurs very quickly, appearing in less than $1/25000^{th}$ of a second between two images at 4.7 kN and 5.2 kN, which is double the load of that in the quasi-static tests. Figure 86 shows the strain fields in the joint loaded at 4.7 kN, prior to any visual indication of damage in the joint. Prior to the initiation of damage in the joint at approximately 50% of the failure load of the joint, the shear and axial strains next to the discontinuity at high rate are very similar to the strains in the joint at loaded quasi statically at 50% failure load.. At the root of the discontinuity the shear and axial strains reach a maximum of 1.1%, and 0.35% respectively at the interface between the adhesive layer and the right hand adherend. The similarity of the strains prior to damage at quasi-static and high speed loading shows that the initiation of damage is predominantly a strain critical response in the brittle epoxy matrix of the right hand adherend at the root of the discontinuity. This is where the geometric discontinuity is the most severe, and the stress is concentrated locally in the adherend. Very small through-thickness strains, with a low signal to noise ratio are observed, due to the low spatial resolution of the image, resulting in a poor correlation of the through-thickness strains, limiting the analysis of the damage initiation event. As a result, analysis of the principal stresses up to failure using the approach shown in Chapter 6 cannot be confidently obtained.

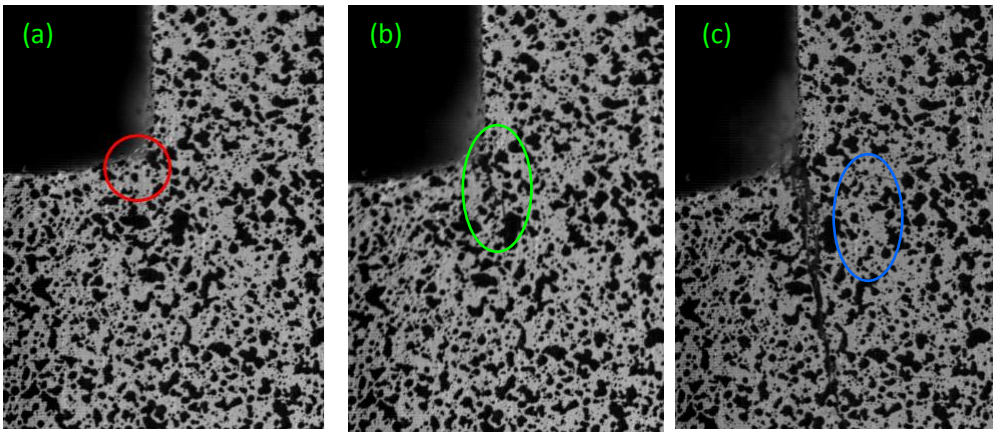

Figure 85 Extracts of the failure sequence at (a) 3.1kN – crack initiation (b) 7.6kN – damage growth at interface (c) 9.7kN – longitudinal cracking in the 90^{o} material prior to final failure

The loading curve in Figure 86 increases to well above 5.2 kN, maintaining significant load carrying capability while damage propagates, up to final failure at 9.7 kN. The strain fields at 8 kN in Figure 87 show high axial strain in the right hand adherend during the propagation of damage in the joint. Axial strain up to 0.65% forms in the undamaged CSM material in the right hand adherend. Transverse cracking of the epoxy matrix is also visible in the 90^{o} fibres in the middle of the adherend due to the high axial strain in the adherend. The axial strains in the CSM material identifies the continued load transfer between adherends in the damaged condition provided by fibre bridging of the CSM layers across the crack front between adherends. This agrees with the heavily damaged failure surfaces, which show fibres pulled out of the adherend aligned parallel to the direction of load. It is suspected that the change in failure surfaces are linked to the viscoelastic behaviour of the epoxy matrix, which experiences a change in the deformation mechanisms due to the high rate of energy input to the material. At high rate this changes to deformation of the electric bonds between atoms from sliding of the polymer molecules. As a result, less deformation is experienced and strengthening of the material occurs. In addition there is a reduction in the energy absorbed by the deformation, which must ultimately be dissipated in the form of greater damage to the material at the failure surfaces. The CSM material appears to have a strong influence in the release of this energy, providing a large number of crack directions in the material.

Testing at high speed shows a large increase in the ultimate strength of the joint due to these viscoelastic effects. Analysis of the strain fields show the initiation of damage to occur at similar strain levels between both loading rates tested; at approximately 50% of the final failure load, exhibiting significant residual strength even when highly damaged The DIC results capture complex strain fields, similar to those seen in Chapter 6, demonstrating significant mixed mode loading and coupled material responses around the discontinuity. As a result, the

strain rate sensitivity of the joint strength cannot be thought of as a single global response, and is instead a function of many different local material and dynamic behaviours in the neighbourhood of the crack-tip. Full analysis of these material and damage mechanics sensitivities ultimately is not possible with the current equipment, due to severe limitations in the spatial and temporal resolutions of the high speed cameras available. Therefore unfortunately, a comprehensive comparison of the material behaviours between loading rates cannot be made.

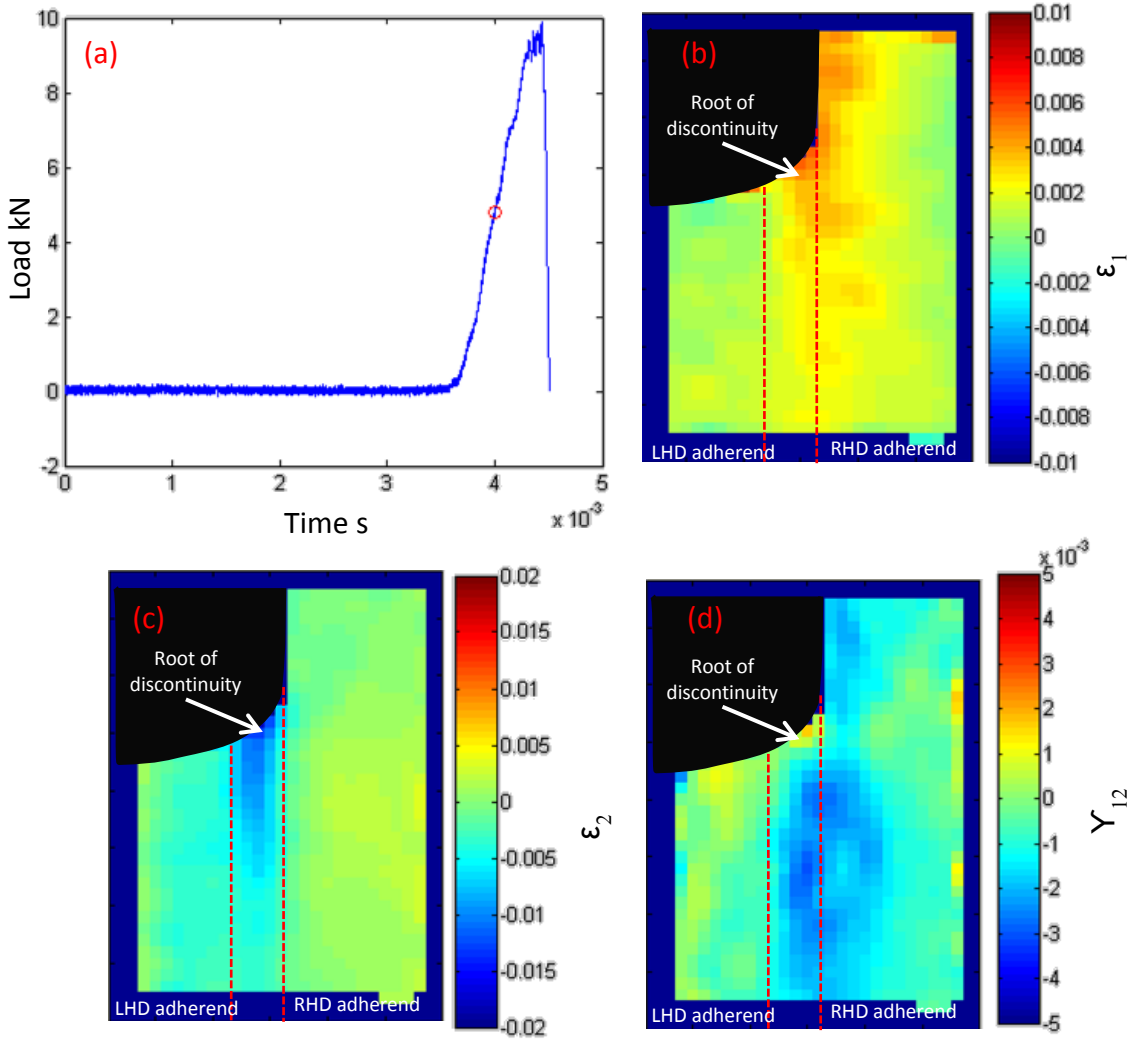

Figure 86: (a) joint loading curve (b)Axial (ε_1) (c)Through-thickness (ε_2) (d) Shear strain (γ_{12}) fields developed around the discontinuity at 4.7 kN

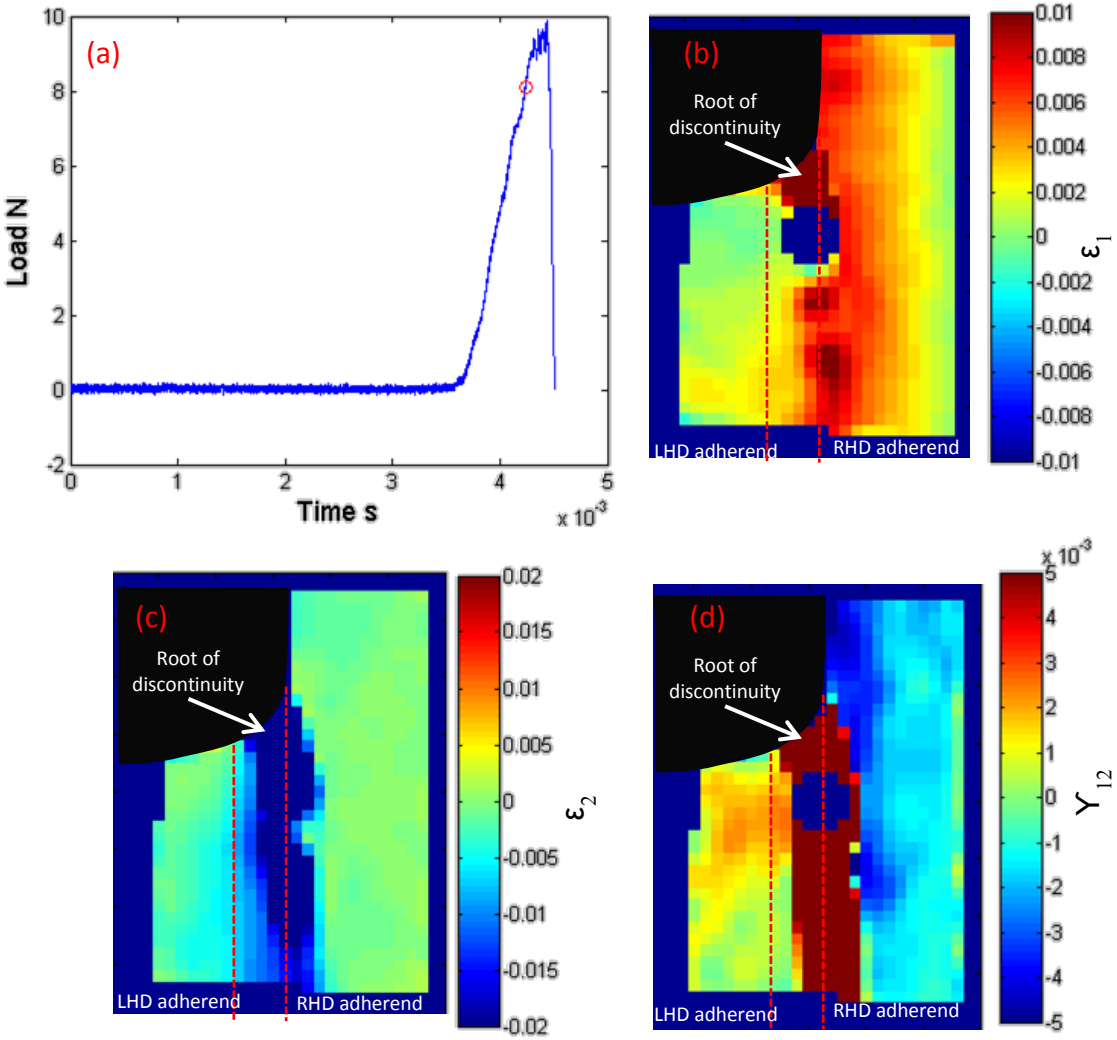

Figure 87 (a) joint loading curve (b)Axial (ε_1) (c)Through-thickness (ε_2) (d) Shear strain (Υ_{12}) fields developed around the discontinuity at 8 kN

8.5 Conclusions

Digital Image Correlation was used to establish the component strain distributions in a composite single lap joint at increasing spatial and temporal resolutions. The joint was tested quasi-statically and at high rate, representative of the dynamic loading often experienced by marine structures. Evaluation of both the global and local strain fields was undertaken during the quasi-static testing, focusing analysis on the root of the discontinuity between adherends. High speed imaging was used to analyse the developing strains fields associated with damage initiation and growth with a high temporal resolution. Significant residual strength is observed

after the initial development of a crack at the root of the discontinuity in the joint at 50% of the final failure load.

Dynamic testing was conducted in an Instron VHS test machine with an actuator velocity of 2.5 m/s, and an approximate strain rate of $100s^{-1}$. The loading and failure of the joint were imaged at 25kHz and analysed using DIC, providing a comparison between the material responses at the different loading conditions. A 100% increase in the failure load of the joint was experienced, identifying significant viscoelastic strengthening of the material. The increase in strength was also attributed to the behaviour of the CSM face sheet material, displaying a change in the interaction between the composite material and the crack front identified from the joint failure surfaces. The initiation of damage occurred at approximately 50% of the failure load showing significant residual strength after the initial development of damage, similar to the quasi static tests. Unfortunately the quality of the DIC data was insufficient to determine the stresses in the joint using the methods in Chapter 8, so a full assessment on the changes in the joint cannot be made. The strain components evaluated prior to failure around the geometric discontinuity were determined to be very similar for both loading conditions, suggesting that the damage initiation to be strain critical at the discontinuity, however this requires further investigation to confirm.

This chapter presents a novel comparison between the material and structural responses at quasi static and high strain rate loading. The DIC experimental technique developed in Chapters 4-7 have been adapted with the use of high speed cameras to provide high temporal and spatial resolution full-field analysis. Unfortunately the results are limited by the currently available high speed hardware, and are unable to analyse the through-thickness strains or principal strain fields up to failure. However, the full-field data clearly shows much greater detail and understanding of the joint behaviour compared to simple global measures, such as failure load or total extension. The complexity of the behaviour identified in the relatively simple single lap joint, demonstrates that the local strain distributions have an important, and often inter-dependent, contribution to the joint strength. This result corresponds with the findings from the previous Chapter's quasi static analysis of the DBSJ. These results therefore show it is vital to investigate the interaction between localised strain features, and the their influence on the initiation of damage in composite structures, using the full-field, data rich experimental approaches; such as those developed in this thesis.

9. Discussion

9.1 Discussion

A wide range of topics have been presented in this thesis, covering the development of full-field experimental methods for the high precision measurement of stresses and strains using optical and infra-red sources at small length scales. These methods have been applied to the analysis of adhesively bonded composite joints, facilitating high resolution analysis of the localised stress and strain distributions responsible for the initiation of damage and failure. A schematic of the workflow in this thesis can be seen in Figure 88 identifying the connections between the work in order to develop confidence and fidelity in the experimental methods. In order to revisit the impact of this research and comment upon its potential beneficiaries an overview of the research is presented alongside a discussion of the most important results.

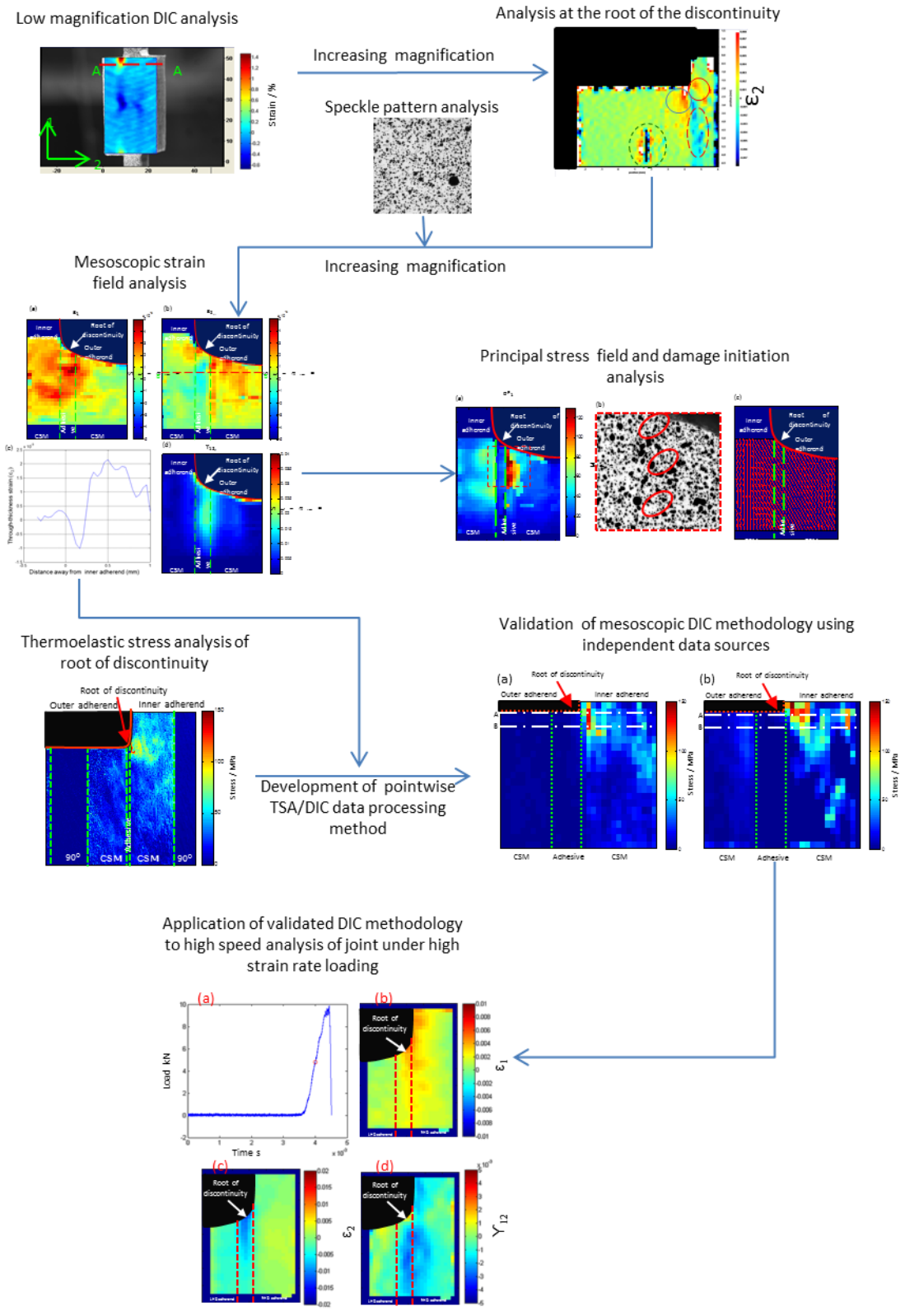

Figure 88: Flowchart of work covered in thesis

9.1.1 Application of full-field methods to deformation and strain measurement of adhesively bonded joints

Digital Image Correlation provided quantitative evaluations of the individual strain components in adhesively bonded composite double butt strap and single lap joints loaded up to failure. The DIC analysis provides detailed full-field depictions of the strain distributions in the joint, which would not be observed using point measurement methods such as electrical resistance strain gauges. From this data high resolution measurements across the whole joint face and locally round the root of the discontinuity were provided. The work presented in this thesis demonstrates that the non-contact DIC technique is a fast, convenient and powerful method for generating informative, data-rich analysis of complex structures under load.

Applying the technique to the analysis of strains in an adhesively bonded composite joint, where the strain responses in the through-thickness direction are low, has pushed the capability of the method outside of its usual operating range. Significant experimental challenges were faced in achieving high levels of both strain accuracy and spatial resolution. High magnification optics were utilised to increase the pixels / mm resolution of the image at the expense of reducing the size of the field of view. Using this approach DIC analysis was conducted on an area measuring 3.1 mm x 2.6 mm around the root of the discontinuity between the inner and outer adherends in the joint. This location was identified as being critical for damage initiation arising from the sharp geometric discontinuity between the adherends and the high localised through-thickness stresses in the outer adherend. The high magnification images have enabled detailed identification of the strain distribution around the discontinuity. Experimental data of this detail has not been available for complex composite structures loaded to failure.

Comparable levels of spatial resolution and strain precision as demonstrated in the thesis have been possible using interferometric techniques such as Moiré and digital speckle patter interferometry. These techniques breakdown with large displacements and it would be impossible to observe the behaviour to failure as is done in the present work. Furthermore such techniques are expensive and cumbersome requiring surface gratings to be applied and the use of optical tables with specialised loading equipment to minimise the effect of vibration sources. However the use of high magnification DIC on the adhesive joints demonstrates that an effective methodology has been developed that can be used with confidence to accurately analyse complex small scale behaviour. Importantly relatively inexpensive and quick to set up equipment are used in the technique in addition to standard test machines. The new method has significant benefits for those interested in conducting analysis of complex structures at small length scales such as around areas of geometric discontinuity from where damage and failure are most likely to initiate.

Complementing the development of the high magnification DIC technique, research was undertaken on the influence of the speckle pattern on DIC measurement error. Assessment of the quality of the applied speckle pattern is an important consideration when undertaking DIC as the displacement measurements extracted from the correlation are directly derived from the spatial information contained within the deforming speckle pattern. The appearance of the speckle pattern under high magnification is fundamentally different and more sparsely populated compared to lower magnifications, limiting its

spatial content. The analysis showed, under high magnification, that patterns with black speckles on a white background produced by an airbrush were most suitable for high magnification DIC resulting in the lowest measurement uncertainty. This investigation removes one of the 'unknowns' associated with the DIC measurement process, providing the user with an image processing based toolset to determine pattern quality. The methodology was shown to be an informative and versatile local measure of pattern properties. It is not only applicable to high magnification images, but can be applied to wide range of patterns and resolutions determining the relative differences between application methods and styles. The work provides users of DIC, at both low and high magnification, confidence that their choice and/or application of speckle pattern is of appropriate quality to minimise errors in their measurements.

A method was also established to manipulate the full-field strain data into component and principal stress distributions in the structure. Although possible with the all DIC set-ups, the component strains are not normally manipulated into stresses as this requires a detailed knowledge of the material elastic properties. In the present work where the component is made up from layers of orthotropic (UD) and quasi isotropic (CSM) materials knowledge of eight elastic constants were required. These were all derived experimentally and in the case of the through-thickness behaviour required the construction of a novel testing approach (see chapter 3). Once the component stresses have been obtained then the principal stresses can be derived. These provided an important part of the quantitative analysis of the adhesive joint behaviour by linking the collected strain data to the failure occurring in the structure. The principal stress analysis of the DBSJ identified the interface between the adhesive layer and the outer adherend as a critical damage initiation location, showing that at a maximum stress of 115 MPa damage is initiated. Evaluation of the principal stresses clearly identifies areas of damage evolution not concisely identified from assessing the strain fields. The data processing routines generated to manipulate the strain fields is very simple and can be easily applied ubiquitously to the analysis of all structural problems using any full-field strain measurement method such as Moiré interferometry, the grid method and electronic speckle pattern interferometry.

9.1.2 Evaluation of complex composite structures using Thermoelastic Stress Analysis and the validation of full-field data

Analysis of the DBSJ in this thesis was also conducted using Thermoelastic Stress Analysis, eliciting a stress metric related to the sum of the principal stresses from the measured temperature change during cyclic loading of the specimen. In previous TSA studies on orthotropic materials an assumption has been made that the principal stress directions and principal material directions are coincident. This is satisfactory where components are subjected to axial loads and do not contain significant discontinuities. Towards the interior of the joints this methodology would apply but at the discontinuity in the joint and at the interface of the bond the principal stress directions are not coincident with the principal material directions. Until now this has represented a significant shortcoming in applying TSA to complex structures and its use as a validation tool for numerical models. It is usually the case that the thermoelastic

constants are established in the principal material directions as these are known. The principal stress directions are not known for a general component. Hence it is necessary to transform the thermoelastic constant to the principal stress axes to make a meaningful quantitative analysis. The difficulty is knowing the transformation angle, here this can be obtained from the DIC. Therefore a new means of interpreting thermoelastic data was established by transforming the thermoelastic constant in the principal material directions to the principal stress direction on a point by point basis so that the data could be calibrated into a principal stress metric. The analysis approach is a valuable addition to the experimental mechanics community's toolbox. It is strongly recommended that this methodology is adopted by users of TSA for analysis of orthotropic composite structures, as small changes in the principal stress direction away from the principal material axes can yield large changes and inaccuracies in the measured stress metric. This approach should not only be considered for analyses at small scales, but to all situations where geometry or loading may result in the principal stress directions not lying coincidental to the principal material directions.

The TSA stress metric also provides an independent experimental means of validating the high magnification DIC methodology and strain results. It is very important to validate the DIC data as the approach with a single camera is highly susceptible to parasitic effects arising from out of plane displacement. As TSA is not a kinematic technique, out of plane displacements have little or no effect on the data. Therefore a technique was developed to manipulate the full-field DIC strain data analysis of the composite DBSJ into the same stress metric form as that provided by the TSA. It was considered that this would provide a validation of the DIC experimental methods and results, even though it was necessary to use the DIC data to obtain the principal stress directions for the TSA. Good agreement between the stress metrics obtained from each technique around the root of the discontinuity was established hence providing confidence in the DIC strain data and the mesoscopic analysis methodology. It should be considered that this method of validation was the only method that could be used to validate the DIC results. This is due to the small length scales and high stress / strain gradients present across the field of view, which would be inadequately captured using traditional contact approaches such as strain gauges.

This technique provides a useful vehicle against which full-field experimental strain data from sources such as DIC, the grid method or Moiré interferometry can be quantitatively compared against independent infra-red temperature measurements, delivering a very high degree of confidence in any analysis. The methodology can be applied to a wide range of engineering components, particularly where safety is a primary concern and hence a need for validation and certainty in the quality of the measured results. Although developed for orthotropic composite materials the methodology is equally suited to analysis of metallic components; here the analysis would be significantly simplified as the principal stresses are not coupled with the coefficient of thermal expansion and hence the stress metric can be directly obtained without a knowledge of the principal stress directions. The experimental validation methodology has provided an important route for more quantitative DIC studies of geometries with complex strain distributions. The approach described in the thesis has provided a new means of assessing the accuracy of the DIC data obtained from specimens with extremely high strain gradients and investigating the effect of the spatial resolution on the data.

9.1.3 Investigation of strain fields in an adhesive joint under high strain rate loading

The knowledge gained from the development of the high magnification DIC methodologies was used to establish an experimental approach to evaluate the component strain distributions in a composite single lap joint at high strain rate. Dynamic testing was conducted in an Instron VHS test machine with an actuator velocity of 2.5 m/s, and an approximate strain rate of 100 s^{-1}. Significant residual strength is observed after the initial development of a crack at the root of the discontinuity in the joint at 50% of the final failure load and a 100% increase in the failure load of the joint was experienced at high rate compared to comparable quasi static testing. The loading and failure of the joint around the root of the discontinuity between adherends were imaged at 25 kHz and analysed using DIC, providing a comparison between the material responses at the different loading conditions. Strain critical failure behaviour was observed between the tests, with the specimens failing at similar strain levels but very different loads indicating a change in the material response at higher strain rates.

The application of DIC at high strain rates has been reported in literature where high speed cameras are used in areas such as blast analysis and high strain rate coupon testing, however quantitative evaluations of strain at high strain rates are few and application of high speed DIC to complex structures such as adhesively bonded joints practically unknown. The novelty in this part of the work is therefore the combination of the high speed imaging and the high resolution DIC methodology described above to obtain quantitative strain data from complex assemblies. The high strain rate investigation in this thesis demonstrates the importance of the recent advances in camera hardware and test machines. However, the work pushes the capability of current technologies, managing the dependencies between spatial resolution, temporal resolution and strain precision. The use of the magnifying optics substitutes the need for cameras with larger sensor architectures which are prohibitively expensive. Here it is clearly demonstrated that quantitative high speed analysis of the strain evolutions under high speed load application can be achieved. To date work has focused on averaging across an area of uniform strain in, for example, a strip loaded in tension. The present initial work has shown that complex assemblies can be assessed which will pave the way for more detailed analyses using the methodologies established in the thesis.

10. Conclusions and Future work

10.1 Conclusions

The overarching objective of this research has been to develop full-field experimental methodologies to evaluate the local stress and strain distributions in adhesively bonded composite joints under quasi static and high strain rate loading. A coherent narrative has been conveyed through each Chapter, building towards the maturity of a high magnification 2D DIC experimental technique. The main conclusions of the thesis can be summarised as follows

- All of the objectives set in Chapter 1 have been met through the analysis presented in Chapters 3-8.
- A high fidelity, high resolution DIC measurement technique, capable of confidently analysing small, yet critical, local strain concentrations in an adhesively bonded composite joint has been established.
- Sources of error in the high magnification DIC methodology were examined, and in particular the influence of the speckle pattern appearance.
- A method for the manipulation of the strain data was developed to analyse the material and principal stresses in the joint under load presenting a concise evaluation of the initiation of damage in the structure.
- The proficiency of the mesoscopic DIC technique was shown through a full validation of the white light DIC data against independent infra-red measurements using TSA.
- A novel and highly important point-wise processing methodology was created for analysis of the TSA data; transforming the thermoelastic constants from the principal material to principal stress directions.
- The developed DIC methodology was applied to analyse the response of the single lap joint during high strain rate loading, providing unprecedented full-field measurement of the transpiring strain fields up to failure.

10.2 Future work

The research presented in this thesis has resulted in the development of, robust and accurate experimental methodologies for the analysis of complex composite structures. The quality of the analysis has been very high; however the analysis is not directly transferable into new joint designs due to the contrived joint geometry which was used. An area of future work which should be investigated is the application of the DIC technique to the analysis of representative adhesively bonded sub-component assemblies, such as top hat stiffeners and panel ribs. This will allow the knowledge transfer from the in-depth studies of this thesis to practical applications and recommendations for engineers.

The technique may also be applied to analyse the effect of parameters such as bondline thickness, adherend geometry and overlap length, which are usually investigated using global measures such as ultimate failure load with little quantitative understanding of the changes in joint response. Running in parallel with this work is the extension of the validated 2D FE model to refine the analysis of the principal stresses in the joint prior to damage initiation. The model may also be confidently used as a highly informative platform to perform geometry optimisation as part of a joint design tool for engineers. Good agreement is seen between the numerical and experimental results at 6 kN prior to damage formation. The FE mode however does not represent any local material inhomogeneity, and therefore may be incapable of evaluating the highly localised stresses responsible for the initiation of damage. Further work to develop the damage modelling capability of the model would be highly beneficial.

Finally, an area which showed great potential, and also the greatest current limitations, is the analysis of the strain fields during dynamic loading. The application of this technique to adhesively bonded joints has never been attempted before, generating very new and interesting results. Ideally similar steps to investigate a range of geometries and joint types could be undertaken. However the capability of the high speed analysis is severely limited by the current high speed camera technology due to the interdependencies between temporal resolution, spatial resolution and strain accuracy. Only when the camera hardware is improved, and the cost reduced will accurate, high resolution testing become a possibility.

11. References

[1] G. Marsh, "Marine composites — drawbacks and successes," *Reinforced Plastics*, vol. 54, no. 4, pp. 18–22, Jul. 2010.

[2] L. Dokos, "Adoption of marine composites – a global perspective," *Reinforced Plastics*, vol. 57, no. 3, pp. 30–32, May 2013.

[3] P. Goubalt and S. Mayes, "Comparative Analysis of Metal and Composite Materials for the Primary Structures of a Patrol Craft," *Naval Engineers Journal*, vol. 108, no. 3, pp. 387–397, 1996.

[4] BYMNews, "Wally 143 under construction," 2006. [Online]. Available: http://www.bymnews.com/photos/displayimage.php?album=156&pos=124.

[5] I. Daniel and O. Ishai, *Engineering Mechanics of Composite Materials*. Oxford University Press, 2005.

[6] J.-L. Tsai, B.-H. Huang, and Y.-L. Cheng, "Enhancing Fracture Toughness of Glass/Epoxy Composites by Using Rubber Particles Together with Silica Nanoparticles," *Journal of Composite Materials*, vol. 43, no. 25, pp. 3107–3123, Sep. 2009.

[7] C. Mahieux, "Ductility versus Brittleness," in *Environmental Degradation of Industrial Composites*, 1st ed., Oxford: Elsevier, 2005, pp. 22–23.

[8] M. D. Banea and L. F. M. da Silva, "Adhesively bonded joints in composite materials: an overview," *Proceedings of the Institution of Mechanical Engineers, Part L: Journal of Materials: Design and Applications*, vol. 223, no. 1, pp. 1–18, Jan. 2009.

[9] C. Borsellino, L. Calabrese, G. Di Bella, and A. Valenza, "Comparisons of processing and strength properties of two adhesive systems for composite joints," *International Journal of Adhesion and Adhesives*, vol. 27, no. 6, pp. 446–457, 2007.

[10] H. K. Lee, S. H. Pyo, and B. R. Kim, "On joint strengths, peel stresses and failure modes in adhesively bonded double-strap and supported single-lap GFRP joints," *Composite Structures*, vol. 87, no. 1, pp. 44–54, 2009.

[11] L. da Silva and R. D Adams, "Techniques to reduce the peel stresses in adhesive joints with composites," *International Journal of Adhesion and Adhesives*, vol. 27, no. 3, pp. 227–235, Apr. 2007.

[12] P. D. Ruiz, F. Jumbo, J. M. Huntley, I. A. Ashcroft, and G. M. Swallowe, "Experimental and Numerical Investigation of Strain Distributions Within the Adhesive Layer in Bonded Joints," *Strain*, vol. 47, no. 1, pp. 88–104, Feb. 2011.

[13] M. Y. Tsai, J. Morton, and F. L. Matthews, "Experimental and Numerical Studies of a Laminated Composite Single-Lap Adhesive Joint," *Journal of Composite Materials*, vol. 29, no. 9, pp. 1254–1275, Jun. 1995.

[14] B. A. Brent and S. Brigham, “Joining composite materials - Mechanical or Adhevise?” [Online]. Available: http://strong.groups.et.byu.net/pages/articles/articles/joining2.pdf. [Accessed: 28-Jan-2013].

[15] S. D. Thoppul, J. Finegan, and R. F. Gibson, “Mechanics of mechanically fastened joints in polymer-matrix composite structures - A review,” *Composites Science and Technology*, vol. 69, no. 3–4, pp. 301–329, 2009.

[16] R. W. Messler, “The challenges for joining to keep pace with advancing materials and designs,” *Materials and Design*, vol. 16, pp. 261–269.

[17] BYMNews, “‘Hydroptère’ construction - torsional stiffener,” 2007. [Online]. Available: http://www.bymnews.com/photos/displayimage.php?album=422&pos=456.

[18] F. Campbell, *Structural Composite Materials*. ASM International, 2010, pp. 449–451.

[19] W. S. Chan and S. Vedhagiri, “Analysis of Composite Bonded/Bolted Joints Used in Repairing,” *Journal of Composite Materials*, vol. 35, no. 12, pp. 1045–1061, Jun. 2001.

[20] O. Jacobs, K. Friedrich, and K. Schulte, “Fretting fatigue of continuous carbon fibre reinforced polymer composites,” *Wear*, vol. 145, no. 1, pp. 167–188, Apr. 1991.

[21] M. A. McCarthy, V. P. Lawlor, W. F. Stanley, and C. T. McCarthy, “Bolt-hole clearance effects and strength criteria in single-bolt, single-lap, composite bolted joints,” *Composites Science and Technology*, vol. 62, pp. 1415–1431.

[22] G. J. Turvey and P. Wang, “Failure of pultruded GRP single-bolt tension joints under hot-wet conditions,” *Composite Structures*, vol. 77, no. 4, pp. 514–520, Feb. 2007.

[23] B. K. Parida, R. V Prakash, P. D. Mangalgiri, and V. K., “Influence of environmental and geometric parameters on the behavior of fastener joints in advanced composites,” *ASTM Special Technical Publication*, vol. 1285, pp. 432–451, 1997.

[24] A. J. Kinloch, *Adhesion and adhesives*. Chapman and Hall, London, 1987.

[25] “www.ami.ac.uk/courses/topics/0206_adh/images/fc_adh_imga.gif.” .

[26] O. Volkersen, “Die Nietkraftverteilung in zugbeanspruchten Nietverbindungen mit konstanten Laschenquerschnitten,” *Luftfahrtforschung*, vol. 15, pp. 41–47, 1938.

[27] L. F. M. da Silva, P. J. C. das Neves, R. D. Adams, and J. K. Spelt, “Analytical models of adhesively bonded joints--Part I: Literature survey,” *International Journal of Adhesion and Adhesives*, vol. 29, no. 3, pp. 319–330, 2009.

[28] M. Goland and E. Reissner, “The stresses in cemented joints,” *Journal of Applied Mechanics*, vol. 11, pp. 17–27, 1944.

[29] W. J. Renton and J. R. Vinson, “The Efficient Design of Adhesive Bonded Joints,” *The Journal of Adhesion*, vol. 7, no. 3, pp. 175–193, 1975.

[30] D. J. Allman, “Theory for elastic stresses in adhesive bonded lap joints,” *Quarterly Journal of Mechanics and Applied Mathematics*, vol. 30, pp. 415–436, 1977.

[31] F. Mortensen and O. T. Thomsen, “Analysis of adhesive bonded joints: a unified approach,” *Composites Science and Technology*, vol. 62, no. 7–8, pp. 1011–1031, 2002.

[32] C. Yang and S.-S. Pang, “Stress-Strain Analysis of Single-Lap Composite Joints Under Tension,” *Journal of Engineering Materials and Technology*, vol. 118, no. 2, p. 247, 1996.

[33] A. R. Rispler, L. Tong, G. P. Steven, and M. R. Wisnom, “Shape optimisation of adhesive fillets,” *International Journal of Adhesion and Adhesives*, vol. 20, no. 3, pp. 221–231, 2000.

[34] S. W. Boyd, J. I. R. Blake, R. A. Shenoi, and J. Mawella, “Optimisation of steel-composite connections for structural marine applications,” *Composites Part B: Engineering*, vol. 39, no. 5, pp. 891–906, Jul. 2008.

[35] G. Belingardi, L. Goglio, and A. Tarditi, “Investigating the effect of spew and chamfer size on the stresses in metal/plastics adhesive joints,” *International Journal of Adhesion and Adhesives*, vol. 22, no. 4, pp. 273–282, 2002.

[36] A. E. Bogdanovich and I. Kizhakkethara, “Three-dimensional finite element analysis of double-lap composite adhesive bonded joint using submodeling approach,” *Composites Part B: Engineering*, vol. 30, no. 6, pp. 537–551, 1999.

[37] R. Kaye and M. Heller, “Through-thickness shape optimisation of typical double lap-joints including effects of differential thermal contraction during curing,” *International Journal of Adhesion and Adhesives*, vol. 25, no. 3, pp. 227–238, Jun. 2005.

[38] L. F. M. da Silva and R. D. S. G. Campilho, *Advances in Numerical Modeling of Adhesive Joints*. Berlin, Heidelberg: Springer Berlin Heidelberg, 2012.

[39] X. He, “A review of finite element analysis of adhesively bonded joints,” *International Journal of Adhesion and Adhesives*, vol. 31, no. 4, pp. 248–264, Jun. 2011.

[40] P. Ruiz, F. Jumbo, A. Seaton, J. Huntley, I. Ashcroft, and G. Swallowe, “Numerical and experimental investigation of three-dimensional strains in adhesively bonded joints,” *The Journal of Strain Analysis for Engineering Design*, vol. 41, no. 8, pp. 583–596, Jan. 2006.

[41] R. Haghani, “Analysis of adhesive joints used to bond FRP laminates to steel members – A numerical and experimental study,” *Construction and Building Materials*, vol. 24, no. 11, pp. 2243–2251, Nov. 2010.

[42] H. J. Phillips, R. A. Shenoi, and C. E. Moss, “Damage mechanics of top-hat stiffeners used in FRP ship construction,” *Marine Structures*, vol. 12, no. 1, pp. 1–19, Jan. 1999.

[43] B. G. Prusty, D. W. Kelly, D. Lyons, and G. D. Peng, “Top hat stiffeners: A study on keel failures,” *Ocean Engineering*, vol. 37, no. 13, pp. 1180–1192, Sep. 2010.

[44] B. G. Prusty and D. W. Kelly, “Delamination failure of composite top-hat stiffeners using finite element analysis,” *Proceedings of the Institution of Mechanical Engineers, Part M: Journal of Engineering for the Maritime Environment*, vol. 227, no. 1, pp. 61–80, Sep. 2012.

[45] I. Herszberg, H. C. H. Li, F. Dharmawan, A. P. Mouritz, M. Nguyen, and J. Bayandor, "Damage assessment and monitoring of composite ship joints," *Composite Structures*, vol. 67, no. 2, pp. 205–216, Feb. 2005.

[46] F. Dharmawan, R. S. Thomson, H. Li, I. Herszberg, and E. Gellert, "Geometry and damage effects in a composite marine T-joint," *Composite Structures*, vol. 66, no. 1–4, pp. 181–187, 2004.

[47] H. J. Phillips and R. A. Shenoi, "Damage tolerance of laminated tee joints in FRP structures," *Composites Part A: Applied Science and Manufacturing*, vol. 29, no. 4, pp. 465–478, Jan. 1998.

[48] T. Keller and T. Vallée, "Adhesively bonded lap joints from pultruded GFRP profiles. Part I: stress-strain analysis and failure modes," *Composites Part B: Engineering*, vol. 36, no. 4, pp. 331–340, 2005.

[49] M. Davis and D. Bond, "Principles and practices of adhesive bonded structural joints and repairs," *International Journal of Adhesion and Adhesives*, vol. 19, pp. 91–105.

[50] F. Fassio and S. Santini, "Tensile tests on bonded double-strap joints between pultruded GFRP profiles," *Construction*, no. Bbfs, pp. 141–148, 2005.

[51] J. De Castro and T. Keller, "Design of robust and ductile FRP structures incorporating ductile adhesive joints," *Composites Part B: Engineering*, vol. 41, no. 2, pp. 148–156, Mar. 2010.

[52] M. Qin and Y. A. Dzenis, "Analysis of single lap adhesive composite joints with delaminated adherends," *Composites Part B: Engineering*, vol. 34, no. 2, pp. 167–173, 2003.

[53] K.-S. Kim, Y.-M. Yi, G.-R. Cho, and C.-G. Kim, "Failure prediction and strength improvement of uni-directional composite single lap bonded joints," *Composite Structures*, vol. 82, no. 4, pp. 513–520, 2008.

[54] H. Murayama, K. Kageyama, K. Uzawa, K. Ohara, and H. Igawa, "Strain monitoring of a single-lap joint with embedded fiber-optic distributed sensors," *Structural Health Monitoring*, vol. 11, no. 3, pp. 325–344, Sep. 2011.

[55] J. Palaniappan, S. L. Ogin, A. M. Thorne, G. T. Reed, A. D. Crocombe, T. F. Capell, S. C. Tjin, and L. Mohanty, "Disbond growth detection in composite–composite single-lap joints using chirped FBG sensors," *Composites Science and Technology*, vol. 68, no. 12, pp. 2410–2417, Sep. 2008.

[56] T. F. Capell, J. Palaniappan, S. L. Ogin, A. D. Crocombe, G. T. Reed, A. M. Thorne, L. Mohanty, and S. C. Tjin, "The use of an embedded chirped fibre Bragg grating sensor to monitor disbond initiation and growth in adhesively bonded composite/metal single lap joints," *Journal of Optics A: Pure and Applied Optics*, vol. 9, no. 6, pp. S40–S44, Jun. 2007.

[57] R. Jones and S. Galea, "Health monitoring of composite repairs and joints using optical fibres," *Composite Structures*, vol. 58, no. 3, pp. 397–403, Nov. 2002.

[58] P. Rastogi and E. Hack, *Optical Methods for Solid Mechanics: A Full-Field Approach*. John Wiley & Sons, 2012.

[59] M. Grediac and F. Hild, *Full-Field Measurements and Identification in Solid Mechanics*. John Wiley & Sons, 2012.

[60] M. Viveiros and Z. C. Lin, "Comparison of a Video Extensometer Over a Clip-on Extensometer and Crosshead Motion as a Strain Measurement Technique for Testing Nitinol Specimens," in *Proceedings of the 2006 International Conference on Shape Memory and Superelastic Technology,*, 2006.

[61] J. de Castro and T. Keller, "Ductile double-lap joints from brittle GFRP laminates and ductile adhesives, Part I: Experimental investigation," *Composites Part B: Engineering*, vol. 39, no. 2, pp. 271–281, 2008.

[62] Y. Zhang, A. P. Vassilopoulos, and T. Keller, "Mode I and II fracture behavior of adhesively-bonded pultruded composite joints," *Engineering Fracture Mechanics*, vol. 77, no. 1, pp. 128–143, Jan. 2010.

[63] C. W. Chang, H. S. Lien, and J. H. Lin, "Determination of reflection photoelasticity fringes analysis with digital image-discrete processing," *Measurement*, vol. 41, no. 8, pp. 862–869, Oct. 2008.

[64] E. A. Patterson, "Digital Photoelasticity: Principles, Practice and Potential," *Strain*, vol. 38, no. 1, pp. 27–39, 2002.

[65] Z. Lei, H. Yun, Y. Zhao, Y. Xing, and X. Pan, "Study of shear transfer in Al/epoxy joint by digital photoelasticity," *Optics and Lasers in Engineering*, vol. 47, no. 6, pp. 701–707, Jun. 2009.

[66] E. Sancaktar and P. O. Lawry, "A Photoelastic Study of the Stress Distribution in Adhesively Bonded Joints with Prebent Adherends," *The Journal of Adhesion*, vol. 11, no. 3, pp. 233–241, Jan. 1980.

[67] C. L. Chow and C. W. Woo, "Photoelastic Determination of Flaw Size and Distribution Effects on Adhesively Bonded Lap Joints," *The Journal of Adhesion*, vol. 19, no. 2, pp. 89–111, Jan. 1986.

[68] B. Pan, "Recent Progress in Digital Image Correlation," *Experimental Mechanics*, Nov. 2010.

[69] M. A. Sutton, J.-J. Orteu, and H. W. Schreier, *Image Correlation for Shape, Motion and Deformation Measurements: Basic Concepts,Theory and Applications*. 2009.

[70] B. Pan, K. Qian, H. Xie, and A. Asundi, "Two-dimensional digital image correlation for in-plane displacement and strain measurement: a review," *Measurement Science and Technology*, vol. 20, no. 6, p. 062001, Jun. 2009.

[71] K. Triconnet, K. Derrien, F. Hild, and D. Baptiste, "Parameter choice for optimized digital image correlation," *Optics and Lasers in Engineering*, vol. 47, no. 6, pp. 728–737, Jun. 2009.

[72] J. C. Dupré, M. Bornert, L. Robert, and B. Wattrisse, “Digital image correlation: displacement accuracy estimation,” *EPJ Web of Conferences*, vol. 6, p. 31006, Jun. 2010.

[73] O. Ronneberger, M. Raffel, and J. Kompenhans, “Ddvanced evaluation algorithms for standard and dual plane particle velocity,” in *9th International Symposia on Applications of Laser Techniques to Fluid Mechanics*, 1998.

[74] P. Bing, X. Hui-min, X. Bo-qin, and D. Fu-long, “Performance of sub-pixel registration algorithms in digital image correlation,” *Measurement Science and Technology*, vol. 17, no. 6, pp. 1615–1621, Jun. 2006.

[75] H. W. Schreier and M. A. Sutton, “Systematic errors in digital image correlation due to undermatched subset shape functions,” *Experimental Mechanics*, vol. 42, no. 3, pp. 303–310, Sep. 2002.

[76] L. Lourenco and A. Krothapalli, “On the accuracy of velocity and vorticity measurements with PIV,” *Experiments in Fluids*, vol. 18, no. 6, pp. 421–428, Apr. 1995.

[77] P. Lava, W. Van Paepegem, S. Coppieters, I. De Baere, Y. Wang, and D. Debruyne, “Impact of lens distortions on strain measurements obtained with 2D digital image correlation,” *Optics and Lasers in Engineering*, vol. 51, no. 5, pp. 576–584, May 2013.

[78] L. C. S. Nunes, “Shear modulus estimation of the polymer polydimethylsiloxane (PDMS) using digital image correlation,” *Materials & Design*, vol. 31, no. 1, pp. 583–588, Jan. 2010.

[79] B. Guo, H. Xie, J. Zhu, H. Wang, P. Chen, and Q. Zhang, “Study on the mechanical behavior of adhesive interface by digital image correlation,” *Science China Physics, Mechanics and Astronomy*, vol. 54, no. 4, pp. 574–580, Feb. 2011.

[80] J. D. S. Goutianos, “Estimations of interface cohesive layws by digital image correlation,” in *Proceedings of the 28th Riso International Symposium on Materials Science: Interface Design of Polymer Matrix Composites Mechanics, Chemistry, Modelling and Manufacturing*, 2007.

[81] M.-P. Moutrille, K. Derrien, D. Baptiste, X. Balandraud, and M. Grédiac, “Through-thickness strain field measurement in a composite/aluminium adhesive joint,” *Composites Part A: Applied Science and Manufacturing*, vol. 40, no. 8, pp. 985–996, Aug. 2009.

[82] C. K.W., M. Das, D. Hahs, J. Gorman, and E. Madenci, “Digital Image Correlation for Adhesive Strains in Bonded Composite Lap Joints,” in *Proceedings of the 49th AIAA/ASME/ASCE/AHS/ASC Structures, Structural Dynamics, and Materials Conference*, 2008.

[83] K. W. Colavito, J. Gorman, and E. Madenci, “Refinements in Digital Image Correlation Technique to Extract Adhesive Strains in Lap joints,” in *Proceedings of the 50th AIAA/ASME/ASCE/AHS/ASC Structures, Structural Dynamics, and Materials Conference*, 2009, p. 5031.

[84] A. J. Comer, K. B. Katnam, W. F. Stanley, and T. M. Young, "Characterising the behaviour of composite single lap bonded joints using digital image correlation," *International Journal of Adhesion and Adhesives*, vol. 40, pp. 215–223, Jan. 2013.

[85] K. B. Katnam, J. X. Dhôte, and T. M. Young, "Experimental Analysis of the Bondline Stress Concentrations to Characterize the Influence of Adhesive Ductility on the Composite Single Lap Joint Strength," *The Journal of Adhesion*, vol. 89, no. 6, pp. 486–506, Jun. 2013.

[86] Z. Y. Wang, L. Wang, W. Guo, H. Deng, J. W. Tong, and F. Aymerich, "An investigation on strain/stress distribution around the overlap end of laminated composite single-lap joints," *Composite Structures*, vol. 89, no. 4, pp. 589–595, Aug. 2009.

[87] K.-S. Kim, J.-S. Yoo, Y.-M. Yi, and C.-G. Kim, "Failure mode and strength of uni-directional composite single lap bonded joints with different bonding methods," *Composite Structures*, vol. 72, no. 4, pp. 477–485, 2006.

[88] R. Haghani, M. Al-Emrani, and R. Kliger, "Effects of geometrical modifications on behaviour of adhesive joints used to bond CFRP laminates to steel members - experimental investigation," in *Proceedings of the Nordic Steel Construction Conference*, 2009.

[89] S. Hashim, C. Berggreen, N. Tsouvalis, D. McGeorge, I. Chirica, P. Moore, S. Boyd, J. Nisar, K. Anyfantis, K. Misirlis, and E. Juin, "Design and analysis of DLS steel/composite thick-adherend adhesive joints."

[90] C. Badulescu, M. Grédiac, and J. D. Mathias, "Investigation of the grid method for accurate in-plane strain measurement," *Measurement Science and Technology*, vol. 20, no. 9, p. 095102, Sep. 2009.

[91] F. Pierron and M. Grédiac, *The virtual fields method. Extracting constitutive mechanical parameters from full-field deformation measurements*, 1st ed. New York: Springer-Verlag, 2012, p. 517.

[92] B. Han, D. Post, and P. Ifju, "Moire interferometry for engineering mechanics: current practices and future developments," *The Journal of Strain Analysis for Engineering Design*, vol. 36, no. 1, pp. 101–117, Jan. 2001.

[93] D. Post and B. Han, "Moiré Interferometry," in *Springer Handbook of Experimental Solid Mechanics*, J. W. Sharpe, Ed. Springe, 2008, p. 1098.

[94] D. Mollenhauer and J. Tyson, "Comparison of Moiré Interferometry and Image Correlation Deformation Measurement Techniques," in *SEM X International Congress & Exposition on Experimental & Applied Mechanics*, 2004.

[95] A. Asundi, "Deformation in adhesive joints using Moiré interferometry," *International Journal of Adhesion and Adhesives*, vol. 7, no. 1, pp. 39–42, Jan. 1987.

[96] M. Y. Tsai and J. Morton, "The effect of a spew fillet on adhesive stress distributions in laminated composite single-lap joints," *Composite Structures*, vol. 32, no. 1–4, pp. 123–131, 1995.

[97] P. D. Ruiz, F. Jumbo, J. M. Huntley, I. A. Ashcroft, and G. M. Swallowe, "Strain Measurement in the Adhesive Layer of a Bonded Joint Using High Magnification Moire Interferometry," *Experimental Analysis of Nano and Engineering Materials and Structures*. pp. 357–358, 2007.

[98] J. Konnerth, A. Valla, W. Gindl, and U. Müller, "Measurement of strain distribution in timber finger joints," *Wood Science and Technology*, vol. 40, no. 8, pp. 631–636, Jul. 2006.

[99] U. Müller, A. Sretenovic, A. Vincenti, and W. Gindl, "Direct measurement of strain distribution along a wood bond line. Part 1: Shear strain concentration in a lap joint specimen by means of electronic speckle pattern interferometry," *Holzforschung*, vol. 59, no. 3, Jan. 2005.

[100] G. Pitarresi and E. Patterson, "A review of the general theory of thermoelastic stress analysis," *The Journal of Strain Analysis for Engineering Design*, vol. 38, no. 5, pp. 405–417, Jan. 2003.

[101] J. M. Dulieu-Barton, "Introduction to thermoelastic stress analysis," *Strain*, vol. 35, no. 2, pp. 35–39, May 1999.

[102] P. Stanley and W. Chan, "The application of thermoelastic stress analysis techniques to composite materials," *The Journal of Strain Analysis for Engineering Design*, vol. 23, no. 3, pp. 137–143, Jul. 1988.

[103] R. A. Tomlinson and E. J. Olden, "Thermoelasticity for the analysis of crack tip stress fields - a review," *Strain*, vol. 35, no. 2, pp. 49–55, May 1999.

[104] R. K. Fruehmann, J. M. Dulieu-Barton, and S. Quinn, "Assessment of fatigue damage evolution in woven composite materials using infra-red techniques," *Composites Science and Technology*, vol. 70, no. 6, pp. 937–946, Jun. 2010.

[105] S. W. Boyd, J. M. Dulieu-Barton, and L. Rumsey, "Stress analysis of finger joints in pultruded GRP materials," *International Journal of Adhesion and Adhesives*, vol. 26, no. 7, pp. 498–510, Oct. 2006.

[106] J. M. Dulieu-Smith, S. Quinn, R. A. Shenoi, P. J. C. L. Read, and S. S. J. Moy, "Thermoelastic stress analysis of a GRP tee joint," *Applied Composite Materials*, vol. 4, no. 5, pp. 283–303, Sep. 1997.

[107] S. Johnson, B. Wei, and R. Haj-Ali, "A stochastic fatigue damage model for composite single lap shear joints based on Markov chains and thermoelastic stress analysis," *Fatigue & Fracture of Engineering Materials & Structures*, vol. 33, no. 12, pp. 897–910, Dec. 2010.

[108] S. W. Boyd, J. M. Dulieu-Barton, O. T. Thomsen, and A. Gherardi, "Development of a finite element model for analysis of pultruded structures using thermoelastic data," *Composites Part A: Applied Science and Manufacturing*, vol. 39, no. 8, pp. 1311–1321, Aug. 2008.

[109] S. W. Boyd, J. M. Dulieu-Barton, O. T. Thomsen, and S. El-Gazzani, "Through thickness stress distributions in pultruded GRP materials," *Composite Structures*, vol. 92, no. 3, pp. 662–668, Feb. 2010.

[110] T. Allen, M. Battley, P. Casari, B. Kerling, I. Stenius, and J. Westlund, “Structural Responses of High Performance Sailing Yachts to Slamming Loads,” in *11th International Conference on Fast Sea Transportation*, 2011, no. September 2011, pp. 585–592.

[111] E. Lolive, P. Casari, and P. Davies, “Loading rate effects on foam cores for marine sandwich structures,” in *Proceedings of the 7th International Conference on Sandwich Structures*, 2005, pp. 895–903.

[112] P. Manganelli, “Experimental investigation of dynamic loads on offshore racing yachts,” University of Southampton, 2006.

[113] M. Hobbs and P. Manganelli, “Measurment of accelerations and keel loads on canting keel race yachts,” in *RINA Modern Yacht Conference*, 2007.

[114] M. A. Battley, T. Allen, P. Pehrson, I. Stenius, A. Rosen, and N. Zealand, “Effects of panel stiffness on slamming responses of composite hull panels,” in *17th International Conference on Composite Materials ICCM17*, 2009.

[115] R. W. Armstrong and S. M. Walley, “High strain rate properties of metals and alloys,” *International Materials Reviews*, vol. 53, no. 3, pp. 105–128, 2008.

[116] G. C. Jacob, J. M. Starbuck, J. F. Fellers, S. Simunovic, and R. G. Boeman, “Strain Rate Effects on the Mechanical Properties of Polymer Composite Materials,” *Polymer*, 2009.

[117] S. Thiruppukuzhi, “Testing and modeling high strain rate behavior of polymeric composites,” *Composites Part B: Engineering*, vol. 29, no. 5, pp. 535–546, Sep. 1998.

[118] H. Hsiao, “Strain rate behavior of composite materials,” *Composites Part B: Engineering*, vol. 29, no. 5, pp. 521–533, Sep. 1998.

[119] T. Iwamoto, T. Nagai, and T. Sawa, “Experimental and computational investigations on strain rate sensitivity and deformation behavior of bulk materials made of epoxy resin structural adhesive,” *International Journal of Solids and Structures*, vol. 47, no. 2, pp. 175–185, 2010.

[120] M. A. Martınez, I. S. Chocron, J. Rodrı, V. Sanchez, and L. A. Sastre, “Confined compression of elastic adhesives at high rates of strain,” *Journal Of Adhesion*, vol. 18, pp. 375–383, 1998.

[121] L. Ã. Goglio, L. Peroni, M. Peroni, and M. Rossetto, “High strain-rate compression and tension behaviour of an epoxy bi-component adhesive,” *Journal Of Adhesion*, vol. 28, pp. 329–339, 2008.

[122] O. Essersi, M. Tarfaoui, S. W. Boyd, F. Meraghni, and R. A. Shenoi, “Dynamic study of adhesively bonded double lap composite joints,” in *17th International Conference on Composite Materials*, 2009.

[123] L. Zachary and C. Burger, “Dynamic wave propagation in a single lap joint,” *Experimental Mechanics*, vol. 20, no. 5, pp. 162–166, May 1980.

[124] L. Ã. Goglio and M. Rossetto, “Impact rupture of structural adhesive joints under different stress combinations,” vol. 35, pp. 635–643, 2008.

[125] C. Galliot, J. Rousseau, and G. Verchery, “International Journal of Adhesion & Adhesives Drop weight tensile impact testing of adhesively bonded carbon / epoxy laminate joints,” *International Journal of Adhesion and Adhesives*, vol. 35, pp. 68–75, 2012.

[126] G. Challita and R. Othman, “International Journal of Adhesion & Adhesives Finite-element analysis of SHPB tests on double-lap adhesive joints,” *International Journal of Adhesion and Adhesives*, vol. 30, no. 4, pp. 236–244, 2010.

[127] S.-S. Pang, C. Yang, and Y. Zhao, “Impact response of single-lap composite joints,” *Composites Engineering*, vol. 5, no. 8, pp. 1011–1027, Jan. 1995.

[128] S. Raykhere, P. Kumar, R. K. Singh, and V. Parameswaran, “Dynamic shear strength of adhesive joints made of metallic and composite adherents,” *Materials and Design*, vol. 31, no. 4, pp. 2102–2109, 2011.

[129] C. Sato and K. Ikegami, “Dynamic deformation of lap joints and scarf joints under impact loads,” *Journal Of Adhesion*, vol. 20, pp. 17–25, 2000.

[130] P. L. Reu and T. J. Miller, “The application of high-speed digital image correlation,” *The Journal of Strain Analysis for Engineering Design*, vol. 43, no. 8, pp. 673–688, Aug. 2008.

[131] M. S. Kirugulige, H. V. Tippur, and T. S. Denney, “Measurement of transient deformations using digital image correlation method and high-speed photography: application to dynamic fracture,” *Appl. Opt.*, vol. 46, no. 22, pp. 5083–5096, Aug. 2007.

[132] L. R. Xu and A. J. Rosakis, “An experimental study of impact-induced failure events in homogeneous layered materials using dynamic photoelasticity and high-speed photography,” *Optics and Lasers in Engineering*, vol. 40, no. 4, pp. 263–288, Oct. 2003.

[133] M. T. Kokaly, J. Lee, and A. S. Kobayashi, “Moiré interferometry for dynamic fracture study,” *Optics and Lasers in Engineering*, vol. 40, no. 4, pp. 231–247, Oct. 2003.

[134] D. A. Crump, J. M. Dulieu-Barton, and R. K. Fruehmann, “Challenges in synchronising high speed full-field temperature and strain measurement,” in *Conference Proceedings of the Society for Experimental Mechanics Series 2011*, 2011.

[135] R. K. Fruehmann, D. A. Crump, and J. M. Dulieu-Barton, “The use of infrared thermography at high frame rates,” in *Conference Proceedings of the Society for Experimental Mechanics Series 2011*, 2011.

[136] S. P. Fernberg and L. A. Berglund, “Bridging law and toughness characterisation of CSM and SMC composites,” *Composites Science and Technology*, vol. 61, no. 16, pp. 2445–2454, 2001.

[137] C. Lundsgaard-Larsen, C. Berggreen, and L. A. Carlsson, “Tailoring Sandwich Face/Core Interfaces for Improved Damage Tolerance—Part II: Experiments,” *Applied Composite Materials*, vol. 17, no. 6, pp. 621–637, Apr. 2010.

[138] Huntsman, “Araldite 2015 Data Sheet,” 2007. [Online]. Available: http://www.intertronics.co.uk/data/ara2015.pdf.

[139] R. . Ferguson, M. . Hinton, and M. . Hiley, "Determining the through-thickness properties of FRP materials," *Composites Science and Technology*, vol. 58, no. 9, pp. 1411–1420, Sep. 1998.

[140] S. Vali-shariatpanahi, "Determination of through thickness properties for Composite thick laminate," in *17th International Conference on Composite Materials*, 2009.

[141] J. L. Abot and I. M. Daniel, "Through-Thickness Mechanical Characterization of Woven Fabric Composites," *Journal of Composite Materials*, vol. 38, no. 7, pp. 543–553, Apr. 2004.

[142] R. Kitching, A. L. Tan, and T. M. N. Abu-Mansour, "The influence of through thickness properties on glass reinforced plastic laminated structures," *Composite Structures*, vol. 2, no. 2, pp. 105–151, Jan. 1984.

[143] A. Inc., *ANSYS Modeling and Meshing Guide : Ansys Relese 10.0*. 2005.

[144] J. N. Reddy, *Mechanics of Laminated Composite Plates and Shells: Theory and Analysis, Second Edition*. CRC Press, 2004.

[145] R. K. Fruehmann, "Stress and damage assessment in woven composite materials by means of thermoelastic stress analysis," University of Southampton, 2009.

[146] S. Yaofeng and J. Pang, "Study of optimal subset size in digital image correlation of speckle pattern images," *Optics and Lasers in Engineering*, vol. 45, no. 9, pp. 967–974, Sep. 2007.

[147] H. W. Schreier, J. R. Braasch, and M. A. Sutton, "Systematic errors in digital image correlation caused by intensity interpolation," *Optical Engineering*, vol. 39, no. 11, p. 2915, 2000.

[148] P.-C. Hung and A. S. Voloshin, "In-plane strain measurement by digital image correlation," *Journal of the Brazilian Society of Mechanical Sciences and Engineering*, vol. 25, no. 3, Sep. 2003.

[149] H. Haddadi and S. Belhabib, "Use of rigid-body motion for the investigation and estimation of the measurement errors related to digital image correlation technique," *Optics and Lasers in Engineering*, vol. 46, no. 2, pp. 185–196, Feb. 2008.

[150] Y. Barranger, P. Doumalin, J. C. Dupré, and a. Germaneau, "Digital Image Correlation accuracy: influence of kind of speckle and recording setup," *EPJ Web of Conferences*, vol. 6, p. 31002, Jun. 2010.

[151] B. Pan, H. Xie, Z. Wang, K. Qian, and Z. Wang, "Study on subset size selection in digital image correlation for speckle patterns.," *Optics express*, vol. 16, no. 10, pp. 7037–48, May 2008.

[152] B. Pan, Z. Lu, and H. Xie, "Mean intensity gradient: An effective global parameter for quality assessment of the speckle patterns used in digital image correlation," *Optics and Lasers in Engineering*, vol. 48, no. 4, pp. 469–477, Apr. 2010.

[153] T. Hua, H. Xie, S. Wang, Z. Hu, P. Chen, and Q. Zhang, "Evaluation of the quality of a speckle pattern in the digital image correlation method by mean subset fluctuation," *Optics & Laser Technology*, vol. 43, no. 1, pp. 9–13, Feb. 2011.

[154] D. Lecompte, a. Smits, S. Bossuyt, H. Sol, J. Vantomme, D. Van Hemelrijck, and a. M. Habraken, "Quality assessment of speckle patterns for digital image correlation," *Optics and Lasers in Engineering*, vol. 44, no. 11, pp. 1132–1145, Nov. 2006.

[155] T. L. Alexander, J. E. Harvey, and A. R. Weeks, "Average speckle size as a function of intensity threshold level : comparison of experimental measurements with theory," *Applied Optics*, vol. 33, no. 35, 1994.

[156] C. Shannon, "A mathematical theory of communication," *Bell System Technical Journal*, vol. 27, p. 379, 1948.

[157] H. Edelsbrunner, D. G. Kirkpatrick, and R. Seidel, "On the shape of a set of points in the plane," in *IEEE Transactions on Information Theory*, 1983, p. 551.

[158] P. Rae, S. Palmer, H. Goldrein, A. Lewis, and J. Field, "White-light digital image cross-correlation (DICC) analysis of the deformation of composite materials with random microstructure," *Optics and Lasers in Engineering*, vol. 41, no. 4, pp. 635–648, Apr. 2004.

[159] A. El Bartali, V. Aubin, and S. Degallaix, "Fatigue damage analysis in a duplex stainless steel by digital image correlation technique," *Fatigue & Fracture of Engineering Materials and Structures*, vol. 31, no. 2, pp. 137–151, Feb. 2008.

[160] D. Zhang, D. Arola, and M. Luo, "Characterization of Mechanical Properties on the Meso-scale with Digital Image Correlation," in *SEM X International Congress & Exposition on Experimental & Applied Mechanics*, 2004.

[161] D. Zhang, M. Luo, and D. D. Arola, "Displacement/strain measurements using an optical microscope and digital image correlation," *Optical Engineering*, vol. 45, no. 3, p. 033605, 2006.

[162] D. Lecompte, S. Bossuyt, S. Cooreman, H. Sol, and J. Vantomme, "Study and Generation of Optimal Speckle Patterns for DIC," in *Proceedings of the SEM Annual Conference & Exposition on Experimental and Applied Mechanics*, 2007.

[163] P. Lava, S. Coppieters, Y. Wang, P. Van Houtte, and D. Debruyne, "Error estimation in measuring strain fields with DIC on planar sheet metal specimens with a non-perpendicular camera alignment," *Optics and Lasers in Engineering*, vol. 49, no. 1, pp. 57–65, Jan. 2011.

[164] W. Possart, "Elastic-plactic Properties of Structural Adhesive Systems," in *Adhesion*, 1st ed., Weinheim: Wiley, 2006.

[165] J. Dulieu-Barton and P. Stanley, "Development and applications of thermoelastic stress analysis," *The Journal of Strain Analysis for Engineering Design*, vol. 33, no. 2, pp. 93–104, Jan. 1998.

[166] P. Stanley and W. K. Chan, “Quantitative stress analysis by means of the thermoelastic effect,” *The Journal of Strain Analysis for Engineering Design*, vol. 20, no. 3, pp. 129–137, Jul. 1985.

[167] J. McKelvie, “Consideration Of The Surface Temperature Response To Cyclic Thermoelastic Heat Generation,” in *SPIE Proceedings*, 1987, pp. 44–55.

[168] M. Becchetti, R. Flori, M. Marsili, M. Moretti, and E. P. Tomasini, “Comparison between Digital Image Correlation and Thermoelasticity for Strain Field Analysis,” 2010, pp. 233–240.

[169] S. Johnson, “Computational modelling, stocastic and experiemtnal analysis with thermoelastic stress anslysis for fiber reinforced polymeric composite material systems,” Georgia Institute of Technology, 2010.

[170] T. Sakagami, S. Kubo, and F. Y, “Full-Field Stress Separation Using Thermoelasticity and Photoelasticity and Its Application to Fracture Mechanics,” in *SEM Annual Conference & Exposition on Experimental and Applied Mechanics*, 2002.

[171] S. Barone and E. a. Patterson, “Full-field separation of principal stresses by combined thermo- and photoelasticity,” *Experimental Mechanics*, vol. 36, no. 4, pp. 318–324, Dec. 1996.

[172] J. M. Dulieu-Barton, “Chapter 8: Thermoelastic Stress Analysis,” in *Optical Methods for Solid Mechanics*, P. Rastogi and E. Hack, Eds. Berlin: Wiley, 2012.

[173] T. Sakagami, N. Yamaguchi, S. Kubo, and T. Nishimura, “A new full-field motion compensation technique for infrared stress measurement using digital image correlation,” *The Journal of Strain Analysis for Engineering Design*, vol. 43, no. 6, pp. 539–549, Jun. 2008.

[174] A. Salerno, A. Costa, and G. Fantoni, “Calibration of the thermoelastic constants for quantitative thermoelastic stress analysis on composites.,” *The Review of scientific instruments*, vol. 80, no. 3, p. 034904, Mar. 2009.

[175] J. . Dulieu-Smith and P. Stanley, “The thermoelastic response of a thinwalled orthotropic cylinder loaded in torsion,” *Proc. SEM spring conference and exhibits*, pp. 498–506, 1994.

[176] D. A. Crump, “Assessment of Non-adiabatic Behaviour in Thermoelastic Stress Analysis of Composite Sandwich Panels,” *Experimental Mechanics*, 2012.

[177] M. Y. Tsai and J. Morton, “An investigation into the stresses in double-lap adhesive joints with laminated composite adherends,” *International Journal of Solids and Structures*, vol. 47, no. 24, pp. 3317–3325, Dec. 2010.

[178] P. Lava, S. Cooreman, and D. Debruyne, “Study of systematic errors in strain fields obtained via DIC using heterogeneous deformation generated by plastic FEA,” *Optics and Lasers in Engineering*, vol. 48, no. 4, pp. 457–468, Apr. 2010.

[179] V. P. Rajan, M. N. Rossol, and F. W. Zok, “Optimization of Digital Image Correlation for High-Resolution Strain Mapping of Ceramic Composites,” *Experimental Mechanics*, vol. 52, no. 9, pp. 1407–1421, Apr. 2012.

[180] B. Revsin and S. . Bodner, “Experiments on the dynamic tensile strength of metals and plastics,” *Isreal Journal of Technology*, vol. 7, pp. 485–493, 1969.